BERGISCHE
UNIVERSITÄT
WUPPERTAL

UNIVERSITY OF WUPPERTAL

DOCTORAL THESIS

Trajectory Analysis on the Asian Tropopause Aerosol Layer (ATAL) based on Balloon Measurements at the Foothills of the Himalayas

---

Sreeharsha HANUMANTHU

A thesis submitted in fulfilment of the requirements
for the degree of Doctor of Natural Science

in the

Faculty of Mathematics and Natural Science

August 19, 2021

Trajectory Analysis on the Asian Tropopause Aerosol Layer (ATAL) based on Balloon Measurements at the Foothills of the Himalayas

Approved by:
Date of the Examination:

Declaration of Originality

I hereby declare that the matter manifested in this thesis contains genuine work and solely carried out by myself. Identical or similar form of this thesis has not yet been submitted. In keeping with the general practice of reporting scientific observations, I have used no other sources than those indicated in the bibliography. This applies to all types of sources.

I understand that violation of this declaration and deliberate deceptions may result in rejection of this work.

_____

Signature

_____

Date & Place

The PhD thesis can be quoted as follows:

urn:nbn:de:hbz:468-urn:nbn:de:hbz:468-20220110-104138-4
[http://nbn-resolving.de/urn/resolver.pl?urn=urn%3Anbn%3Ade%3Ahbz%3A468-20220110-104138-4]

DOI: 10.25926/nwh7-3j35
[https://doi.org/10.25926/nwh7-3j35]

Contents

List of Figures

List of Tables

Abstract

The South Asian summer monsoon is associated with a large-scale anticyclonic circulation in the Upper Troposphere and Lower Stratosphere, which confines the air mass inside. During boreal summer, the confinement of this air mass leads to an accumulation of aerosol between about 13 km and 18 km (360 K and 440 K potential temperature), this accumulation of aerosol constitutes the Asian Tropopause Aerosol Layer (ATAL). In this thesis balloon-borne aerosol back-scatter measurements of the ATAL are presented by the Compact Optical Backscatter Aerosol Detector (COBALD) instrument in Nainital in Northern India in August 2016, and in the post-monsoon time in November 2016. The presence of an ATAL is then detected by the enhancement of the August measurements compared to the November measurements. The measurements demonstrate a strong variability of the ATAL's altitude, vertical extent, aerosol backscatter intensity and cirrus cloud occurrence frequency. Such a variability cannot be deduced from climatological means of the ATAL as they are derived from satellite measurements. To explain this observed variability a Lagrangian back-trajectory analysis was performed using the Chemical Lagrangian Model of the Stratosphere (CLaMS). We identify the transport pathways of air parcels contributing to the ATAL over Nainital in August 2016, as well as the source regions of the air masses contributing to the composition of the ATAL. The analysis reveals a variety of factors contributing to the observed day-to-day variability of the ATAL: continental convection, tropical cyclones (maritime convection), dynamics of the anticyclone and stratospheric intrusions. Thus, the ATAL is a mixture of air masses coming from different atmospheric height layers. In addition, contributions from the model boundary layer originate in different geographic source regions. The location of strongest updraft along the backward trajectories reveal a cluster of strong upward transport at the southern edge of the Himalayan foothills. From the top of the convective outflow level (about 13 km; 360 K) the air parcels ascend slowly to ATAL altitudes within a large-scale upward spiral driven by the diabatic heating in the anticyclonic flow of the South Asian summer monsoon at UTLS altitudes. Cases with a strong ATAL typically show boundary layer contributions from the Tibetan Plateau, the foothills of the Himalayas

and other continental regions below the Asian monsoon. Weaker ATAL cases show higher contributions from the maritime boundary layer, often related to tropical cyclones, indicating a mixing of clean maritime and polluted continental air. On the one hand increasing anthropogenic emissions in the future are expected because of the strong growth of Asian economies, on the other hand implementation of new emission control measures (in particular in China) have reduced substantially the anthropogenic emissions of some pollutants contributing to the ATAL. It needs to be monitored in the future, whether the thickness and intensity of the ATAL will further increase, which likely impacts surface climate.

Motivation

Climate change is affecting the entire Earth; one of the major contributors to this is industrial evolution in recent years and decades. There have been a lot of precautionary measures put forward by scientific communities all over the world. The Word Meteorological Organization (WMO) has suggested that more care needed to be invested to monitor the water vapor concentrations over the Upper Troposphere and Lower Stratosphere (UTLS). Even at these great technologically advanced times, the UTLS has remained one of the only remotely accessible regions. Satellite observations are one way of obtaining information on the UTLS, however such observations have only limited spatial resolution. It is well known that understanding the chemical composition of the atmosphere at UTLS altitudes requires high resolution data. To achieve this goal good in-situ data are required. So in-situ observations throughout the UTLS will be key to understand UTLS processes.

One of the major elements involved is the transport of polluted air into the UTLS from Asia. These emissions are caused by an too efficient development in the industrial era all over Asia, which is particularly rapid over South Asia and South East Asia countries. The developing Asian nations are still lacking the necessary infrastructure to put precautionary measures in place to control emissions.

From past studies it is well understood that the key role in the transport to the UTLS is played by the monsoons over Asia. Considerable transport of pollutants from ground to UTLS happens in particularly during the summer monsoon season. Identifying the source regions of these pollutants contributing to the composition of the UTLS will be a way of understanding the processes behind the impact of Asian pollution on the chemical composition of air at UTLS altitudes. This involves complex phenomena, because the vertical transport is mainly driven by tropical convection which is driving the tropical air masses to the upper troposphere. This leads to the consideration of the Tropical Tropopause Layer (TTL) region where all these complex phenomena actively interact.

From recent studies it is understood that during the monsoon period, a huge aerosol concentration over the UTLS region also known as the Asian Tropopause Aerosol Layer (ATAL)

exists. This aerosol layer has been observed using satellite data at these altitudes. As UTLS exchange involves pollutants originating from different source regions, ATAL can be a serious factor in defining the status of weather and climate of the Earth system. ATAL contributors may influence the constant exchange happening between the lower stratosphere and upper troposphere as a natural phenomenon. To understand this influence using observed data is crucial, such data are here combined with model simulations.

In this thesis many open questions regarding the ATAL are addressed using measurements and simulations of the Chemical Lagrangian Model for Stratosphere (CLaMS). To achieve this goal, a number of balloon-borne campaigns have been conducted in the Asian monsoon region during the peak monsoon season period of year 2016 in the month of August.

In this thesis, the focus is on analysing the data of a recent instrument namely the COBALD (Compact Optical Back Scatter Aerosol Detector) which is used to identify the ATAL. The COBALD information is observed as a back-scatter ratio.

Chapter 1

Introduction

Monsoon systems all over the world have major impact on Climate both directly and indirectly. The Asian monsoon system is one of the strongest of all. The South Asian summer monsoon (SASM) (also referred to as the Indian summer monsoon) sustains the livelihood of millions of people. Droughts associated with a weak South Asian summer monsoon have a very strong impact on regional water security and thus on agriculture [Cook et al., 2010; Krishnan et al., 2016]. Both during the last two centuries and in history, famines caused by droughts in the Indian region have caused the death of millions of people [Passmore, 1951; Mishra et al., 2019]. Several different factors contribute to a weakening of the monsoon, including El Niño [Kumar et al., 1995], regional land-use changes [e.g., Krishnan et al., 2016], and anthropogenic aerosol forcing [e.g., Ramanathan et al., 2005; Krishnan et al., 2016; Fadnavis et al., 2019a]. For these reasons there was a need for a comprehensive assessment of monsoon, drought, tropical cyclones and other impact of climate change for India. This need has resulted in the first national climate change assessment for India [Raghavan et al., 2020].

The focus of this thesis is on anthropogenic aerosols at tropopause altitudes in the Indian monsoon, the so-called Asian Tropopause Aerosol Layer (ATAL). The existence of an ATAL in northern Hemisphere summer during the June-September period was first discovered in satellite observations of aerosol particles [Vernier et al., 2011, 2015, see also Sect. 1.5 below]. In the future, increasing industrial emissions in Asia will likely lead to a wider and thicker ATAL, which has the potential to amplify the severity of droughts in India [Fadnavis et al., 2019a]. Severe future droughts would have fatal consequences on Indian agriculture and therefore severe socio-economic impact in one of the most densely populated parts of the

world.

1.1 Meteorological background

1.1.1 Upper troposphere, lower stratosphere and tropopause

The Upper Troposphere and Lower Stratosphere (UTLS) are two distinct atmospheric layers which are separated by an intermediate layer called Tropopause [Hoinka, 1997], at which vertical mixing is restricted. The World Meteorological Organization (WMO) defined the tropopause as the location where the temperature lapse rate decreases to 2°K/km or less[1]. The tropopause is thus the thermodynamic gradient stratification layer which marks the top of the troposphere. The lower stratosphere region is very much linked dynamically, radiatively and chemically with the upper troposphere.

Further, a dynamical tropopause [Kunz et al., 2011] may be defined in terms of fast changes in potential vorticity with altitude (potential vorticity is much higher in the stratosphere than in the troposphere) or a chemical tropopause [Hoinka, 1997; Gettelman et al., 2011; Pan et al., 2018] as an abrupt increase of ozone with altitude. Another important concept is the cold-point tropopause, which is the coldest point in the temperature profile [Pan et al., 2018].

1.1.2 Tropical tropopause layer

The Tropical Tropopause Layer (TTL) is a critical region in the atmosphere, which may extend over several kilometres in the vertical (Fig. 1.1). The TTL is a tropical phenomenon that is the result of tropospheric upward transport of air and export of convective outflow at great altitudes [Fueglistaler et al., 2009]. In Fig. 1.1, cloud processes and transport are shown in the left hand panel and a zonal mean circulation picture is shown in the right hand panel. Figure 1.1 shows the the possible pathways through the TTL to neighboring atmospheric regions [Fueglistaler et al., 2009], in that arrows indicate circulation, black dashed line is the clear-sky level of zero net radiative heating (LZRH), and black solid lines show level of constant potential temperature (in K, based on European Centre for Medium-Range Weather Forecasts 40-year reanalysis (ERA-40) [e.g. Simmons et al., 2004]. Figure 1.1, further marks

[1]More precisely, the classical lapse rate tropopause [Hoinka, 1997] is defined as the lowest level where the absolute value of the temperature lapse rate decreases to below 2K/km. To count as a tropopause, the average lapse rate between this level and all higher levels within 2km should not exceed 2K/km.

the pathways in the TTL by letters. The letter 'a' indicates deep convection: main outflow around 200 hPa, rapid decay of outflow with height in the TTL, and rare penetrations of convection across the tropopause. The letter 'b' indicates radiative cooling (i.e., subsidence). The letter 'c' indicates subtropical jets, which limit quasi-isentropic exchange between the troposphere and stratosphere (see Sect. 1.3.2 below).

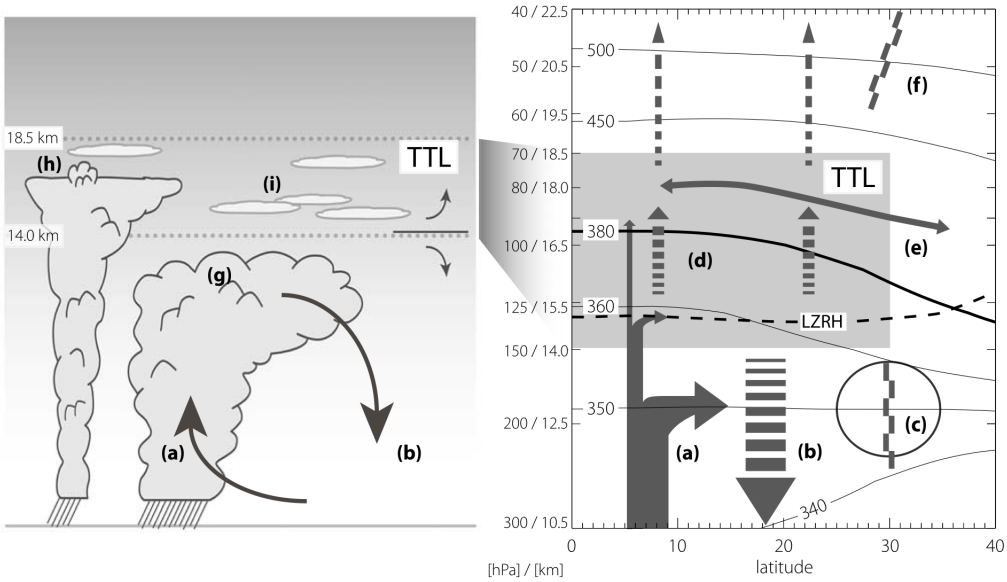

Figure 1.1: Schematic diagram of cloud processes(right) and transport (right) of zonal mean circulation in the tropical tropopause layer (TTL). Figure has been adapted from Fueglistaler et al. [2009].

The letter 'd' indicates radiative heating and the letter 'e' indicates rapid meridional transport of tracers. The letter 'f' indicates the edge of "the tropical pipe" [Plumb, 1996; Volk et al., 1996] relative isolation of the tropics, and stirring over extra-tropics ("the surf zone") [McIntyre and Palmer, 1984]. The letter 'g' indicates deep convective clouds. The letter 'h' indicates the convective core overshooting its level of neutral buoyancy [e.g. Schiller et al., 2009]. The letter 'i' indicates ubiquitous optically (and geometrically) thin, horizontally extensive cirrus clouds, often formed in-situ [Krämer et al., 2016]. The height-pressure-potential temperature relations are based on tropical annual mean temperature fields, with height values rounded to the nearest 0.5 km.

Figure 1.2 summarizes the possible boundaries for the upper troposphere and lower stratosphere and associated characteristics. The bottom of the TTL is considered to be 150 hPa and 70 hPa is considered as the top of the TTL [Fueglistaler et al., 2009]. The structure of the TTL is somewhat different in the Asian Monsoon, in particular, the tropopause is located at somewhat greater altitudes in the monsoon compared to the tropics in general [e.g. Brunamonti et al., 2018].

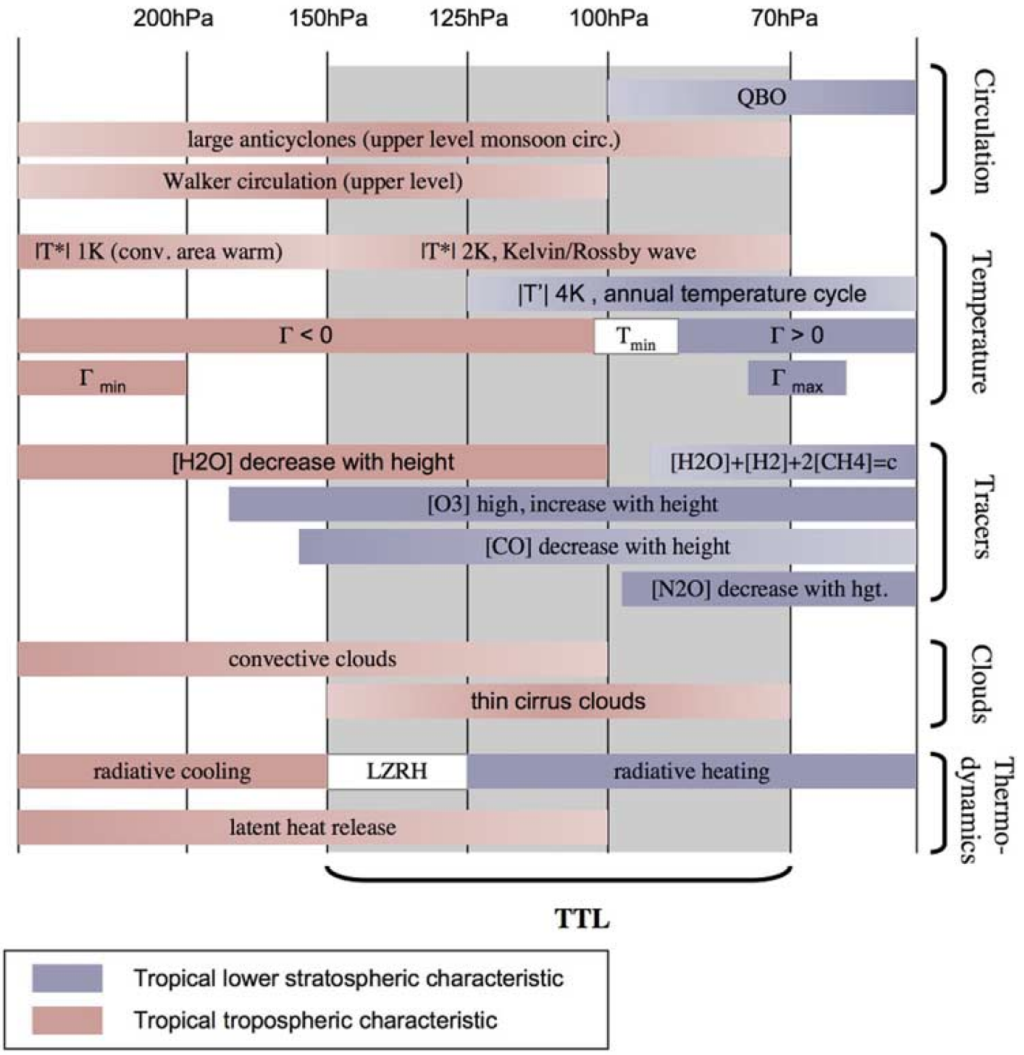

Figure 1.2: Schematic summary of tropospheric/stratospheric characteristics and transitions thereof (symbolically shown as fade out of colored pattern). G = temperature lapse rate; $T_{\min}$ = temperature minimum of profile; T^* = amplitude of quasi-stationary zonal temperature anomaly; T_0 = amplitude of tropical mean temperature seasonal cycle; T' = amplitude of the mean temperature seasonal cycle QBO = quasi biennial oscillation. Figure has been adapted from Fueglistaler et al. [2009].

1.1.3 Inter tropical convergence zone

The Inter-tropical Convergence Zone (ITCZ), is the area where the north-east and south-east trade winds converge. Precipitation in the ITCZ is driven by moisture convergence associated with the northerly and southerly trade winds that collide near the Equator. It accounts for more than 30% of the global precipitation [Kang et al., 2018]. A climatology of the ITCZ and its impact on global precipitation is shown in Fig. 1.3. It encircles Earth near the thermal Equator, though its specific position varies seasonally. When it lies near the geographic Equator, it is called the near-equatorial trough. Where the ITCZ is drawn into and merges with a monsoonal circulation, it is sometimes referred to as a monsoon trough,

a terminology common in Australia and parts of Asia. Climate data show that strong Asian monsoon years are indeed associated with anomalously strong northward movement of the ITCZ. During boreal summer, northward movement of the ITCZ accompanied by heating over the Tibetan Plateau (TP) strongly enhances northward cross-equatorial atmospheric mass transport in the lower troposphere associated with the Hadley circulation. The ITCZ migrates into the northern Hemisphere in response to warmer northern and cooler southern Hemisphere tropics and subtropics [Basha et al., 2015]. Over Asia, this migration is accompanied by northward migration of the upper-tropospheric subtropical zonal westerly jet [Schiemann et al., 2009], which moves north of the TP during mid-summer. When it does so, it enhances the Tibetan high circulation pattern, at the same time, boreal summer heating over the TP (30°N) drives onshore air mass transport, in which sensible heating from latent heat release in the mid-troposphere strongly drives convective and monsoon general circulation [Walker et al., 2015].

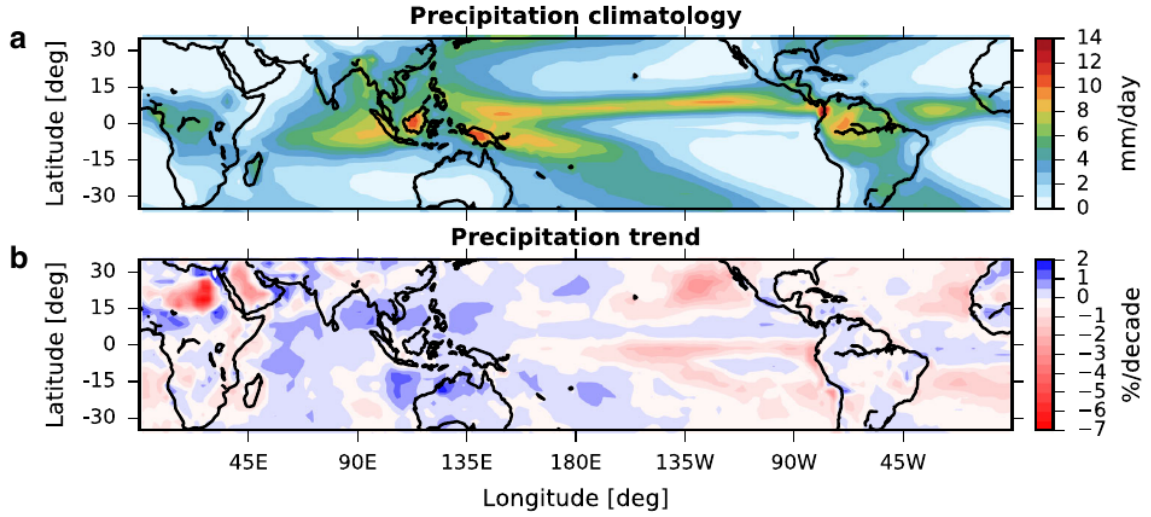

Figure 1.3: a) Global Precipitation Climatology Project (GPCP; version 2.3) 2.5° × 2.5° annual-mean precipitation climatology from 1979-2017. b) Trends in deseasonalized GPCP monthly-mean precipitation over 1979-2017. Figure has been adapted from Byrne et al. [2018].

1.1.4 Tropical cyclones

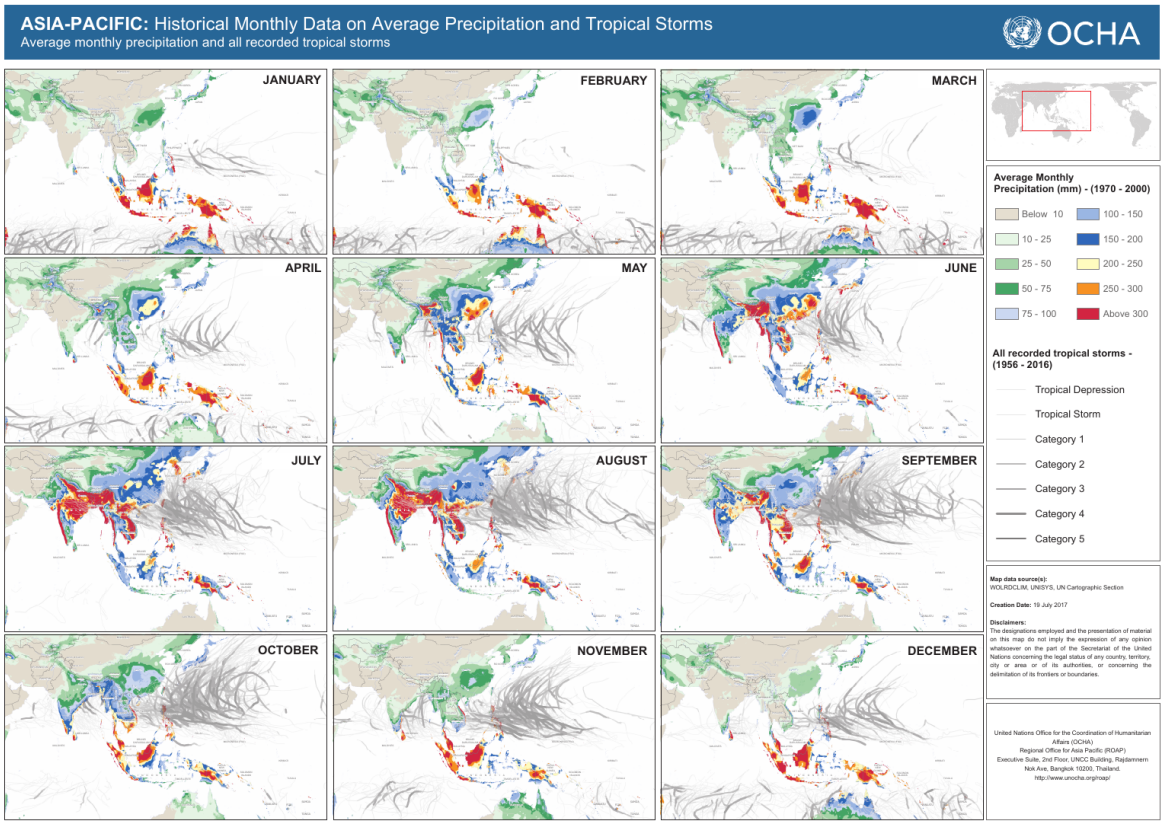

Figure 1.4: Asia-Pacific: Historical monthly data on average precipitation and tropical storms: Average monthly precipitation (1970 - 2000) and all recorded tropical storms (1956 - 2016). Figure has been adapted from UN Office for the Coordination of Humanitarian Affairs.

A tropical cyclone is a rapidly rotating storm system characterized by a low-pressure center, a closed low-level atmospheric circulation, strong winds, and a spiral arrangement of thunderstorms that produce heavy rain or squalls. The Bay of Bengal (BoB) is one of the most active regions for the formation of deep-convection-associated cyclones which contain strong updrafts. The same is true for the West Pacific (Fig 1.4). Earlier studies have shown a close relationship between cyclones and moistening of the upper troposphere [Rosenlof and Reid, 2008]. Figure 1.4 shows the average monthly precipitation and also tropical storm activity over the Asian region. Most relevant for this thesis are typhoons which occur most frequently over western Pacific from July to October [Matsuura et al., 2003]. Moreover, a statistical analysis of balloon measurements in China shows that the strongest impact of typhoons is found at altitudes between 14.5 and 17 km (365-375 K). Low ozone values (50-80 ppbv) were observed between 370 and 380 K due to the strong vertical upward transport of ozone-poor maritime surface air within tropical cyclones [Li et al., 2017].

1.2 The monsoon systems

The global monsoon systems are very much enriched in their local structures influenced by the Earth's revolution around the sun (i.e. by the seasons) and by many other factors, such as land-sea distribution, the interactions of the two Hemispheres and the topography. A consistent definition of the monsoon for meteorological purposes has been developed by Wang and LinHo [2002] as well as by Zhang and Wang [2008] who used a combination of rainfall amounts, the timing of the onset and cessation of the rainy season as well as atmospheric pressure to distinguish monsoons from other climates characterized by marked wet and dry seasons. Fig. 1.5 reflects the belt of global monsoons as recognized by Zhang and Wang [2008]. They all lie at the low latitudes, this demonstrates their origins as the seasonal migration of ITCZ (see Sect. 1.1.3). Based on the study of Zhang and Wang [2008], a classification of global monsoon regimes is developed here taking both winds and precipitation into consideration. In Fig. 1.5b; the domains are shown of the South Asian summer monsoon (SASM) also referred as Indian summer monsoon, the East Asian summer monsoon (EASM), the western North Pacific monsoon, the Indonesian - Austrailan summer monsoon (I-ASM) and the north African summer monsoon (NAfSM). It requires a land-sea thermal contrast along with the northward propagation of the ITCZ to establish a monsoon. The Asian monsoon very much depends on positive feedback between latent heat release and circulation patterns. The Asian summer monsoon system is subdivided into South Asian monsoon (SAM) or South Asian summer monsoon (SASM), the East Asian monsoon (EAM) or East Asian summer monsoon (EASM), and the transitional area (TA) which is an interaction between the SAM and EAM (see Fig. 1.5 for more details).

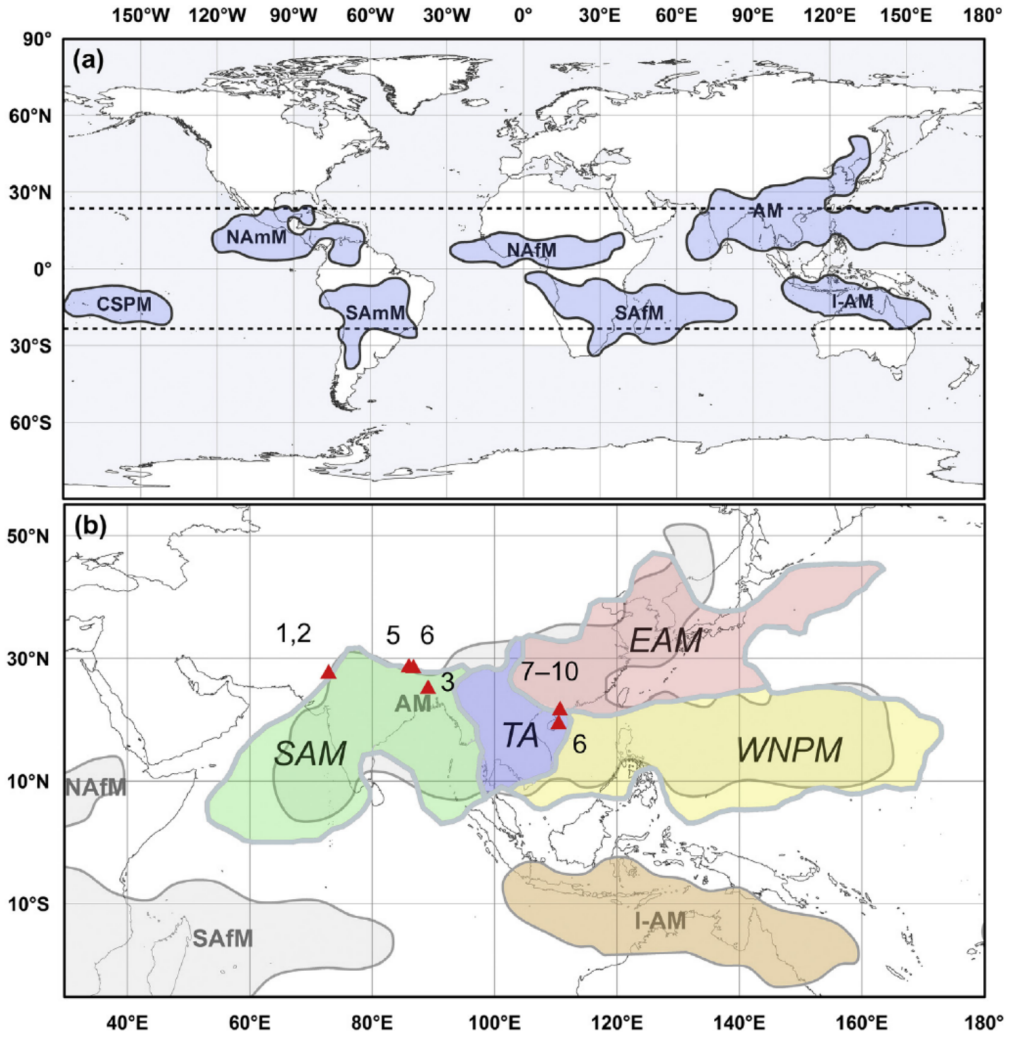

Figure 1.5: a) Map showing the positions and spatial extent of monsoons as defined by the meteorological parameters of Zhang and Wang [2008]. CSPM - Central Pacific Summer Monsoon, NAmM - North America Monsoon, SAmM - South America Monsoon, NAfM - North Africa Monsoon, SAfM - South Africa Monsoon; AM - Asia Monsoon, I-AM - Indonesia-Australia Monsoon. b) Map of Southern Asia showing the areas influenced by the South Asia Monsoon (SAM), the East Asia Monsoon (EAM), the Western northern Pacific Monsoon (WNPM), and the Indonesia - Australia Monsoon (I-AM) and the Transitional Area of interaction of the SAM and EAM. Thus Asian Monsoon is a composition of SAM, EAM and WNPM. Monsoon boundaries are based on meteorological parameters of Wang and LinHo [2002]. This figure has been adapted from Spicer [2017].

The monsoons of the southern Hemisphere, namely the Central Pacific summer monsoon (CPSM), the South American monsoon (SAmM), the South African monsoon (SAfM) and the Indonesia-Australia Monsoon (IAM) will no longer be considered here; the same is true for the North African Monsoon (NAfM). The focus of this thesis will be the Asian monsoon in spite of similarities with the North American summer monsoon [e.g. Yan et al., 2019] (the tranport of young wet tropospheric air masses into the stratosphere, however the North American monsoon (NAmM) is much weaker). The NAmM will not further be discussed.

1.2.1 The Asian summer monsoon

The focus of this thesis is on the Asian summer monsoon (AM as in the Fig. 1.5a). The Asian monsoon has significant winter and summer monsoon systems but efficient UTLS transport is mostly associated with summer monsoon and it is termed as Asian summer monsoon. The most dominant of summer monsoon regimes are notably East Asian summer monsoon (EASM), the South Asian summer monsoon (SAM), which is also referred to as Indian monsoon and the transition region (TA) between SAM and EAM (see Fig 1.5b). There is also the Western North Pacific monsoon (WNPM), which does not play a great role for the impact of the Asian monsoon at UTLS altitudes. So it is very important to have a greater insight on dynamics surrounding weather and climatic systems to understand the Indian summer monsoon as a whole.

For this thesis the understanding of monsoon atmosphere and its dynamics is essential. These dynamical features are schematically shown in Fig. 1.6 in terms of mean annual precipitation (MAP). The Asian summer monsoon (ASM) is dynamically bounded by the geographical features (see red line in Fig. 1.6). Interior Asia has active influence during winter (i.e., Siberian High) which is however weak during summer (Fig. 1.6). In addition, during summer Tibetan Plateau is a feature which helps the Indian Monsoon as it blocks the cold and dry air from polar regions and at the same time behaves like wall for the tropical air-masses and hinders the warm tropical air-masses to escape further north. This feature is unique to the Asian region. Westerlies which are mainly driven by the westerly jet (i.e., subtropical Jet-stream), bring in Atlantic moisture towards the Asian region, the southern boundary of the monsoon is mainly constrained by the warm Indian Ocean (warmest ocean of all respective oceanic regions) and low level jet (i.e. Somali jet transporting air from northern Africa towards India). The easterly transport from the Pacific ocean is mainly driven by western North Pacific monsoon (WNPM) and associated tropical cyclones.

The seasonal cycle of solar insolation leads to temperature gradients at the surface. In summer, this leads to a cross-equatorial pressure gradient from the Mascarene High in the southern Indian Ocean to the monsoon trough over northern India. Orography helps to steer the cross-equatorial flow back towards India and isolate South Asia from dry air in the north: the summer diagram shows a line (in red, see Fig. 1.7, top left) representing the location of maximum vertically integrated Moist Static Energy (MSE), bounding the northward extent of the monsoon Hadley-type circulation. Over the ocean, rainfall is located over the warmest SST, whereas maxima over India occur near the Western Ghats and Himalaya, and near the

Burmese mountains. During summer, upper-level jet structure moves north of the Tibetan Plateau. This leads to upper-level easterly flow over the peninsular South Asia, indeed the strength of the vertical shear at Indian latitudes has been shown to correlate with the Asian summer monsoon circulation [Webster and Yang, 1992].

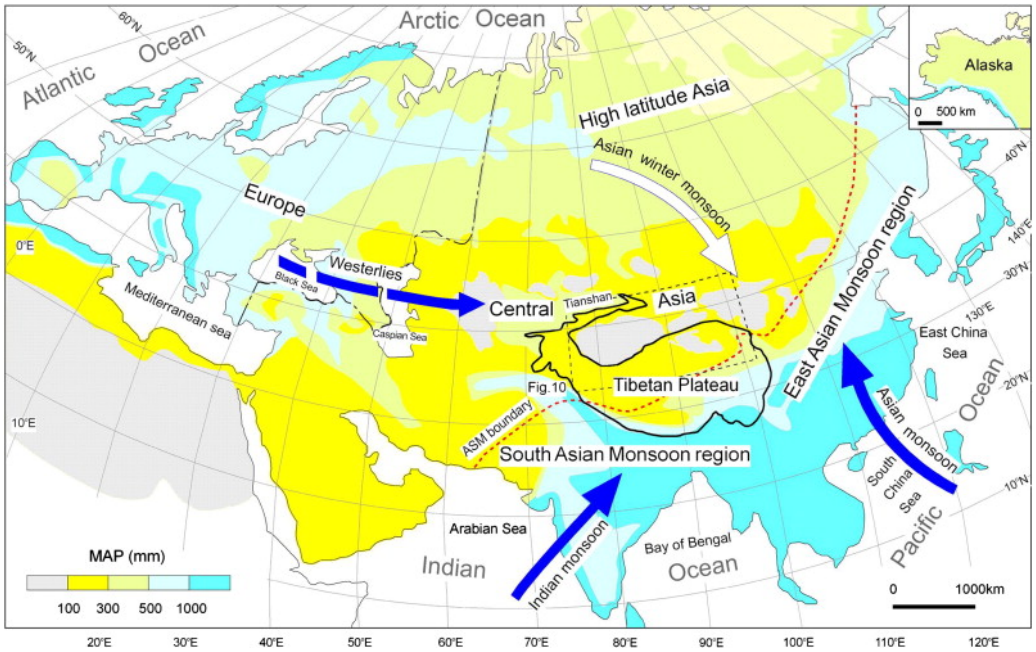

Figure 1.6: Asian summer monsoon system and dynamical phenomenon around it. The physical geography and distribution of precipitation throughout Eurasia. The main precipitation resources that influence Asia shown in terms of mean annual precipitation (MAP) are, Atlantic ocean moisture brought by the Westerlies, west Pacific moisture transport from western North Pacific summer monsoon (WNPM) flow, Indian Ocean moisture brought by the East Asian monsoon (EAM) and South Asian monsoon (SAM) and also moisture transport from Asian winter monsoon. Asian summer monsoon (ASM) limit is shown by a red dashed line. This figure has been adapted from Miao et al. [2012].

The Asian monsoon system is one of the largest and most dominant features on Earth (see Fig. 1.5). It is stronger than any of the other monsoon systems because of the topography of the Tibetan region, which insulates warm, moist air over South Asia (the sub-Himalayan countries of the Indian subcontinent) from the cold and dry extra-tropics. Heat emitted from the Tibetan plateau as dry heat and water vapour has long been assumed to be the main driver of the South Asian summer monsoon, but new work suggests that in fact it is the neighboring mountains that have the major influence. Boos and Kuang [2010] use an atmospheric model to show that flattening the Tibetan plateau has little effect on the monsoon, as long as the Himalayas and surrounding mountain ranges remain. The plateau boosts rainfall locally along its southern edge, it is the build-up of hot, moist air over India, insulated from colder, drier air by the Himalayas that drives large-scale monsoon circulation [Boos and Kuang, 2010]. This leads to a global maximum of surface moist static energy at

the South-western flank of the Himalayas [Boos and Hurley, 2013], which drives deep convective updrafts during northern Hemispheric summer. As the monsoon season progress elevated surface heating over the Tibetan plateau [Fu et al., 2006], predominantly northward surface winds plus orographic uplifting at the southern/South-western slopes of the Himalayas [Li et al., 2005; Liu et al., 2009] and deep convection over the Bay of Bengal [Park et al., 2009; Nützel et al., 2016] all contribute additionally to an overall ascending air current. This ascent drives an anticyclonic circulation, centered at 200 to 100 hPa [Dunkerton, 1995; Randel and Park, 2006; Garny and Randel, 2016]. This circulation is further discussed in Sect. 1.4.

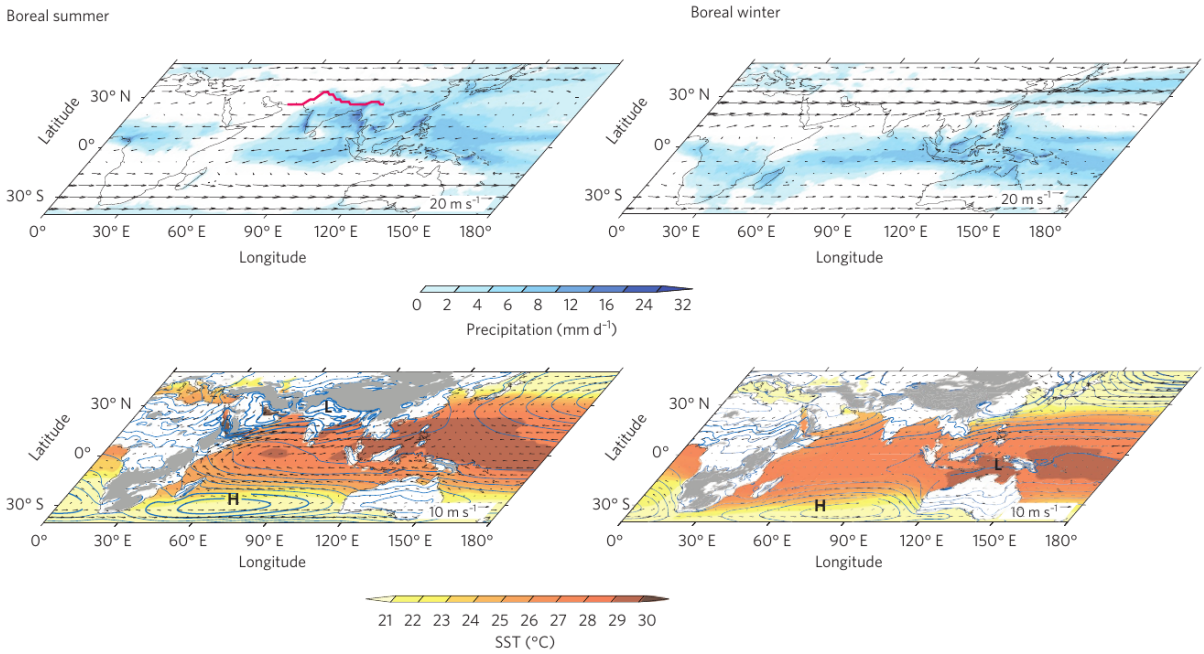

Figure 1.7: Schematic of boreal summer (June-September) and winter (December-February) atmospheric conditions in the South Asian monsoon region. The summer and winter panels depict the Asian and Australian monsoons, respectively. In each case, the lower panels show: orography (>1000 m, shaded grey); Sea surface temperature (SST)s from the Hadley Centre Sea Ice and Sea Surface Temperature data set for 1979-2010 [Rayner et al., 2003] (shaded yellow/orange); sea-level pressure for 1979-2010 (blue contours, interval−2 hPa) and lower tropospheric (850 hPa) winds from the European Centre for Medium-Range Weather Forecasts Interim Reanalysis [Dee et al., 2011]. 'H' and 'L' refer to the monsoon highs and lows, respectively, in the both summer and winter. In summer, the high reaches around 1024 hPa, where as the low is approximately 1000 hPa. The upper panel show upper tropospheric (200 hPa) wind vectors and Tropical Rainfall Measuring Mission (TRMM) monthly rainfall for 1998-2010 (shaded blue) [Huffman et al., 2007]. This figure has been adapted from Turner and Annamalai [2012].

1.2.2 South Asian summer monsoon

An important part of the Asian monsoon is the South Asian summer monsoon which is also referred to as the Indian summer monsoon. The Indian summer monsoon is connected to

neighboring monsoon systems (Fig. 1.5) and is significantly affected by the Indian landmass over which it establishes.

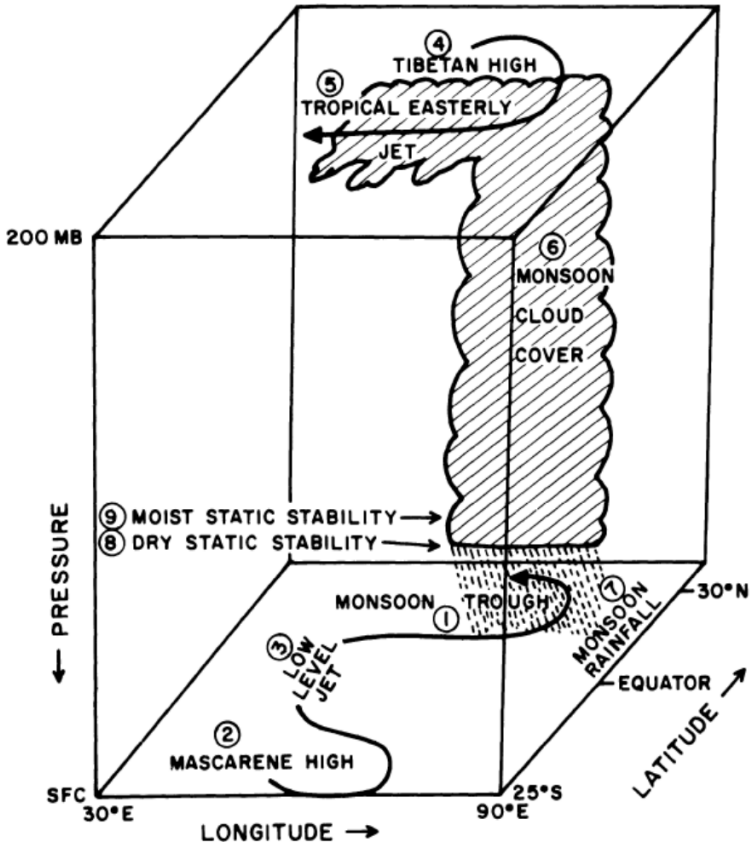

Figure 1.8: The different elements involved in the South Asian Monsoon system. This figure is adapted from Krishnamurti and Bhalme [1976].

The seasonal feature of a Tropical Easterly jet existence over the Indian landmass is a clear signal for the monsoon establishment over the Asian region. Tropical Easterly jet flows from east to west (see Fig. 1.8) at an altitude of 6-12 km above the Earth surface over the Indian Peninsular landmass. It comes into existence in early June during the monsoon period. The jet has a wind speed of roughly 40-50 m/s. The tropical easterly jet establishment during summer over the Indian peninsular region is a key element for an efficient monsoon season rainfall. This jet is very much responsive to the Tibetan high. The Tibetan high intensity will have an impact on Asian monsoon rainfall through modulating the easterly jet. The heat over Tibetan Plateau is very much important for the establishment of the Tibetan high, which is essential for the tropical easterly jet. This high is responsible for the monsoon trough intensity over the Indian subcontinent.

Asian monsoon seasonal features have been identified by the following key elements. The major features of the summer monsoon are demonstrated in Fig 1.8 as follows, 1. Semi-stable trough over the Indian peninsular region. 2. Strong high pressure zone over South

Indian Ocean called Mascarene High. 3. Cross-equatorial low-level jet establishment over western Indian ocean near Somali region called Somali Jet. 4. High pressure zone over the Tibetan Plateau called Tibetan High due to northward extension of subtropical jet. 5. Tropical Easterly Jet, a seasonal feature which is key to the Asian monsoon rainfall patterns. 6 and 7. Monsoon cloud cover associated with lows and depressions over the Asian region. 8 and 9. Moist static stability and dry static stability

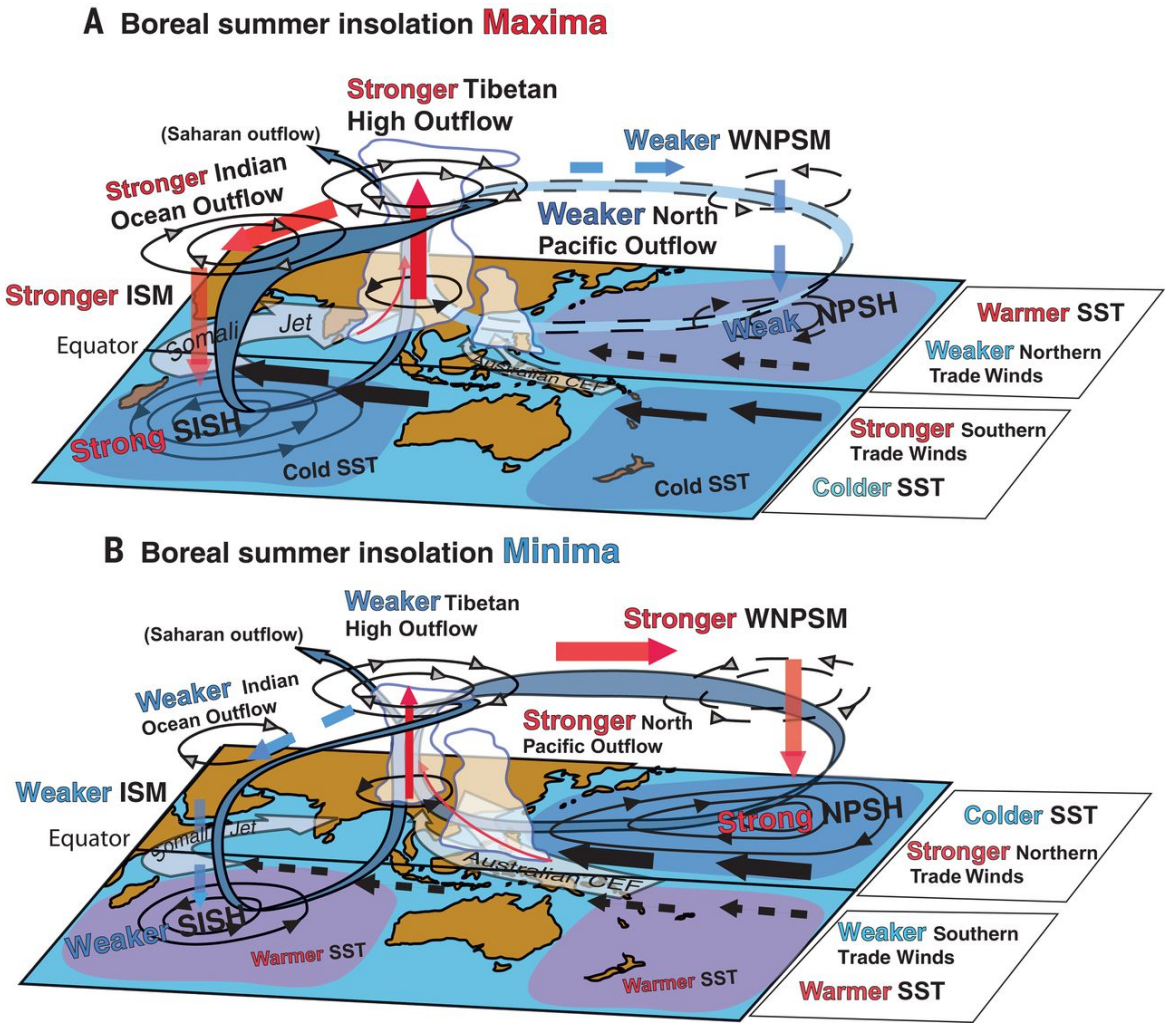

Figure 1.9: The Asian monsoon teleconections has been demonstrated in the above figure. Inter-tropical seesaw: Orbitally induced changes in solar insolation mimic the seasonal inter-hemispheric heating-cooling cycle in the tropics and subtropics. (A) During boreal summer insolation maxima, Tibetan high outflow to the southern Indian Ocean subtropical high (SISH) is increased in response to two factors: (i) colder SST in the South Indian ocean, which enhances the surface anticyclone there, and (ii) earlier seasonal transition of the upper-tropospheric subtropical zonal westerly jet [Schiemann et al., 2009; Zhu, 2012; Fu and Lin, 2011] to the north side of the TP, strengthening the Tibetan high. Both factors enhance Hadley circulation and result in strengthening trade winds and Somali jet in the Indian ocean, strengthening the Indian Summer Monsoon. At the same time, outflow to the North Pacific subtropical high (NPSH) is reduced in consequence to warmer north Pacific SST, producing weaker northern trade winds and smaller onshore pressure gradient in the North Pacific, weakening the Western North Pacific monsoon (WNPM). (B) During Boreal summer insolation minima, the opposite occurs. This figure has been adapted from Beck et al. [2018].

These complex features tend to repeat every year to make the Indian monsoon unique. Indian Monsoon turns out to be a global feature increasingly effecting different parts of the world through feedback circulations like El Niño and vice-versa. The typical strong monsoon domains with contrasting wet-dry seasons and reversals in winds are shown Fig. 1.7.

Figure 1.9 is an another demonstration of complexities involved in the monsoon progression and circulation patterns. It shows the inter-tropical seesaw: Orbitally induced changes in solar insolation mimic the seasonal inter hemispheric heating-cooling cycle in the tropics and subtropics [Beck et al., 2018].

1.3 Features of the South Asian summer monsoon

1.3.1 Monsoon on-set and withdrawal

The Monsoon onset is a very important event for the Indian society as it marks the monsoon arrival and associated precipitation over the Indian landmass. The climatological mean of the monsoon onset falls between 31st May and 1st of June [Ananthakrishnan and Soman, 1991]. But in general the onset varies from year to year with a standard deviation of 8.5 days. Such an indication is maintained over a long period of time by Indian Meteorological Department. Important events in the course of the monsoon are Monsoon Breaks which cause dry spells. Breaks in monsoon normally exist over days to weeks, see Fig. 1.10 to understand the slow progression of monsoon over the Indian landmass. Figure 1.10, top panel demonstrates how monsoon progression happens in climatology (i.e., normal, red) and how in 2016 the monsoon advancement (i.e., actual, shown in green) dates are varying, This year is when the measurements in India used in this PhD thesis were performed. Figure 1.10, bottom panel demonstrates withdrawal of monsoon phenomenon over the Indian region by showing climatology (i.e., normal, dark red in color) and how in 2016 the (i.e., actual, dark green in color) dates are varying. So overall, the monsoon in the year of 2016 had normal conditions from a meteorological point of view.

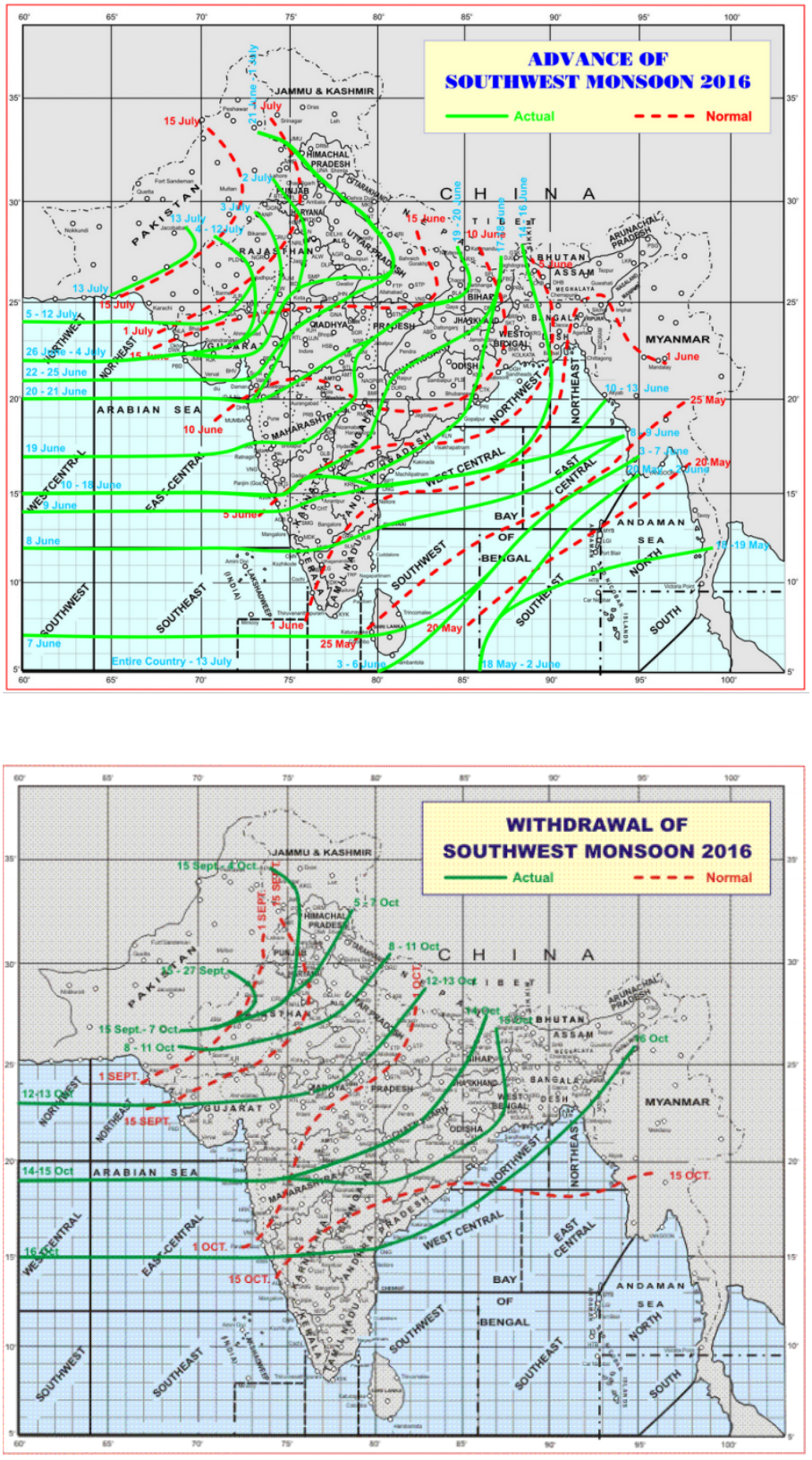

Figure 1.10: 2016 is the year when the measurements were performed. Top: shows (green) and advance of South Asian Summer Monsoon season in 2016 compared to the normal (Climatology) situation. It demonstrate monsoon actual season progression w.r.t climatology (i.e., red) of the following regions and also for the year 2016 (green). Bottom: shows withdrawal dates of monsoon year 2016 over the Indian region w.r.t climatology (i.e., normal, dark red) and also for the year 2016 (i.e., actual, dark green). Figures are adapted from the seasonal reports issued every year by the Indian Meteorological Department (IMD).

1.3.2 Subtropical jet stream

A jet stream is indicated wherever it is reliably determined that wind speeds equals or exceeds 50 knots. A subtropical jet (STJ) stream is confined to a band of relatively strong winds concentrated between 20° and 40° latitude in the middle and upper troposphere. The Jet stream is strongest off the Asian coast. The subtropical jet-stream varies greatly from day to day. The northern extension of STJ is key for Asian monsoon precipitation.

STJ is a salient feature of the subtropical upper- level flow and a key player in the dynamical processes that link the tropics with the subtropics and the extra-tropics. STJ is co-aligned with the band of strong potential vorticity (PV) gradients and therefore acts as a wave guide for synoptic scale Rossby waves [Hoskins and Ambrizzi, 1993; Schwierz et al., 2004].

The Meiyu (Baiu) front is an extension of confluent subtropical jet influence over East Asia, which stretches from north of the Tibetan Plateau to Japan and tends to cause heavy rainfall over eastern China and Japan during monsoon (JJA) [Ninomiya and Shibagaki, 2007]. The Meiyu front generally occurs from mid to late spring through early to mid-summer. The moisture source is typically the South China Sea and sometimes the Bay of Bengal. This front serves as a focus for persistent heavy convective rainfall associated with meso-scale convective systems (MCS).

1.3.3 Monsoon precipitation

Asian regions are clearly depending on the monsoon throughout the year as the monsoon may last for 6 months in some parts of the region. So monsoon is specified as pre-monsoon (MAM), summer monsoon (JJAS), post-monsoon or winter monsoon (ON) and Spring (DJF). Interannual variability of the Indian Summer Monsoon Rainfall depends on the internal dynamics and external drivers as well (El Niño, La Niña, Indian ocean dipole (IOD) etc.). The status of Indian monsoon and the associated rainfall over the years since 1870 in regard to El Niño and La Niña events over the Pacific is shown in Fig. 1.11. The year 2016 was a normal year in terms of precipitation; neither a strong El Niño nor a strong La Niña occurred.

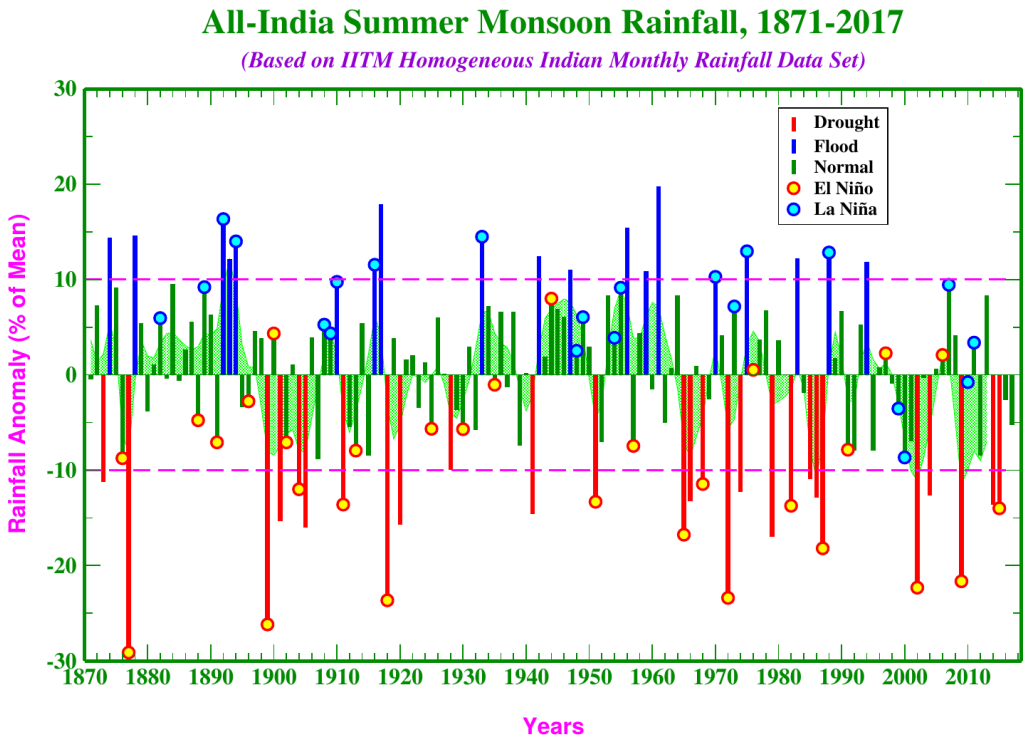

Figure 1.11: The status of Asian summer monsoon rainfall ,El Niño, La Niña over the years. This figure shows the time series evolution of all India summer monsoon rainfall (AISMR) anomalies, expressed as percent departures from its long-term mean, over more than a century in the past. These anomalies demonstrate that there is a huge complexity involved in the monsoon evolution over the years. This figure has been adapted from https://www.tropmet.res.in/ kolli/MOL/Monsoon/Historical/air.html.

The annual cycle of monsoon precipitation can be described as a manifestation of the seasonal migration of the ITCZ (see Sect. 1.1.3) and an associated shift in the rain band from southern to northern Indian Ocean. There is a consistent variability in the rainfall over India with strong convection over the western ghats, Himalayan foothills due to orography and over central India due to low level convergence. The strength of summer monsoon rainfall is modulated by the intra-seasonal variability by active and break spells over India. Intra-seasonal oscillations are influenced by various factors such as variations in the position and strength of the continental monsoon trough, quasi-periodic oscillations of the monsoon, as well as synoptic systems such as lows and depressions. Much of the monsoon rainfall over the central plains of India is associated with the low-pressure systems which develop over the northern bay of Bengal and move onto the subcontinent along a west-north-westerly track.

1.3.4 El Niño southern oscillation influence on Asian monsoon circulation

The El Niño–southern Oscillation (ENSO) affects the Indian summer monsoon rainfall by altering the atmospheric circulation over the Tropical Indian Ocean (TIO) and western Pacific region. Anomalous subsidence associated with ENSO induces TIO warming by altering surface heat flux [e.g. Chowdary and Gnanaseelan, 2007] and the entire TIO experiences strong SST warming in the peak El Niño phase.

Generally, strong El Niños peak towards the end of the calendar year (December to February: DJF) and terminate by the following spring (March to May; MAM) or summer (June to September; JJAS) [Chowdary et al., 2014]. These El Niño events tend to have significant impact on the Asian monsoon circulation patterns by having large scale feedback circulations [Chowdary et al., 2017]. It is necessary to look at the large scale dynamics to understand the changes in Asian monsoon.

1.3.5 Rossby wave breaking and eastward eddy shedding

The subtropical jet-stream (see Sect. 1.3.2) is modulated by Rossby waves, which may break and lead to a quasi-isentropic stratosphere-tropospheric exchange [Homeyer and Bowman, 2013]. The Rossby wave breaking [Ungermann et al., 2013] occurrence frequency is influenced by the Monsoon cycle. Global simulations using artificial tracers of air mass origin [Vogel et al., 2014, 2016] indicate transport mechanisms via Rossby wave breaking from the Asian monsoon region into the lower stratosphere in the mid-latitudes. The eastward migrating air masses of the Asian monsoon anticyclone are mainly originating in the regions of India and China. Further, these air-masses are confined by the anticyclonic circulation and, on the polar side, by the subtropical jet [e.g. Ploeger et al., 2015].

Eastward eddy shedding from the monsoon anticyclone is caused by the oscillations of the subtropical jet. This eddy shedding causes air mass transport eastwards along the subtropical jet and thereafter into the lower stratosphere by quasi horizontal transport in a region of double tropopauses most likely associated with Rossby wave breaking events. A clear example of an eastward eddy shedding event that occurred in 1997 and was observed in the pollution tracer PAN has been described by Ungermann et al. [2016]. As a result of Rossby wave breaking, thin filaments with enhanced signatures of tropospheric trace gases were measured in the lower stratosphere over Europe during the TACTS/ESMVal

campaign in September 2012 in very good agreement with model simulations. These simulations demonstrate [Vogel et al., 2014, 2016] that source regions in Asia and in the Pacific Ocean have a significant impact on the chemical composition of the lower stratosphere of the northern Hemisphere. This finding is consistent with the recent analysis of water vapour measurements during the same time period by Rolf et al. [2018]; young, moist air masses, in particular at the end of the monsoon season in September/October 2012, flooded the extratropical lower stratosphere in the northern Hemisphere with contributions of up to 30 % at 380 K (with the remaining fraction being aged air). In contrast, the contribution of young air masses to the southern Hemisphere is much lower. At the end of October 2012, approximately 1.5 ppmv water vapour is found in the lower northern Hemisphere stratosphere (at 380 K) from source regions both in Asia and in the tropical Pacific compared to a mean water vapour content of 5 ppmv. In addition to this main transport pathway from the Asian monsoon anticyclone to the east along the subtropical jet with subsequent transport into the northern lower stratosphere, a second horizontal transport pathway out of the anticyclone to the west into the tropics (TTL) is found in agreement with MIPAS HCFC-22 measurements [Vogel et al., 2016].

1.4 Asian summer monsoon anticyclone

A large anticyclonic circulation (Asian summer monsoon anticyclone or Asian monsoon anticyclone) exists in boreal summer (from about June to September) at UTLS altitudes [e.g. Park et al., 2008; Randel et al., 2010; Vogel et al., 2019]. The anticyclone is linked to deep convection in summer over south-east Asia and the associated diabatic heating [Dunkerton, 1995; Hoskins and Rodwell, 1995; Randel and Park, 2006, see also Sect. 1.2] . Deep convection occurs primarily just South of and over the lower elevations of the Himalayan barrier; isolated deep convective events occur over the Tibetan Plateau [Houze Jr. et al., 2007]. The main level of convective outflow occurs in the vicinity of the lapse rate minimum (Fig. 1.12) at $13-14$ km (170-180 hPa or 362-364 K). The cold point tropopause in the ASMA is located at $\approx 17-17.5$ km (90-100 hPa), whereas the top of the ASMA is at $\approxeq 70$ hPa (see Fig. 1.12).

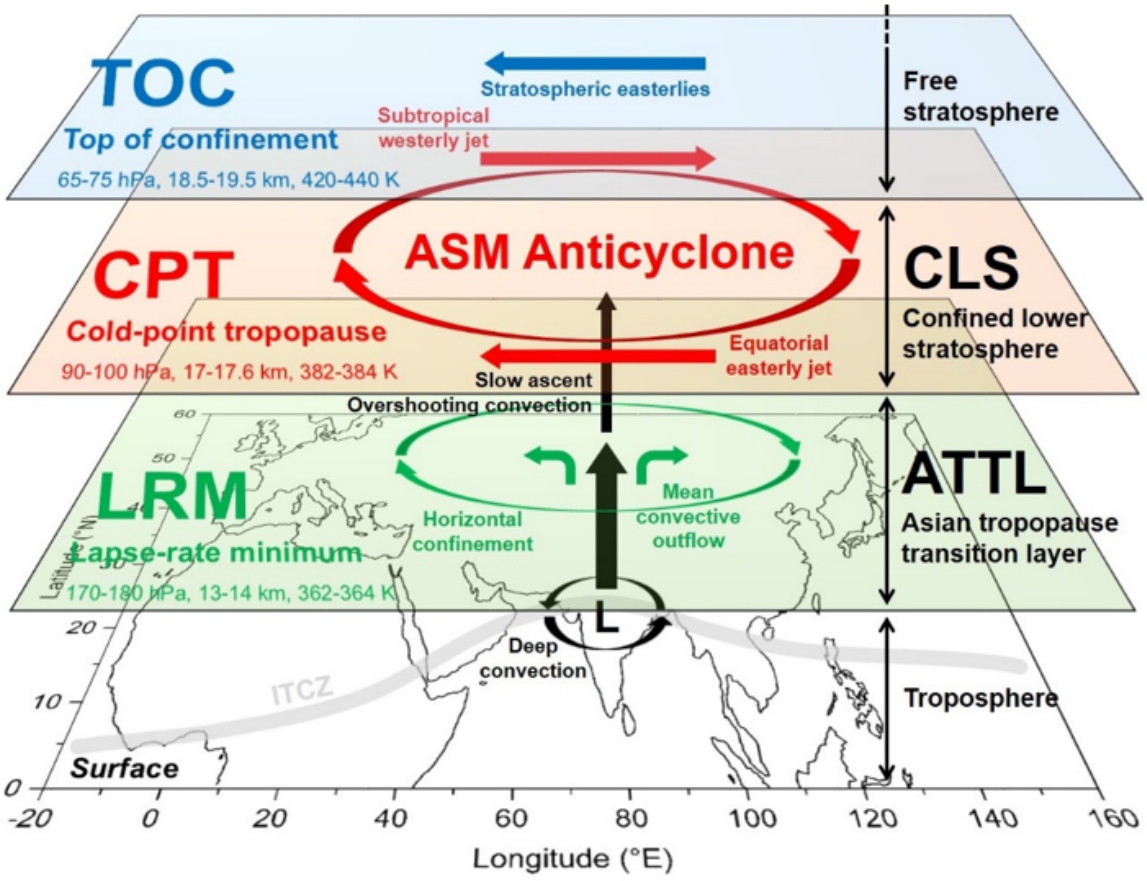

Figure 1.12: Schematic view the Asian Summer Monsoon Anticyclone above the Asian Monsoon System through its different weather phenomenon's at certain atmospheric layers. Figure has been adapted from Brunamonti et al. [2018].

This deep convection in the region of the Asian monsoon anticyclone transports pollutants (e.g., CO, HCN, C_2H_6, SO_2, PAN, NH_3) emitted at the surface over Asia to UTLS altitudes, where they are confined in the anticyclonic circulation in summer to a certain extent [e.g., Park et al., 2008; Randel et al., 2010; Ploeger et al., 2015; Garny and Randel, 2016; Ungermann et al., 2013; Santee et al., 2017; Höpfner et al., 2019]. Model analysis shows that the convective upward transport from the ground to the anticyclone occurs mainly in the region over North East India, Nepal, and the southern Tibetan Plateau [Bergman et al., 2013; Vogel et al., 2019]. This convection also causes lower concentrations of stratospheric tracers, in particularly ozone, in the monsoon anticyclone, whereas water vapour shows a local maximum in the monsoon anticyclone [e.g., Park et al., 2007; Bian et al., 2012; Randel et al., 2015]. The convective transport in the monsoon anticyclone causes a tropospheric signature up to altitudes of about 360 K, above which a region of relatively slow diabatic uplift in the anticyclonic motion is located; this region is referred to by Vogel et al. [2019] as "upward spiralling range" (see Fig. 1.14).

Particularly strong emissions of NO_x, SO_2, CO, NH_3, and aerosol particles occur in northern India and China [van der A et al., 2017; van Damme et al., 2018; Zheng et al., 2018, see Fig. 1.13], which impact ozone and aerosol particles in the upper troposphere. Ozone changes in the upper troposphere in turn have a radiative impact over the region [Roy et al., 2017; Fadnavis et al., 2018]. However, after the year 2013, because of the implementation of new emission control measures in China, China's anthropogenic emission of some pollutants decreased substantially (e.g., SO_2, NO_x, CO) while emissions of NH_3 and non-methane volatile organic compounds remained stable during 2010-2017 [Zheng et al., 2018].

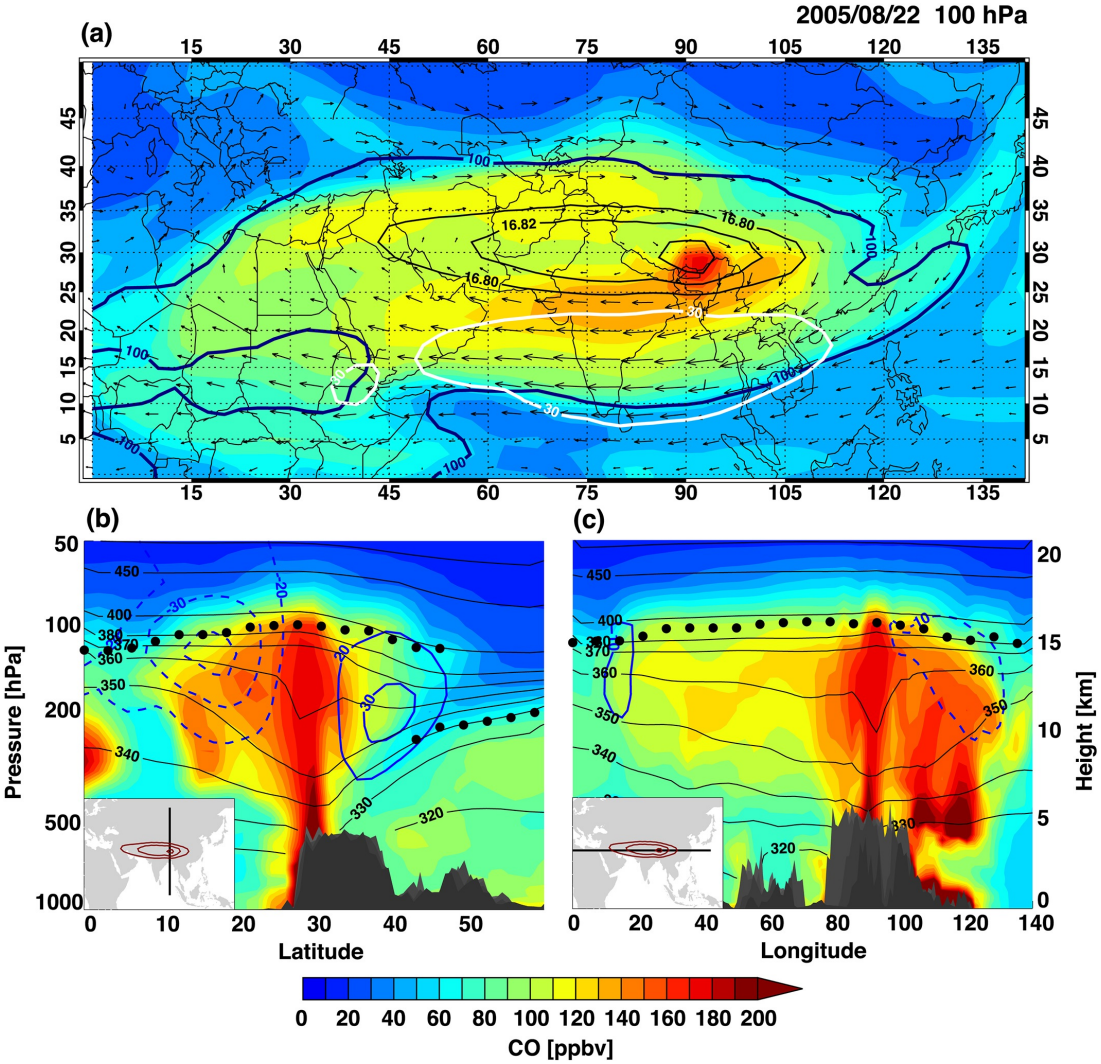

Figure 1.13: CO mixing ratio (ppbv) distribution from WACCM4-SD simulations on 22 August 2005. (a) CO at 100 hPa (color shading) with horizontal wind (arrows); selected GPH (thin black contours); 100 hPa tropopause (blue contour) i.e., the interception of the tropopause with the 100 hPa pressure surface; and easterly jet location indicated by the 30 m/s zonal wind (white contour). (b) Latitude-pressure/altitude cross-section of CO (ppbv) along 90°E (as shown on the location map at the lower corner). Also shown are the tropopause height (black dots), selected isentropes (K; thin black lines), and the locations of the easterly and westerly jets as indicated by selected zonal wind contours (m/s; blue dash and solid, respectively). (c) Same as b, but for longitude-pressure/ altitude cross-section. This figure is taken from Pan et al. [2016].

Figure 1.14 (top panel) shows a longitude-theta cross-section at about 30°N through the monsoon anticyclone [Vogel et al., 2019]. At the top of the Asian monsoon anticyclone (above≈360 K) air masses circulate around the anticyclone in a large-scale upward spiral extending from northern Africa to the western Pacific. In the upward spiraling range air masses from inside the Asian monsoon anticyclone (shown in blue) are mixed with air masses convectively uplifted outside the core of the Asian monsoon anticyclone in the tropical adjacent regions e.g. uplifted by tropical cyclones in the western Pacific ocean (shown in red). The higher above the thermal (lapse rate) tropopause the larger is the contribution of air masses from outside the Asian monsoon anticyclone from the stratospheric background intruding into the upward spiraling flow (shown in green). The levels of pressure are marked by thin white lines and the thermal tropopause is shown by black dots. Figure 1.14, bottom panel, shows a latitude-theta cross-section at about 90°E: The transport of air masses from the region of the Asian monsoon into the tropical-pipe occurs in three distinct steps: first, very fast uplift within the convective range up to ≈360 K within the Asian monsoon anticyclone and outside in the tropical adjacent regions (within a few days); second, uplift above 360 K (up to ≈460 K) within the upward spiraling range (within a few months), and third, transport within the tropical pipe to altitudes higher than 460 K associated with the large-scale Brewer-Dobson circulation (within one year). The thermal tropopause (black dots) and horizontal winds (black lines) are shown. The horizontal winds mark the edge of the anticyclone at its northern and southern flank. The levels of pressure are marked by thin white lines. Large grey arrows indicate isentropic transport from the Asian monsoon anticyclone into the tropics. The dashed line marks the tropical pipe, which largely isolates tropical air masses from isentropic mixing with mid-latitude air [e.g. Plumb, 1996; Volk et al., 1996].

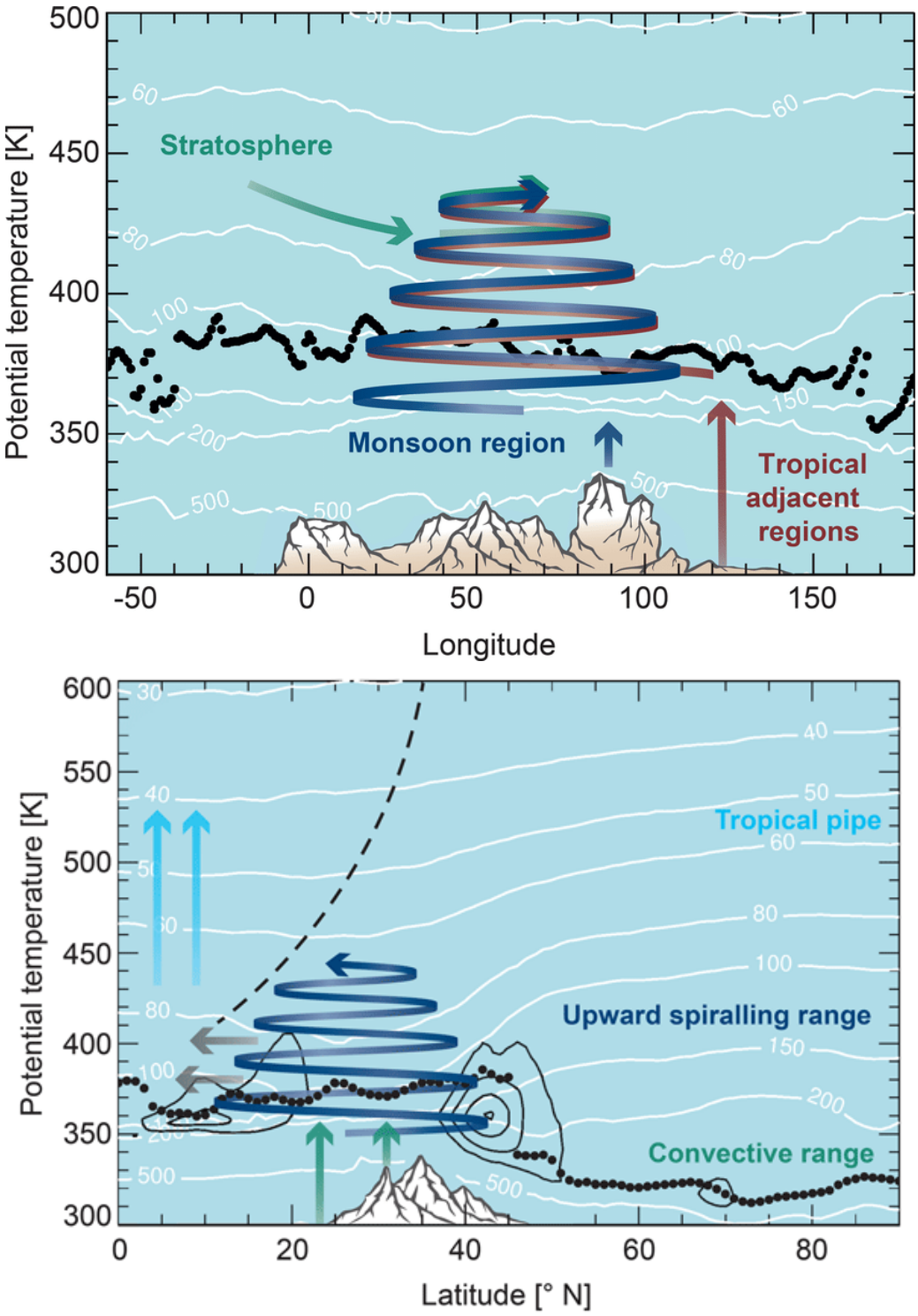

Figure 1.14: This schematic diagram of possible transport pathways of exchange between upper troposphere and lower stratosphere. The convective transport in the monsoon anticyclone causes a tropospheric signature up to altitudes of about 360 K, above which a region of relatively slow diabatic uplift in the anticyclonic motion is located; as an "upward spiraling range". Figure has been taken from Vogel et al. [2019].

The location, shape and strength of the Asian summer monsoon anticyclone (ASMA) strongly vary on intra-seasonal, inter-annual and longer timescales [Dunkerton, 1995; Kunze et al., 2010], which is subject to ongoing discussion [Pan et al., 2016; Nützel et al., 2016]. The

Asian monsoon in the UTLS does not constitute a stable, persistent uni-modal anticyclonic circulation (as it sometimes appears in climatology), but can be bi-modal (with an Iranian and a Tibetan mode) and moreover shows a strong day-to-day variability [Zhang et al., 2002; Yan et al., 2011; Vogel et al., 2015; Nützel et al., 2016]. There is also a substantial inter-annual variability of the monsoon circulation with impact on the concentration of tracers confined in the monsoon circulation [Santee et al., 2017; Yuan et al., 2019]. This variability of the monsoon circulation has an impact on the variability of trace gases [Santee et al., 2017; Luo et al., 2018]. The typical strong monsoon domains with contrasting wet-dry seasons and reversals in winds are shown Fig. 1.7.

1.5 Asian tropopause aerosol layer

Tropospheric aerosol is currently a hot topic both in the scientific community and in the general public because of its associated short and long term effects. Scientists know it as a particulate matter, cloud condensation nuclei (CCN) or ice nuclei (IN) while aerosol is known to the general public as environmental pollution which has become an increasing concern due to its health risks for people. Stratospheric aerosol, however, very far away from the Earth's surface, receives much less attention, partly because its formation is closely related to natural sources (such as volcanic plumes and oceanic dimethyl sulfide).

From previous balloon measurements in the Asian monsoon anticyclone (AMA) [Vernier et al., 2018] it is clear that a belly like enhancement of back-scatter ratio (BSR) occurs in the vertical profile where a high concentration signal of aerosol particles prevails between $360-400$ K. This enhancement occurs in the Asian monsoon anticyclone. The sustainability of the Asian monsoon over a longer period of time results in a continuous supply of aerosol and aerosol precursors to the Asian tropopause aerosol layer (ATAL) through convection over the Asian monsoon region and over Tibet.

Aerosols will have a much longer lifetime than in the troposphere (10 - 50 times longer) after their arrival at greater altitudes, above $\Theta \approx 360$ K, so the ATAL and distribution of ATAL particles to the entire northern hemisphere will significantly affect the Earth's energy budget. ATAL will also have impact on stratospheric ozone though heterogeneous chemistry, as aerosols have taken an important role in the depletion of the ozone layer which started $\approx$ in the late 1970s and still continues today [Müller et al., 2008; Grooß and Müller,

2021]. Owing to these important issues, the ATAL has received much attention in the scientific community.

The existence of an ATAL in northern Hemisphere summer (June, July and August) was first discovered in Cloud-Aerosol Lidar and Infrared Pathfinder Satellite Observation (CALIPSO) lidar measurements of aerosol particles in the Upper Troposphere/Lower Stratosphere (UTLS) [Vernier et al., 2011, 2015]. The ATAL occurs above about 360 K (between about 13 and 18 km); based on CALIOP measurements, the thickness of the ATAL layer is estimated to be 3-4 km between 30° and 40°N and is thinner near the Equator [Vernier et al., 2011, 2015, 2018]. The existence of an ATAL is confirmed by balloon-borne back-scatter measurements [Vernier et al., 2015, 2018; Brunamonti et al., 2018; Hanumanthu et al., 2020]. Solar occultation observations by the Stratospheric Aerosol and Gas Experiment (SAGE) II [Thomason and Vernier, 2013] indicated that there was no ATAL prior to 1999, although a recent study suggested that an ATAL already existed in 1997 [Höpfner et al., 2019].

The confinement of air masses of tropospheric origin in the monsoon anticyclone also affects the aerosol particles constituting the ATAL [Yu et al., 2017; Vernier et al., 2018]. Particles in the ATAL originate from ground sources (both gas-phase precursors and aerosol particles), which are lifted to UTLS altitudes by convection [e.g., Vernier et al., 2018; Lau et al., 2018; Höpfner et al., 2019]. The formation mechanism of the aerosol particles constituting the ATAL is not well characterised, but there is evidence that formation of secondary aerosol in the upper troposphere within the Asian monsoon anticyclone at relatively high humidity and at low temperatures is important [Vernier et al., 2015; Yu et al., 2017; Vernier et al., 2018].

1.5.1 Measurements of the Asian Tropopause aerosol layer

Only a few measurements of size distributions of particles in the ATAL are available, but measurements with an optical particle counter (OPC) [Deshler et al., 2003] from Hyderabad, India and measurements with a Printed Optical Particle Spectrometer (POPS) [Gao et al., 2016] from Kunming, China, indicate that ATAL particles are dominated by particles with a size of $\approx 0.1\ \mu$m [Yu et al., 2017; Vernier et al., 2018].

In the frame of the SWOP (sounding water vapour, ozone, and particle) campaign during the Asian summer monsoon (ASM), ozone and water vapour profiles were measured by balloon-borne sensors launched from Lhasa (29.66° N, 91.14° E, elevation 3650 m), China, measurements were performed at different sites in China during the last decade. In the year

2013 balloon launches were performed during August as a part of the SWOP campaign. In total, 24 soundings were launched, nearly half of which show strong variations in the relationship between ozone and water vapour in the tracer-tracer correlation in the upper troposphere and lower stratosphere (UTLS). SWOP measurements were also conducted in the following years and continue until the present day (Bian et al. [2020]).

Based on CALIOP measurements, the summertime aerosol optical depth over Asia associated with the ATAL has increased from ≈ 0.002 to 0.006 between 1995 and 2013, resulting in a short-term regional forcing at the top-of-the-atmosphere of -0.1 W/m^2 (compensating about one-third of the comparable radiative forcing associated with the global increase in CO_2) [Vernier et al., 2015, see also Fig. 1.15]. The regional radiative forcing caused by the ATAL, differs for clear- and total-sky conditions; total-sky calculations show less shortwave radiative forcing over the monsoon region because of cloudiness [Vernier et al., 2015].

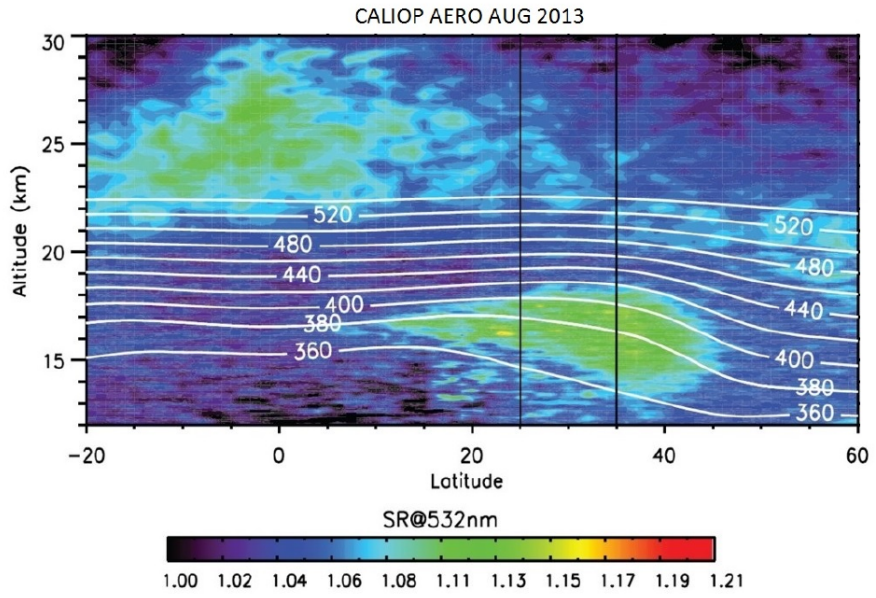

Figure 1.15: Mean CALIOP scattering ratio cross-section averaged between 60°E and 120°E in August 2013. Potential temperature isentropes from GOES-5 model are shown with the white lines. Note that clouds observed by CALIOP are filtered when the volume depolarization exceeds 5%, a third method independent from the balloon measurements. This figure demonstrates the ATAL extension meridionally between 15° - 45°N. Figure has been adapted from Vernier et al. [2015].

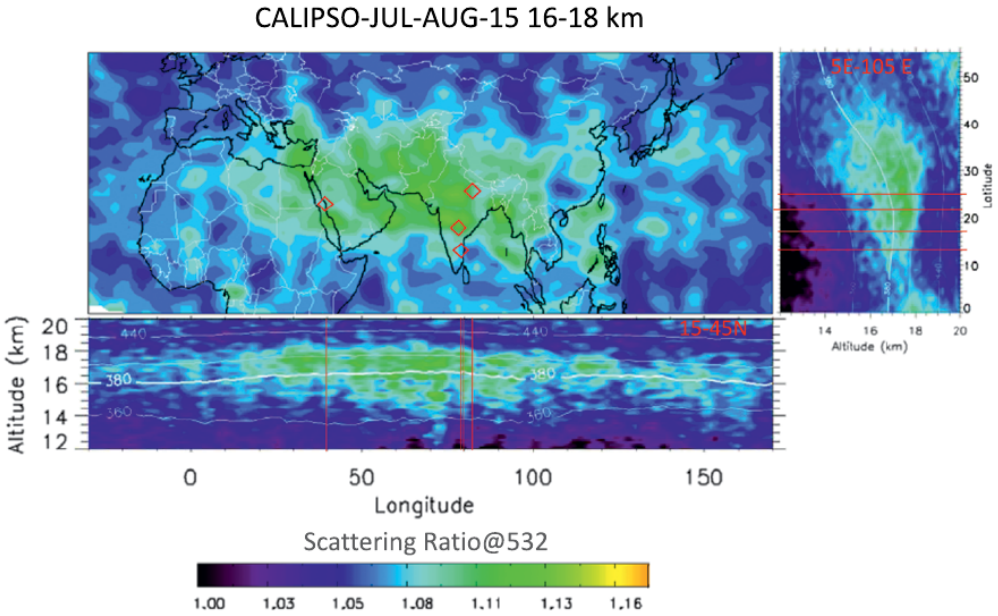

Figure 1.16: (top) Map of scattering ratio (SR) at 532nm after averaging the CALIPSO cloud-cleared data between 16 and 18 km in July-August 2015. Corresponding cross-sections from averaged data between (bottom) 15°and 45°N and (right) 5° and 105°E depict the 3D extension of ATAL.The white lines show isopleths of potential temperature (K). The locations of the balloon launches launches during the BATAL deployments are shown by red diamonds on the map and red lines on the cross-sections (Gadanki, Hyderabad, Thuwal, and Varanasi). This figure is adapted from Vernier et al. [2018].

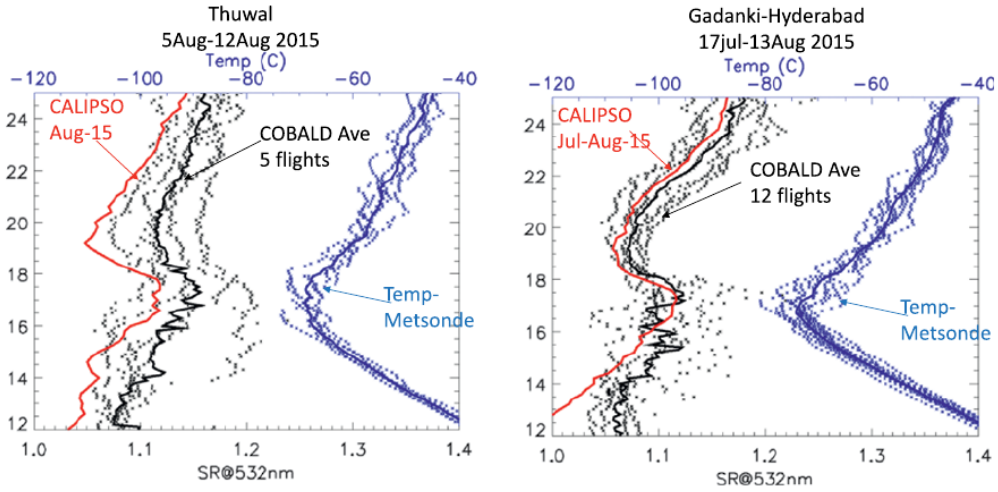

Figure 1.17: SR profiles at 532nm derived from the COBALD balloon flights in (left) Thuwal between 5 and 12 Aug 2015 and (right) Gadanki Hyderabad between 17 Jul and 13 Aug 2015. Averaged COBALD profiles (black line) and CALIPSO profiles (red line) within ±5° latitude and ±30° longitude are shown. Radiosonde individual (blue stars) and averaged (blue line) temperature profiles are also shown. This figure has been adapted from Vernier et al. [2018].

It is likely that, over Asia in the past ∼ 20 years, the altered radiative forcing has led to summertime reductions in surface temperature, although this effect has not been quantified yet. However, the radiative forcing caused by the ATAL could be compared with the global

aerosol forcing caused by moderate volcanic eruptions since 2000, which corresponds to a surface cooling of 0.05 to 0.12 K [Ridley et al., 2014].

The co-occurrence of the ATAL with volcanic eruptions in the region further enhances the radiative forcing by the ATAL; Fairlie et al. [2014, Fig. 8], based on monthly accumulations of CALIOP aerosol data between 14 and 40 km altitude, reported a top-of-the-atmosphere radiative forcing locally over Asia and Europe during July 2011 in response to the Nabro volcanic eruption of about -0.8 to $-1.5\,W/m^2$. Therefore, periods of volcanic eruptions are removed in some ATAL studies, because the volcanic signal is much stronger than the ATAL signal itself, which will thus mask the ATAL [e.g. Thomason and Vernier, 2013; Vernier et al., 2015].

The impact of the ATAL is furthermore modulated by El Niño. During El Niño, the ATAL is thicker and broader over the Indian region, resulting in a reduction of the solar flux and a surface cooling of about 1 K over northern India. An elevated ATAL over South Asia exacerbates the severity of Indian droughts [Fadnavis et al., 2019b].

The chemical signature of air masses within the monsoon anticyclone (e.g. tropospheric pollutants, water vapour) is exported to the northern Hemisphere during summer and fall through quasi-isentropic transport from low latitudes [e.g., Ploeger et al., 2013; Vogel et al., 2014, 2016, 2019; Spang et al., 2015; Garny and Randel, 2016; Müller et al., 2016; Fadnavis et al., 2018; Rolf et al., 2018; Yan et al., 2019]. Because of this export of air from the Asian monsoon circulation to the northern Hemisphere, the ATAL particles contribute significantly ($\sim 15\%$) to the northern Hemisphere stratospheric column aerosol surface area on an annual basis [Yu et al., 2017].

1.5.2 Chemical composition of Asian tropopause aerosol layer particles

Only limited information on the chemical composition of the ATAL particles is available from measurements so far. From simulations, there is evidence that desert dust is lifted to UTLS altitudes and entrained into the ATAL [Fadnavis et al., 2013; Lau et al., 2018; Yuan et al., 2019]. Further, simulations show elevated aerosol concentrations of sulfute, nitrate, ammonium, black carbon and organic carbon within the ATAL with dominating contributions of nitrate [e.g. Gu et al., 2016; Fairlie et al., 2020]. Moreover, Fairlie et al. [2020] found in model simulations for summer 2013 a different chemical composition of the ATAL depending on the location within the Asian monsoon anticyclone with nitrate aerosol as a dominating component on the southern flank of the anticyclone. Aircraft in situ measurements

suggest that at lower altitudes the chemical composition of ATAL particles is dominated by carbonaceous and sulfate materials, consistent with the expectation that aerosol trends in the UTLS in the past decades are under increasing influence of sulfur emissions in Asia [Martinsson et al., 2014; Vernier et al., 2015; Fadnavis et al., 2019a]. However, the first offline (balloon-borne filter samples) chemical analysis of ATAL particles suggested the presence of nitrate aerosol, but undetectable concentrations of sulfute ions [Vernier et al., 2018]. Also, the evaluation of a set of remote sensing measurements indicates a strong contribution of solid ammonium nitrate particles to the ATAL [Höpfner et al., 2019].

The monsoon anticyclone shows strong day-to-day variability (see Sect. 1.4); this variability of the monsoon circulation impacts also the variability of aerosol distributions [Lau et al., 2018; Yuan et al., 2019].

1.5.3 Asian tropopause aerosol layer and cirrus coexistence

The strong convective activity in the Asian summer monsoon region also impacts the temperature in the monsoon region and the formation of cirrus clouds. Enhanced convection is linked to cold anomalies in the subtropical lower stratosphere [Park et al., 2007; Randel et al., 2015]. Further, the occurrence fraction of cirrus in the middle to upper (16–18 km) tropical tropopause layer (TTL) [e.g., Fueglistaler et al., 2009] exhibits a pronounced maximum over the Asian monsoon region, both in observations and in model simulations [Ueyama et al., 2018]. Convection is likely the dominant driver of localised upper tropospheric H_2O and cloud maxima in the region [Park et al., 2007; Ueyama et al., 2018]. Ice clouds in the tropical deep convective regions are important as they exert a considerable net warming effect [Hong et al., 2016].

To address fundamental open questions and uncertainties regarding the Asian summer monsoon anticyclone and the ATAL, a number of balloon-borne campaigns have been conducted in summer in the Asian monsoon region employing the Compact Optical backscatter Aerosol Detector (COBALD) instrument [Bian et al., 2012, 2020; Vernier et al., 2018; Brunamonti et al., 2018].

1.6 Overview of this thesis

An analysis is presented in this thesis, of the balloon-borne measurements of aerosol back-scatter over northern India at Nainital in August and November 2016 (see Chap. 2). The signature of the ATAL is clearly visible in most of the soundings in August (but not in every single one), but a substantial day-to-day variability of the ATAL (see Chap. 3) is found, both in back-scatter intensity and in altitude range of the ATAL. A Lagrangian back-trajectory analysis is performed (see Chap. 4) in order to identify the air mass origin in the model boundary layer and the transport pathways of air parcels contributing to the ATAL over Nainital in August 2016 (see Chap. 5).

The core scientific content of the work presented here has been already published in the scientific literature, a lot of the presentation of the results in the chapters below follow this publication:

- ***Hanumanthu, S.**, Vogel, B., Müller, R., Brunamonti, S., Fadnavis, S., Li, D., Ölsner, P., Naja, M., Singh, B. B., Kumar, K. R., Sonbawne, S., Jauhiainen, H., Vömel, H., Luo, B., Jorge, T., Wienhold, F. G., Dirkson, R., and Peter, T.: Strong variability of the Asian Tropopause Aerosol Layer (ATAL) in August 2016 at the Himalayan foothills, Atmospheric Chemistry and Physics, 10.5194/acp-20-14273-2020, URL https://acp.copernicus.org/articles/20/14273/2020/, 2020.*

Further results of the measurement campaigns in Nainital in August and November 2016 and in Dhulikhel in July and August 2017, which form the observational basis of this Ph.D work were presented in the following three publications

- *Brunamonti, S., Jorge, T., Oelsner, P., **Hanumanthu, S.**, Singh, B. B., Kumar, K. R., Sonbawne, S., Meier, S., Singh, D., Wienhold, F. G., Luo, B. P., Boettcher, M., Poltera, Y., Jauhiainen, H., Kayastha, R., Karmacharya, J., Dirksen, R., Naja, M., Rex, M., Fadnavis, S., and Peter, T.: Balloon-borne measurements of temperature, water vapor, ozone and aerosol backscatter on the southern slopes of the Himalayas during StratoClim 2016–2017, Atmospheric Chemistry and Physics, 18, 15 937–15 957, doi.org/10.5194/acp-18-15937-2018, URL https://www.atmos-chem-phys.net/18/15937/2018/, 2018.*

- *Jorge, T., Brunamonti, S., Poltera, Y., Wienhold, F. G., Luo, B. P., Ölsner, P., **Hanumanthu, S.**, Sing, B. B., Körner, S., Dirksen, R., Naja, M., Fadnavis, S., and Peter, T.: Understanding cryogenic frost point hygrometer measurements after contamination by mixed-phase clouds, Atmos. Meas. Tech., doi.org/10.5194/amt-14-239-2021, URL https://doi.org/10.5194/amt-14-239-2021, 2021.*

- *Bhupendra Bahadur Singh, R, Krishnan, Ayantika Dey Choudhury, Ramesh K. Vellore, T P Sabin, Brunamonti, S.,* ***Hanumanthu, S.****, Jorge, T., Ölsner, P., Naja, M., Sunil Sonbawne, Fadnavis, S., and Peter, T. and Manoj K. Srivastava : Linkage of water vapor distribution in the lower stratosphere to organized Asian summer monsoon convection, Climate Dynamics, doi.org/10.1007/s00382-021-05772-2, URL https://link.springer.com/article/10.1007/s00382-021-05772-2, 2021.*

Furthermore, contributions were made to a study regarding the transport of air masses in the Asian monsoon:

- *Vogel, B. and Müller, R. and Günther, G. and Spang, R. and* ***Hanumanthu, S.*** *and Li, D. and Riese, M. and Stiller, G. P.: Lagrangian simulations of the transport of young air masses to the top of the Asian monsoon anticyclone and into the tropical pipe, Atmospheric Chemistry and Physics, 19, doi:10.5194/acp-19-6007-2019, URL https://www.atmos-chem-phys.net/19/6007/2019/, 2019.*

Chapter 2

Instrumentation and the balloon campaigns in India and Nepal

2.1 Overview of the balloon measurements in northern India 2016 and Nepal 2017

Figure 2.1: A balloon launch on a cloudy day at Nainital base camp. Test flights were launched in July 2016 under the supervision of Peter Ölsner from GCOS Reference Upper Air Network (GRUAN) [Dirksen et al., 2014].

Within this PhD thesis, measurements from two campaigns were used: one in Nainital, India (29.35° N, 79.46° E) August and November in 2016 and one in Dhulikhel, Nepal (27.62° N, 85.54° E) in July and August of 2017. During these two campaigns, a total of 56 balloon soundings were performed, out of which 28 from Nainital in summer (2-31 August 2016), in

winter (8-12 November) and 28 from during Dhulikhel in summer (30 July-12 August 2017). The author has participated both in the Nainital and the Dhulikhel campaign (see details below); however the focus of the data analysis presented here is on the Nainital campaign.

Figure 2.2: The balloon launch preparation and logistics at Nainital balloon camp base on July 2016.

2.2 Balloon-borne campaign in Naintal, India 2016

The measurements analyzed in this thesis were performed in the framework of the StratoClim project (`http://www.stratoclim.org`) funded by the European Union. And were carried out from the station of Nainital, India (29.35° N, 79.46° E) during August and November of 2016 (see Figs. 2.1 and 2.2 for an impression of the conduction of the balloon activities). Nainital is located at an elevation of 1820 m above sea level. The Aryabhatta Research Institute of Observational Sciences (ARIES) provided the campaign base to perform the launches in Nainital. The measurements in Nainital were conducted by an international team of scientists from different institutions in India and Europe. The team who performed all the launches are Simone Brunamonti (ETH), Peter Ölsner (DWD), Teresa Jorge (ETH), Sreeharsha Hanumanthu (FZJ), Bhupendra Singh (IITM), Ravi Kumar (IITM) and Sunil Sonbawne (IITM). Nainital is located at the southern slopes of Himalayas, and due to steep orography is subject to persistent deep convection during the ASM season [e.g. Houze Jr. et al., 2007;

Vellore Ramesh et al., 2016]. This region is a hot-spot for transport of polluted air to the ASM anticyclone.

The campaign featured balloon-borne measurements of H_2O, temperature, ozone and aerosol back-scatter: an overview of all the data collected is given in Brunamonti et al. [2018]; Brunamonti [2018]; Brunamonti et al. [2019]; Jorge et al. [2021]; Hanumanthu et al. [2020]. The evolution of the H_2O measurements regarding the distribution of water vapor in the lower stratosphere is described by Singh et al. [2021]. The instrumentation is briefly described below, more details are given in Sect. 2.3. Water vapor measurements were performed using the RS41-SGP radiosondes (hereafter "RS41") manufactured by Vaisala, Finland [Vaisala, 2017] and by cryogenic frost-point hygrometers (CFH) manufactured by En-Sci, USA [Vömel et al., 2007, 2016] see Sect. 2.3.1 and Sect. 2.3.3. RS41 is the new model of Vaisala radiosonde and is currently replacing the older model (RS92) in monitoring networks such as the GCOS Reference Upper Air Network (GRUAN) [e.g. Dirksen et al., 2014]. RS41 has a resolution of 0.1% RH, and a combined uncertainty in soundings of 4% RH [Vaisala, 2017].

CFH is a cryogenic frostpoint hygrometer based on the chilled-mirror principle [e.g. Vömel et al., 1995] in which frostpoint temperature (T_{fp}) is inferred from changes in reflectivity of an ice-coated mirror. In order to cool the mirror, a cryogenic refrigerant liquid (trifluormethane: CHF_3) is used. The uncertainty of CFH is estimated to be smaller than 10% in H_2O mixing ratio up to about 28 km altitude [Vömel et al., 2007, 2016], making it a state-of-the-art instrument for stratospheric H_2O measurements. Here, T_{fp} information by CFH are converted to H_2O mixing ratio using the parameterization for saturation vapor pressure over ice by Murphy and Koop [2005].

The aerosol and cirrus measurements analyzed within this thesis are based on balloon -borne back-scatter instrument measurements by the compact optical back-scatter aerosol detector (COBALD, see also Sect. 2.4). COBALD operates at optical wavelengths of 455 nm (blue visible) and 940 nm (infrared) and was developed at the ETH Zürich [e.g. Wienhold, 2008; Brabec et al., 2012]. For the measurements analyzed here, it was hosted by a standard RS41-SGP meteorological radiosonde and the DigiCORA MW41 sounding system [Vaisala, 2017]. In addition, the balloon payload included an electrochemical concentration cell (ECC, manufacturer: EN-SCI, USA) [Komhyr, 1969; Komhyr et al., 1995] for measuring the ozone mixing ratio. Here the pressure measured by the RS41 as the main vertical coordinate is needed for all instruments. The ATAL analysis is mainly based on the COBALD 455 nm

measurements, in particular on the back-scatter ratio (BSR), which is defined as the ratio of the COBALD raw signal (from particulates and air molecules) over the pure molecular scattering (derived from the ambient molecular number density, using the temperature and pressure measured by RS41). For the detection of aerosol particles, the short wavelength channel (455 nm) is considered here, which is more sensitive to smaller particles than the long wavelength channel (940 nm). It also provides a smaller value for the maximum uncertainty (1% and 5% for the shortwave and longwave channel, respectively) and is thus less noisy [Brabec et al., 2012]. Details regarding the measurements at 455 nm and 940 nm can be found in Sect. 2.4

2.3 The balloon payload

Meteorological balloon soundings (or radio-soundings) are performed daily from thousands of stations worldwide, and are used for operational weather forecasts as well as for data assimilation in global models [e.g. Hersbach et al., 2020]. In standard balloon soundings a meteorological radiosonde is attached to a latex balloon filled with helium or hydrogen gas, which ascends in the atmosphere. Standard meteorological radiosondes measure atmospheric parameters such as temperature, pressure and relative humidity with good accuracy, but for relative humidity typically only up to the tropopause. Radiosondes are equipped with ultra-high frequency (UHF) antennas to transmit the data as a radio signal to a receiving station at the ground. For stratospheric research, [e.g. Brunamonti et al., 2018; Vernier et al., 2018; Jorge et al., 2021; Bian et al., 2020; Hanumanthu et al., 2020], radiosondes are complemented by more sophisticated additional instruments for accurate water vapor measurements up to the stratosphere (cryogenic frost-point hygrometers, CFH), as well as for ozone (electrode chemical concentrations cell, ECC) and aerosol back-scatter (COBALD sondes) measurements.

The schematic in Fig. 2.3 illustrates how the four instruments composing the payload, namely RS41, ECC, CFH and COBALD, as well as RS92 and the balloon train are assembled together for a launch with the full payload. The preparation procedures for each instrument and the payload assembly and preparation for launch are outlined detail in the “Sounding preparation and execution protocol”, developed by Simone Brunamonti and Teresa Jorge (ETH Zürich) for the StratoClim balloon campaigns and can be found in Brunamonti [2018].

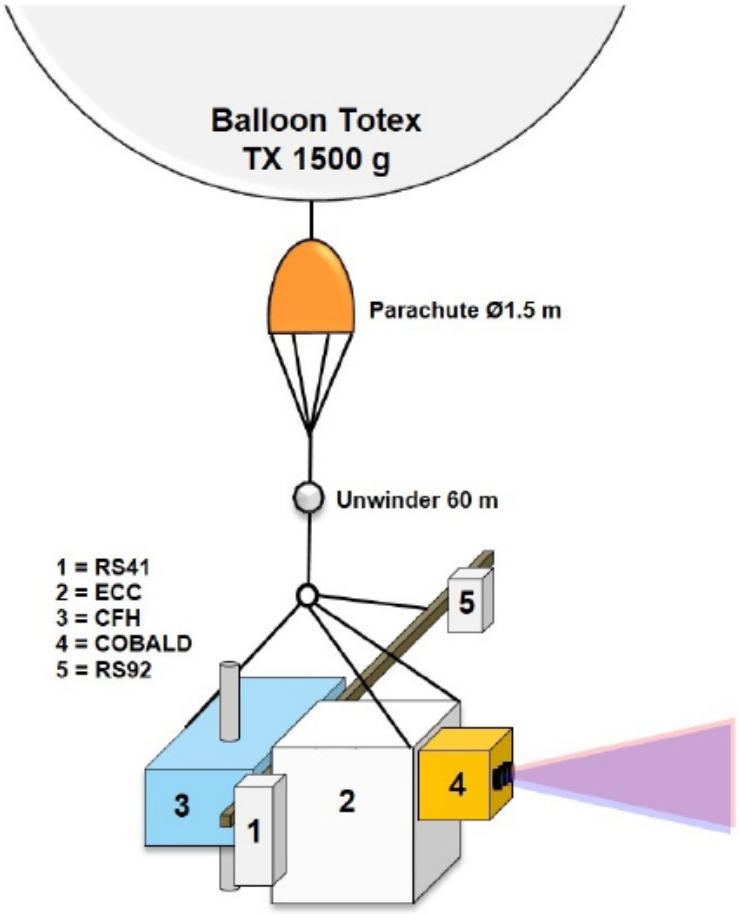

Figure 2.3: Schematic of the payload configuration and balloon train for a sounding with payload: RS41/ECC/CFH/COBALD/RS92, of the Nainital 2016 campaign (Figure adapted from Brunamonti [2018]).

2.3.1 Vaisala RS41-SPG radiosonde

The radiosonde RS41 [Vaisala, 2017], was used for the balloon measurements, in Nainital and provides measurements of pressure, temperature, relative humidity, the position of sonde via a Global Positioning System (GPS) receiver, and importantly it is used to host the data streams of all additional instruments flying on the same payload, and to transmit all data to the ground station. In previous campaigns employing similar payloads, iMet radiosondes [iMet, 2006] were employed [e.g., Bian et al., 2012; Vernier et al., 2015, 2018]. However the larger band-width of RS41 allows its operation together with multiple additional instruments. The campaign in Nainital was the first intensive field activity successfully employing RS41 radiosondes together with a complex balloon payload (see Fig. 2.3). RS92 was just added for the comparison with the RS41. Finally, for logistical constraints, the first two soundings at Nainital in August 2016, employed iMet-1-RSB radiosondes [iMet, 2006], instead of RS41, and using SkySonde version 1.9 [Hall et al., 2016] as data acquisition

software.

2.3.2 Electrochemical Concentration Cell (ECC)

The schematics of an ECC sonde is shown in Fig. 2.4. Electrochemical concentration cells (ECCs) have been used for balloon-borne ozone (O_3) measurements for several decades [e.g., Komhyr, 1969; Komhyr et al., 1995]. The ECC obtains its driving electromotive force from the difference in the concentration of potassium iodide solutions in cathode and anode chambers of the instrument. When ozone enters the sensor, iodine is formed in the cathode half cell. The cell then converts the Potassium Iodine to molecular iodide, counting an electron flow.

$$O_3 + KI + H_2O \rightarrow 2\,KOH + I_2 + O_2 \tag{2.1}$$

By measuring the electron flow and the rate at which ozone enters the cell per unit time, atmospheric ozone concentrations can be determined. The performances of ECC are tested extensively in laboratory [Smit et al., 2007] and are shown to produce reliable time series of stratosphere measurements [Terao and Logan, 2007]. Further details on ECC measurements can be found elsewhere [Smit et al., 2007; Brunamonti, 2018].

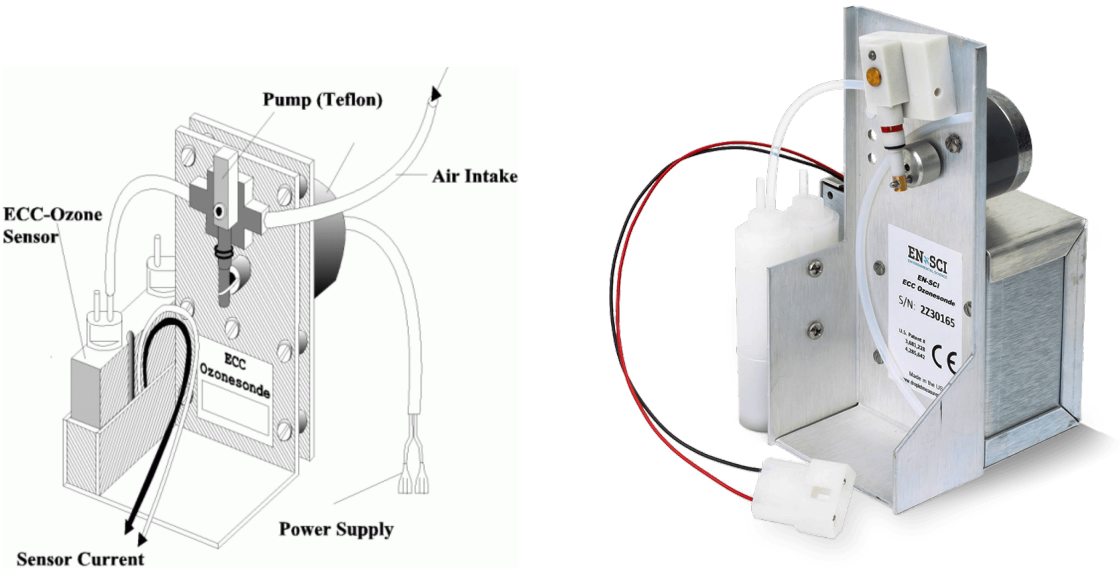

Figure 2.4: Left: Schematics of an ECC ozonesonde (adapted from JOSIE, Jülich) [Smit et al., 2007]. Right: Picture of an ECC ozonesonde (from Manufacturers webpage).

2.3.3 Cryogenic frostpoint hygrometer

The Cryogenic frost-point hygrometer (CFH, see Fig. 2.5, manufactured by En-Sci (USA), is a frost-point hygrometer based on the chilled-mirror principle [e.g. Vömel et al., 1995]. Balloon-borne and aircraft-operated frost-point hygrometers are used since early stratospheric water vapor measurements [e.g. Brewer, 1949], and CFH is the latest product of the long history of the development of hygrometers for stratospheric H_2O measurements [e.g. Mastenbrook and Dinger, 1961; Jorge et al., 2021, and references therein]. Inter-comparison experiments of different water vapor detectors in a cloud simulation chamber ranked cryogenic frost-point hygrometers as the state-of-the-art for stratospheric H_2O measurements [Fahey et al., 2014]. CFH sondes are used for stratospheric water vapor measurements worldwide [e.g. Vömel et al., 1995; Vömel et al., 2002; Thölix et al., 2016] and, together with ECC, are regularly deployed in the ASM region since 2009 [Bian et al., 2012; Li et al., 2018; Bian et al., 2020; Singh et al., 2021].

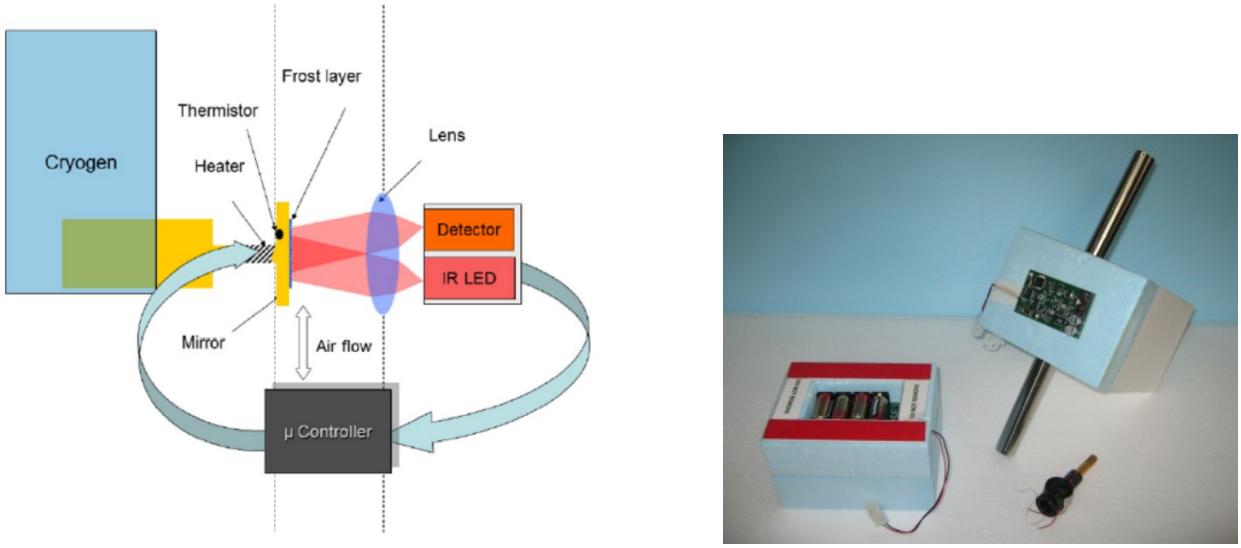

Figure 2.5: Left: Schematics of the CFH hygrometer (adapted from Vömel et al. [2007]). Right: CFH sonde ready for flight (the photo was taken during the Nainital Campaign in 2016).

2.3.4 Compact optical back-scatter aerosol detector (COBALD)

COBALD (compact optical back-scatter aerosol detector, see Fig. 2.6) is a light-weight detector for balloon-borne aerosol back-scatter measurements developed by Dr. Frank Wienhold at ETH Zürich, it constitutes a modern version of the back-scatter sonde originally proposed by Rosen and Kjome [1991]. COBALD soundings provide vertical profiles of back-scatter ratio (BSR) at optical wavelengths of 455 nm (blue visible) and 940 nm (infrared) by

aerosols and molecules (see Sec. 2.4 for details). COBALD was designed for the analysis of cirrus clouds [Brabec et al., 2012; Cirisan et al., 2014] and also for polar stratospheric clouds [Khaykin et al., 2013; Engel et al., 2014]. However, measurements from Lhasa (China) [Bian et al., 2012, 2020] showed that COBALD also provides valuable information for the characterization of the ATAL, and for the validation of back-scatter satellite measurements by the Cloud Aerosol Lidar and Infrared Pathfinder Satellite Observation (CALIPSO) [Vernier et al., 2015, 2018]. All balloon soundings with a COBALD instrument in Nainital were launched at night-time between 23:00 Indian standard time (IST) (corresponding to coordinated universal time (UTC) +5:30 h) and the next day 03:00 IST. Due to the high sensitivity of its photo diode detector, COBALD can only be deployed during the night-time.

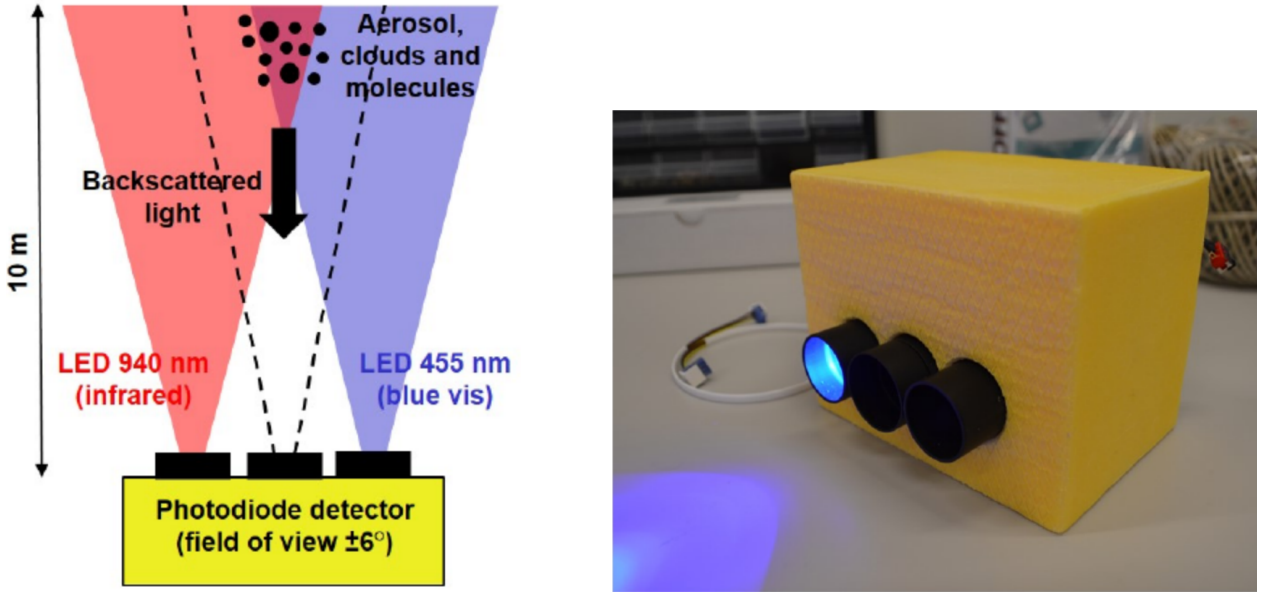

Figure 2.6: Schematics (left) and picture (right) of a COBALD sonde (adapted from Brunamonti [2018])

.

The ATAL analysis is mainly based on the COBALD 455 nm measurements (see Sec. 2.4). The COBALD data are expressed as backscatter ratio (BSR), i.e., the ratio of the total-to-molecular backscatter coefficient. This is calculated by dividing the total measured signal by its molecular contribution, which is computed from the atmospheric extinction according to Bucholtz [1995], and using the air density derived from the RS41 temperature and pressure measurements. The colour index (CI), defined as the 940-to-455 nm ratio of the aerosol component of the BSR, i.e. $CI = (BSR_{940} - 1)/(BSR_{455} - 1)$ is a useful indicator of particle size and can thus be employed to discriminate aerosol and cirrus measurements [Cirisan et al., 2014; Vernier et al., 2015; Brunamonti et al., 2018]. The CI for all balloon flights over Nainital in August 2016 is shown in Fig. 3.1. For the detection of aerosol particles, we consider the short

wavelength channel (455 nm), which provides a smaller value for the maximum uncertainty (1% and 5% for the shortwave and long-wave channel, respectively) and is thus less noisy [Brabec et al., 2012, see Sec. 2.4 for details].

2.4 Detection of the aerosol in the observed shortwave and long-wave channel

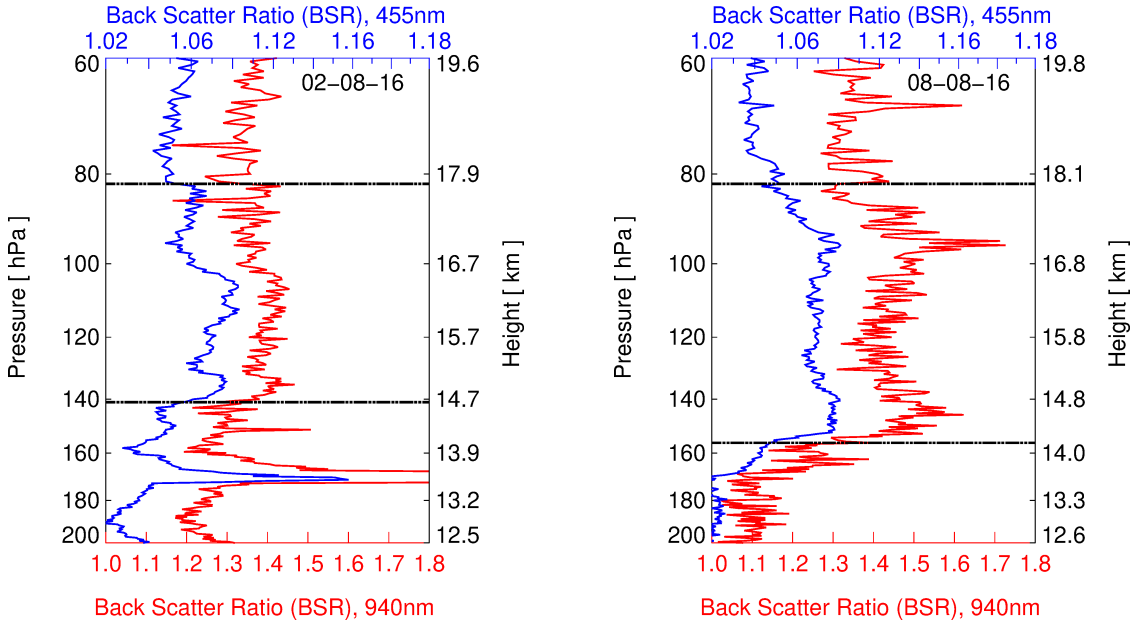

Figure 2.7: COBALD BSR_{455} (blue) and BSR_{940} (red) measurements in the UTLS region versus pressure 60-200 hPa for two flights in August 2016 (2 August, left panel, and 8 August, right panel). Shown are the measured data in pressure bins without further processing (see [Hanumanthu et al., 2020]). The top and bottom boundaries of the ATAL (see Table 3.1 in the Hanumanthu et al. [2020]) are marked by horizontal dashed-dot black lines. (Note the different scaling for BSR_{455} and BSR_{940}.)

The aerosol measurements analyzed in this thesis (see also [Hanumanthu et al., 2020]) are based on balloon-borne back-scatter measurements employing the COBALD detector (see Sect. 2.3.4), which operates at optical wavelengths of 455 nm (blue visible) and 940 nm (infrared) [Brabec et al., 2012]. Commonly, the colour index (CI) is defined as the 940-to-455 nm ratio of the aerosol component of the BSR [Cirisan et al., 2014; Brunamonti et al., 2018, see also Sec 3.1] and provides some estimate of particle size. The BSR for both wavelength will give an indication of the presence of the ATAL. The same is true for cirrus particles, i.e., they can be detected by both the blue and the red channel, individually. But only by using the CI a clear discrimination of ice ($CI > 7$) and aerosol ($CI < 7$) is possible (see Sec 3.2), which is the advantage of measuring at two wavelengths.

In this thesis, like in previous works [Vernier et al., 2015, 2018; Brunamonti et al., 2018; Hanumanthu et al., 2020] the ATAL analysis is based on the COBALD 455 nm BSR measurements. Indeed, the 455 nm BSR measurement is the preferred channel for the detection of the ATAL. The main reason is that the 455 nm COBALD BSR measurement has a better precision and has a higher signal-to-noise ratio (although BSR is lower at 455 nm than 940 nm, the raw signal is higher at 455 nm). Further, the accuracy is better for 455 nm, as the scale parameter in the data processing is taken directly from the sonde profile. The 940 nm channel builds on that and the BSR values are restricted by the assumption that the CI has to remain in a certain range.

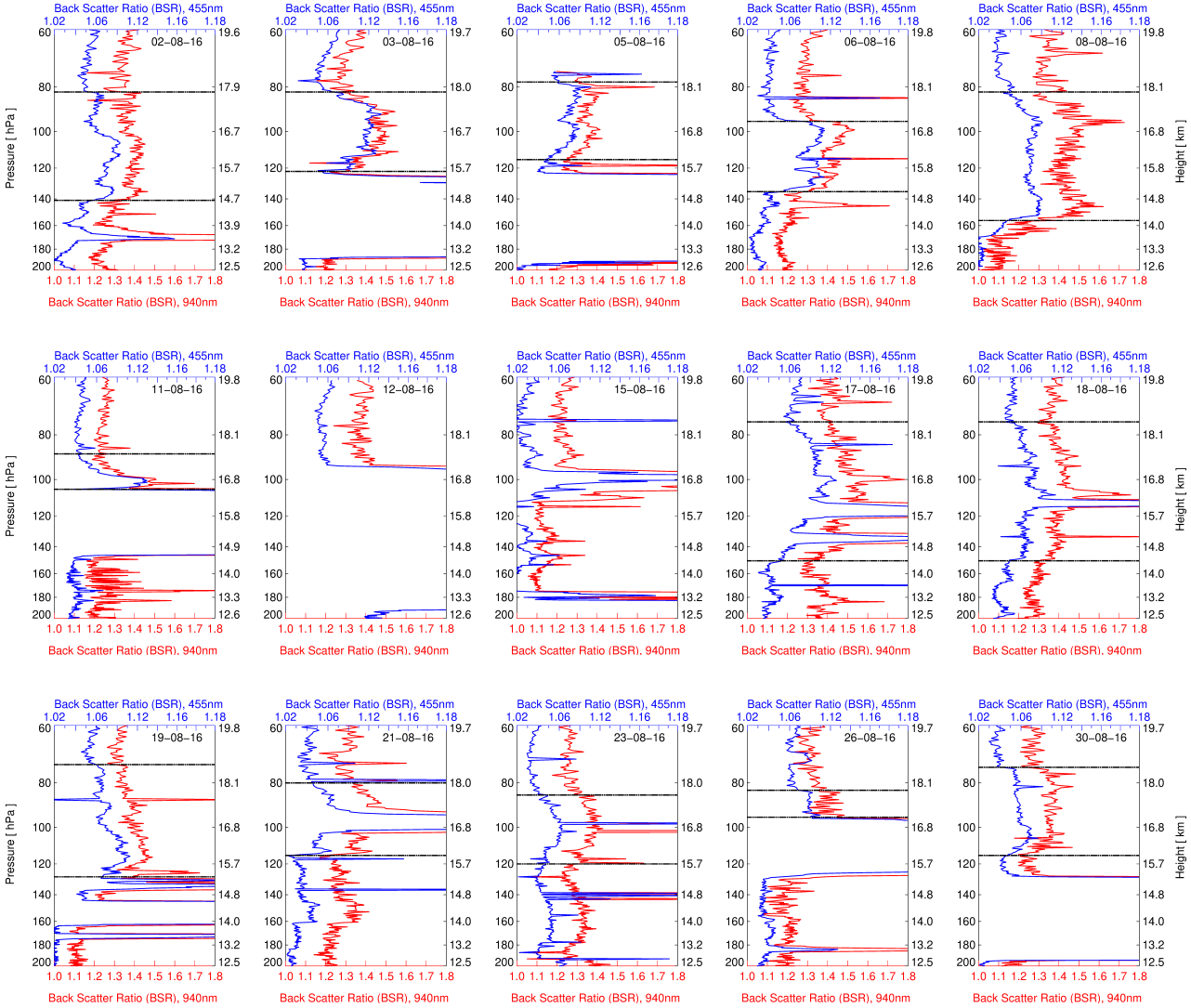

Figure 2.8: As Fig. 2.7, here measurements are shown for all days (see Tab. 3.1 for an overview).

In Fig. 2.7 the measured BSR_{455} (blue line) and BSR_{940} (red line) profiles are shown from the COBALD measurements in Nainital in 2016 for two days in August (with no interference

from cirrus layers or spike artefacts). The discussed features are clearly visible; although the ATAL can be detected using both the BSR_{455} and BSR_{940} measurements, the 455 nm channel is less noisy, so it constitutes the preferred channel for the detection of the ATAL in COBALD balloon measurements. An overview of BSR_{455} and BSR_{940} measurements for all days of the Nainital campaign is given in Fig. 2.8.

2.5 First results of measured ozone and water vapor in Nainital 2016

An overview of the results of the balloon-borne measurements conducted in the campaigns in 2016 and 2017 is given in Fig. 2.9. Shown are the mean profiles of the measurements at Nainital in August 2016 (blue) and November 2016 (green) as well as in Dhulikhel in 2017 (red). The panels show temperature (left), water vapor (middle) and ozone (right). The bottom panel of Fig. 2.9 shows the zoomed version of the top panel over the tropopause region (40-180 hPa).

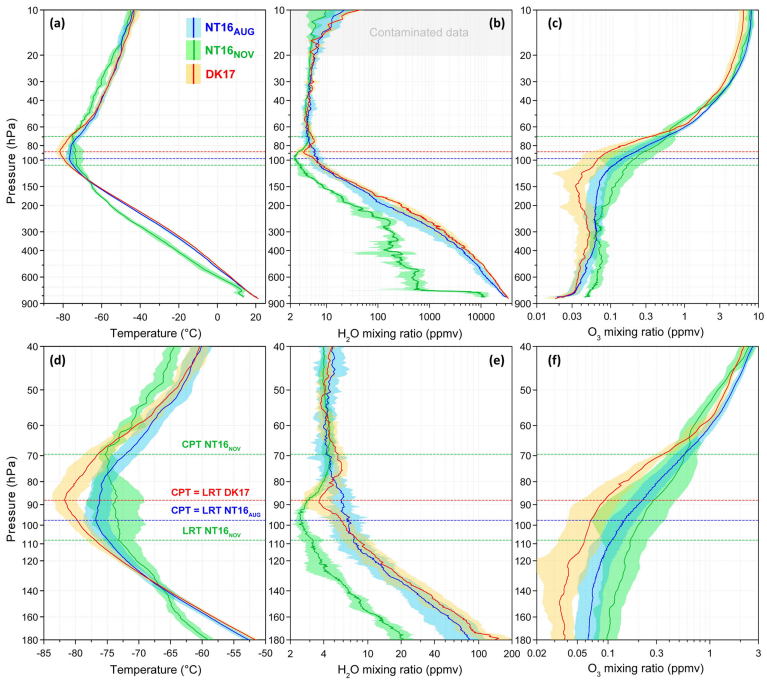

Figure 2.9: Mean profiles (solid lines) and standard deviations (color shading) of all balloon borne measurements of temperature (panels a, d), water vapor mixing ratio (b, e), and ozone mixing ratio (c,f) as a function of pressure, for Nainital August, 2016 NT16 $_{AUG}$ (blue)), Nainital November, 2016 (NT16 $_{NOV}$ (green)) and Dhulikehl, 2017 (DH17 (red)). Upper row (a-c): measured profiles from the surface to 10hPa. Bottom row (d-f): zoom into the tropopause region (40-180 hPa). See chapter 2 for details on the measurement techniques. Above figures have been adapted from Brunamonti et al. [2018],(courtesy of S. Brunamonti).

The mean temperature measurements clearly show a mean lapse-rate tropopause and also a mean cold point tropopause marked in Fig. 2.9. The middle and right hand column shows the dryness of the stratosphere above the tropopause and the increase in ozone with altitude in the stratosphere.

Chapter 3

Results of COBALD Measurements

From Nainital, at the foothills of the Himalayas, 15 successful night-time balloon launches were conducted during the peak of the monsoon season in August 2016 (see Tab. 3.1 and Chap. 2 for more details on the campaign). The frequency of soundings was adjusted depending on the meteorological conditions. Out of a total 35 balloon soundings according to Brunamonti et al. [2018] (see Chap. 2). We present here 17 launches, which were performed with the COBALD instrument as part of the payload (Tab. 3.1). Four launches in August 2016 were excluded in our analysis. The 16 August launch burst below 3 km altitude due to harsh weather conditions, and on 28 August the data showed very low signal-to-noise ratio in the stratosphere, likely caused by optical contamination. The post processing of the COBALD data requires the normalization of the raw signal to a reference value, which is typically based on the measurements from above 30 km altitude (i.e. above the stratospheric aerosol layer). Due to the low absolute BSR (back-scatter ratio, see Chap. 2) signal of the ATAL, a careful calibration of all profiles is critical here. Since no stratospheric data are available on 5 and 12 August due to early balloon bursts (below 20 km altitude), for the sake of consistency, we exclude these two profiles from our analysis.

3.1 Color index and ice saturation

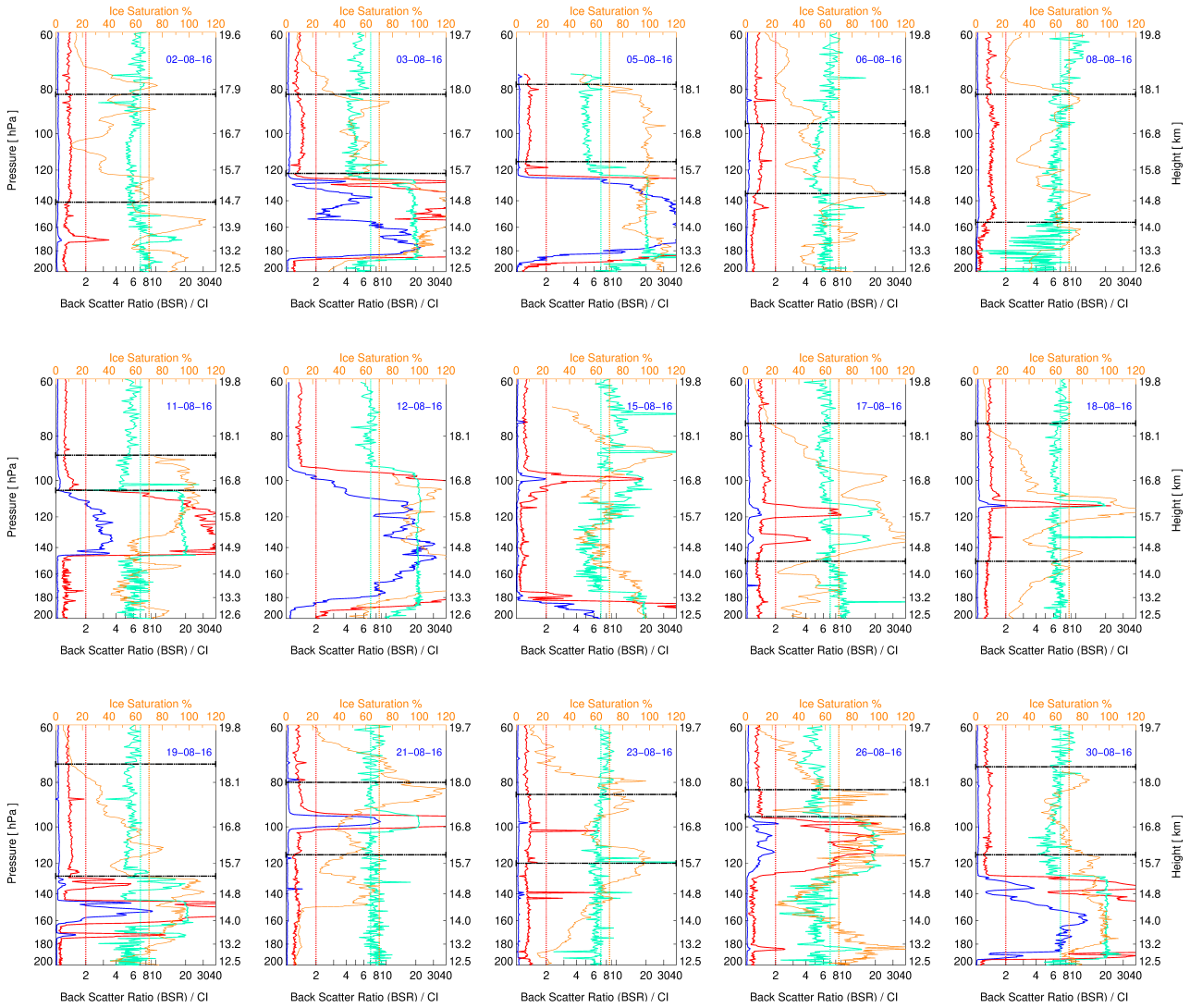

Figure 3.1: COBALD BSR_{455} (blue) and BSR_{940} (red) soundings in the UTLS region versus pressure 60−200 hPa for each flight in August 2016. In addition, the colour index (CI = $(BSR_{940} - 1)/(BSR_{455} - 1)$; green) and the ice saturation (S_{ice}, orange) is shown. Corresponding height calculated using both measured pressure and temperature is also given for orientation (see right-hand y-axis). In our analysis, layers with CI > 7.0 (CI = 7; dotted green line), $BSR_{940} \geq 2$ (BSR_{940} = 2; dotted red line) and $S_{ice} > 70\%$ (S_{ice} = 0.7; dotted orange line) were rejected as cirrus clouds. The top and bottom boundaries of the ATAL (see Tab. 3.1) are marked by horizontal dashed black lines, except for 12 and 15 August, as no ATAL was detected on these days (as in Fig. 3.3)(Figure has been adapted from Hanumanthu et al. [2020]).

During the balloon ascents from Nainital in August and November 2016 measurements were performed of backscatter at wavelengths of 455 nm (blue visible) and 940 nm (infrared) [Wienhold, 2008; Brabec et al., 2012] and of water vapour mixing ratio by cryogenic frost-point hygrometer [Vömel et al., 2007, 2016] (see Sect. 2.2). These measurements allow the

definition of the colour index (CI) [Cirisan et al., 2014]. The Color Index (CI), is defined as the 940-to-455 nm ratio of the aerosol component of the BSR,

$$\mathrm{ColorIndex(CI)} = (\mathrm{BSR}_{940} - 1)/(\mathrm{BSR}_{455} - 1) \tag{3.1}$$

The CI is a useful indicator of particle size and can thus be employed to discriminate aerosol and cirrus measurements [Cirisan et al., 2014; Vernier et al., 2015; Brunamonti et al., 2018]. The CI for all balloon flights over Nainital in August 2016 is shown in figure 3.1. The frost-point hygrometer measurements allow the calculations of ice saturation (S_{ice}) during the balloon ascent. S_{ice} is defined as the ratio of the ambient water partial pressure over the vapor of water over ice. The vapour pressure of water over ice in a function of ambient temperature and is calculated according to Murphy and Koop [2005]. Both Color Index (CI) and ice saturation (S_{ice}) are considered in the analysis presented here to discriminate aerosol and cirrus clouds (ice particles) in the back-scatter measurements and are shown in the Fig. 3.1.

No.	Date	Pressure[hPa]	Pot. temperature[K]	$\overline{\text{BSR}}_{455}$	σ	Note
NT001	02-08-16	141 – 82	365 – 405	1.067	0.008	
NT002	03-08-16	122 – 82	368 – 400	1.092	0.013	bottom Cirrus
NT003	05-08-16	115 – 78	374 – 415	1.067	0.010	
NT004	06-08-16	135 – 95	364 – 388	1.083	0.009	
NT005	08-08-16	156 – 82	362 – 408	1.071	0.005	
NT007	11-08-16	105 – 88	367 – 400	1.070	0.024	bottom Cirrus
NT009	12-08-16	140 – 92	363 – 385	—	—	Cirrus
NT011	15-08-16	140 – 92	366 – 389	1.023	0.009	no ATAL
NT015	17-08-16	150 – 75	363 – 422	1.076	0.014	
NT017	18-08-16	150 – 75	362 – 422	1.065	0.008	
NT018	19-08-16	128 – 73	365 – 420	1.073	0.010	bottom Cirrus
NT023	21-08-16	115 – 80	372 – 404	1.056	0.011	
NT025	23-08-16	120 – 85	369 – 398	1.054	0.007	
NT027	26-08-16	95 – 83	382 – 398	1.080	0.004	bottom Cirrus
NT029	30-08-16	115 – 74	370 – 418	1.059	0.006	
NT033	10-11-16	140 – 92	365 – 394	1.037	0.006	post-monsoon
NT034	11-11-16	140 – 92	359 – 401	1.034	0.003	post-monsoon

Table 3.1: Table of all night-time balloon launches analyzed here (see also [Hanumanthu et al., 2020]). Listed are number, date, top and bottom of the ATAL noted in both pressure and potential temperature, the mean value of the back-scatter ratio ($\overline{\text{BSR}}_{455}$ excluding cirrus contributions) and its standard deviation (σ) (see text for more details). Top of the ATAL is defined as the pressure level, where either the BSR_{455} profile has the strongest gradient or where BSR_{455} merge to the November background. The bottom is defined using the same criteria, except for cases where ATAL is limited to below by a cirrus cloud (3, 11, 19 and 26-August). On 12-August, the UTLS is filled by a 5 km thick cirrus cloud, hence the ATAL cannot be diagnosed. On 15-August 2016, the UTLS was largely cloud-free but without any indication of the ATAL. The November soundings are post-monsoon without the ATAL. For soundings without the ATAL a reference pressure (140-92 hPa) and potential temperature (calculated from the measured temperature and pressure) range is given. This reference range allows comparisons with the ATAL observations to be made (details see Sects. 5.4). (Table has been adapted from Hanumanthu et al. [2020]).

3.2 Data analysis and processing

In order to identify the ATAL, it is necessary to discriminate aerosol and cirrus clouds (ice particles) in the back-scatter measurements. For this purpose, the ice saturation (S_{ice}) from the CFH instrument and the CI from the COBALD measurements was used [Cirisan et al.,

2014]. Layers with CI > 7.0, $BSR_{940} \geq 2$ and $S_{ice} > 70\%$ were rejected as cirrus clouds [Vernier et al., 2015; Li et al., 2018; Brunamonti, 2018; Brunamonti et al., 2018]. Other sections of the profiles measured during the August soundings, which show substantially elevated values of BSR_{455} between $\sim$140 and 70 hPa ($\approx$ 14–18 km), are classified as ATAL. As we will see below, the classification is considerably simplified by the fact that the COBALD profiles reveals the fingerprints of the ATAL clearly; i.e. the top and bottom of the aerosol layer can be identified with reasonable precision. The elevated values of BSR_{455} are quantified by comparing the August profiles with the mean of the November measurements, when there is no ATAL during post-monsoon [Brunamonti et al., 2018]. The enhancement of BSR_{455} for the ATAL remains below 1.12 (and the CI below 7). Conditions with cirrus clouds embedded within the ATAL can also be easily identified, as the cirrus clouds have 10–100 times larger BSR_{455}. As they completely mask these ATAL particles, these cannot be detected and quantified under such conditions.

Following earlier work [Brabec et al., 2012; Brunamonti et al., 2018], vertically binned data are used here for the CFH and COBALD instrument. BSR_{455}, BSR_{940}, CI and S_{ice} are binned in pressure intervals of 1 hPa for pressure greater than 300 hPa and 0.5 hPa for pressure less than 300 hPa, which yields an improved signal to noise ratio. This binning corresponds to a vertical resolution of approximately 25 m in the UTLS. All data were carefully quality-checked and measurements showing evidence of anomalous instrumental behaviour were rejected, as described by Brunamonti et al. [2018]. The processing of COBALD includes the rejection of moon spikes that may arise due to the oscillatory motion of the payload 60 m below the balloon, when the detector happens to be pointing towards the moon. Moon spikes affect only a tiny fraction of the COBALD data and care is taken not to confuse them with thin cirrus clouds

To identify these anomalous "spikes", we used a simple criterion; we consider the signal to be an anomalous spike when BSR_{455} nm > 1.12 and CI < 7. These spikes are then removed from the data set, where the condition CI < 7 ensures that cirrus clouds will be retained. Finally, some specific cases with spikes in the BSR_{455} measurements of a very small vertical extent still remained in the binned data, where $BSR_{455} < 1.12$ and $7 <$ CI < 10. These specific cases occurred for 3, 15, 21, 23 and 30 August; the corresponding data points were also removed from the data set used here.

3.3 Aerosol back-scatter measurements in August 2016

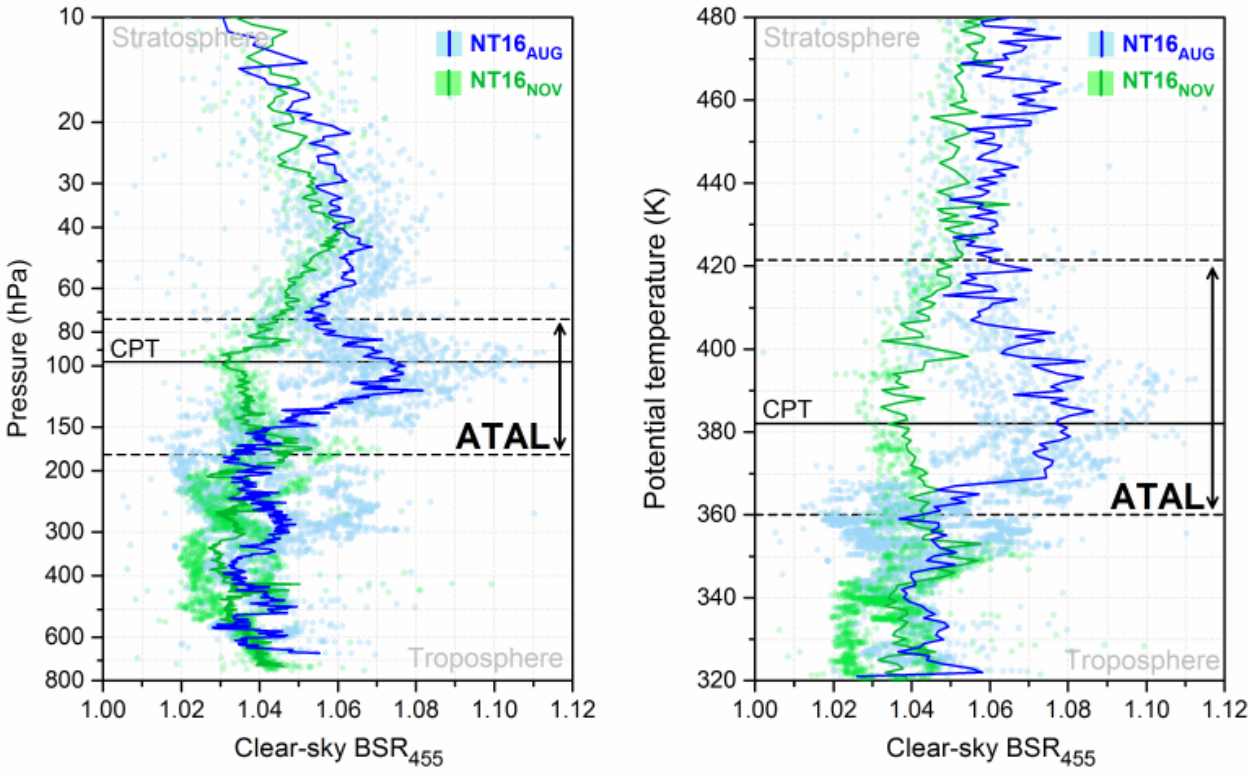

Figure 3.2: Back-scatter measurements (BSR_{455}) in Nainital, India, in August 2016 versus pressure (left) and versus potential temperature (right). Shown are BSR_{455} values for aerosol (dots) and averaged aerosol profiles (solid lines), both without cirrus contributions for August (blue) and November (green). Black lines show the mean temperature lapse-rate minimum (lower dashed), cold point tropopause (CPT, solid) and top of confinement (upper dashed). The vertical black arrows indicate the ATAL region (Left panel: adapted from Fig. 11 of Brunamonti et al. [2018]; Right panel: the ATAL boundaries and CPT from Tab. 3 in Brunamonti et al. [2018]). (Figure has been adapted from Hanumanthu et al. [2020]).

An overview of the Nainital aerosol back-scatter observations in August (blue) and November (green) 2016 with pressure as the vertical coordinate is provided in Fig. 3.2 (left). Like for other years and locations [Vernier et al., 2015, 2018], the ATAL is clearly visible as an enhancement in back-scatter ratio (BSR_{455}) in August compared to the November measurements, with the averaged back-scatter (BSR_{455}) values in August reaching about 1.08 (Fig. 3.2). In Brunamonti et al. [2018], the ATAL is defined between the mean potential temperature lapse-rate minimum and the top of the confined lower stratosphere (Fig. 3.2, dashed lines). The potential temperature lapse-rate minimum coincides approximately with the top of the convective outflow level (≈180 hPa) [e.g., Gettelman and de Forster, 2002; Brunamonti et al., 2018].

Fig. 3.2 (right) shows the same BSR_{455} values, but with potential temperature as the vertical coordinate. Using the back-scatter measurements with potential temperature as the altitude scale, a somewhat different picture emerges than when using pressure as the altitude scale due the fact that in this altitude region the potential temperature has a large vertical gradient. In particular, a sharp increase in the averaged BSR_{455} in August around 360–365 K is clearly noticeable. This steep gradient represents the top of the convective outflow region [e.g., Gettelman and de Forster, 2002], i.e. below this level more frequent deep convection scavenges the aerosol. An enhancement of the averaged BSR_{455} in August compared to November is noticeable up to potential temperatures of about 420 K ($\sim$75 hPa), but especially when considering potential temperature as the vertical coordinate, a top of the ATAL is not clearly defined. Only a slow decrease of averaged BSR_{455} with altitude is observed (Fig. 3.2, right). This observation is consistent with a decreasing confinement of the air mass within the Asian monsoon anticyclone with increasing potential temperature [Brunamonti et al., 2018; Vogel et al., 2019].

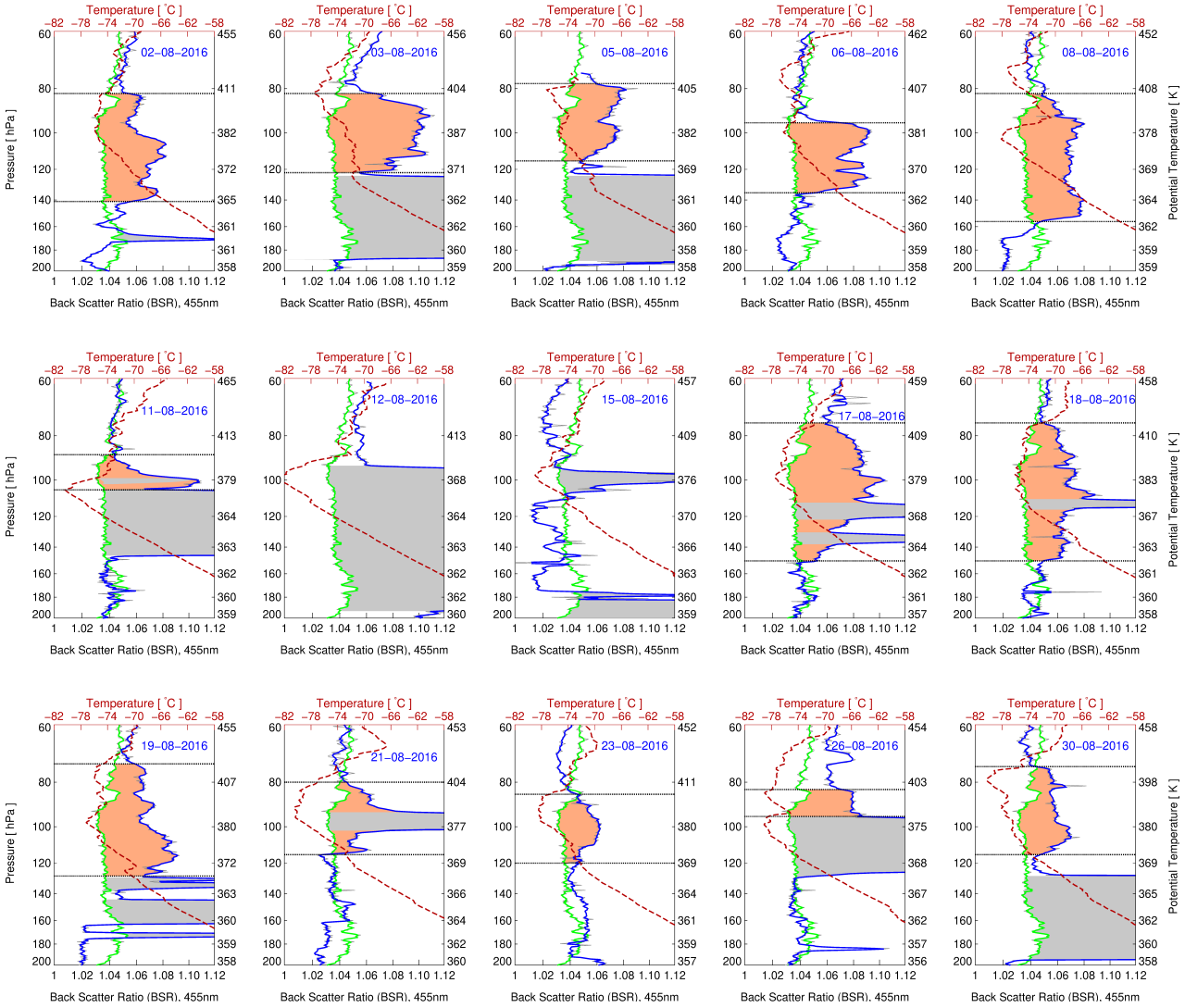

Figure 3.3: COBALD BSR_{455} measurements in the UTLS region versus pressure 60–200 hPa for each flight in August 2016 (blue line). Corresponding potential temperature calculated using both measured pressure and temperature is also given for orientation (see right-hand y-axis). The averaged BSR_{455} profile of the two November measurements is shown in green. The blue and the green lines show a slightly smoothed representation (three point smoothing) of the original 0.5 hPa binned data (light grey lines; see Sect. 3.2 for details). The measured temperature for each day in August 2016 is shown in red. The ATAL is highlighted by the orange shading and cirrus clouds are indicated by the grey shading. The top and bottom boundaries of the ATAL (see Tab. 3.1) are marked by horizontal dashed black lines, except for 12 and 15 August, as no ATAL was detected on these days (Figure has been adapted from [Hanumanthu et al., 2020]).

In Fig. 3.3, all 15 investigated COBALD balloon profiles in August 2016 (see also Tab. 3.1) are shown individually (blue lines) in comparison to the average of the two November measurements (green lines) used as a background signal. The top and bottom of the ATAL was determined for each balloon profile individually (quantified in Tab. 3.1) and these levels are shown in Fig. 3.3 as horizontal black dashed lines. Here the top and bottom of the ATAL is approximated by the pressure level where the BSR_{455} profile has the strongest gradients or where the BSR_{455} merges with the November background. The bottom is set using the

same criteria as for the top of the ATAL, except for cases where a cirrus cloud was detected directly below the ATAL. In these cases the top of the cirrus cloud is set to the bottom of the ATAL which is hidden by the cirrus cloud (3, 11, 19, 26 August).

The mean value of the back-scatter intensity ($\overline{\mathrm{BSR}}_{455}$) between bottom and top is individually calculated for each balloon sounding using the binned data (see Tab. 3.1). Cirrus clouds between top and bottom are excluded in the calculation of $\overline{\mathrm{BSR}}_{455}$ and its standard deviation. Therefore, no $\overline{\mathrm{BSR}}_{455}$ value is shown in Tab. 3.1 for the 'no ATAL flight' on 12 August, because over the entire altitude range where the ATAL is expected cirrus was detected.

Chapter 4

Model description and meteorological conditions

4.1 The chemical Lagrangian model of the stratosphere

The Chemical Lagrangian Model of the Stratosphere (CLaMS) is a comprehensive chemical transport model, which simulates chemistry, advection, and mixing in the stratosphere and upper troposphere [e.g., McKenna et al., 2002a,b; Konopka et al., 2007; Grooß et al., 2018]. Because of the Lagrangian representation of transport, with the intensity of mixing in model transport being driven by the strength of flow deformation, the model is especially suited for the simulation of tracer transport in the vicinity of strong transport barriers and the associated tracer gradients [e.g., Grooß et al., 2005; Konopka et al., 2009; Poshyvailo et al., 2018; Vogel et al., 2019]. The model can be driven by different reanalysis products from different Centres [e.g., Ploeger et al., 2019; Yan et al., 2019].

The model employs a hybrid vertical coordinate (in units of K) that corresponds to isentropic coordinates above a certain pressure level p_r (e.g., 100 hPa or 300 hPa) but smoothly transforms into a pressure-based orography following coordinate below p_r [Mahowald et al., 2002; Ploeger et al., 2013; Pommrich et al., 2014]. More accurately, for pressure p exceeding a reference level of $p/p_{\text{surface}} = 0.3$) the potential temperature co-ordinate transforms into the hybrid coordinate ζ (in units of K).

This hybrid coordinate allows the tropospheric upwelling as it is represented in the pressure tendencies of the reanalysis data from different centers to be represented in the CLaMS

transport [Konopka et al., 2007]; above p_r also latent heat release contributes to the vertical velocity. However, a comprehensive parametrization of sub-grid scale convectively driven vertical transport, is not included in CLaMS. A parametrization for including convective uplift and additional tropospheric mixing in CLaMS has recently been described by Konopka et al. [2019].

The CLaMS model also contains a detailed comprehensive stratospheric chemistry scheme including heterogeneous chemistry on the surfaces of cold sulfate aerosol and polar stratospheric clouds, photolysis calculations in three dimensions and catalytic ozone loss cycles [Becker et al., 2000; McKenna et al., 2002a], which has been applied to a variety of problems [e.g., Vogel et al., 2003; Grooß et al., 2011; Grooß and Müller, 2021]. A simplified chemistry scheme is also available [Pommrich et al., 2014], which focuses on simulations of stratospheric CO and describes long lived tracers including CH_4, N_2O, $CClF_3$, and CO_2. The chemical scheme is however not used in this thesis.

4.2 Trajectory calculations

For the model analysis presented here, we employ the trajectory module of the three- dimensional Lagrangian chemistry transport model CLaMS [Sutton et al., 1994; McKenna et al., 2002b; Pommrich et al., 2014] driven by dynamic fields from the European Centre of Medium-Range Weather Forecasts (ECMWF) interim reanalysis (ERA-Interim) employing a horizontal resolution of $1^\circ \times 1^\circ$ [Dee et al., 2011]. In ERA-Interim changes are implemented to improve deep and mid-level convection compared to previous reanalysis data [Dee et al., 2011]. CLaMS back trajectory calculations are very well suited to analyze the detailed transport pathway of an air parcel, although they consider only the advective transport, neglecting mixing processes entirely. Earlier, CLaMS trajectories were applied to problems including polar chemistry, moreover in the last years CLaMS trajectory calculations have been dealt with in transport in the tropics, in particularly in the region of the Asian monsoon and in tropical cyclones [Ploeger et al., 2010, 2012; Vogel et al., 2014, 2019; Li et al., 2017, 2018, 2020]. To analyze the transport pathways and the origin of air masses contributing to the ATAL in August 2016 over Nainital, CLaMS 40-day backward trajectory calculations were performed. As the starting point for backward trajectory calculations, the pressure levels of the measurements recorded every second (i.e. no binned data) are used. The same trajectory model set-up is used as in several previous publications [Vogel et al., 2014; Li et al.,

2017, 2018, 2020]. In the CLaMS model, potential temperature is used as the vertical coordinate when the pressure is less than $p_r \approx 300\,\text{hPa}$, (i.e. in the upper troposphere and in the stratosphere); when the pressure is greater than about 300 hPa (see Sect. 4.1) a pressure-based orography-following coordinate is used [Ploeger et al., 2010; Pommrich et al., 2014]. When the back trajectory dives into the CLaMS model boundary layer, the air mass origin is considered to be reached at the Earth's surface. The model boundary layer is defined as the hybrid vertical coordinate ζ is lower than 120 K [Pommrich et al., 2014; Vogel et al., 2019], which corresponds to a layer $\approx$ 2–3 km above the surface of the Earth considering orography.

4.3 Meteorological conditions of the Asian monsoon 2016

4.3.1 Monsoon anticyclone

The meteorological conditions under which the balloon soundings were performed are summarized in this section. In the Asian monsoon anticyclone, there is a large variability from day to day in spatial extent, strength, and location. This variability has also described as the "dance" of the Asian monsoon (see Stroh and Team [2020]; Sect. Meteorological overview). The geopotential height (GPH) values at particular pressure layers indicate the location of the Asian monsoon anticyclone roughly. The pressure levels considered for our analysis are 700 hPa, 200 hPa and 110 hPa. The Asian Monsoon Anticyclone is quite homogeneous in nature, so 110 hPa (ATAL layer altitude), 200 hPa (convective outflow), and 700 hPa (free Troposphere) are chosen here. By this, synoptic scale features of the atmosphere can be understood.

Figures 4.1, Fig. 4.2, Fig. 4.3, Fig. 4.4, Fig. 4.5 and Fig. 4.6 will represent the ASMA oscillatory nature throughout the monsoon season which peaks in August. In general ASMA gets to its peak by the month of August over the Third pole (Tibetan Plateau; see Sect. 1.2). Figure. 4.7, Fig. 4.8 and Fig. 4.9 demonstrates the low-pressure systems and in a few cases where cyclonic systems also were observed. This meteorological overview over the region throughout in the ERA-Interim [Dee et al., 2011] world shows the transport pathways created by the dynamical behavior of the Asian monsoon anticyclone.

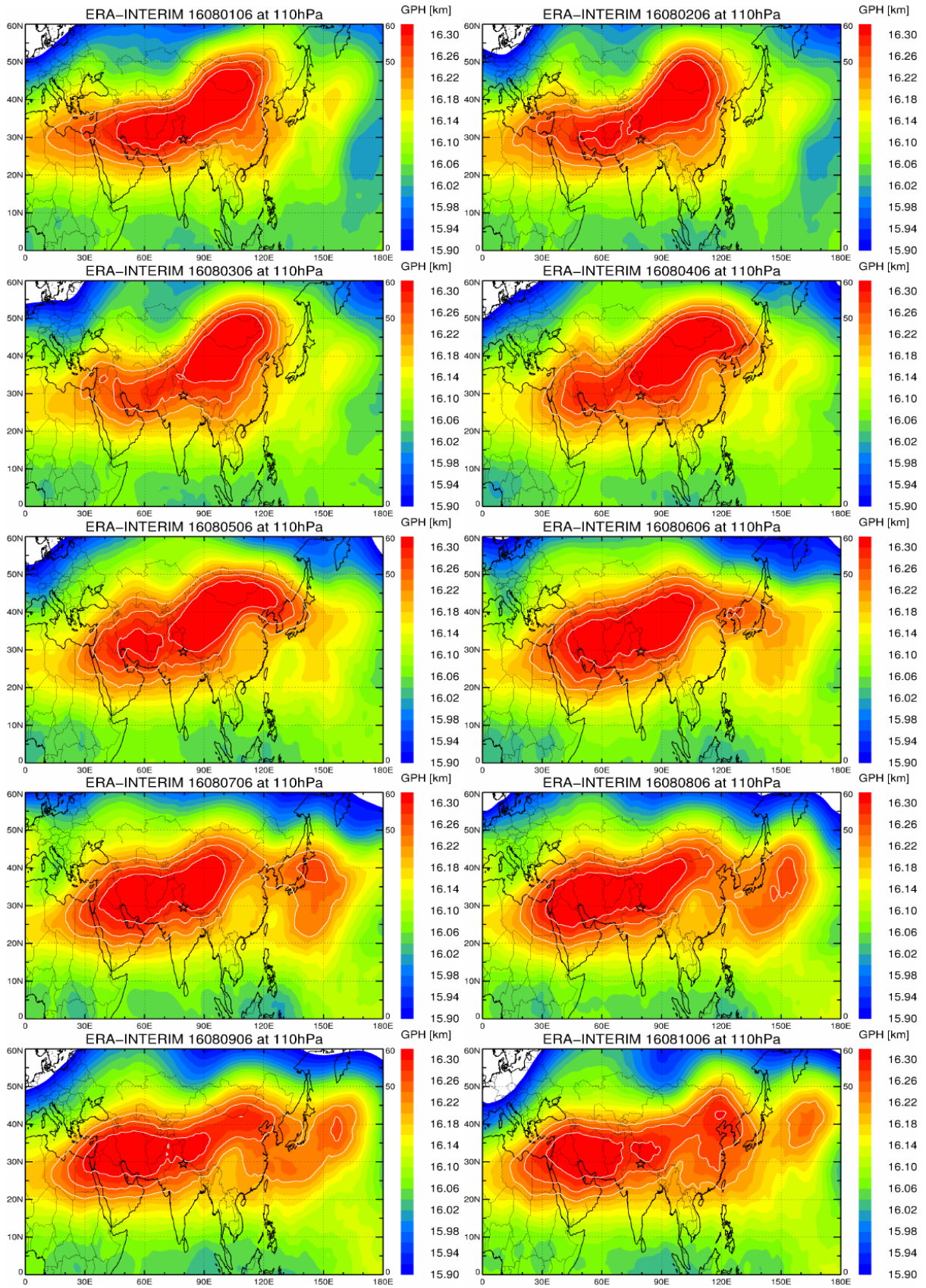

Figure 4.1: The development of GPH at 110 hPa for the first half of August month i.e., from 01-08-2016 till 10-08-2016 for the analysis of balloon soundings over Nainital. Data are from ERA-Interim reanalysis.

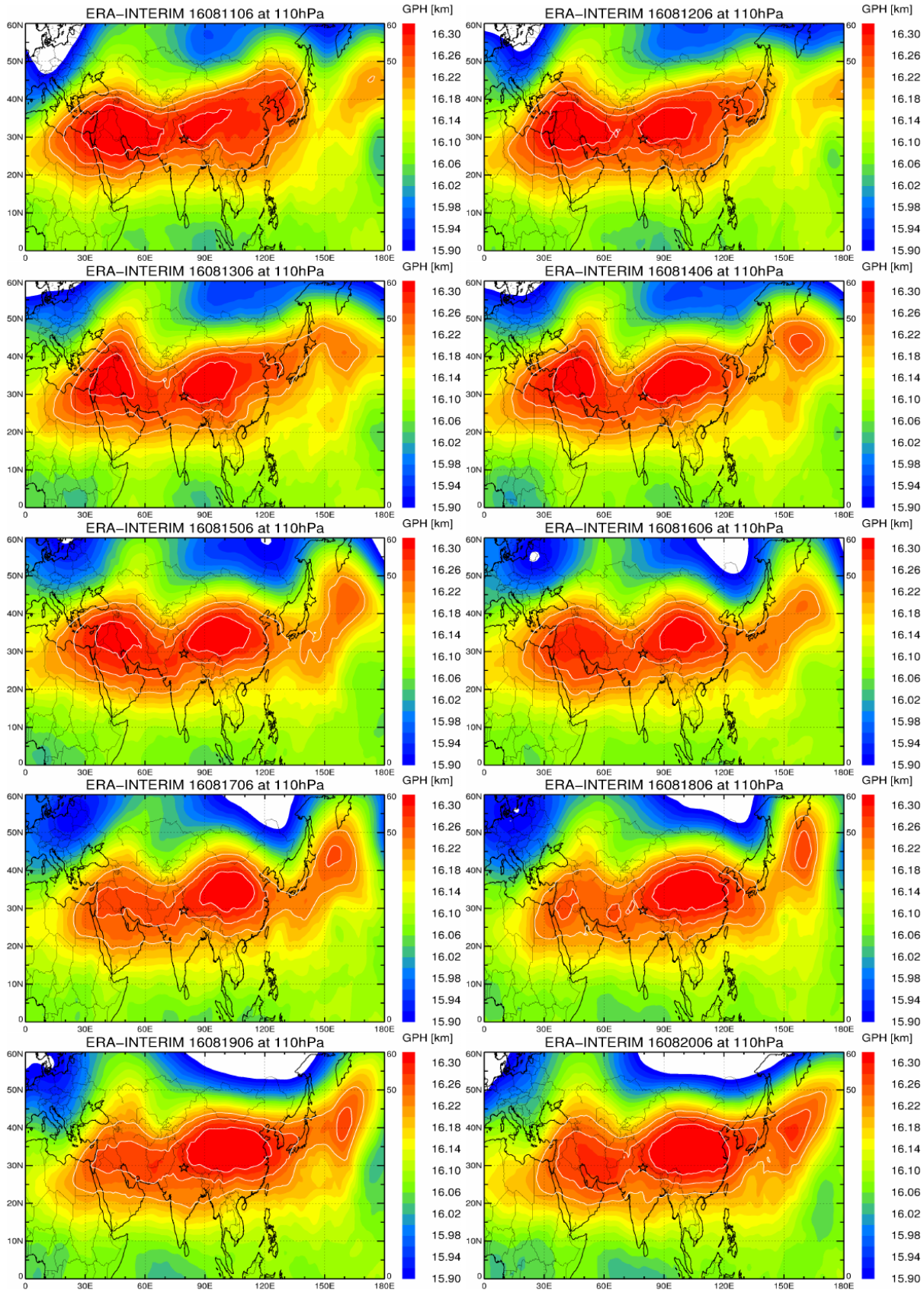

Figure 4.2: The development of GPH at 110 hPa for the second half of August month i.e., from 11-08-2016 till 20-08-2016 for the analysis of balloon soundings over Nainital. Data are from ERA-Interim reanalysis.

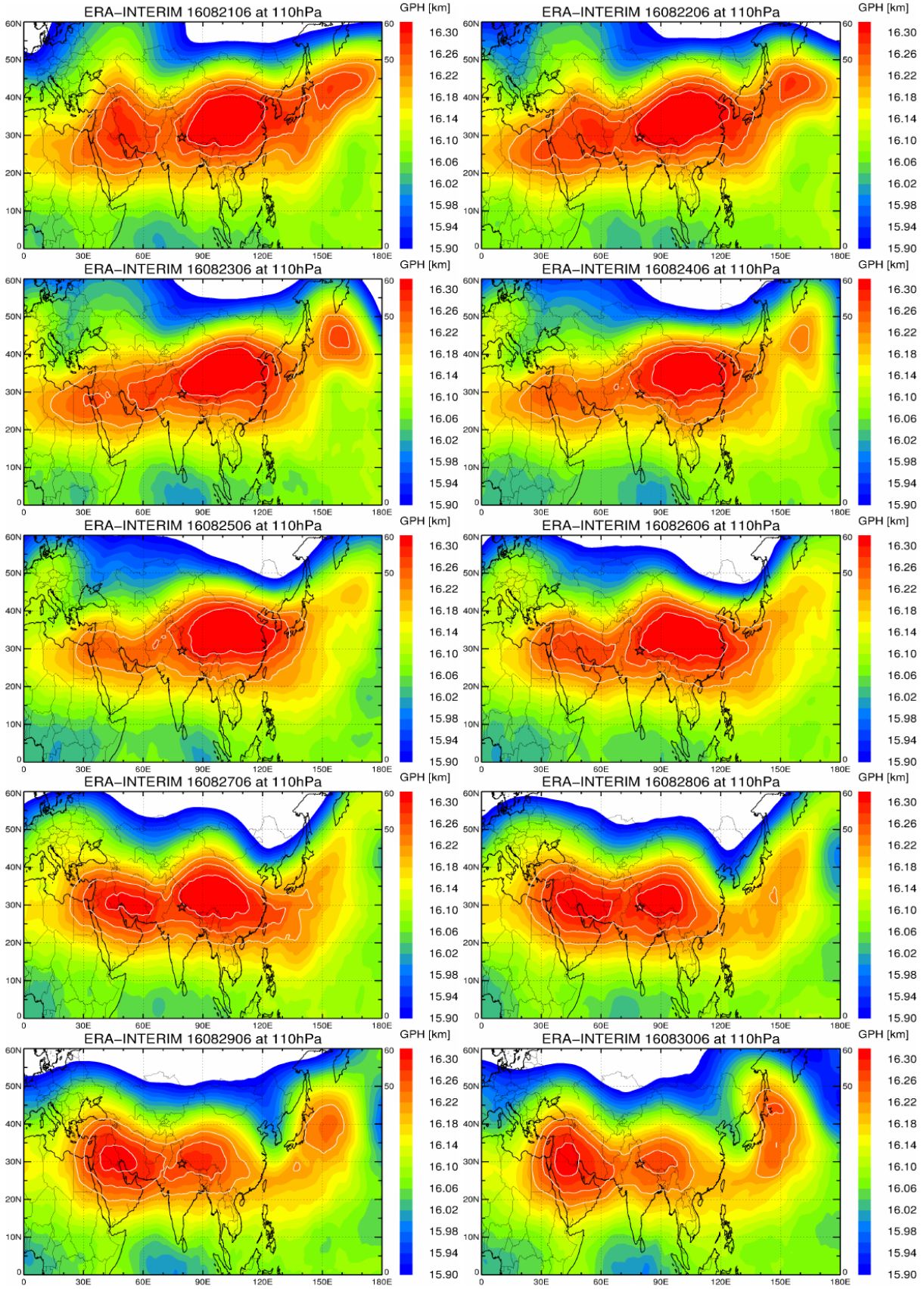

Figure 4.3: The development of GPH at 110 hPa for the second half of August month i.e., from 21-08-2016 till 30-08-2016 for the analysis of balloon soundings over Nainital. Data are from ERA-Interim reanalysis.

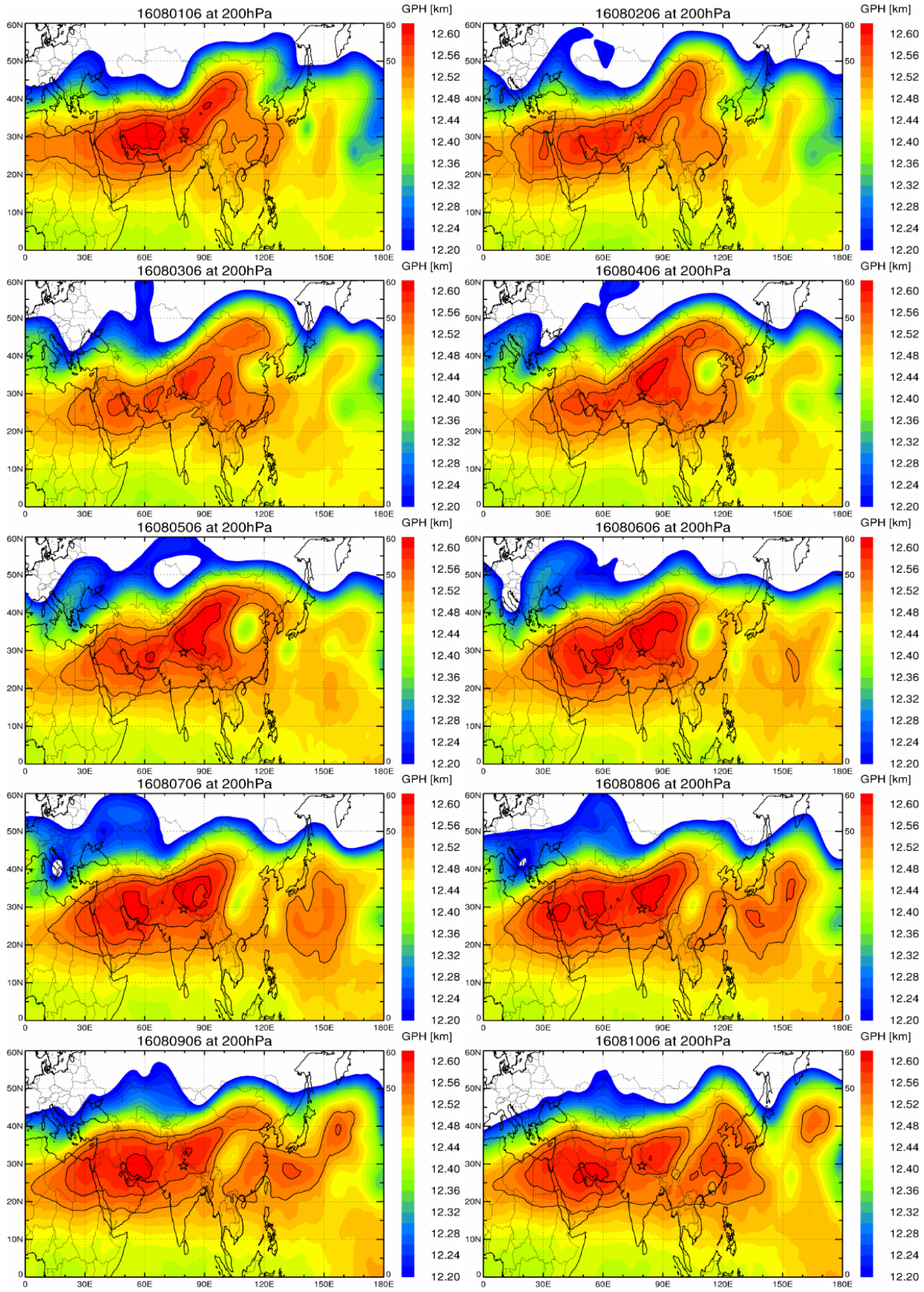

Figure 4.4: As Fig. 4.1 but for 200 hPa.

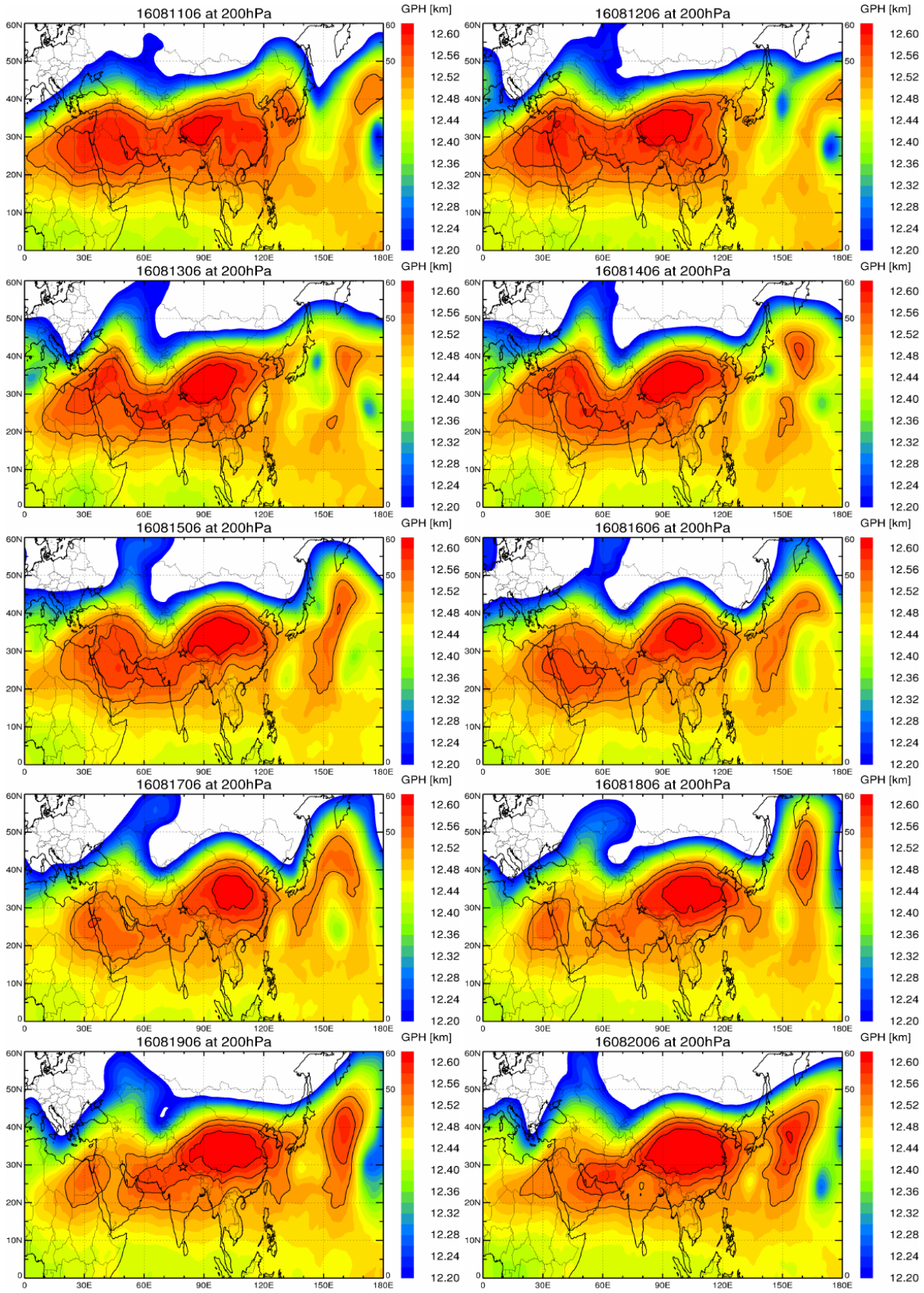

Figure 4.5: As Fig. 4.2 but for 200 hPa.

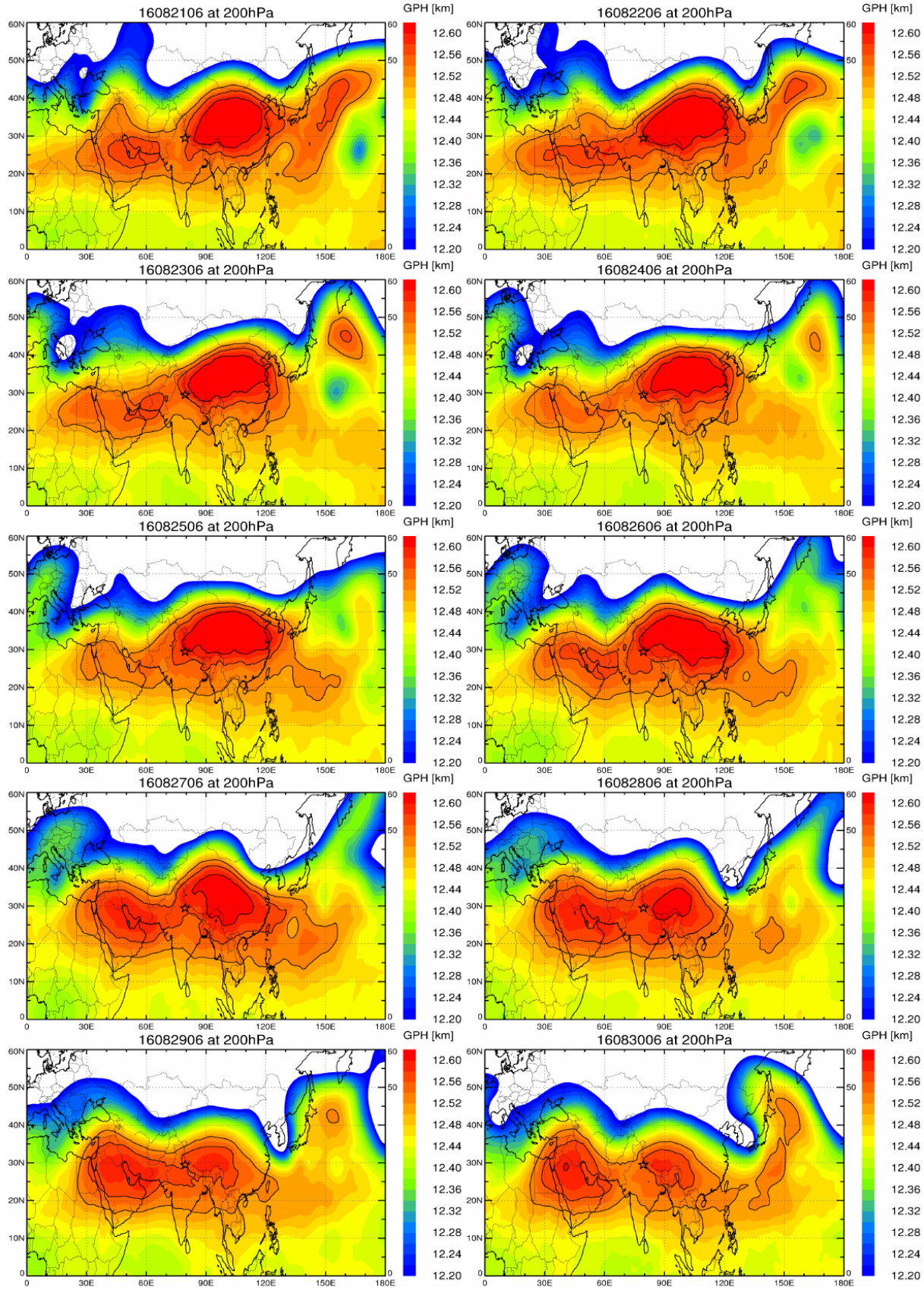

Figure 4.6: As Fig. 4.3 but for 200 hPa.

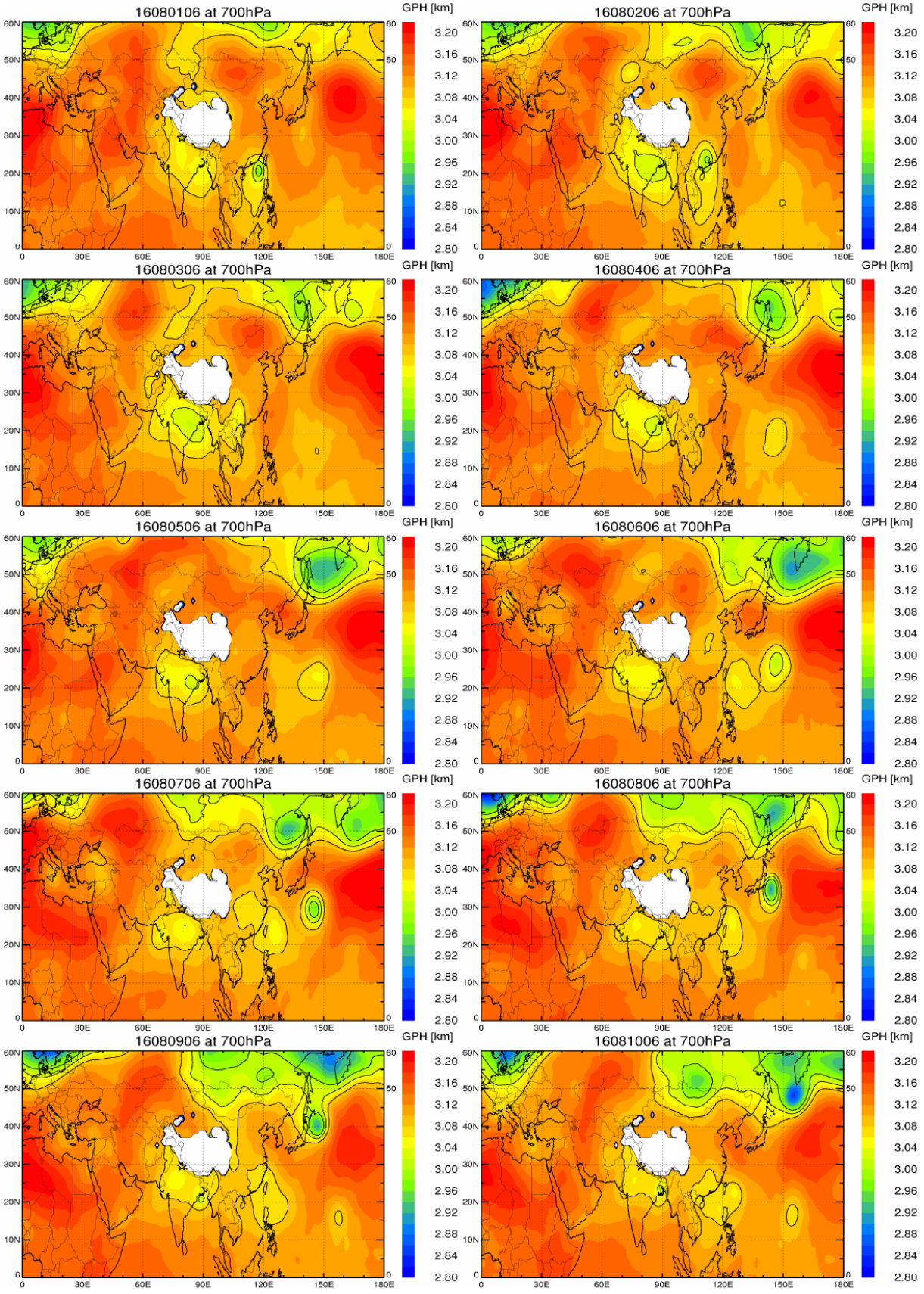

Figure 4.7: As Fig. 4.1 but for 700 hPa.

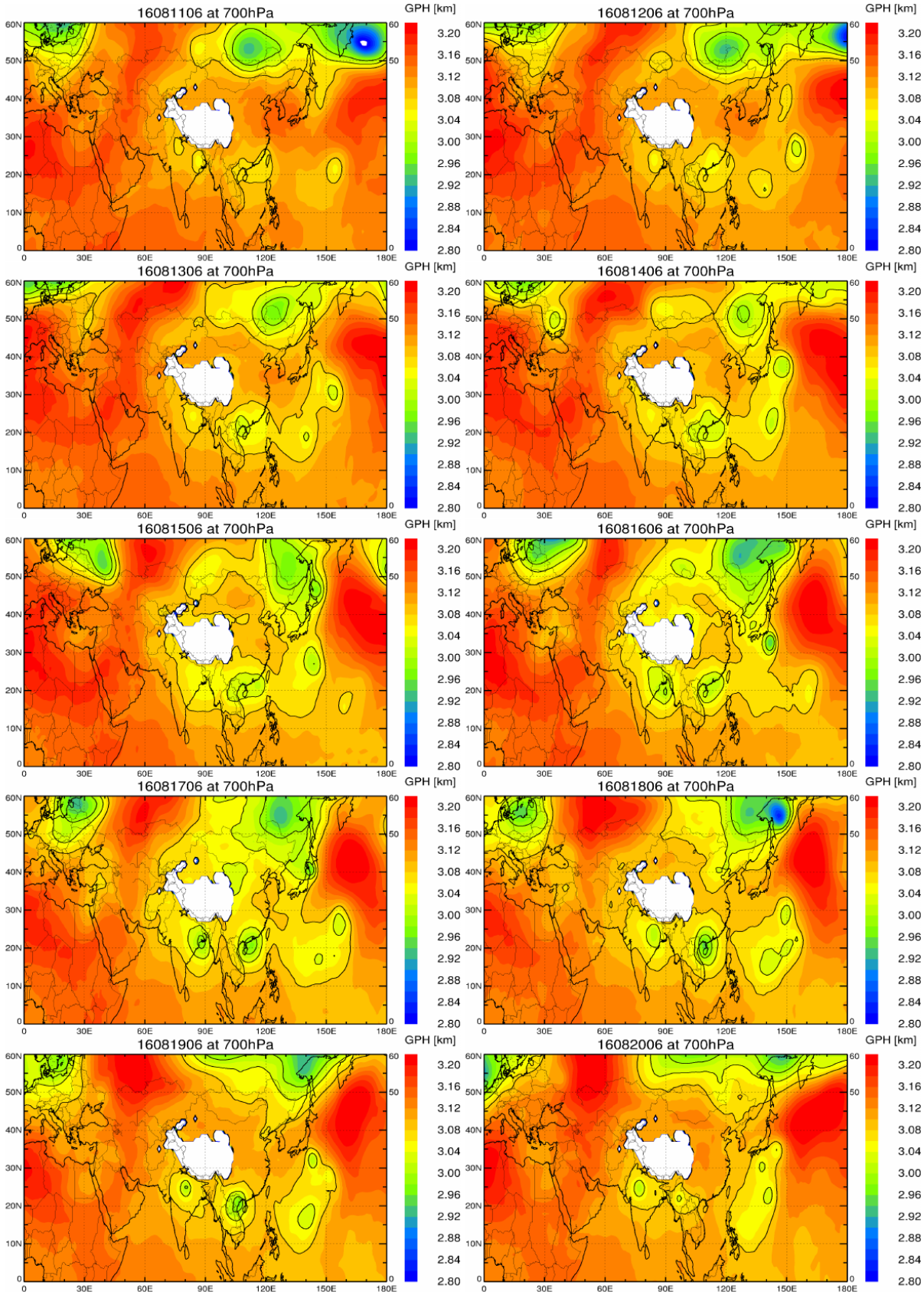

Figure 4.8: As Fig. 4.2 but for 700 hPa.

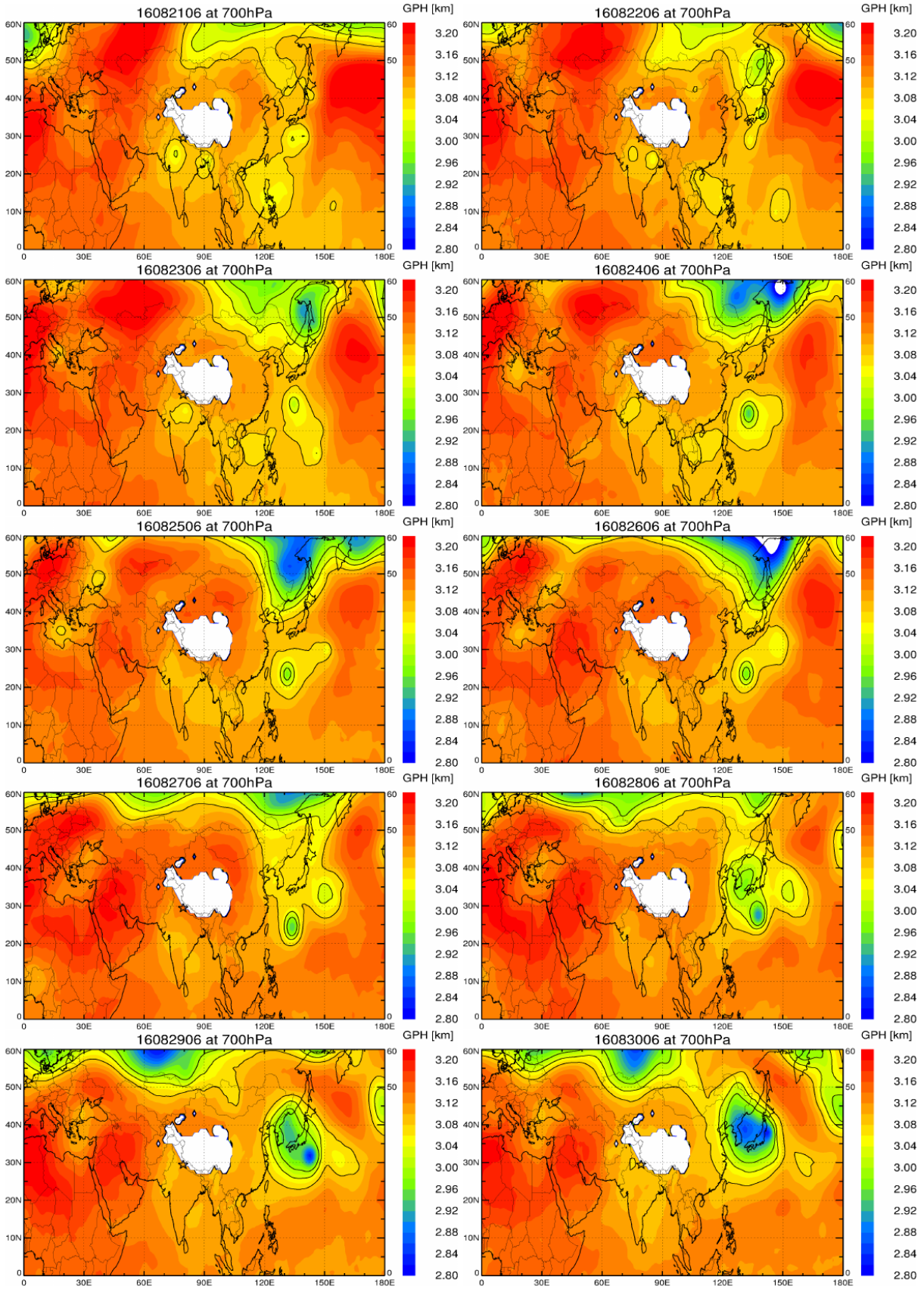

Figure 4.9: As Fig. 4.3 but for 700 hPa.

4.3.2 El Niño southern oscillation status on 2016

El Niño happened to be neutral for the year of 2016 but in 2015 an El Niño occurred. This effected the monsoon rainfall pattern of 2016 significantly. It is also observed in the delayed onset of the monsoon. For more details on the Monsoon and El Niño teleconnections during the decay phase of monsoon please look at Chowdary et al. [2017]. Delayed El Niño condition is consistent with the monsoon report on rainfall of the South West monsoon season published by IMD [IMD, 2016]. That report concluded that the monsoon was normal during the year 2016 while El Niño tended to be on its decaying phase, which favored subsidence conditions over the South Asian region.

Chapter 5

Model Results

5.1 Day-to-day variability of the Asian tropopause aerosol layer

The enhancement of BSR_{455} for the individual balloon borne measurements in August compared to the mean of the two November measurements is shown in Fig. 3.3 (orange shading). There is a strong variability of the altitude, the vertical extent and the BSR_{455} intensity within the ATAL. There are even days, when no ATAL is observed over Nainital (12 and 15 August 2016). In addition, on many balloon flights, a cirrus cloud is observed (e.g. as a very strong enhancement of BSR_{455}, see also Sect 3.2 above); cirrus clouds are marked in grey in Fig. 3.3. These cirrus clouds can occur below the ATAL, but there are also cases when cirrus clouds (ice particles) of a moderate vertical extent ($\sim$10 K) are measured within the ATAL (17, 18, and 21 August 2016). From the measurements alone, can not exclude that the ATAL and cirrus clouds can coexist in this region (see Sect. 3.2 and discussion in Sect. 6.1).

From a seasonal average perspective, the ATAL extends in the longitudinal direction from the Middle East to East Asia and meridionally between 15°-45°N [e.g., Vernier et al., 2015; Fairlie et al., 2020]. This climatological picture is also true for the Asian monsoon anticyclone itself [e.g., Park et al., 2008; Vogel et al., 2016]. Likewise, for the Asian monsoon anticyclone, there is a large variability from day to day in spatial extent, strength, and location, manifesting in an oscillation between a state with one anticyclone and two separated anticyclones (two modes) [e.g., Zhang et al., 2002; Yan et al., 2011; Vogel et al., 2015; Nützel et al., 2016].

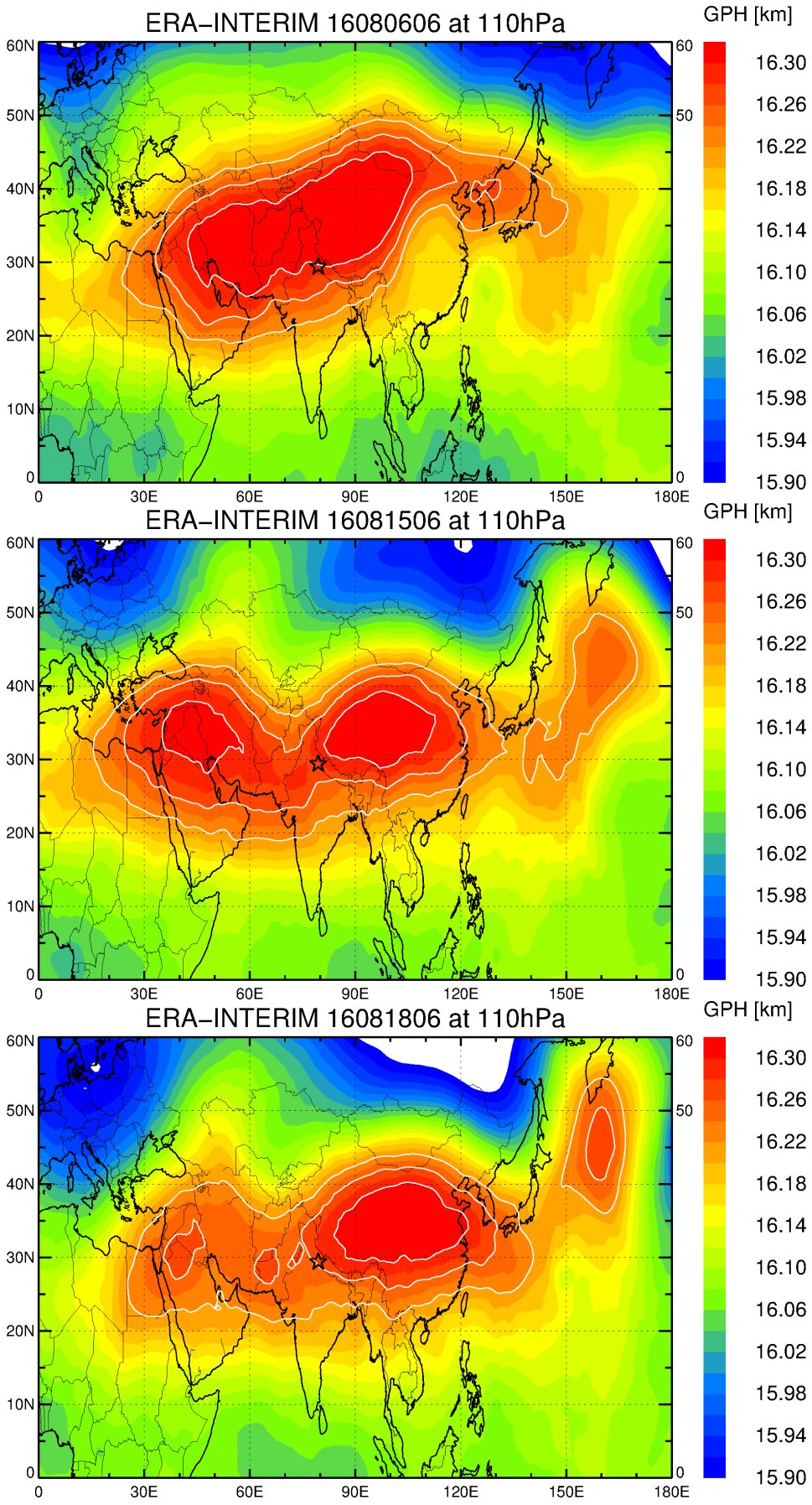

Figure 5.1: Location of the Asian monsoon anticyclone measured by the geopotential height at 110 hPa for 6 August, 15 August and 18 August 2016 at 06:00 UTC (corresponding to 02:30 local time (IST) in Nainital). The GPH of 16.22, 16.26, and 16.30 km is shown as white contour lines. The location of Nainital is marked by a black star symbol. Figure taken from Hanumanthu et al. [2020].

In the following, three specific days will be considered more closely which are examples of particular cases (see Sect. 5.4). A case for which an established ATAL was observed (6 August 2016), a case in which "no ATAL" was observed (15 August 2016) and a case influenced by a typhoon (18 August 2016). The 6 August is selected because the mean value of the backscatter intensity ($\overline{\text{BSR}}_{455}$=1.083) is the highest out of all ATAL cases and is not influenced by cirrus. From the two"no ATAL" cases (12 and 15 August), 15 August is chosen because the cirrus cloud is thinner than on 12 August.

The measurement in Nainital on 18 August 2016 was partially influenced by air uplifted in a tropical typhoon (this case will be discussed in detail in Sect. 5.4.3). On 18 August the ATAL occurs in an broader altitude range compared to 6 August; however the intensity of the ATAL is in general lower ($\overline{\text{BSR}}_{455}$=1.065) than on 6 August.

The location of the Asian monsoon anticyclone for these three days is shown in Fig. 5.1. The Asian monsoon anticyclone is indicated here by geopotential height at 110 hPa (GPH = Φg^{-1} with geopotential Φ ([$m^2 s^{-2}$]) and $g = 9.81$ ([ms^{-2}])) using ERA-Interim reanalyses for 6, 15, and 18 August 2016. The 110 hPa pressure level is selected because this level is located within the ATAL for most balloon flights in August 2016.

For the case of an established ATAL (6 August 2016), a single-modal anticyclone is found. For the case with no observation of an ATAL (15 August 2016), a bi-modal structure of the anticyclone is found, and Nainital is located between the eastern and western mode of the Asian monsoon anticyclone. For the ATAL case impacted by a tropical cyclone (18 August 2016), a single-modal anticyclone is found with pronounced eddy shedding events (outflow from the anticyclone) towards both the east and the west [e.g. Vogel et al., 2015, 2016].

5.2 Trajectory calculation and classification

To analyse the transport pathway and the origin of the air masses contributing to the ATAL, for each sounding in August 2016 backward trajectories were calculated over a time period of 40 days. The dependence of the results of the trajectory calculations on the trajectory length (40, 60, and 80 days) will be discussed in detail below (Sect.. 5.3.3).

The backward trajectories were started every second along the measured balloon profile for which an ATAL was detected during the flight (see Tab. 3.1 and Fig. 3.3, orange). The back-trajectory calculations are based on 1-sec data having a higher vertical resolution than

the BSR_{455} values in Fig. 3.3 (binned data in pressure intervals of 0.5 hPa). In cases with a thin cirrus cloud embedded in the ATAL (17, 18, and 21 August 2016), the region of the cirrus cloud is included in the backward trajectory calculation because it is likely that ATAL and ice particles coexisted in this region (see Sect. 3.2 and discussion in Sect. 6.1). For the two no ATAL cases (12 and 15 August 2016) as well as both post-monsoon measurements (10 and 11 November 2016), backward trajectories were started in a pressure range between 140 and 92 hPa, to allow comparison with the ATAL observations.

The origin of the air masses found in the ATAL are classified according to sources in the model boundary layer, in the lower troposphere (LT), in the upper troposphere (UT) and in the lower stratosphere (LS) (Tab. 5.1). Trajectories are considered ending in the model boundary layer (BL) when they are located for the first time below about 2–3 km (i.e., hybrid coordinate $\zeta \leq 120$ K). The location of this point is referred to as 'end point' of the trajectory in the model boundary layer. The trajectory length for these trajectories ending in the BL is in general shorter than 40 days because they reach the BL before 40 days. Within 40 days $\approx$ 14–64% of the trajectories are reaching the model boundary layer. For the remaining trajectories ending at atmospheric altitudes, a potential temperature criterion is employed to discriminate between origins in the lower troposphere (LT), in the upper troposphere (UT) and in the lower stratosphere (LS) (see Tab. 5.1).

In addition, the maximum updraft within a time interval Δt of several hours along these 40-day backward trajectories is calculated as the point for which the change in potential temperature is maximum ($\Delta\Theta_{max}$) along the 40-day backward trajectories (calculated as running mean over the change in potential temperature within the time interval Δt). The location of the maximum updraft in the interval Δt is calculated as the mean position of the trajectory within Δt for $\Delta\Theta_{max}$. As will be discussed in detail below, the position of the end points and of the strong-updraft may differ substantially. Hanumanthu et al. [2020] presented results for $\Delta t = 18$ hours. Below (see Sect. 5.3.1), the sensitivity of the conclusions on the origin of air on the choice of Δt will be investigated in more detail.

The trajectories originating from the BL are from the region of the Asian monsoon anticyclone and from the western Pacific. To obtain a deeper insight into the origin of air masses contributing to the ATAL, trajectories originating in the BL are further separated. In a latitude–longitude box from 60°E to 160°E and from 5°S to 45°N (Tab. 5.2) this area is also shown in Fig. 5.2, It is distinguished between Tibetan Plateau (Tibet), foothills (Foothills) including the Himalayan foothills, the remaining continental (land) and maritime area (ocean).

The continental areas were separated according to geopotential (Φ) or GPH (Φg^{-1}). The Tibetan Plateau is defined as the altitude above a geopotential Φ of 40000 [m^2s^{-2}] (above GPH $\approx$ 4000 m), the foothills as $20000 < \Phi < 40000$ [m^2s^{-2}] (GPH $\approx 2000-4000$ m), the remaining continental area as $\Phi < 20000$ [m^2s^{-2}] (below GPH $\approx$ 2000 m). Trajectories originating outside the latitude–longitude box are classified as residual.

5.3 Source regions of air masses contributing to the Asian tropopause aerosol layer

5.3.1 Sensitivity of strong-updraft location

In ERA-Interim the global data are available 6-hourly. It is important investigate the sensitivity in the location of the strong-updraft along the trajectories depending on the used time interval Δt . Sensitivity of the locations of strong-updraft on Δt using (Δt =) 6hr, 12hr, 18hr, 24hr, 48hr and also 7 days is shown in Fig 5.2. This sensitivity has been analyzed for all the available days for which ATAL is observed. Consistent differences in the behavior depending on Δt are found. If a too short time interval Δt is chosen, the deduced region of strong-updraft depends only on one input data set at one particular time step. However, the longer the time interval Δt the higher the uncertainty of the location of maximum updraft along the trajectories. This is because the vertical updraft by convection in CLaMS trajectories is driven by vertical velocities deduced from ERA-Interim and is not restricted to very narrow regions (e.g. see Fig. 5.6) below. For this reason, the locations of $\Delta\Theta_{max}$ are spread out increasingly over the region of the southern slope of the Himalayas with an increasing time interval Δt (Fig. 5.2). To avoid the uncertainty caused by a too large time interval and because of the fact that convection occurs on a time frame of a few hours, a time interval of $\Delta t = 18$ hours was chosen. This choice also ensures that at least 3 input data sets from ERA-Interim (with 6 hour resolution) are included to localize the preferred regions of strong-updraft in the region of the Asian monsoon. Based on the sensitivity analysis, a 18hr time average is used for Δt further analysis. The trajectory behavior depends also on Asian Monsoon Anticylone (AMA) status at that particular time. To address this issue, a case study analysis has been done and the results are reported in Sect. 5.4.

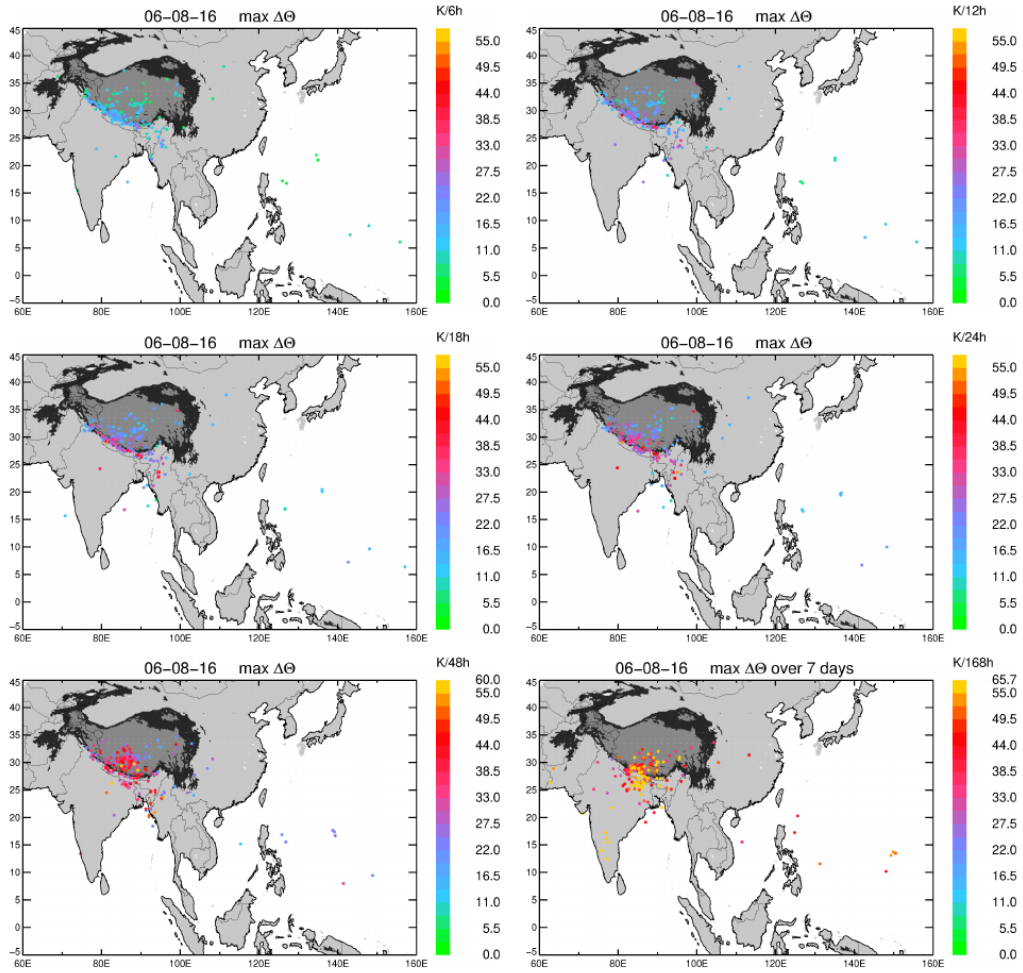

Figure 5.2: The location of the strong-updraft in dependence of the averaging time intervals Δt, strong-updraft regions are calculated from 40-day backward trajectories (see Tab. 5.1 and Sect. 5.2), the difference between backward trajectory calculations depending on the time periods considered which are $\Delta t = 6$, 12, 18, 24 and 48 hrs and also 7 days on 6th of August. Light grey areas indicate land, black area the Himalayan foothills, and the dark grey area the Tibetan plateau (see also Sect. 5.2).

5.3.2 Diversity in boundary layer sources

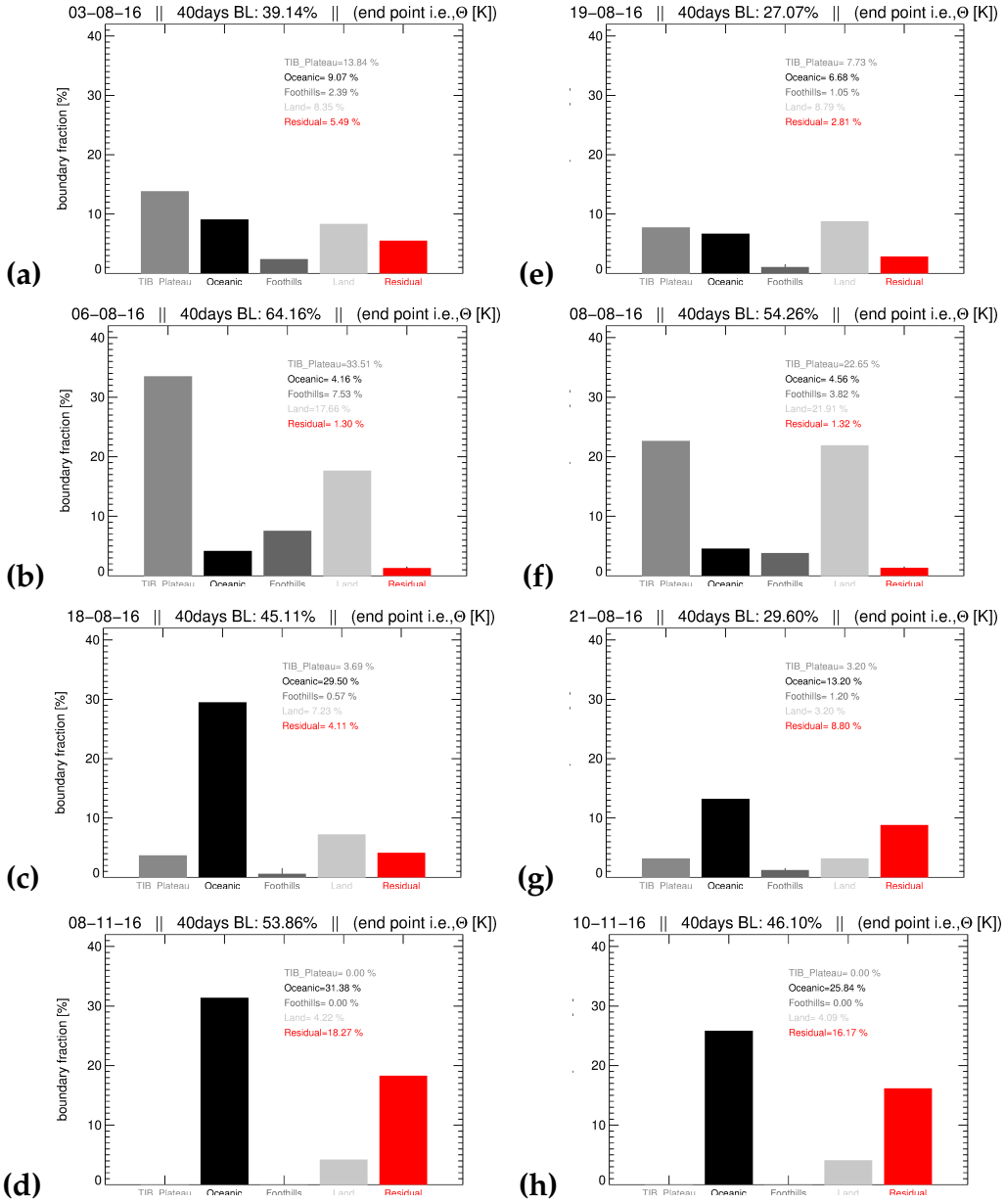

Figure 5.3: Fractions of 40-day backward trajectories ending in the BL source regions: Tibetan Plateau, oceanic, Foothills, land and residual. Top row shows ATAL measurements with cirrus below (a: 3-08-16, e: 19-08-16) ATAL beneath cirrus, second row only ATAL (b: 06-08-16, f: 08-08-16), third row cirrus inside ATAL (c: 18-08-16, g: 21-08-16) and bottom row November case (d: 08-11-16, h: 10-11-16) which was taken as background. Compare this with Fig. 5.4 to see confinement of source regions.

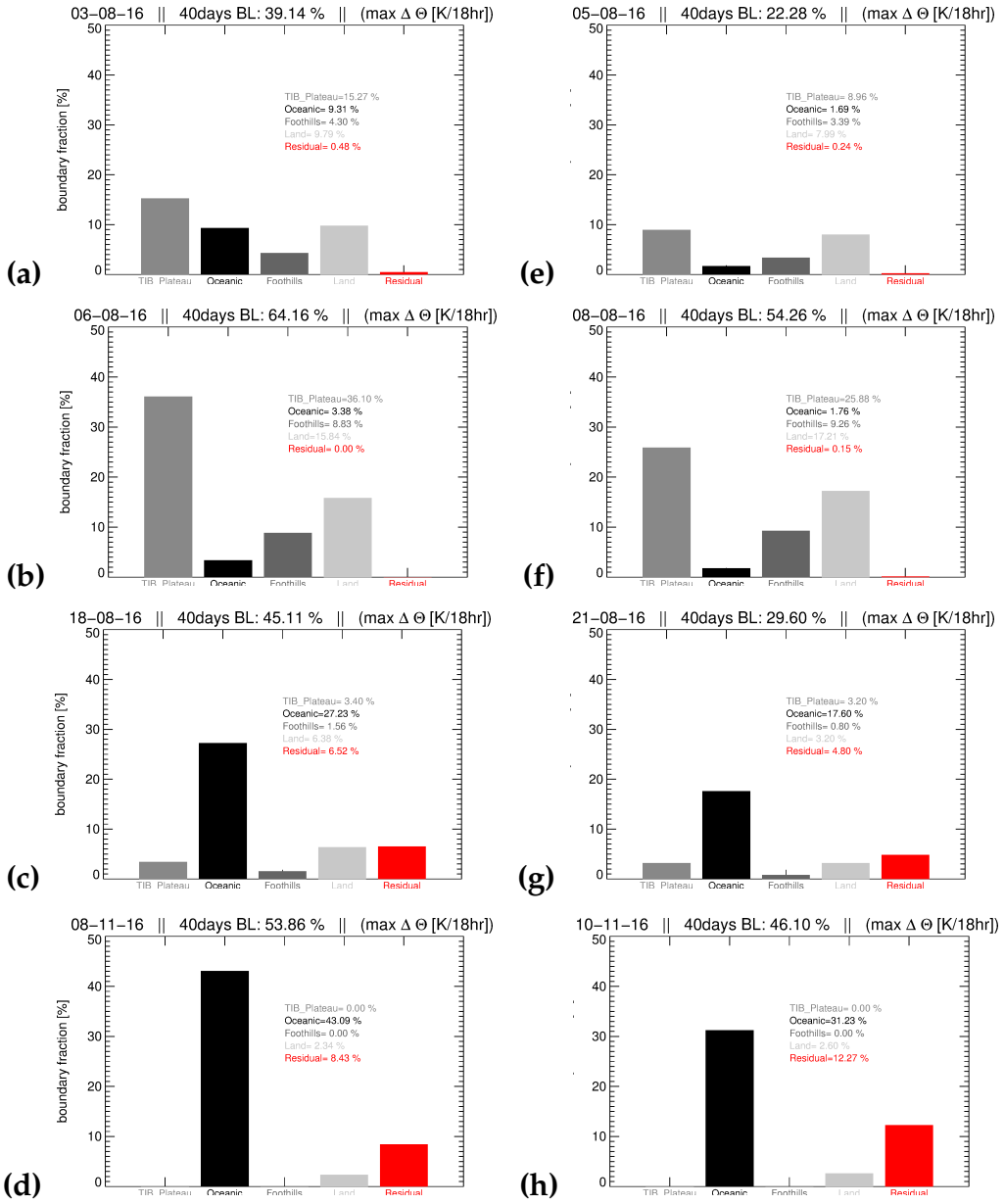

Figure 5.4: Same as Fig. 5.3 but showing the location of strong-updraft with(Δt) = 18 hr along 40-day backward trajectories.

Various source regions in the boundary layer are defined (see Sect. 5.2 and Fig 5.2). There are significant similarities between the outputs of trajectory runs mostly because of the similarities in dynamical situations over the trajectory path. Figure 5.3 shows August observations on 3rd (a) and 19th (e) having cirrus beneath ATAL which in PDF results show a similar source distribution (see Fig. 3.3 for actual BSR observations). Like wise 6th (b) and 8th (f) as stong ATAL cases, 18th (c) and 21st (g) as Cirrus inside ATAL and even in the November, 8th (d) and 10th (h) show some similarities in source distributions but consistent observations and more data is required in order to obtain a better statistical analysis on those similarities. Sources of the August observations are constrained over the Asian regions mainly north of

the Equator most likely due to the Inter Tropical Convergence Zone (ITCZ) establishment over the landmass. But for the November observations, the trajectory sources are mainly concentrated over the oceanic regions and their existence is mostly confined to Equatorial particularly to the Equatorial west Pacific (Fig 5.3) for which warm-pool convection happens in general. It is clear that trajectory behavior is also modulated by the local phenomena like cyclones, depression zones over the Asian regions. It is also evident that AMA movement also has a significant effect on the trajectory behavior, which means that if the trajectories are more in the center of AMA then sources are more confined to the landmass or from the Tibetan plateau. But to define accurate sources of the trajectories it is very important to have high resolution in the model over foothills of the Himalayas because the pronounced orography happens to have impact on the trajectory. Likewise, when the trajectory drifts to the outer part of AMA then the sources are from the outer part of the Asian region likely influenced by the subtropical jet or by cyclones. Figure 5.3 shows the contributions of different boundary layer regions to the air masses sampled within the ATAL. Figure 5.3 indicate the location of strong-updraft within 18 hr along the 40-day backward trajectories. A comparison of Fig. 5.3 and Fig. 5.4 shows that the origins of ATAL air masses in the model boundary layer can differ from the location of the strong-updraft along the trajectories.

5.3.3 Sensitivity on backward trajectory length

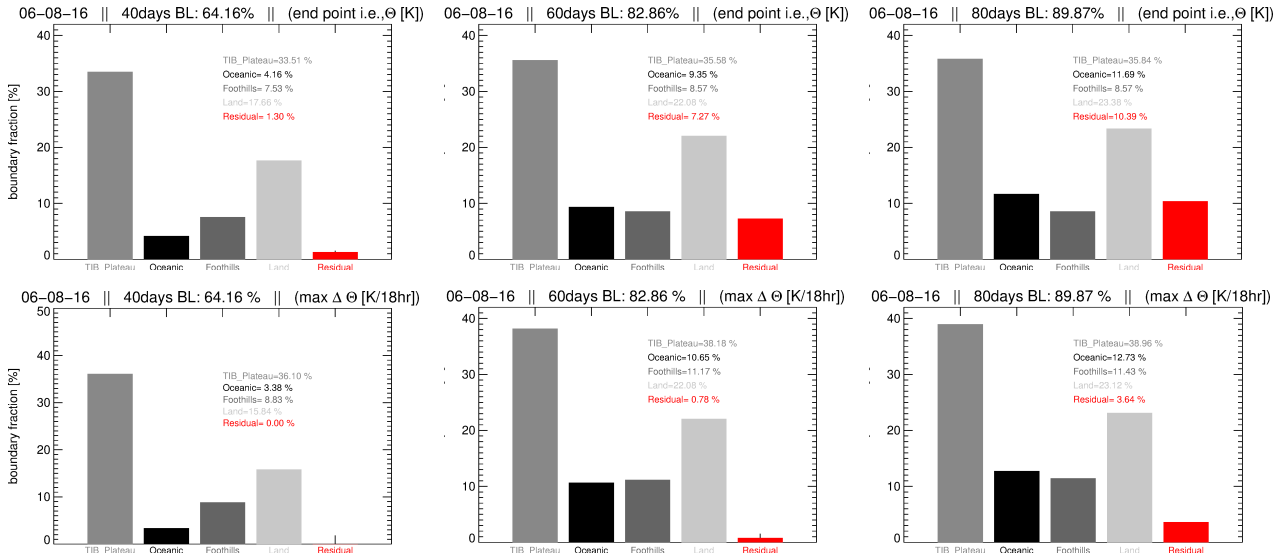

Figure 5.5: From Endpoint (Θ, top) and strong-updraft over 18hr time interval ($\Delta\Theta_{max}$, bottom) criterion. Shown are results of a 40, 60 and 80 day backward trajectory calculations (left, middle and right panels) for 6 August 2016, which is identified here as a strong ATAL case.

To test the sensitivity of our analysis on the trajectory length, in addition trajectories of a length 60 and 80 days are calculated. The change in contribution of trajectory sources from endpoint to strong-updraft criterion made it clear that maximum change in Θ along the trajectory path has happened at the strong-updraft region ($\Delta\Theta_{max}$) are the location for which air-masses might be influenced by the actual uplift. In order to check the sensitivity in the trajectory behavior for longer trajectory time periods, both Endpoint and strong-updraft locations have been analyzed. Figure 5.5 demonstrates the variability in the locations of the endpoints when trajectories are run for longer time scales. The residual contributions increase for the longer time scales. This is in particular the case for the residual contributions for the endpoint criterion. Observations using the strong-updraft criterion show that the sources are confined to the defined Asian region. The source studies explain the importance of using both the endpoint (Θ) and strong-updraft criterion ($\Delta\Theta_{max}$) for a better analysis. Figure 5.5 demonstrates change in source of 60 and 80 day because of longer time scales with greater contributions from residual (red). Thus the source contributions tend to experience more diffusion for the endpoint (Θ) criterion than for strong-updraft ($\Delta\Theta$). For other cases see Appendix A.3.

5.4 Results of the back-trajectory analysis: Three cases

There is a strong variability of the contributions of different atmospheric height layers (BL, LT, UT and LS) to the air masses in the ATAL (Tab. 5.1) demonstrating that within the ATAL a mixture of air masses of different origin exists. Before the results of the back-trajectory calculations are discussed for all balloon flights in Nainital, three days representing typical situations encountered during the measurements in August 2016 (see Sect. 5.1) are presented in detail: the case of an established ATAL (6 August 2016), a case without the observation of an ATAL (15 August 2016), and a case, for which the measurements are heavily influenced by air masses uplifted in a tropical cyclone (18 August 2016).

5.4.1 Case 1: Established Asian tropopause Aersol layer on 6 August 2016

On 6 August 2016 the ATAL was observed between 364 K to 388 K (135−95 hPa). The back-trajectory analysis of 40 days (Tab. 5.1) shows that 64% of the trajectories are from the boundary layer (BL), 14 % from the lower troposphere (LT), 22 % from the upper troposphere (UT) and only 0.3 % from the lower stratosphere (LS). The 40-day backward trajectories (potential

No.	Date	BL %	LT %	UT %	LS %	Num. Traj.
		$\zeta \leq 120$ K	$\zeta > 120$ K $\theta \leq 340$ K	$\zeta > 120$ K 340 K $< \theta \leq 370$ K	$\zeta > 120$ K $\theta > 370$ K	
NT001	02-08-16	47.0	10.4	30.3	12.3	670
NT002	03-08-16	39.1	17.2	36.5	7.2	419
NT003	05-08-16	22.3	13.8	44.6	19.4	413
NT004	**06-08-16**	64.2	14.0	21.6	0.3	385
NT005	08-06-16	54.3	15.4	30.3	0.0	680
NT007	11-08-16	40.9	11.2	24.9	23.0	269
NT009	12-08-16	28.7	11.0	54.6	5.6	463
NT011	**15-08-16**	44.8	19.8	30.2	5.2	444
NT015	17-08-16	31.8	11.1	41.6	15.5	651
NT017	**18-08-16**	45.1	10.6	29.5	14.8	705
NT018	19-08-16	27.1	10.5	29.9	32.5	569
NT023	21-08-16	29.6	19.6	24.8	26.0	250
NT025	23-08-16	63.7	11.5	18.7	6.0	331
NT027	26-08-16	13.3	16.7	50.8	19.2	120
NT029	30-08-16	29.6	17.3	34.7	18.4	392
NT033	10-11-16	46.1	35.9	17.5	0.6	538
NT034	11-11-16	13.9	22.4	57.8	6.0	519

Table 5.1: Contributions of the origin of the air masses found in the ATAL using 40-day backward trajectories according to sources in the boundary layer (BL), in the lower troposphere (LT), in upper troposphere (UT) and in the lower stratosphere (LS). The number of backward trajectories (starting within the ATAL layer) calculated along each balloon profile is given in the last column. The dates of three balloon flights representing typical situations encountered during the measurements in August 2016 are marked in bold type: the case of an established ATAL (6 August 2016), a case without the observation of an ATAL (15 August 2016), and a case, for which the measurements are heavily influenced by air masses uplifted in a tropical cyclone (18 August 2016). This table is taken from Hanumanthu et al. [2020].

temperature versus time) classified by the location of the trajectory end points at different atmospheric height layers are shown in Fig. 5.6.

Air masses from the BL are mainly uplifted very fast by individual convection events within short time periods of $1-2$ days up to $\approx 360\,\mathrm{K}$. Subsequently, slower updraft above 360 K occurs within the Asian monsoon anticyclone (at longitudes between 0°E and 140°E) for which the air masses follow the anticyclonic flow (see Fig. 5.7). This region is referred to as 'upward spiralling range' by Vogel et al. [2019]. Trajectories from the LT are very similar to those from the BL, however there are more trajectories originating outside of the Asian monsoon region from western longitudes. Most trajectories from the UT experienced radiatively driven updraft within the upward spiralling range. In contrast, the trajectory originating in the LS descends in the stratosphere (coming from northern America) and subsequently ascends within the anticyclone.

Trajectories with boundary layer origins are mainly from the Asian monsoon region and from the western pacific (Fig. 5.13). Origins are separated between Tibetan plateau, foothills, land and ocean (see Sect. 5.2 for details). Trajectories outside the latitude longitude box of 60°E to 160°E and 5°S to 45°N (Sect. 5.2 and Fig. 5.8) are classified as residual. Fig. 5.8a shows the location of the end points of all trajectories ending in the BL for 6 August 2016 colour-coded by the transport time from the boundary layer to the location of the measurements. The shortest transport times of about $15-20$ days are found for trajectories originating on the Tibetan Plateau. In addition there is a cluster of trajectories from north-east India with transport times of about 25 days.

In addition, the location of the maximum updraft within 18 hours along these 40-day backward trajectories is determined (see Sect. 5.2). The location of the maximum updraft within the 18 hours is then shown in Fig. 5.8b. It is evident that the location of the end points (Fig. 5.8a) and of the strong-updraft (Fig. 5.8b) differ substantially. The calculations show a cluster of locations with an updraft larger then $25\,\mathrm{K}\,18\mathrm{h}^{-1}$ within a belt along the southern edge of the Himalayas and over Myanmar. The area of the foothills (GPH $\approx 2000-4000\,\mathrm{m}$) is very small because the gradient of the GPH is very steep at the southern slope of the Himalayas, therefore it is difficult to highlight this belt using only the GPH as criterion to discriminate the foothills. Nevertheless, the number of trajectories with the location of strong-updraft on the foothills (9%) or on the Tibetan Plateau (36%) is slightly enhanced compared to the end points of these trajectories (8%, 34%) (Tab. 5.2 and Tab. 5.3). Finally location of $\Delta\Theta_{\mathrm{max}}$ depends strongly on the time interval over which the change in potential

temperature is calculated (see Sect. 5.3.1).

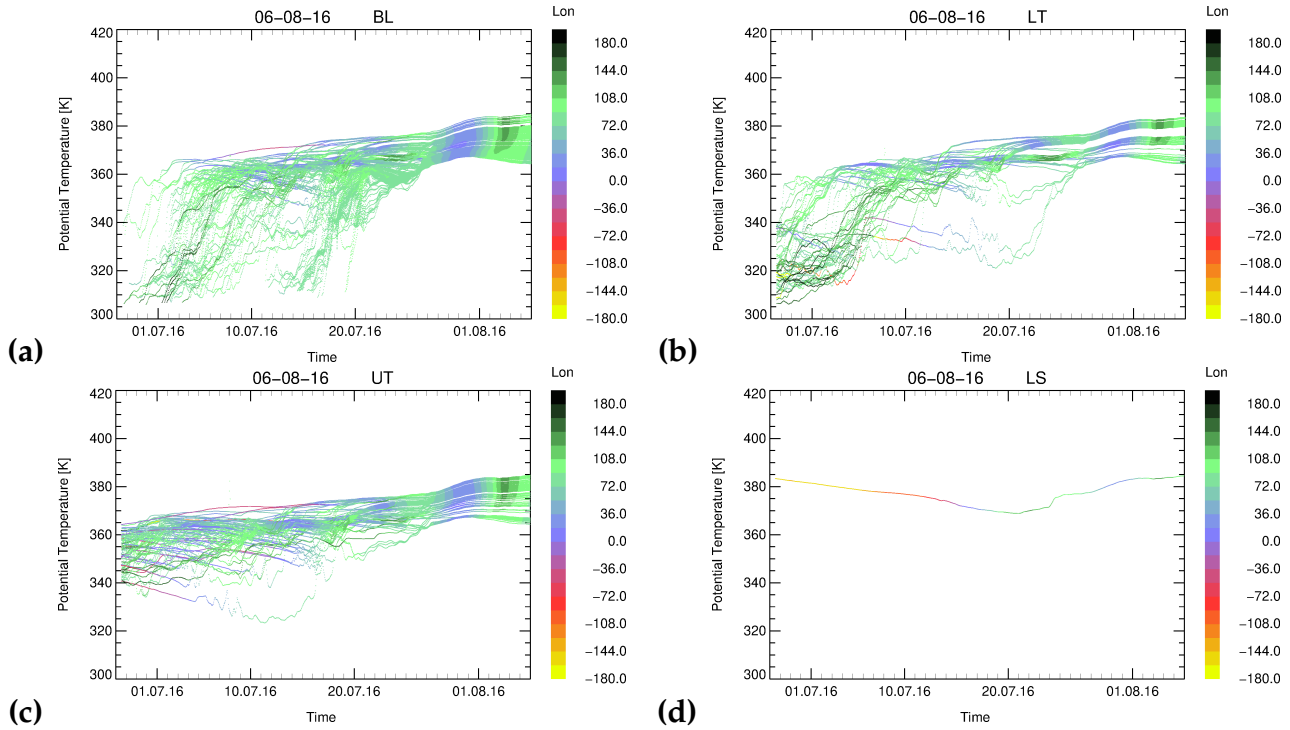

Figure 5.6: 40-day backward trajectories initialized on 6 August 2016 at the location of the ATAL measurement (see Tab. 3.1). The trajectories are sorted by air mass origin in the boundary layer (BL), in the lower troposphere (LT), in the upper troposphere (UT) and in the lower stratosphere (LS). The fractions of the different atmospheric height layers (BL, LT, UT, LS) to the composition of the ATAL are shown in Tab. 5.1. The colour indicates the location of the trajectory in longitude. This figure is taken from Hanumanthu et al. [2020].

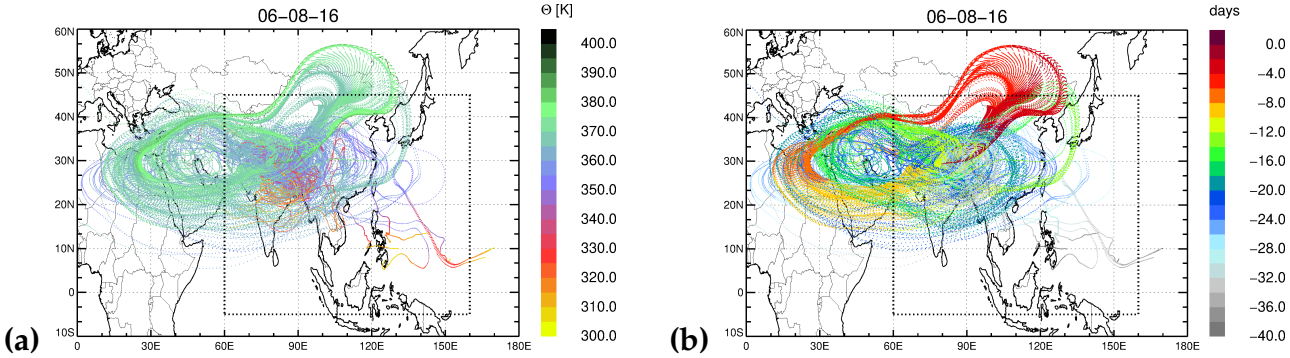

Figure 5.7: 40-day backward trajectories initialized within the ATAL on 6 August 2016 originating in the BL (same trajectories as shown in Fig. 5.6a) colour-coded by potential temperature **(a)** and by days back from 6 August 2016 **(b)**. In a latitude–longitude box from 60°E to 160°E and from 5°S to 45°N indicated by dashed lines the air mass origin in the BL is further analysed (see Sect. 5.2 Fig. 5.8, Tab. 5.2). This figure is taken from Hanumanthu et al. [2020].

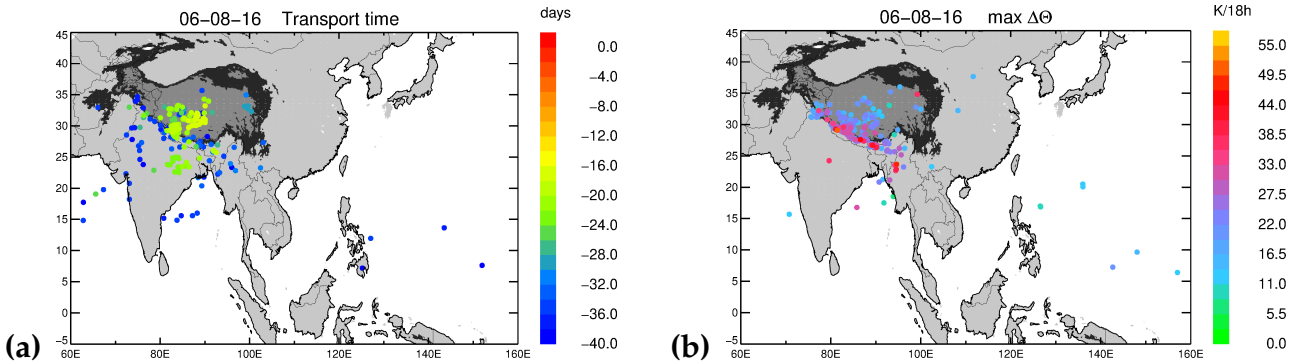

Figure 5.8: **(a)** Location of end points of the trajectories, initialized on 6 August within the ATAL, for which they reach the model boundary layer (BL) within 40 days. The end points are color-coded by the transport time between BL and measurement. **(b)** Location of the strong-updraft along the 40-day backward trajectories colour-coded by the strongest change in potential temperature within 18 hours [in $\mathrm{K\,18h^{-1}}$]. The Tibetan Plateau (dark grey), foothills (black), the remaining continental area (land; light grey) and maritime area (ocean; white) are indicated (see Tab. 5.2). This plot shows the area of the latitude–longitude box shown in Fig. 5.7 This figure has been taken from Hanumanthu et al. [2020].

No.	Date	BL %	Tibet %	Foothills %	Land %	Ocean %	Residual %
NT001	02-08-16	47.0	18.5	3.0	16.9	6.9	1.8
NT002	03-08-16	39.1	13.8	2.4	8.4	9.1	5.5
NT003	05-08-16	22.3	7.5	1.7	8.0	4.1	1.0
NT004	**06-08-16**	64.2	33.5	7.5	17.7	4.2	1.3
NT005	08-08-16	54.3	22.6	3.8	21.9	4.6	1.3
NT007	11-08-16	40.9	22.3	2.6	14.1	1.5	0.4
NT009	12-08-16	28.7	14.3	1.1	7.6	4.5	1.3
NT011	**15-08-16**	44.8	16.9	2.7	16.2	5.2	3.8
NT015	17-08-16	31.8	16.4	2.6	7.7	3.5	1.5
NT017	**18-08-16**	45.1	3.7	0.6	7.2	29.5	4.1
NT018	19-08-16	27.1	7.7	1.1	8.8	6.7	2.8
NT023	21-08-16	29.6	3.2	1.2	3.2	13.2	8.8
NT025	23-08-16	63.7	23.6	3.0	19.9	14.5	2.7
NT027	26-08-16	13.3	2.5	0.0	3.3	6.7	0.8
NT029	30-08-16	29.6	6.1	2.3	7.9	11.5	1.8
NT033	10-11-16	46.1	0.0	0.0	4.1	25.8	16.3
NT034	11-11-16	13.9	0.0	0.0	0.0	1.0	12.9

Table 5.2: Fraction of 40-day backward trajectories (for all soundings in August 2016), which are ending in the boundary layer (BL) separated into the Tibetan Plateau (Tibet), foothills (foothills), the remaining continental area (land) and the maritime area (ocean) in a latitude–longitude box from 60°E to 160°E and from 5°S to 45°N shown in Fig. 5.8, and finally all remaining trajectories reaching the BL outside the latitude–longitude box (residual). The fraction 100% - BL% are those trajectories, which are from the LT, UT and LS (i.e. do not reach the BL within 40 days as shown in Tab. 5.1). The Tibetan Plateau is defined as the altitude above a geopotential Φ of $40000\,\mathrm{m^2s^{-2}}$ (about 4000 m), the foothills as $21000 < \Phi < 40000\,\mathrm{m^2s^{-2}}$ (about 2000−4000 m), the remaining continental area as $\Phi < 21000\,\mathrm{m^2s^{-2}}$ (below about 2000 m). This table has been taken from Hanumanthu et al. [2020].

No.	Date	BL %	Tibet %	Foothills %	Land %	Ocean %	Residual %
NT001	02-08-16	47.0	17.2	9.0	17.8	2.8	0.3
NT002	03-08-16	39.1	15.3	4.3	9.8	9.3	0.5
NT003	05-08-16	22.3	9.0	3.4	8.0	1.7	0.2
NT004	**06-08-16**	64.2	36.1	8.8	15.8	3.4	0.0
NT005	08-08-16	54.3	25.9	9.3	17.2	1.8	0.1
NT007	11-08-16	40.9	24.9	3.7	11.5	0.7	0.0
NT009	12-08-16	28.7	11.4	7.1	6.9	3.0	0.2
NT011	**15-08-16**	44.8	16.0	5.2	17.8	4.3	1.6
NT015	17-08-16	31.8	15.7	5.5	6.6	3.7	0.3
NT017	**18-08-16**	45.1	3.4	1.6	6.4	27.2	6.5
NT018	19-08-16	27.1	7.6	3.7	8.8	5.4	1.6
NT023	21-08-16	29.6	3.2	0.8	3.2	17.6	4.8
NT025	23-08-16	63.7	24.8	7.9	22.4	7.3	1.5
NT027	26-08-16	13.3	3.3	0.0	1.7	8.3	0.0
NT029	30-08-16	29.6	6.9	3.1	7.1	12.5	0.0
NT033	10-11-16	46.1	0.0	0.0	2.6	31.2	12.3
NT034	11-11-16	13.9	0.0	0.0	0.2	0.8	12.9

Table 5.3: Same as Tab. 5.2, but for the location of strong-updraft along the 40-day backward trajectories ending in the BL. The strong-updraft is calculated by the maximum change in potential temperature within 18 hours along the trajectories. The location of the maximum updraft within the 18 hours is then calculated as the mean location of the trajectory within 18 hours. This table has been taken from Hanumanthu et al. [2020].

5.4.2 Case 2: No Asian tropopause aerosol layer on 15 August 2016

On 15 August 2016 no ATAL was detected by the COBALD measurements. To compare this flight with the other cases for which an ATAL was probed during August 2016, CLaMS backward trajectories are initialised in a pressure range between 140 hPa to 92 hPa (365 K to 389 K). In this pressure range 45% of the trajectories are from the BL, that is 20% less than the BL contribution of Case 1 (64%). Therefore, much higher contributions of the UT (30%) and LT (20%) as well as from the LS (5%) are found on 15 August in contrast to Case 1 (22%, 14%, 0.3%) (see Tab. 5.1). The lesser contribution of the BL can be explained by the location of the anticyclone related to the location of the measurements. On 6 August 2016 the Asian monsoon anticyclone was over Nainital, while on 15 August Nainital was located between the western and the eastern mode of the anticyclone (see Fig. 5.1).

The 40-day backward trajectories for the 15 August 2016 are shown in Fig. 5.9. In contrast to Case 1 no pronounced individual convection events are noticeable in the trajectories from BL and LT on 15 August. Here, an alternating up and downward transport is found along most of the trajectories below 360 K and only a few trajectories show a strong upward transport (convection) up to 360 K within $1-2$ days.

Focusing on the trajectories from the BL (Fig. 5.10) two branches, a western and eastern branch, of trajectories are found depending on the altitude of the measurements (Fig. 5.9a); trajectories from above 370 K are from eastern and from below 370 K are from western longitudes. In the western branch of the trajectories the air masses are transported around the western mode of Asian monsoon anticyclone, while air masses from the eastern branch are coming from the Pacific ocean and are transported along the southern edge of the eastern mode of the anticyclone to the measurement location in Nainital. During the first half of August several tropical storms occurred in the western Pacific. Typhoon Omais was active between 2-12 August 2016 (`https://www.jma.go.jp/jma/jma-eng/jma-center/rsms-hp-pub-eg/besttrack.html`; storm ID: 1605 (last access: 26 May 2020) and `https://en.wikipedia.org/wiki/2016_Pacific_typhoon_season` (last access: 26 May 2020)) and impacted the sounding on 15 August (see Fig. 5.11).

Fig. 5.11a shows the location of the end points of back-trajectories in the BL colour-coded by the transport time from the BL to the location of the measurement. Lesser contributions from the Tibetan Plateau (17%) and the foothills (3%) are found compared to Case 1 (34%, 8%). Due to the dynamics of the bi-modal anticyclone the locations of the end points in the BL are much more widely spread over Asia (e.g. Pakistan, Afghanistan, China), the western Pacific, and the residual Earth's surface (≈5 %; see Tab. 5.2) as compared to Case 1. In Case 1, the end points are more clustered demonstrating the more frequent occurrence of individual convection events. A few trajectories ending on the Tibetan Plateau have short transport times of about 10 to 12 days; these are shorter times than found for Case 1 (Fig. 5.8) and are caused by convection between 2 and 5 August.

Similar as for Case 1, in Case 2 the location of the end points in the model BL (Fig. 5.11a) and of the strong-updraft (Fig. 5.11b) differ substantially. A cluster of locations with an updraft larger than 25 K 18h^{-1} is found at the southern edge of the Himalayas, over Myanmar, and west of the Tibetan Plateau.

In Fig. 5.11, the location of the end points in the model BL of the strong-updraft for trajectories that started in the cirrus cloud, found between 376 and 381 K potential temperature on 15 August (see Fig. 3.3), is marked by a star symbol. End points in the BL of the cirrus cloud are found in different regions, demonstrating that the air masses in the cirrus cloud have a mixture of different origins. Thus the locations of the strongest updraft for trajectories initialised within the cirrus cloud are found over the Pacific as well as over continental areas. Cirrus formation as well as likely the details of transport pathways that lead to cirrus

formation are not represented in our trajectory calculations based on ERA-Interim reanalysis.

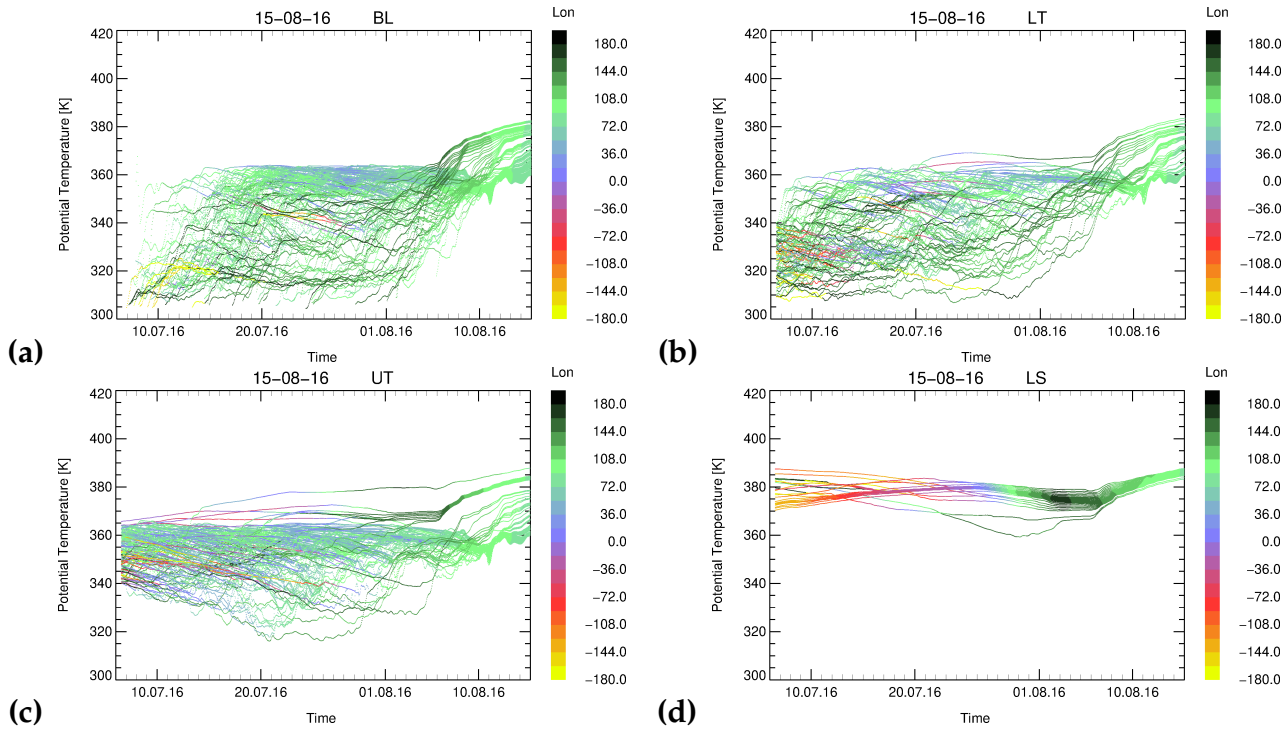

Figure 5.9: The same as Fig. 5.6, but for the no ATAL case on 15 August 2016 (Case2). The trajectories are calculated in a pressure range between 140 hPa and 92 hPa (365 K to 389 K). This figure has been taken from Hanumanthu et al. [2020].

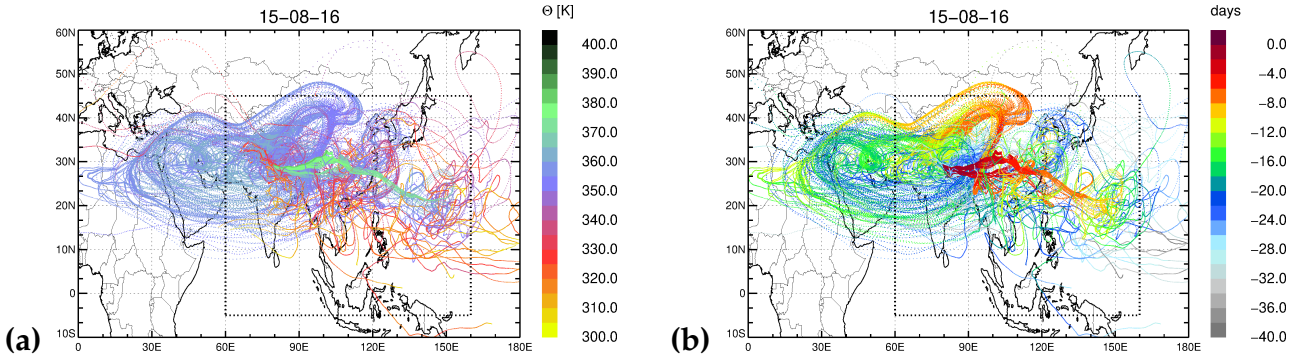

Figure 5.10: The same as Fig. 5.7, but for the balloon flight on 15 August 2016 (Case 2). In addition to Case 1 shown in Fig. 5.7, the impact of tropical cyclone activity in the western Pacific is found in Case 2. This figure has been taken from Hanumanthu et al. [2020].

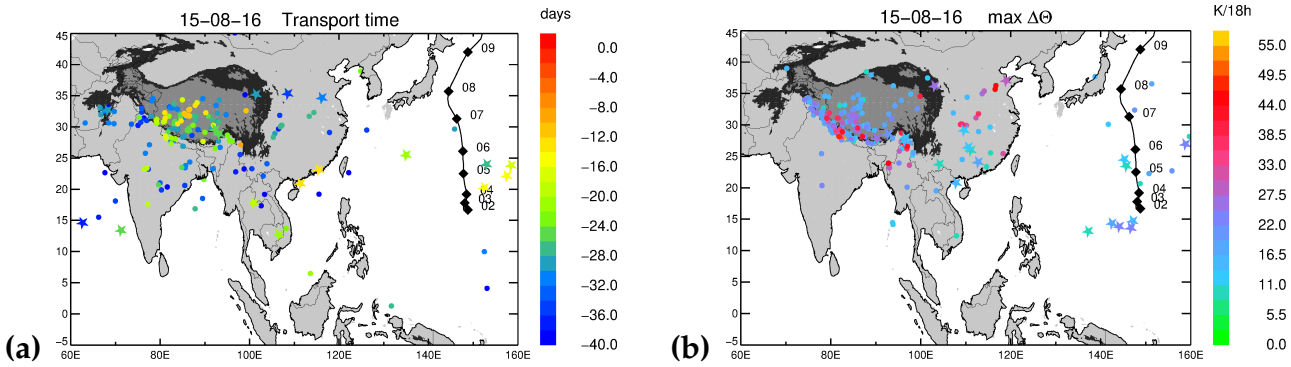

Figure 5.11: The same as Fig. 5.8, but for the no ATAL case on 15 August 2016. Locations of end points and locations of the strong-updraft of trajectories initialised within the cirrus cloud are indicated by a star symbol. The 40-day backward trajectories are impacted by typhoon Omais. Its storm track is shown (black line), and the location at noontime is additionally marked (black diamonds); the numbers indicate the day in August 2016. This figure has been taken from Hanumanthu et al. [2020].

5.4.3 Case 3: Typhoon influence on 18 August 2016

On 18 August 2016, the ATAL occurs over a broader potential temperature range from 362 K to 422 K compared to 6 August (364 K to 388 K, Case 1); however the ATAL intensity ($\overline{\text{BSR}}_{455}$ =1.065) is lower compared to Case 1 ($\overline{\text{BSR}}_{455}$ =1.083) (Fig. 3.3 and Tab. 3.1). The contributions from the BL are 45% and similar to Case 2, but much lower than for Case 1 (64%, Tab. 5.1). For Case 3, a stratospheric contribution of 15% is found, which is much higher than for Case 1 (0.3%) and Case 2 (5%) because of the considered top level of potential temperature (Case 1 up to 388 K, Case 2 up to 389 K and Case 3 up to 422 K) (see Figs. 5.6d, 5.9d and 5.12d). The stratospheric contributions are air masses from the northern extratropical lower stratosphere. These air masses are transported along the subtropical jet and subsequently were slowly uplifted in the anticyclonic large-scale upward spiral around the

Asian monsoon anticyclone by diabatic heating. In general, the higher within the upward spiralling range at the top of the Asian monsoon anticyclone, the more contributions from the stratospheric background are found [Vogel et al., 2019].

Fig. 5.12a shows very strong convection between 6 and 15 August with a strong-updraft within a few days of up to 360 K. These air masses originate from the western Pacific and Bay of Bengal and are transported from the western Pacific directly to Nainital (Fig. 5.13). Another branch of BL air from the western Pacific is transported around the outer edge of the Asian monsoon anticyclone to Nainital (Fig. 5.13).

The location of the end points in the BL for Case 3 are shown in more detail in Fig. 5.14. The major fraction of the BL contribution is from the ocean (30%) in contrast to Case 1 (4%) and Case 2 (5%). Also the location of $\Delta\Theta_{max}$ is found in the western Pacific, however at slightly different locations as the end points. The strong-updraft over the Pacific is caused by tropical cyclone activity. Typhoon Nida was active between 29 July and 3 August over the western Pacific (`https://www.jma.go.jp/jma/jma-eng/jma-center/rsmc-hp-pub-eg/besttrack.html`; storm ID: 1604 (last access: 26 May 2020) and `https://en.wikipedia.org/wiki/2016_Pacific_typhoon_season` (last access: 26 May 2020)) and impacted the balloon sounding on 18 August 2016. Thus, in Case 3 polluted air masses within the ATAL layer measured below 400 K are diluted by air from the maritime boundary layer. At higher potential temperature levels (above 400 K) mixing with air masses from the stratosphere occurs.

In Fig. 5.14, the location of the end points in the model BL of the strong-updraft for trajectories that started in the cirrus cloud found between 370 and 373 K potential temperature on 18 August (see Fig. 3.3), is marked by a star symbol. End points in the BL of the cirrus cloud are found in different regions, similar as for the cirrus on 15 August, demonstrating that the air masses in the cirrus have a mixture of different origins as well as in the ATAL itself. As mentioned in Sect. 5.4.2, cirrus formation as well as likely the details of transport pathways that lead to cirrus formation are not represented in our CLaMS trajectory calculations.

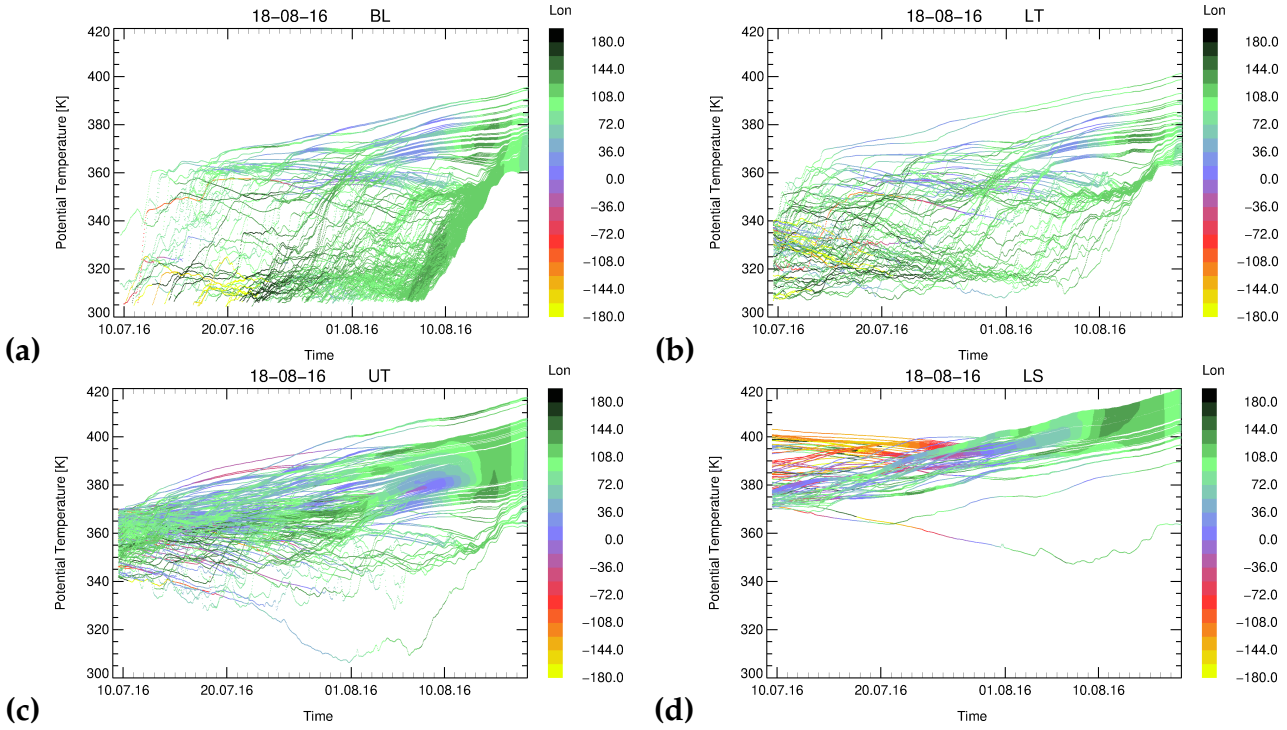

Figure 5.12: The same as Fig. 5.6 and Fig. 5.9, but for Case 3 the typhoon influenced ATAL on 18 August 2016. The trajectories are calculated in a potential temperature range between 150 hPa to 75 hPa(362 K to 422 K). This figure has been taken from Hanumanthu et al. [2020].

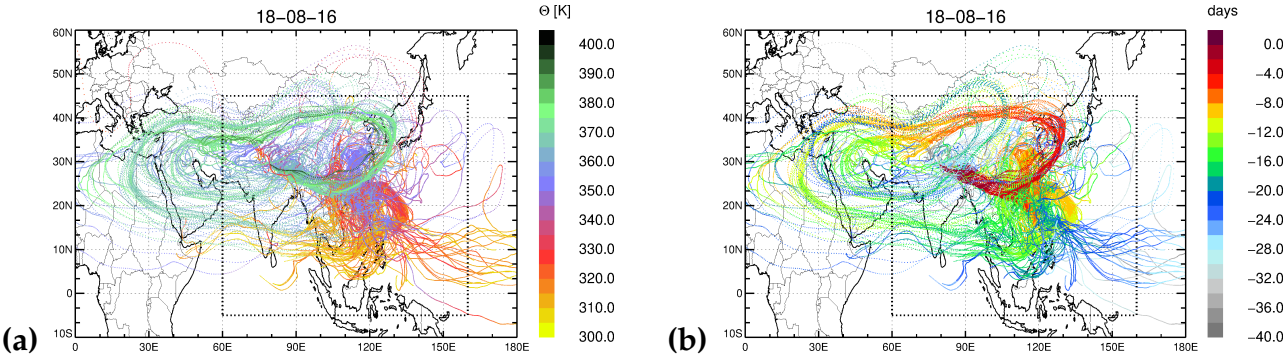

Figure 5.13: The same as Fig. 5.7 and Fig. 5.10, but for the balloon flight on 18 August 2016 heavily influenced by a typhoon in the western Pacific (Case 3). This figure has been taken from Hanumanthu et al. [2020].

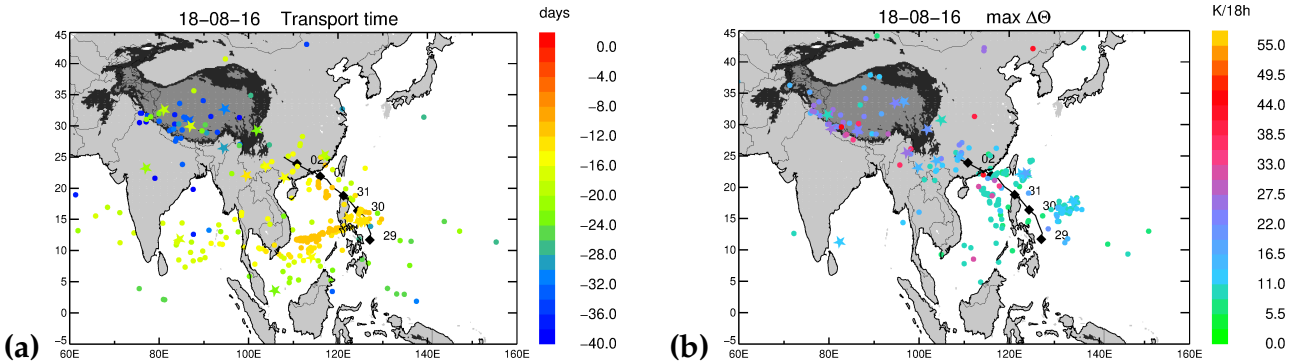

Figure 5.14: The same as Fig. 5.8 and Fig. 5.11, but for the typhoon-influenced case on 18 August 2016 (Case 3). Locations of end points and locations of the strong-updraft of trajectories initialised within the cirrus cloud which was found within the ATAL are indicated by a star symbol. The 40-day backward trajectories are impacted by typhoon Nida. Its storm track is shown (black line) and the location at noon time is additionally marked (black diamonds); the numbers indicate the day in July and August 2016. This figure has been taken from Hanumanthu et al. [2020].

5.5 Results for all flights

In Sects. 5.4.1, 5.4.2, and 5.4.3, the fractions of the different atmospheric height layers (BL, LT, UT, LS) contributing to the composition of air masses within the ATAL were discussed in detail for three specific days, namely 6, 15 and 18 August 2016 (see also Sect. 5.1). In Fig. 5.15 (top), the fractions of the different atmospheric height layers for all flights in August and November 2016 are shown as a bar chart (see Tab. 3.1 and Tab. 5.1) for 40-day backward trajectories. Due to the strong variability of the vertical extent of the ATAL and the variability of cirrus clouds marking the bottom of the ATAL for certain days, the number of back-trajectories varies strongly from a number of 119 to up to 704. For better comparison the fractions of the different atmospheric height layers are normalised by the total number of trajectories for each day (Fig. 5.15, top). The fractions from the BL are between 14% and 64% and from the LS between 0% and 33%. Thus there is a strong variability of the fractions of the different atmospheric height layers contributing to the ATAL as well as for the no ATAL cases in August and post-monsoon cases in November within the corresponding pressure levels between 140 and 92 hPa. However, from the analysis of different atmospheric height layers, no clear relation between these height layers and the occurrence of ATAL was found, which may explain the difference between the ATAL and no ATAL cases as well as between ATAL and post-monsoon soundings in November.

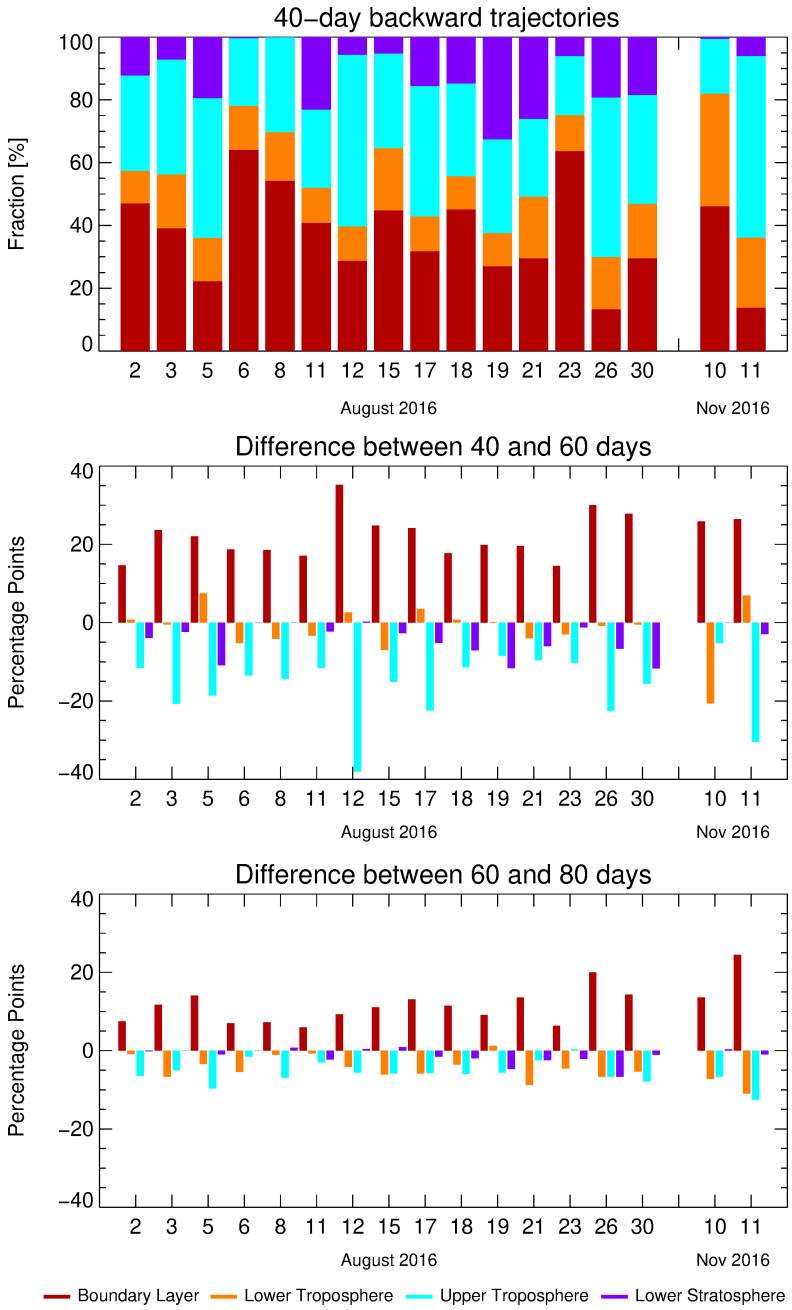

Figure 5.15: The fractions of the different atmospheric height layers (BL, LT, UT, LS) for all flights in August and November 2016 normalised by the total number of trajectories of each day calculated from 40-day backward trajectories (top) (see Tab. 5.1), the difference between 40 and 60 days (middle) backward trajectory calculations as well as between 60 and 80 days (bottom). This figure has been taken from Hanumanthu et al. [2020].

During the monsoon season air masses from the BL accumulate within the Asian monsoon anticyclone, thus in the altitude range of the ATAL. Therefore, back-trajectory calculations with a length of 60 and 80 days were also performed to consider the sensitivity of our results regarding the trajectory length (see Sect. 5.3.3). In general the fractions from the BL contributing to the ATAL increase with trajectory time. The fractions from the BL range

between 14% and 64% for 40 days (Fig. 5.15, top), from 40% to 83% for 60 days and from 56% to 90% for 80 days. There is an increase of the fractions from the BL between 14 and 36 percentage points between 40 and 60 days (Fig. 5.15, middle) and between 6 and 25 percentage points between 60 and 80 days (Fig. 5.15, bottom). Simultaneously the fractions from the UT decrease with time. They range between 17% to 58% for 40 days, from 8% to 28% for 60 days and from 6% to 21% for 80 days (see Fig. 5.15). A decrease is found of the fractions from the UT between 5 and 38 percentage points between 40 and 60 days (Fig. 5.15, middle) and between 0 and 12 percentage points between 60 and 80 days (Fig. 5.15, bottom). The fractions from the LT do not change significantly with increasing trajectory length. They vary between -7 and 8 percentage points between 40 and 60 days (except for 10 November 2016, here the difference is -21 points) and between -11 and 1 points between 60 and 80 days. The fractions from the LS decrease by up to -11 percentage points between 40 and 60 day and up to -7 points between 60 and 80 days.

To deduce a possible relation between the ATAL intensity and the air mass origin within the boundary layer, Fig. 5.16a shows a bar chart with the contributions of Tibet, foothills, land, ocean and residual for which the individual measurements are sorted by increasing back-scatter ratio ($(\overline{\mathrm{BSR}}_{455}\text{-}1) \times 100$) (see Tab. 3.1 and Tab.5.2). The contributions are normalised by the total number of trajectories within the boundary layer for each day for better comparison. The balloon flight on 12 August is excluded because a cirrus cloud was detected between 140 and 92 hPa and therefore no aerosol back-scatter ratio could be measured in this pressure range. Because of the low statistics we exclude all flights (11, 21, 23 and 26 August) for which the trajectory number is lower than 50% of the maximum number of trajectories (# 704) calculated on 18 August 2016 (these cases are included in Fig. 5.17).

There is a lot of variability of the air mass origin within the boundary layer contributing to ATAL cases characterised by a back-scatter ratio $\overline{\mathrm{BSR}}_{455}$ larger than 1.058 (Fig. 5.16, top). stong ATAL cases with $\overline{\mathrm{BSR}}_{455}$ values larger than 1.067 show fractions of air mass origin in the boundary layer from continental outflow higher than 70% and in particular higher than 30% from Tibet (Fig. 5.16, top). For weak ATAL cases (18 and 30 August), the $\overline{\mathrm{BSR}}_{455}$ values are lower ($1.059-1.065$) and the fractions from continental outflow is below 70%. For these cases high fractions from maritime boundary layer sources (ocean $> 12\%-30\%$) are found which are caused by the impact of tropical cyclones on the composition of the ATAL as discussed in Sect. 5.4.3.

For both post-monsoon cases in November 2016 low $\overline{\mathrm{BSR}}_{455}$ values of 1.034 and 1.037 are

measured, these measurements are used as background signal for aerosols in the UTLS (no ATAL has been observed during winter). For these cases the air mass origin is very different, compared to the ATAL cases. In 40-day back-trajectory calculations no contributions from Tibet and foothills are found for both flights, only a contribution from land of 4% is found for the balloon flight on 11 November 2016. The origins of air masses in the boundary layer are from ocean and from residual mainly from South of 5°S. It is known that during boreal winter efficient transport into the stratosphere is found over the west Pacific and Maritime Continent, caused by strong convection and in addition by the ascending branch of the Walker circulation located over the Maritime Continent [e.g. Bergman et al., 2012; Hosking et al., 2012].

Case 2, the no ATAL case from 15 August 2016, has a $\overline{\mathrm{BSR}}_{455}$ value of 1.023 which is lower than both November cases, however an air mass origin in the boundary layer is found of around 80% from continental sources (Tibet, foothills and land). This BL fraction is similar to fractions from the BL as for the ATAL cases. Case 2 is discussed in detail in Sect. 5.4.2 and it was shown that on 15 August a bi-modal structure of the anticyclone is found and Nainital is located between the eastern and western part of the anticyclone (Fig. 5.1). This bi-modal structure is found between 11 and 16 August (see Fig. 4.1). Thus also the no ATAL case on 12 August and the balloon flight on 11 August are impacted by this dynamical situation in the UTLS. Therefore, the dynamics in the UTLS seems to be the reason that on 15 August 2016 no ATAL was measured over Nainital, although a similar air mass origin was found on 15 August as for the ATAL cases. Unfortunately, during August 2016 only one no ATAL case could be measured (which is not completely masked by a cirrus cloud), therefore a more general result regarding no ATAL measurements during the peak monsoon season in India cannot be deduced. During August 2016, a second period with a bi-modal structure of the anticyclone is found between 27 and 28 August, but here Nainital is located more in the centre of the eastern mode (not shown here). However, it can not be excluded that also aerosol removal processes depending on temperature and S_{ice} such as in-situ cirrus formation contribute to the existence of the no ATAL measurement on 15 August 2016 (for details see Sect. 5.4.2 and Sect. 6.1).

The change between the ATAL intensity and the air mass origin within the boundary layer (Tibet, foothills, land, ocean and residual) between 40 and 60 days (Fig. 5.16b) as well as between 60 and 80 days (Fig. 5.16c) is also analysed. In general, the fractions of the residual is increasing with the trajectory length for all balloon flights, except for 11 November. Thus

the longer the trajectories, the more older air masses are taken into account to contribute to the ATAL coming from outside the latitude–longitude box from 60°E to 160°E and from 5°S to 45°N. For strong ATAL cases, in general an increase of the fractions from ocean up to ∼7 percentage points are found (Fig. 5.16b) indicating the impact of maritime convection between 40 and 80 days before the soundings. In contrast, for weak ATAL cases, the fraction of continental convection (Tibet, foothills, and land) is increasing, indicating the impact of continental convection between 40 and 80 days before the soundings.

Figs. 5.8, 5.11 and 5.14 show that on 6, 15 and 18 August the strong-updraft locations differ from the endpoint locations of the trajectories. A cluster of strong-updraft locations is found at the southern edge of the Himalayan foothills. Tab. 5.3 shows the fractions of Tibet, foothills, land, ocean and residual of the strong-updraft locations within 18 hours for all flights. The definition of the foothills at the southern edge of the Himalaya results in this region being only a small belt identified by the orography. Thus not all trajectories having their strong-updraft at the southern edge of of the Himalayan foothills are captured by our definition of the foothills and therefore these trajectories are still counted as fractions of land. Fig. 5.16d shows the difference between the location of the end points and the location of strong-updraft for 40-day backward calculations. For some soundings (3, 5, 6, 8 and 30 August) the fractions from foothills and Tibet for the location of strong-updraft are greater than for the location of the end points indicating strong convective activity at the Himalayan foothills during early August 2016.

Fig. 5.17 shows the fractions of Tibet, foothills, land and ocean versus ($\overline{\mathrm{BSR}}_{455}$-1) × 100 (see Tab. 3.1) for the location of the end points of the trajectories (top) (see Tab. 5.2) and for the location of the strong-updraft (bottom) (see Tab. 5.3). The fractions are not normalised to the number of trajectories within the BL as was done in Fig. 5.16. Therefore, in Fig. 5.17 also the contribution from the other atmospheric layers (LT, UT and LS) to the ATAL are taken into account. Further, the low statistic flights (with a relatively low absolute number of trajectories, 11, 21, 23 and 26 August) are also considered. There is a lot of variability between individual soundings. However, in general an increase of the fractions from Tibet, foothills and land is found for increasing ATAL intensity, while the contributions from the ocean are decreasing for both the location of end points and the locations of strongest updraft. The gradient of the linear fit for the fractions of Tibet and foothills is somewhat steeper for the locations of strongest updraft compared to the location of the endpoints highlighting the role of the southern Himalayan foothills and the Tibetan Plateau in the uplift of ATAL aerosols

and their chemical precursors from the Earth's surface to ATAL altitudes.

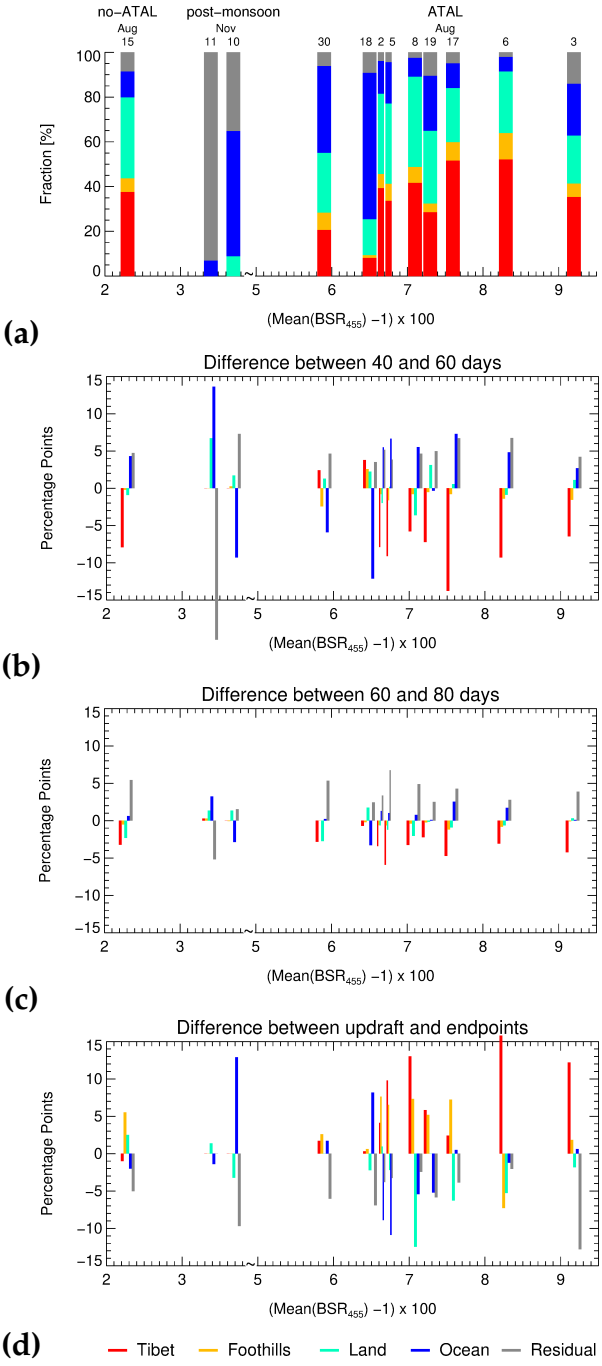

Figure 5.16: Contributions of Tibet, foothills, land, ocean and residual to the boundary layer (BL) sorted by increasing back-scatter ratio ($\overline{BSR}_{455}$-1) $\times$ 100) (see Tabs. 3.1 and 5.2) for 40-day backward trajectories **(a)**. The contributions are normalised by the total number of trajectories within the boundary layer for each day. The days of the soundings in August and November are indicated above the top of the bars. For better representation, the range between 4.0 and 5.0 is removed from the x-axis. Low statistics flights (11, 21, 23 and 26 August) for which the trajectory number is lower than 50% of the maximum number of trajectories (# 704) calculated on 18 August 2016 are not shown as well as the 12 August, when the UTLS is filled by a 5 km thick cirrus cloud. The difference between 40 and 60-day **(b)** and between 60 and 80-day **(c)** backward trajectory calculations as well the difference between the location of the end points and the location of strong-updraft **(d)** for 40-day backward calculations is also shown. This figure has been taken from Hanumanthu et al. [2020].

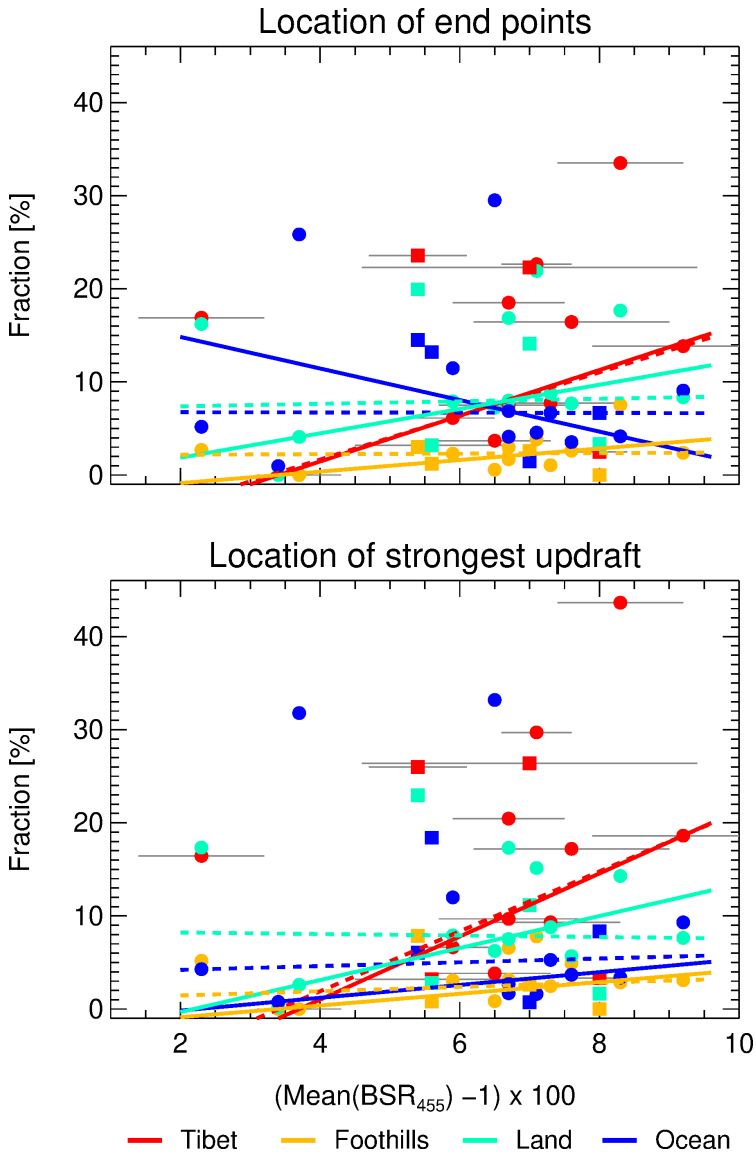

Figure 5.17: Fractions of Tibet, foothills, land and ocean versus ($\overline{\text{BSR}}_{455}$-1) $\times$ 100 (see Tab. 3.1) for the location of the end points of the trajectories (top) (see Tab. 5.2) and for the location of the strong-updraft (bottom) (see Tab. 5.3). The standard deviation (σ) of the back-scatter ratio is indicated for each sounding (grey lines). Low statistics flights (11, 21, 23 and 26 August) for which the trajectory number is lower than 50% of the maximum number of trajectories (# 704) calculated on 18 August 2016 are also shown (indicated by squares instead of circles). For each region a linear fit (using the least absolute deviation method) was calculated using all measurements except the one on 12 August(Tab. 3.1), when the UTLS is filled by a 5 km thick cirrus cloud (dashed lines). Further, a linear fit excluding in addition the flights on 11, 21, 23 and 26 August as well as the no ATAL flight (15 August) is shown (lines). An increase of the fractions from Tibet, foothills and land is found for increasing ATAL intensity, while the contributions from the ocean decrease for the locations of end points. Top panel of the figure has been taken from Hanumanthu et al. [2020].

Further, the Pearson correlation coefficients between the different regions (Tibet, foothills, land and ocean) and the backscatter intensity averaged over the ATAL altitude range (($\overline{\text{BSR}}_{455}$-1) $\times$ 100) for the location of the end points of the trajectories as well as for the location of

the strong-updraft along the trajectories are calculated (Tab. 5.4). Low positive correlations (i.e. values from 0.3 to 0.5) are found for the location of the end points of Tibet and foothills as well as for the location of the strong-updraft of Tibet.

Moreover, the Pearson correlation coefficients are calculated, also excluding the flights with a relatively low absolute number of trajectories (11, 21, 23 and 26 August) and the no ATAL case on 15 August. The no ATAL case is excluded because the low backscatter intensity is not completely explained through the backward trajectory analysis presented here. Moderate positive correlations (i.e. values from 0.5 to 0.7) are found for Tibet, foothills and land, with the largest correlation coefficient of 0.7 for the location of endpoints in Tibet. Low negative correlations (i.e. values from -0.3 to -0.5) are found for contributions from the ocean. Overall, our findings show that the stronger the backscatter intensity averaged over the ATAL altitude range, the higher the continental contributions from Tibet, foothills and land. The weaker the ATAL is during August 2016, the higher are the maritime contributions.

Pearson Correlation Coefficients				
Location of	Tibet	Foothills	Land	Ocean
end points	0.33	0.35	0.14	−0.19
strong-updraft	0.41	0.09	−0.00	−0.19
end points*	0.70	0.63	0.56	−0.27
strong-updraft*	0.69	0.52	0.58	−0.32

Table 5.4: Pearson correlation coefficients between the different regions (Tibet, foothills, land and ocean) and the backscatter intensity averaged over the ATAL altitude range ($(\overline{\mathrm{BSR}}_{455}\text{-}1) \times 100$) for the location of the end points of the trajectories (see Fig. 5.17) and for the location of the strong-updraft. For each region the Pearson correlation coefficient was calculated using all measurements except the one on 12 August, when the UTLS is filled by a 5 km thick cirrus cloud. Further, the Pearson correlation coefficients are also calculated excluding in addition low statistics flights (11, 21, 23 and 26 August) for which the trajectory number is lower than 50% of the maximum number of trajectories (#704) calculated on 18 August 2016 (see Fig. 5.16) as well as the no ATAL case on 15 August (marked by *). This table has been taken from Hanumanthu et al. [2020].

Chapter 6

Discussion and summary

6.1 Discussion

COBALD measurements using the CI, the 940-to-455 nm ratio of the aerosol component of the BSR, can be used to discriminate aerosol and cirrus measurements (see Sect. 3.1). However, in case of a cirrus cloud, the dominant ice particle backscatter does not allow the COBALD sonde to detect, whether aerosol particles coexist with ice particles or not. Krämer et al. [2016] describe two types of cirrus: (1) in situ origin cirrus observed at the altitudes at which they are formed on soluble solution aerosol particles or on solid ice nucleating particles; (2) liquid origin cirrus, which are glaciated liquid clouds lifted from below to the cirrus temperature region. The formation mechanism of the cirrus cloud will have implications for the aerosol concentration in the cirrus layers within the ATAL.

For the back-trajectory calculations, as described in Chap. 4 and 5, thin cirrus clouds within the ATAL are included to infer the origin of air masses contributing to the ATAL. If it is assumed that these cirrus clouds are of cirrus type (2), the aerosol concentration within the ATAL would not be affected by the formation process of the cirrus particles; However the uplift (convection) of air masses from the lower troposphere could transport enhanced concentrations of aerosol particles from close to the ground to ATAL altitudes without much influence of aerosol in the middle troposphere (see Fig. 3.3). This concept is consistent with the results of Vernier et al. [2018], who found in Optical Particle Counter (OPC) balloon-borne measurements of the ATAL from Hyderabad, India, in summer 2015 that aerosol concentrations in the boundary layer and in the ATAL are of the same magnitude, while much lower

aerosol concentrations prevail in the middle troposphere. In their balloon measurements Vernier et al. [2018] further found that the presence of cirrus is associated with a reduction or a minimum in aerosol concentration possibly caused by aerosol removal processes through the formation of cirrus particles of type (1). Therefore, for both cirrus types, it is important to include the back-trajectory calculations of thin cirrus clouds found within the ATAL to identify the air mass origin. Further, depending on the lifetime of the cirrus clouds within the ATAL, the occurrence of cirrus particles (e.g. through sedimentation or uptake on the ice surface) could have implications on the ATAL even when the cirrus particles are no longer present.

Note that the calculation of $\overline{\mathrm{BSR}}_{455}$ (see Tab. 3.1) is based on binned data (with an altitude resolution of $\sim$25 m in the UTLS). Thin cirrus clouds found within the ATAL are excluded for the calculation of the mean value of $\overline{\mathrm{BSR}}_{455}$, because here the BSR_{455} value for cirrus is much higher than for aerosol (Sect. 3.3). However, the calculation of the fraction of air masses uses the high-resolution measurement data (with a resolution of 1 sec) for back-trajectories including the altitude ranges where thin cirrus clouds within the ATAL were detected. In the altitude range of thin cirrus clouds, the aerosol concentration could be enhanced by convection or reduced by aerosol removal processes such as in situ cirrus formation. In both cases it is important to include the air masses in the altitude range where thin cirrus clouds were detected to identify the origin of air masses contributing to the ATAL.

However, cirrus clouds detected directly below the ATAL are excluded in our trajectory analysis, even if aerosol and cirrus coexisted here, the bottom of the ATAL is highly uncertain. Therefore, in our analysis there is an uncertainty in the vertical altitude range of the ATAL. To solve this uncertainty balloon-borne measurements in addition to COBALD would be required such as the measurements of the particle size distribution (e.g. using an optical particle spectrometer, POPS; Gao et al. [2016]).

6.2 Conclusions

In this thesis, a series of balloon-borne measurements was presented which were performed by the COBALD instrument conducted in Nainital, northern India, during August and November 2016. The BSR_{455} measurements show a strong day-to-day variability of the altitude, the vertical extent and the backscatter intensity of the ATAL at UTLS altitudes over Nainital in August 2016. In contrast to high-resolution in situ measurements, space-borne

observations often do not allow the day-to-day variability of ATAL profiles to be studied; therefore mean values of the ATAL profiles were frequently used in previous studies based on satellite observations. [e.g. Vernier et al., 2011, 2015].

Further, there are frequent observations of cirrus layers embedded in the ATAL (see Chap. 3); depending on the duration and formation mechanism of the cirrus layers, there will be an impact of cirrus on the properties of the aerosol particles constituting the ATAL. In general, the BSR_{455} values measured in August 2016 are higher than values measured during post-monsoon in November, which represent the aerosol background. However, there is one observation on 15 August showing no ATAL (here the BSR_{455} is lower than in November).

Lagrangian back-trajectory calculations were performed (see Chap. 5) using the CLaMS model driven by ERA-Interim reanalysis data to identify the air mass origin in the model boundary layer and the transport pathways of air parcels contributing to the ATAL over Nainital in August 2016. In this thesis, it was demonstrated that there is a variety of factors impacting the variability of the ATAL: continental convection, tropical cyclones (maritime convection), dynamics of the anticyclone and stratospheric intrusions. All these factors contribute to the observed day-to-day variability of the ATAL found over Nainital in August 2016. Clearly the details of the vertical transport would differ if a higher resolution, more recent reanalysis data set were used; (e.g. ERA5; see Hersbach et al. [2020]). However the general transport patterns would likely remain unaltered. For example, the convective upward transport by tropical cyclones is found consistently for ERA-Interim and ERA5 in diabatic calculations [Li et al., 2020]. Further, the ATAL is also impacted by other processes related to the formation and growth of aerosol as well as by aerosol removal processes such as in situ cirrus formation.

A major finding from this thesis is that air masses contributing to the ATAL are a mixture of air masses from different origins and not exclusively from the boundary layer. The trajectories originating from the boundary layer are separated according to geopotential height and further, for low geopotential heights, between continental and maritime sources. Strong ATAL cases have high contributions from the Tibetan Plateau (Tibet), the remaining continental (land) area and the foothills of the Himalayas (foothills). Weaker ATAL cases have higher contributions from the maritime area (ocean) caused by the impact of tropical cyclones. Here, mixing with unpolluted air masses from the maritime boundary layer cause a dilution of the ATAL. The no ATAL case of the 15 August 2016 has similar contributions

from the Tibetan Plateau (Tib), the remaining continental (land) area and the foothills of the Himalayas (foothills) as the strong ATAL cases, however on this day there is a bi-modal structure of the anticyclone and Nainital is located between the western and eastern mode of Asian monsoon anticyclone (see Sect. 5.1). In this thesis, the hypothesis is put forward that the main driver for no ATAL cases during the monsoon season is the dynamics of the Asian monsoon anticyclone. However, there is only one no ATAL measurement in August 2016 (partly influenced by cirrus), therefore it cannot be excluded that also aerosol removal processes such as in situ cirrus formation contribute to the existence of no ATAL measurements. More balloon-borne measurements would be required to either validate or falsify the hypothesis, importance of the anticyclone dynamics.

Moreover, the locations of strongest updraft within 18 hours along the backward trajectories were calculated (see Sect. 5.3). A cluster of such locations was found at the southern edge of the Himalayan foothills over northern India, Nepal and Bhutan. Further for balloon-measurements impacted by tropical cyclones, locations of the strongest updraft are also found over the western Pacific ocean. Within the ATAL, a mixture of air parcels with different transport times is found; i.e. the transport times from the Earth's surface to ATAL altitudes vary strongly. The shortest transport times found for 6, 15, and 18 August are between 10 and 15 days. These trajectories originate either on the Tibetan Plateau or at the location of tropical cyclones in the western Pacific. Shorter transport times below 10 days are only found for the 12 August (when the UTLS is filled with a 5 km thick cirrus cloud) and for 17 August for air masses originating on the Tibetan Plateau.

Finally, CLaMS backward trajectory calculations allow the transport pathways from the Earth's surface to ATAL altitudes to be identified (see Chap. 5). Very fast uplift in a convective range transports air masses up to the top of the convective outflow level ($\sim$360 K) within a few days. Subsequently, the air parcels are slowly uplifted by diabatic heating within a large-scale upward spiral driven by the anticyclonic flow in the UTLS over the Asian monsoon region from about 360 K up to ATAL altitudes. Over Nainital in summer 2016, a maximum ATAL altitude of 422 K (75 hPa) was measured. This slow uplift caused by diabatic heating in a large-scale upward spiral is consistent with concepts referred to as "an upward spiralling range" [Vogel et al., 2019] or as "a confined lower stratosphere" [Brunamonti et al., 2018].

This thesis contributes to the deduction of the source regions of emissions of precursors of ATAL particles at the Earth's surface and their transport pathways to the UTLS which is

important to develop recommendations for regulations of anthropogenic surface emissions of ATAL precursors. In a recent study, Fadnavis et al. [2019b] argue that further increasing industrial emissions in Asia will lead to a wider and thicker ATAL, with the potential to amplify the severity of droughts in India. Severe droughts would have fatal consequences for agriculture on the Indian subcontinent and therefore would result in strong socio-economic impacts in one of the most densely populated parts of the world. On the other hand, the ATAL impacts the radiative balance of the Earth's atmosphere and could have positive side effects in terms of reducing Earth's surface temperatures [Fadnavis et al., 2019b]; therefore more future research about the ATAL and its impacts is required.

Appendix A

A.1 Measured raw signal of balloon soundings

The aerosol measurements analyzed here are based on balloon-borne back-scatter ratio information employing the COBALD detector. Here, presented actual raw signal obtained from the observations and to have an understanding of the raw signal range. Demonstrated the variability it has in the observational high resolution signal. Individual measurements from August and November explain the change in BSR signal during Peak-monsoon (in general August is considered as peak-monsoon period over South Asian region [Lau et al., 2018, see chapter 1]) to post-monsoon. Orange shading w.r.t August measurements shows the aerosol signal. It is compared to the aerosol signal in November which is taken as background signal.

A.1.1 Comparing measured raw data to binned data

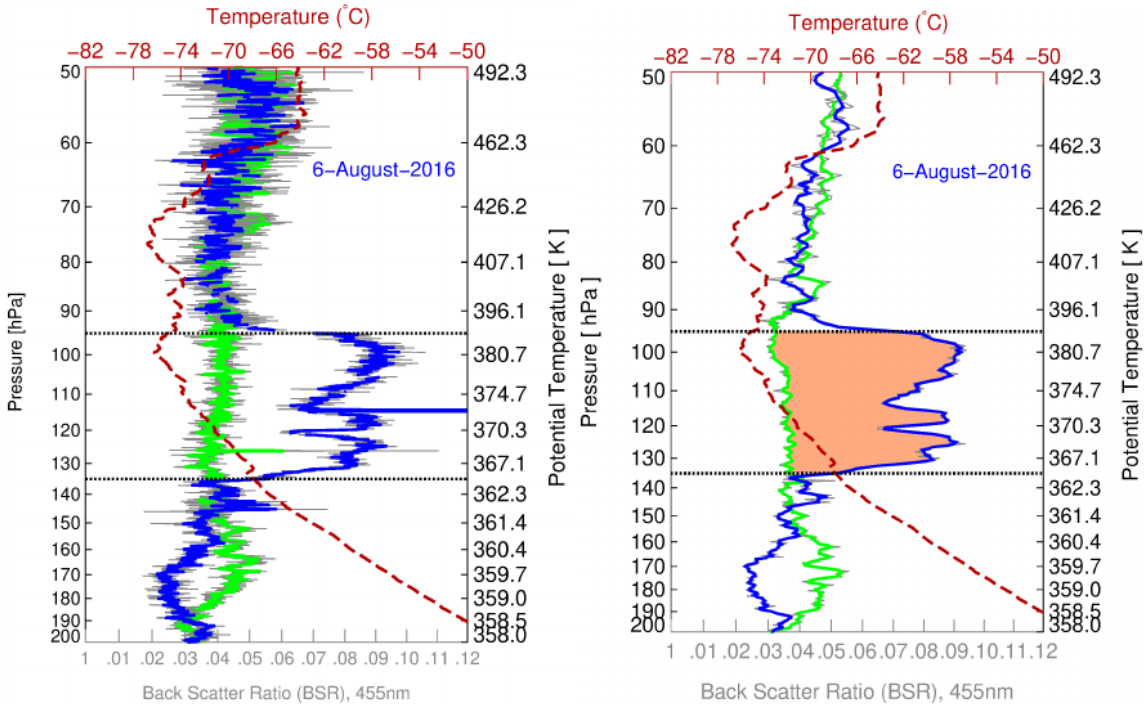

Figure A.1: Raw BSR signal of the sounding on 2nd August (Blue in color) in comparison with averaged November cases (Green in color) are drawn without binning and also with 3 point running mean along the Y-axis on left. On the right binned BSR signal of sounding on 2nd August(Blue in color) in comparison with averaged November cases (Green in color) drawn after binning and also with 3 point running mean along the Y-axis.

In order to obtain a consistent data set, all variables are binned in pressure intervals of 1 hPa for $p > 300$ hPa, and 0.5 hPa for $p < 300$ hPa, yielding an improved signal-to-noise ratio and a dataset with consistent vertical levels. This binning corresponds to a vertical resolution of approximately 25 m in the UTLS. A quality-check is performed for all instruments, based on interpretation of their house-keeping data, and data points showing anomalous behavior are rejected. To avoid instrumental artifacts, all measurements at pressures levels have been considered. The COBALD data are expressed as backscatter ratio (BSR), i.e. the ratio of the total-to-molecular backscatter coefficient. This is calculated by dividing the total measured signal to its molecular contribution, which is computed from the atmospheric extinction according to Bucholtz [1995], and using air density derived from the measurements of temperature and pressure [Cirisan et al., 2014]. Uncertainty on COBALD BSR as inferred by this technique is estimated to be around 5% [Vernier et al., 2015]. Pressure measurements by RS41 are used as the main vertical coordinate throughout this work (as well as for the binning discussed above), and are subject to instrumental uncertainties of 0.6/1 hPa for

pressures lower/higher than 100 hPa, respectively, as given by the manufacturer [Vaisala, 2017]. Due to all these reasons we considered in this the analysis binned data version of the for better intercommunication between instruments to have better understanding of the data. See Fig A.1 for clarification.

A.2 Sensitivity of 40 day run in different time-lengths

A.2.1 Spatial view

Here, placed all the launches to demonstrate the diffusion coefficient consideration by calculating max change in Θ which is causing variability in updraft regions in the ERA-Interim world. In order to minimize that diffusion we did some test runs to identify reasonable time period which can enable our trajectories look for possible source regions of ATAL air masses. Following spatial view figures visualize the source distribution change over the years. From figure A.2 to figure A.13 will demonstrate why an 18hr time period was chosen for the further analysis.

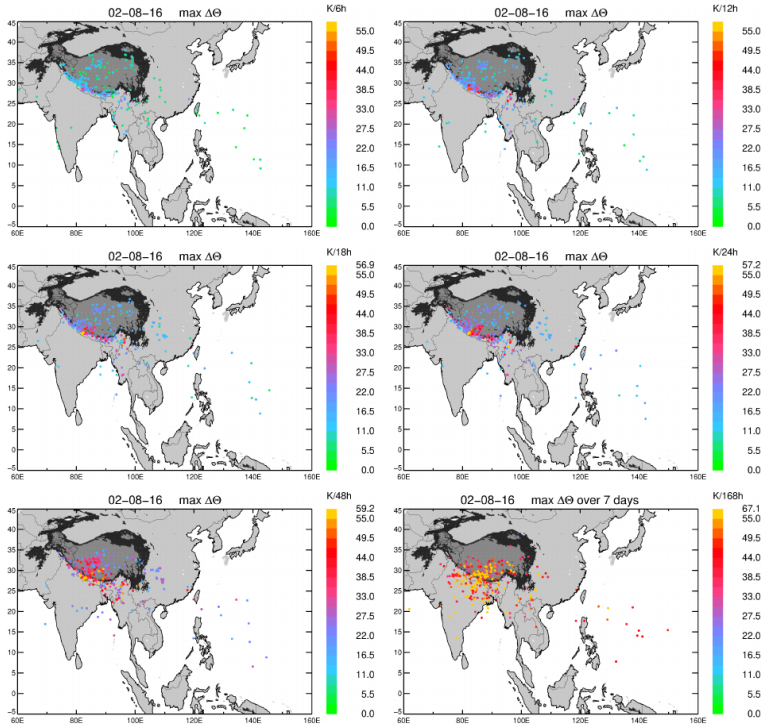

Figure A.2: the change in trajectories contributions w.r.t averaging time intervals, strongest updraft regions are calculated from 40-day backward trajectories (see Tab. 5.1), the difference between backward trajectory calculations depending on the time periods considered which are 6, 12, 18, 24 and 48 hrs and also 7days on 2nd of August.

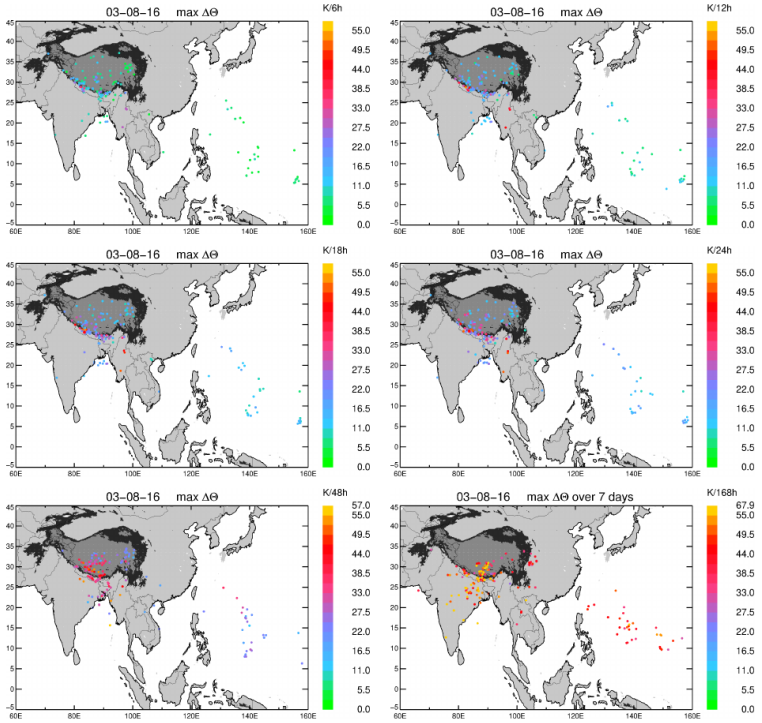

Figure A.3: the change in trajectories contributions w.r.t averaging time intervals, strongest updraft regions are calculated from 40-day backward trajectories (see Tab. 5.1), the difference between backward trajectory calculations depending on the time periods considered which are 6, 12, 18, 24 and 48 hrs and also 7days on 3rd of August.

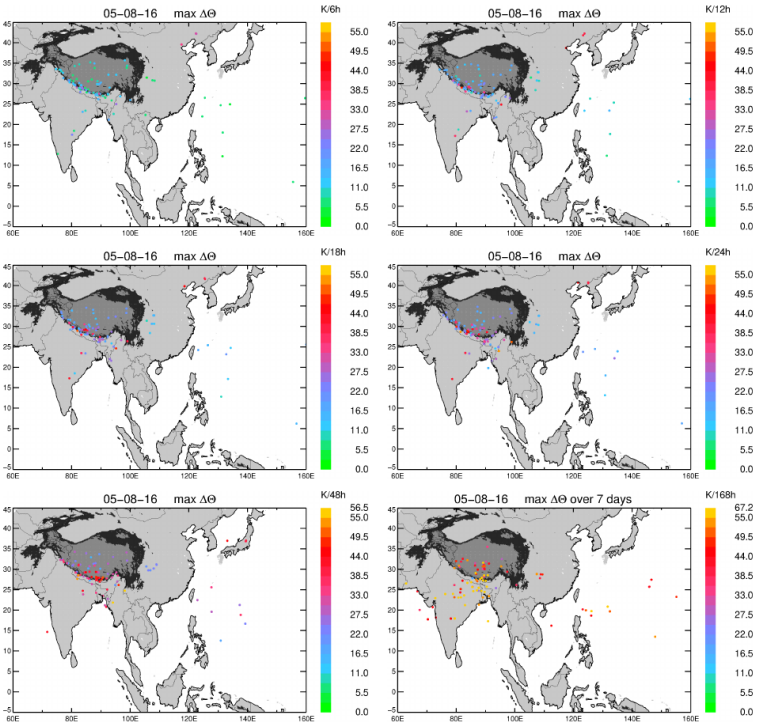

Figure A.4: the change in trajectories contributions w.r.t averaging time intervals, strongest updraft regions are calculated from 40-day backward trajectories (see Tab. 5.1), the difference between backward trajectory calculations depending on the time periods considered which are 6, 12, 18, 24 and 48 hrs and also 7days on 5th of August.

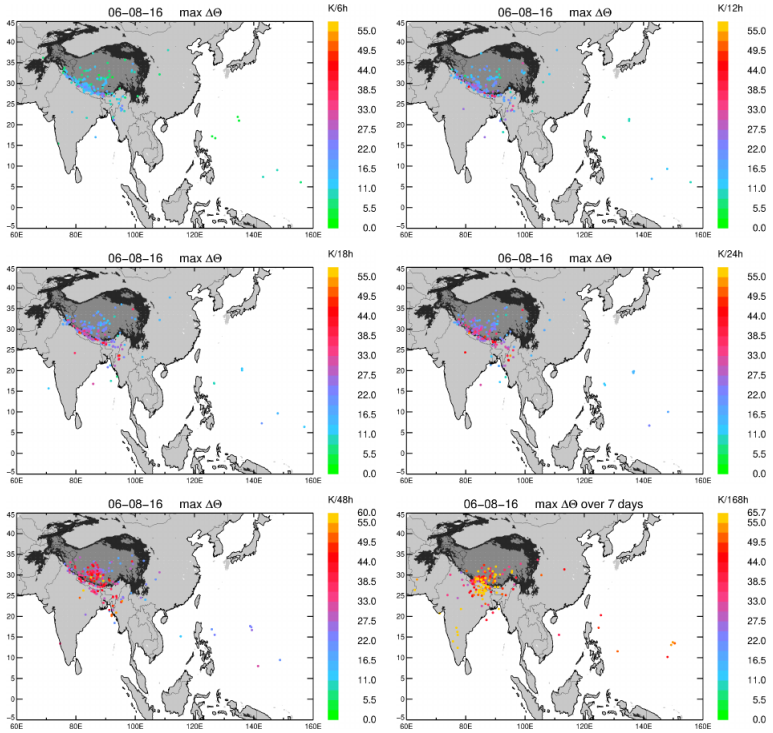

Figure A.5: the change in trajectories contributions w.r.t averaging time intervals, strongest updraft regions are calculated from 40-day backward trajectories (see Tab. 5.1), the difference between backward trajectory calculations depending on the time periods considered which are 6, 12, 18, 24 and 48 hrs and also 7days on 6th of August.

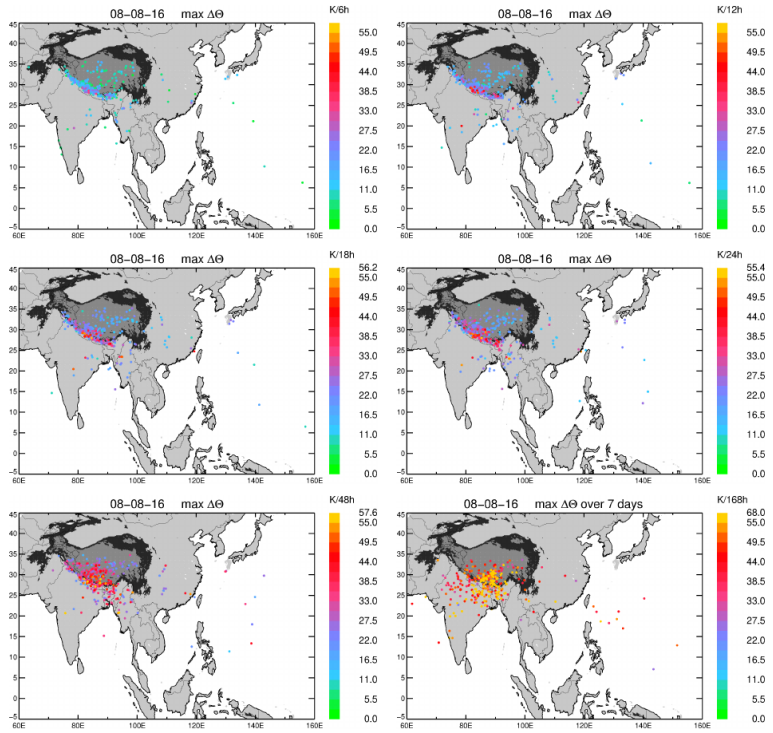

Figure A.6: the change in trajectories contributions w.r.t averaging time intervals, strongest updraft regions are calculated from 40-day backward trajectories (see Tab. 5.1), the difference between backward trajectory calculations depending on the time periods considered which are 6, 12, 18, 24 and 48 hrs and also 7days on 8th of August.

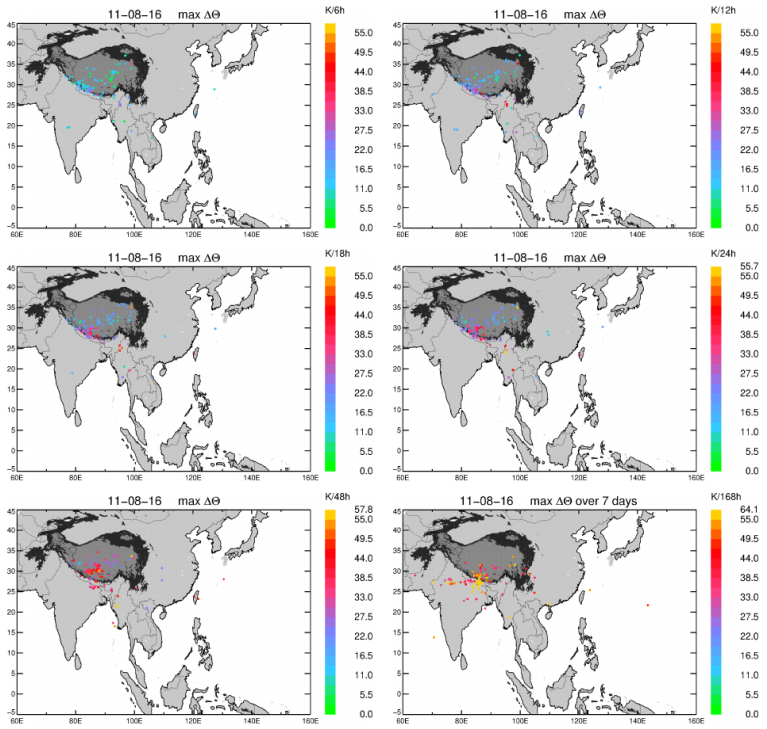

Figure A.7: the change in trajectories contributions w.r.t averaging time intervals, strongest updraft regions are calculated from 40-day backward trajectories (see Tab. 5.1), the difference between backward trajectory calculations depending on the time periods considered which are 6, 12, 18, 24 and 48 hrs and also 7days on 11th of August.

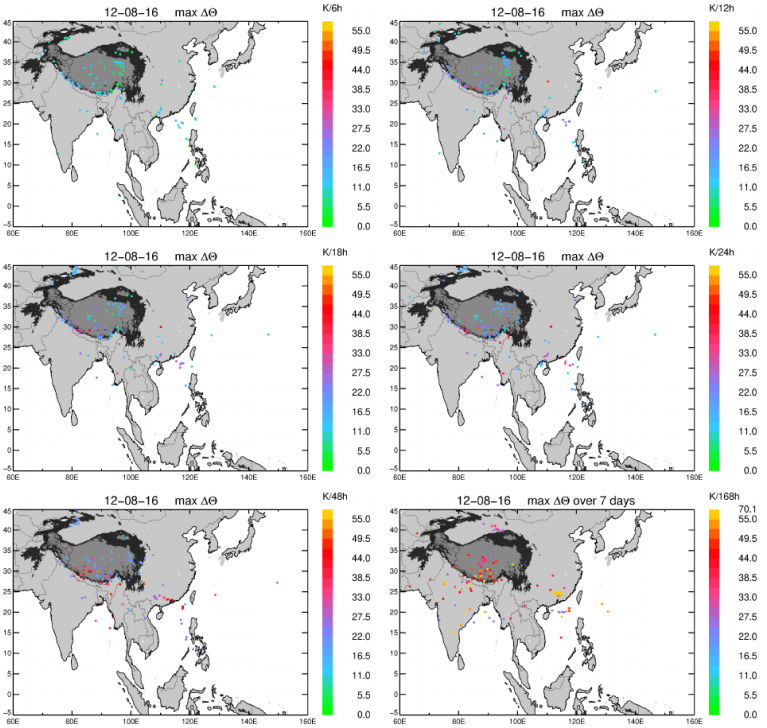

Figure A.8: the change in trajectories contrbutions w.r.t averaging time intervals, strongest updraft regions are calculated from 40-day backward trajectories (see Tab. 5.1), the difference between backward trajectory calculations depending on the time periods considered which are 6, 12, 18, 24 and 48 hrs and also 7days on 12th of August.

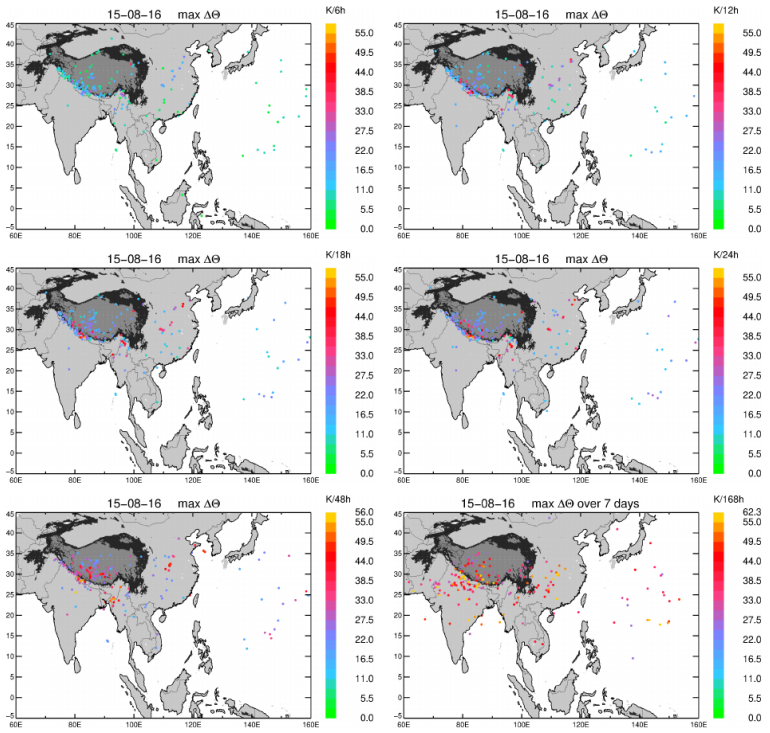

Figure A.9: the change in trajectories contributions w.r.t averaging time intervals, strongest updraft regions are calculated from 40-day backward trajectories (see Tab. 5.1), the difference between backward trajectory calculations depending on the time periods considered which are 6, 12, 18, 24 and 48 hrs and also 7days on 15th of August.

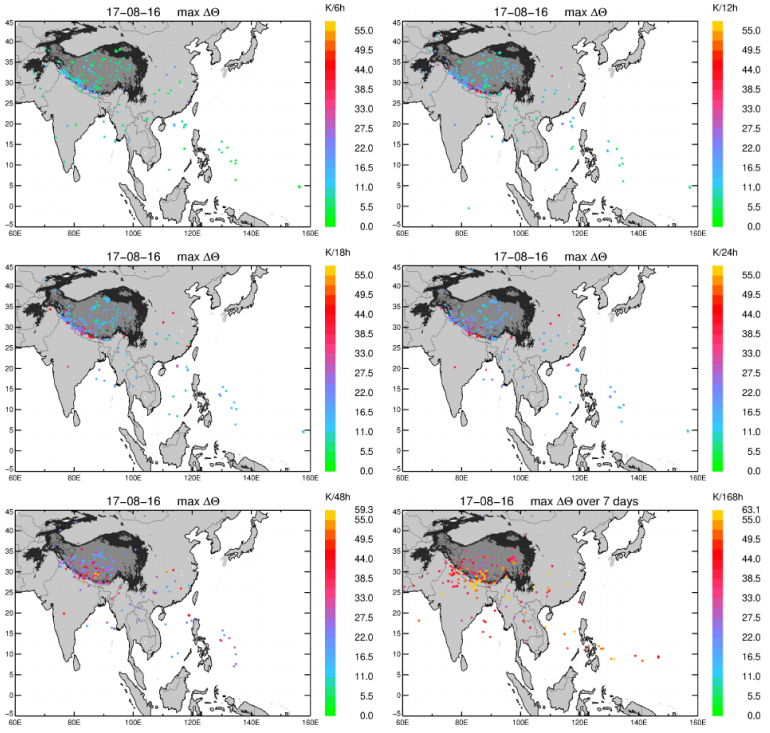

Figure A.10: the change in trajectories contributions w.r.t averaging time intervals, strongest updraft regions are calculated from 40-day backward trajectories (see Tab. 5.1), the difference between backward trajectory calculations depending on the time periods considered which are 6, 12, 18, 24 and 48 hrs and also 7days on 17th of August.

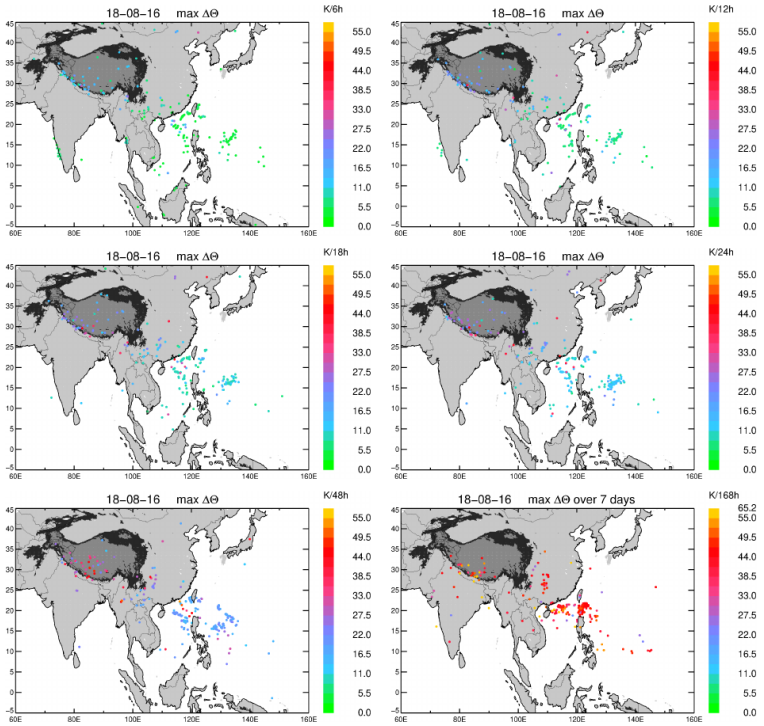

Figure A.11: the change in trajectories contributions w.r.t averaging time intervals, strongest updraft regions are calculated from 40-day backward trajectories (see Tab. 5.1), the difference between backward trajectory calculations depending on the time periods considered which are 6, 12, 18, 24 and 48 hrs and also 7days on 18th of August.

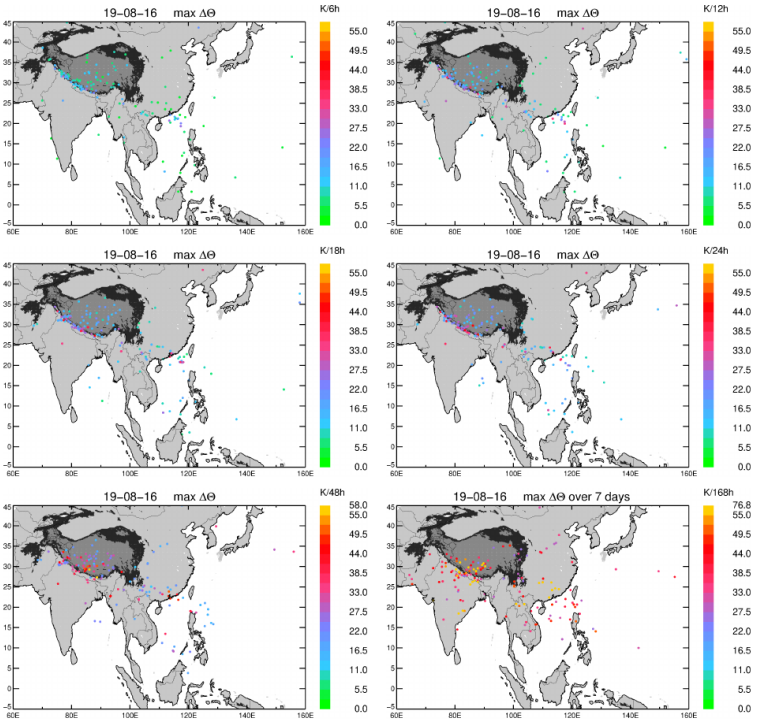

Figure A.12: the change in trajectories contributions w.r.t averaging time intervals, strongest updraft regions are calculated from 40-day backward trajectories (see Tab. 5.1), the difference between backward trajectory calculations depending on the time periods considered which are 6, 12, 18, 24 and 48 hrs and also 7days on 19th of August.

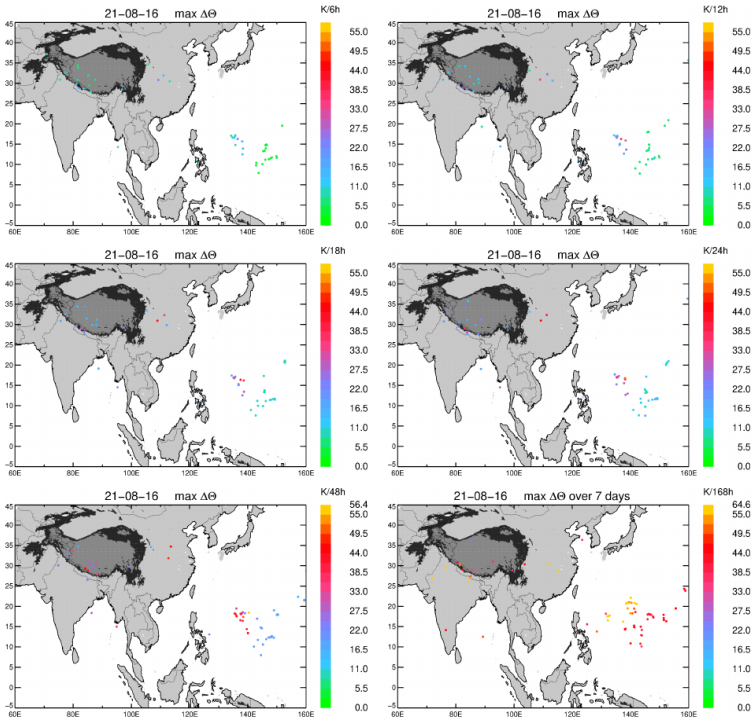

Figure A.13: the change in trajectories contributions w.r.t averaging time intervals, strongest updraft regions are calculated from 40-day backward trajectories (see Tab. 5.1), the difference between backward trajectory calculations depending on the time periods considered which are 6, 12, 18, 24 and 48 hrs and also 7days on 21st of August.

A.2.2 Sensitivity in the air mass origin

The fraction of trajectory end points and the fraction of locations of strongest updraft in different boundary layer regions are shown. The following figures demonstrate the possible changes in the source regions according to change in the $\Delta\theta$ criteria. This enabled to investigate the range of variability in the origins. The key identity of this analysis is that strong vertical updrafts are confined to Asian monsoon region except when there is cyclonic activity happening in West Pacific. This can be observed in residual percentage increase on 18th and 21st August (see Fig. A.11, Fig A.23 and Fig A.13, Fig A.25).

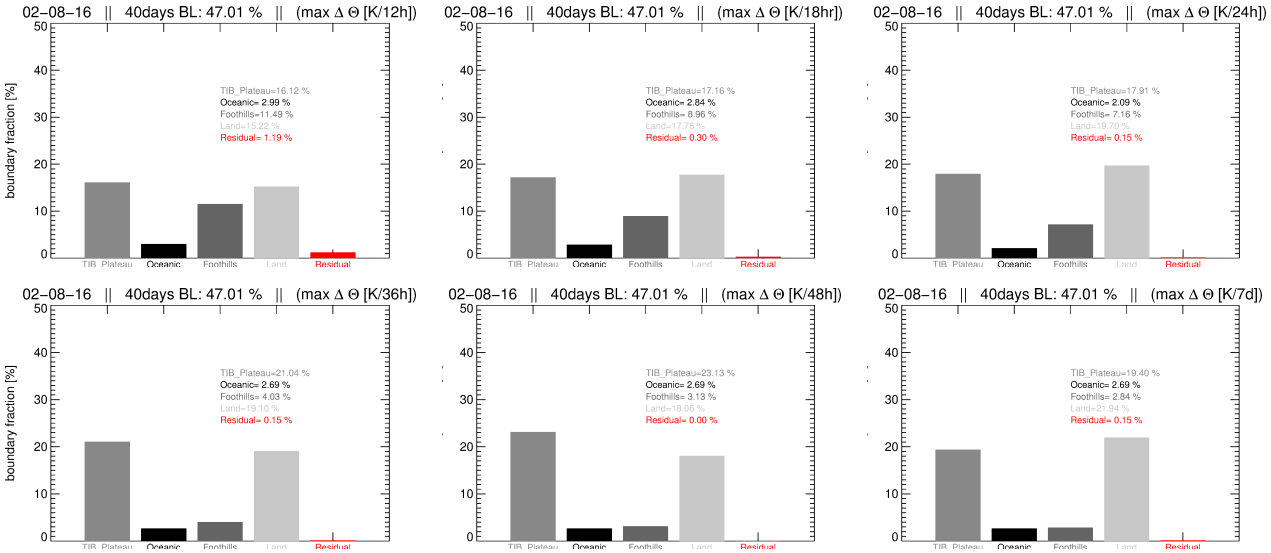

Figure A.14: Strong Updraft criterion followed trajectory sources of 40 day backward run on 2nd August.

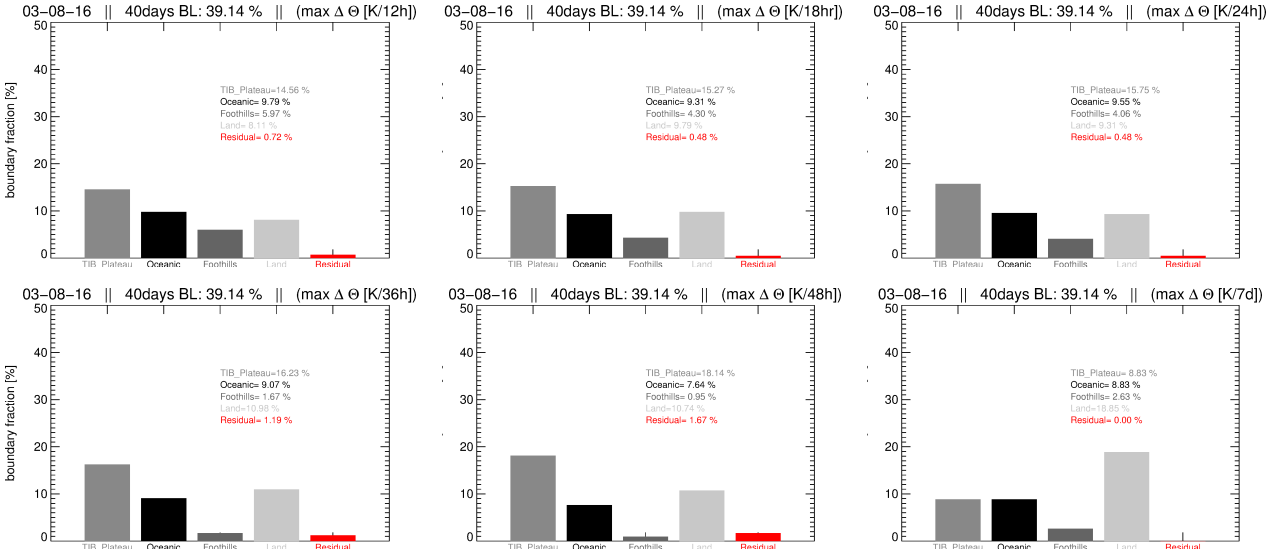

Figure A.15: Strong Updraft criterion followed trajectory sources of 40 day backward run on 3rd August.

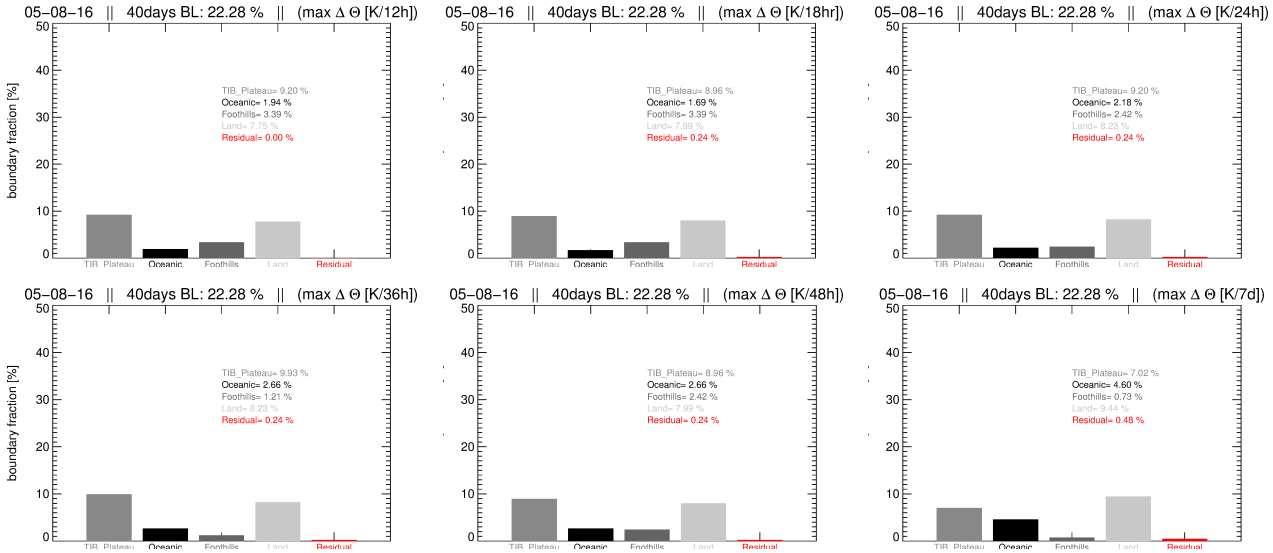

Figure A.16: Strong Updraft criterion followed trajectory sources of 40 day backward run on 5th August.

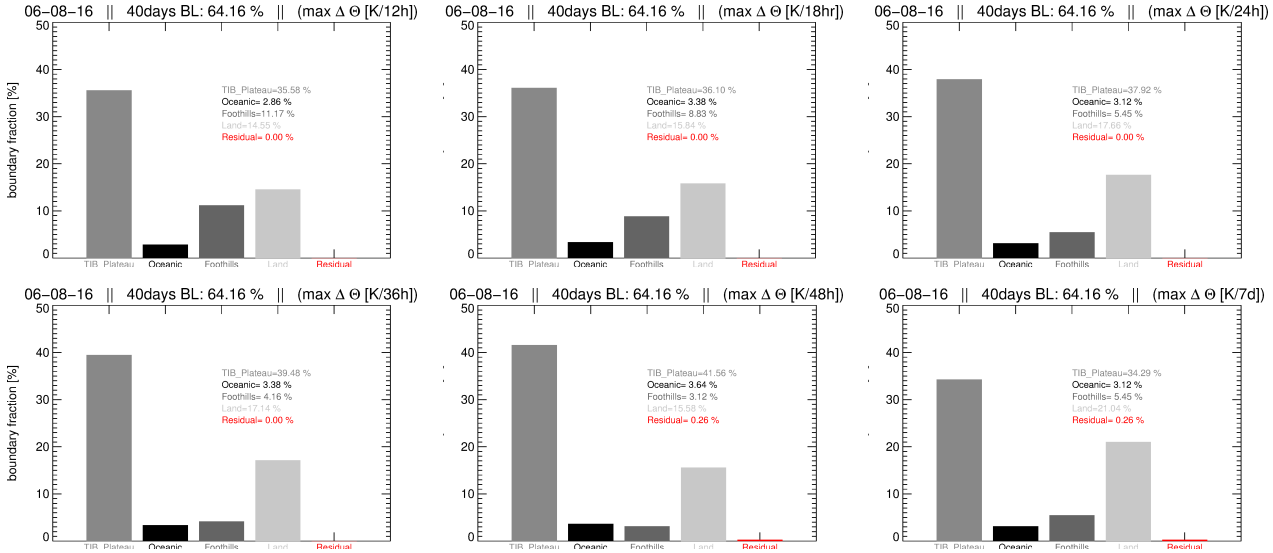

Figure A.17: Strong Updraft criterion followed trajectory sources of 40 day backward run on 6th August.

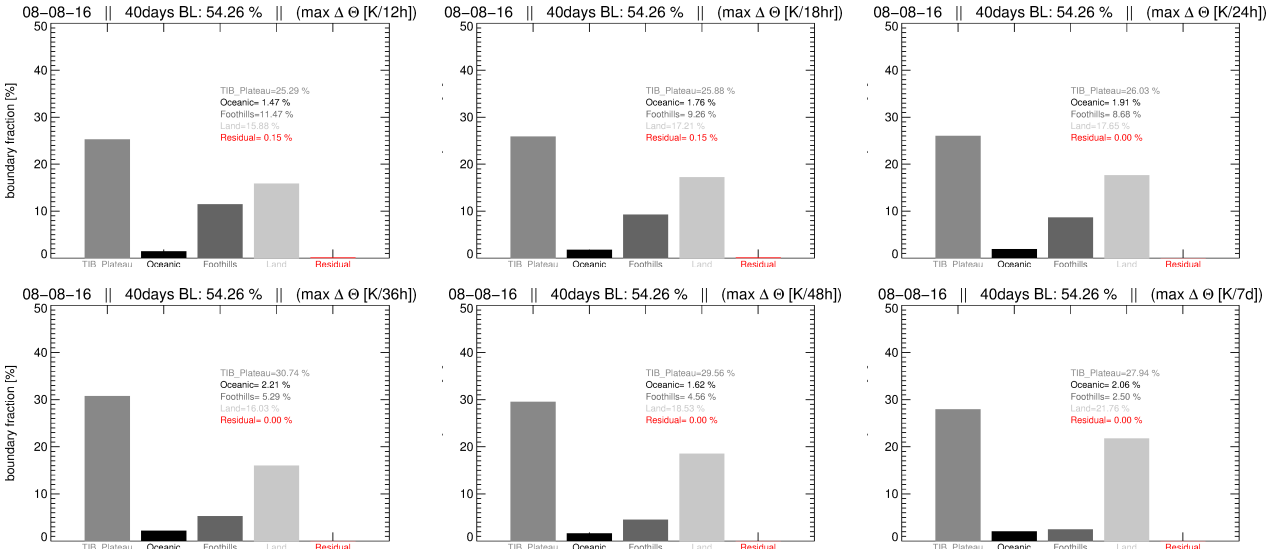

Figure A.18: Strong Updraft criterion followed trajectory sources of 40 day backward run on 8th August.

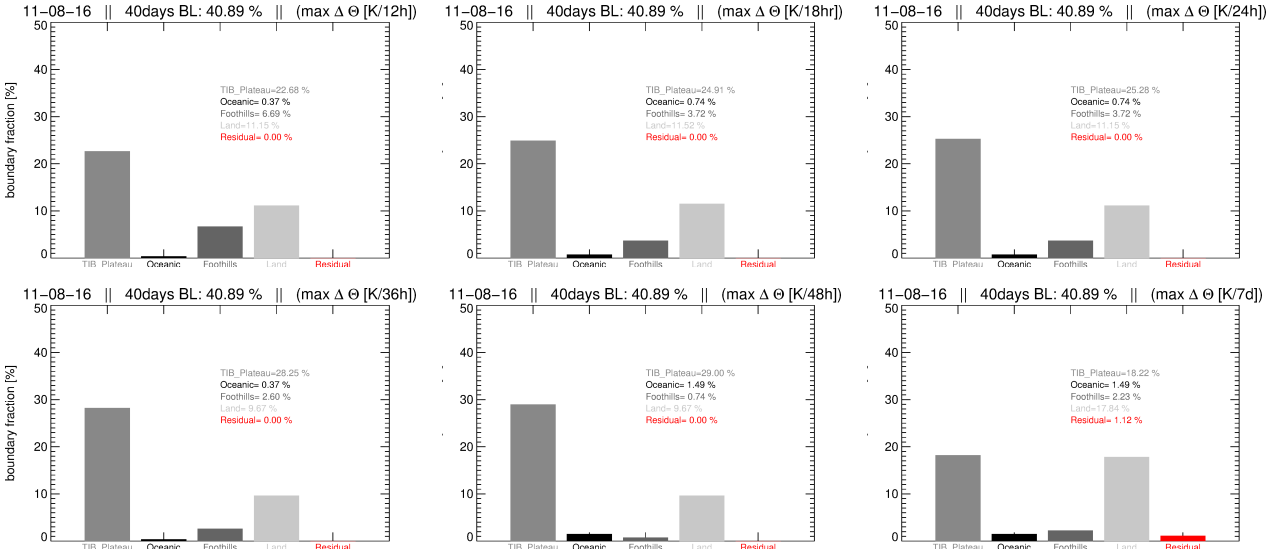

Figure A.19: Strong Updraft criterion followed trajectory sources of 40 day backward run on 11th August.

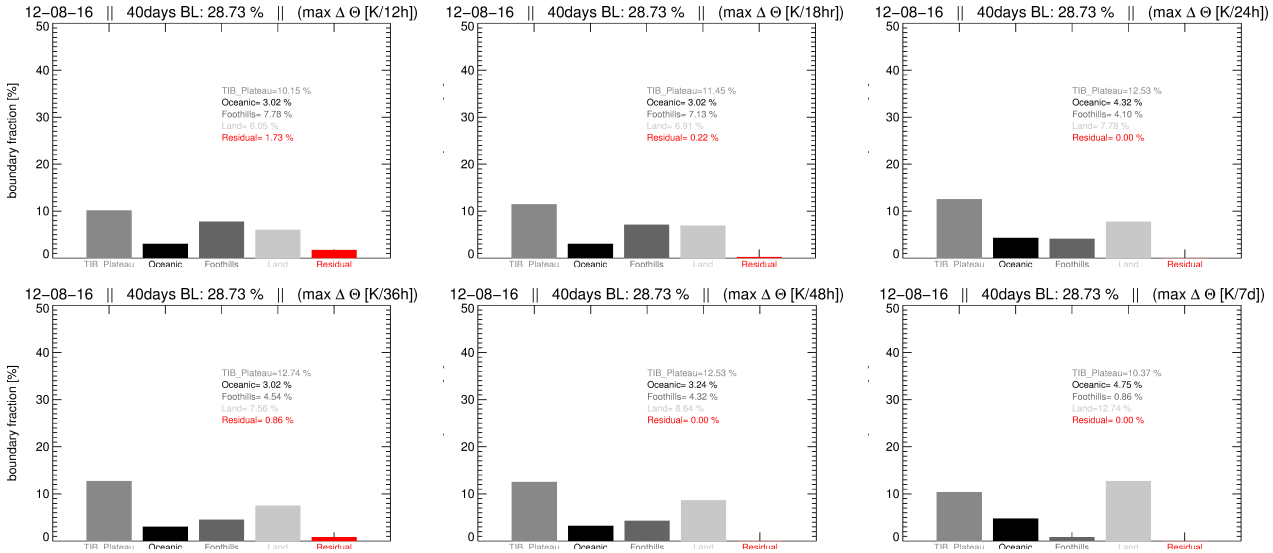

Figure A.20: Strong Updraft criterion followed trajectory sources of 40 day backward run on 12th August.

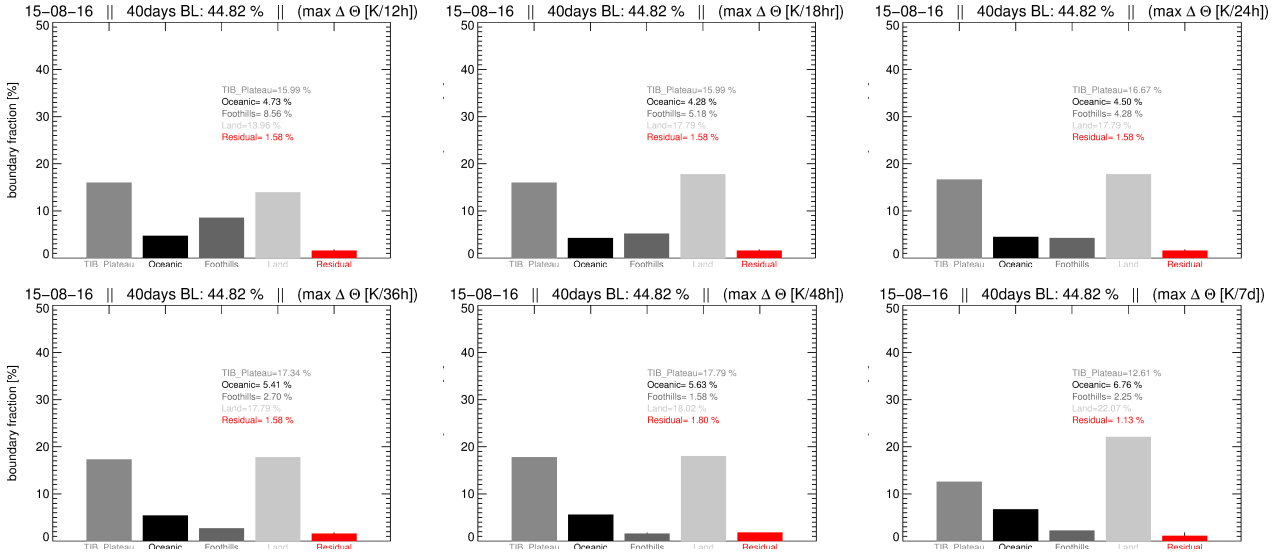

Figure A.21: Strong Updraft criterion followed trajectory sources of 40 day backward run on 15th August.

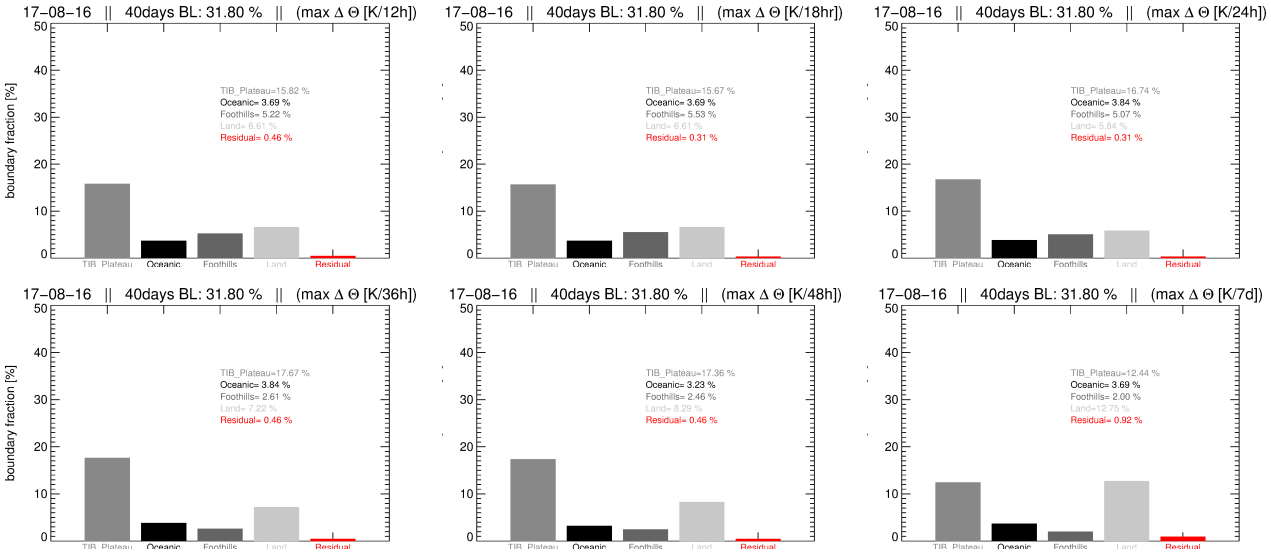

Figure A.22: Strong Updraft criterion followed trajectory sources of 40 day backward run on 17th August.

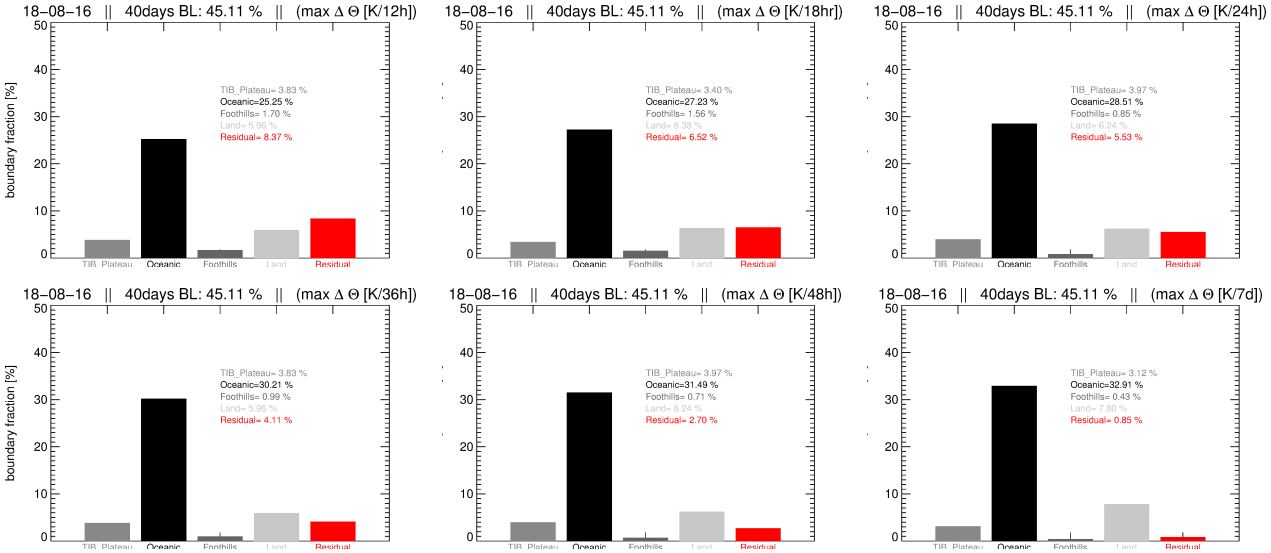

Figure A.23: Strong Updraft criterion followed trajectory sources of 40 day backward run on 18th August.

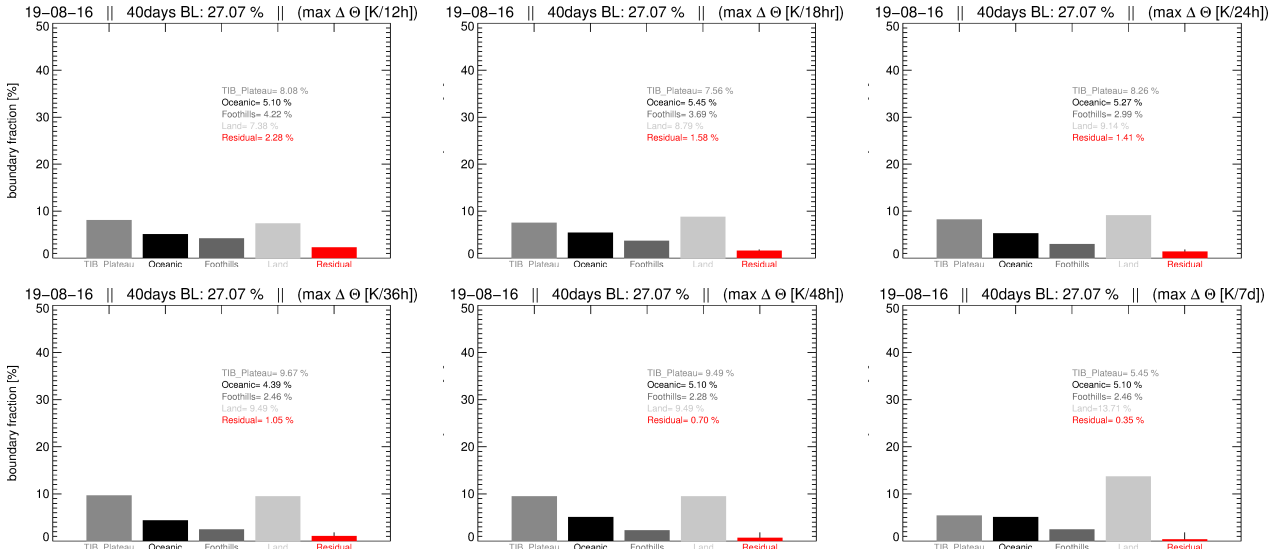

Figure A.24: Strong Updraft criterion followed trajectory sources of 40 day backward run on 19th August.

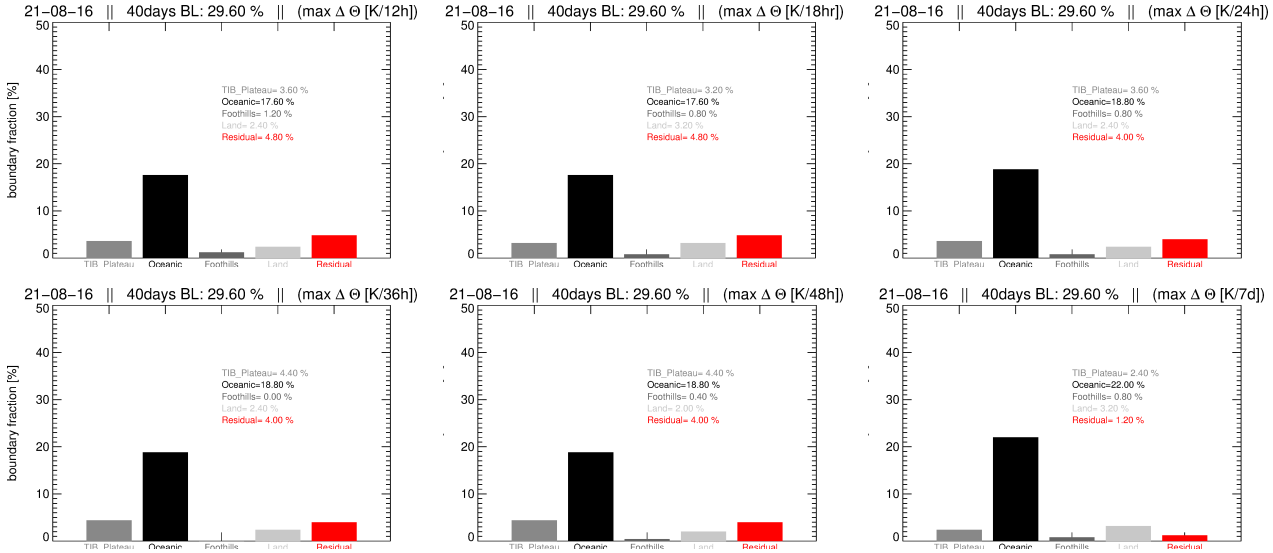

Figure A.25: Strong Updraft criterion followed trajectory sources of 40 day backward run on 21st August.

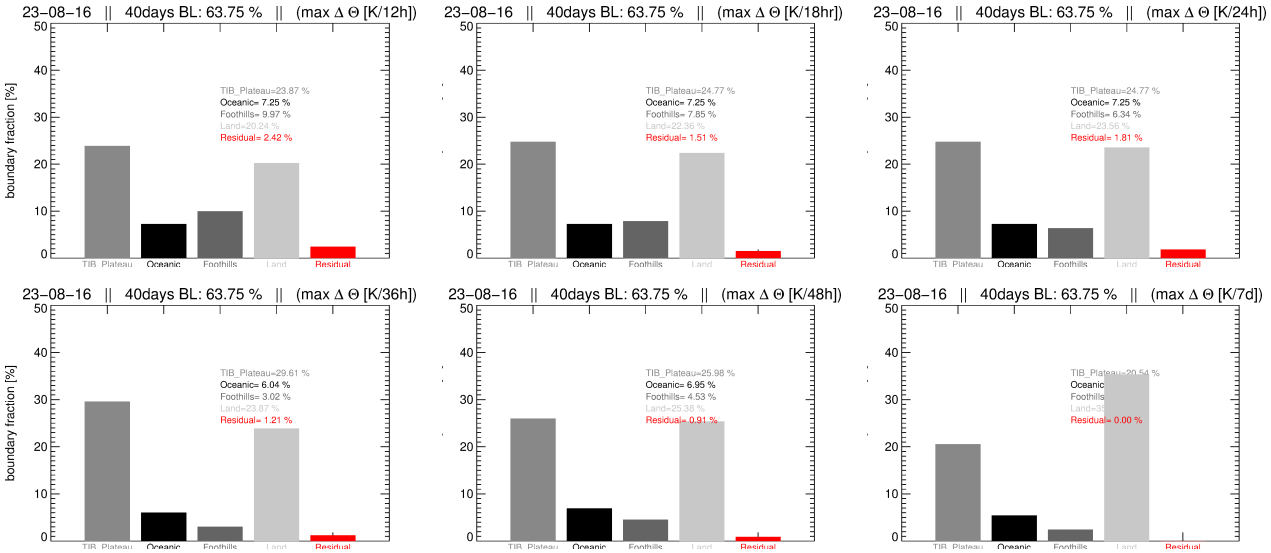

Figure A.26: Strong Updraft criterion followed trajectory sources of 40 day backward run on 23rd August.

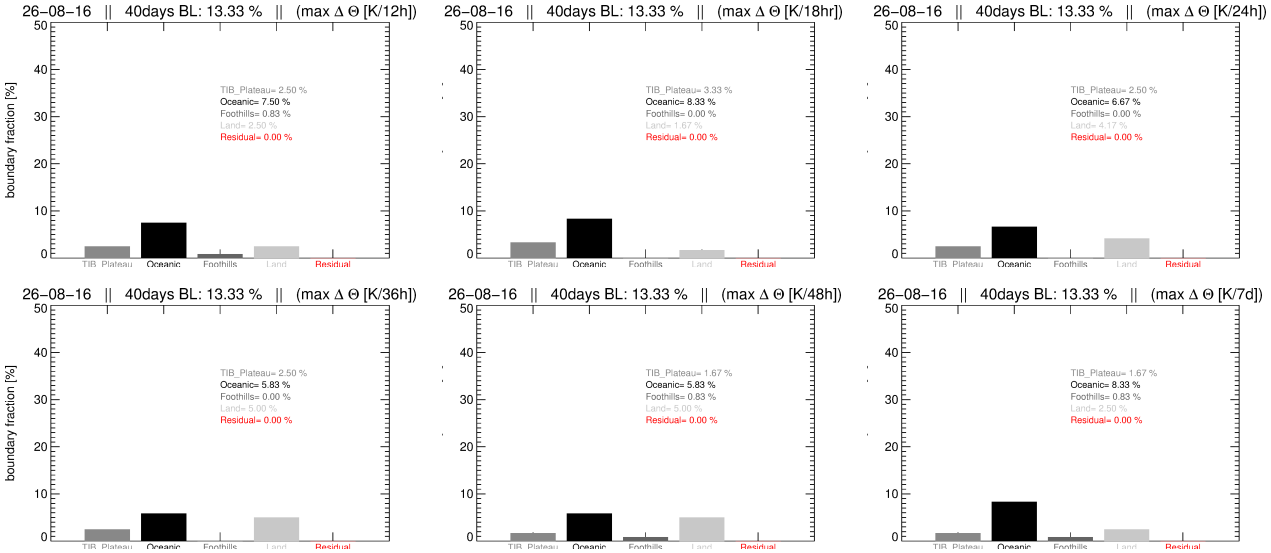

Figure A.27: Strong Updraft criterion followed trajectory sources of 40 day backward run on 26th August.

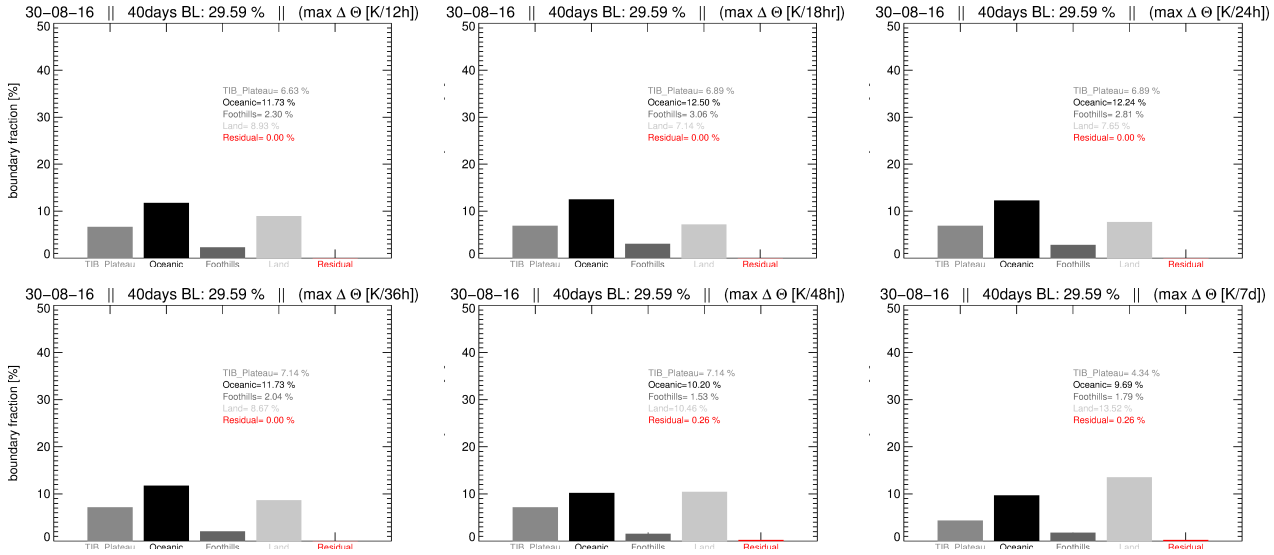

Figure A.28: Strong Updraft criterion followed trajectory sources of 40 day backward run on 30th August.

A.3 40, 60 and 80 day trajectory variability in source regions

These trajectory outputs demonstrate the variability in source regions according to trajectory time lengths. This analysis allow us to identify basic features dominating source regions and possible reasons for the change in impact of source regions. In one case (see Fig A.29), you can observe that all the regions have similar impact on the source contribution. In actual observations from which trajectory run is specified, this particular case ATAL and cirrus layers have no clear separation except small change in strength of the signal. This specifies that the bottom of the signal is not clearly identified due to the clear masking of cirrus layer on this case (see Fig 3.3). Source calculations show a consistent effect over the longer time periods as well. Adding to that, source contributions show that differences are not significant when $\Delta\Theta_{max}$ criterion (bottom panel) calculations were compared to endpoint (top panel) criterion. But these situations are not observed in case (Fig A.31) where signal range is clear and show consistent differences in the source contributions which is essential for our analysis.

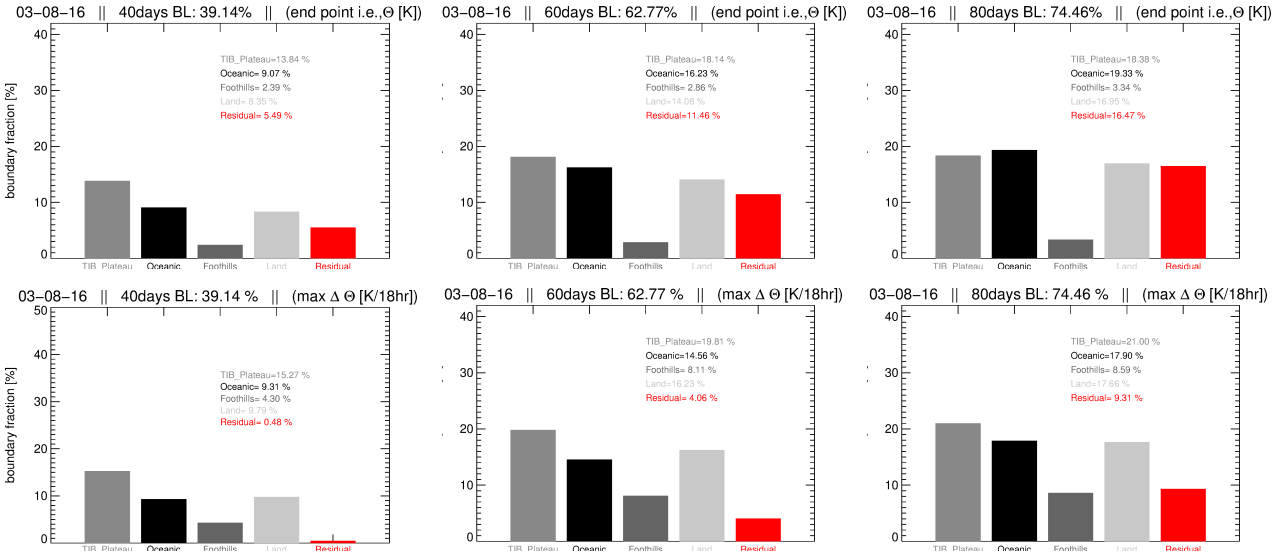

Figure A.29: PDF outputs from endpoint (top column) and strong updraft (bottom column) criterion followed trajectory sources of a 40, 60 and 80 day backward run of ERA-Interim world of the 3rd August 2016, which is considered as one of Strong ATAL with significant spread over top of the UTLS layer, in addition to that there is a broad cirrus structure just beneath of the ATAL.

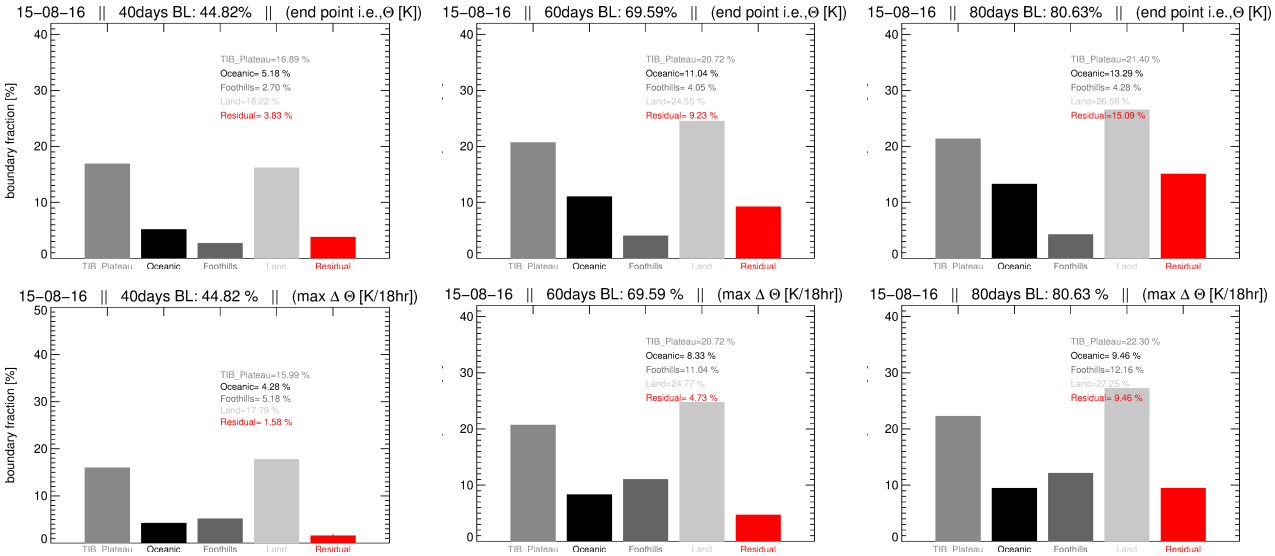

Figure A.30: PDF outputs from endpoint (top column) and strong updraft (bottom column) criterion followed trajectory sources of a 40, 60 and 80 day backward run of ERA-Interim world of the 15th August 2016, which is considered as no-ATAL case(means most likely clear sky pass of a balloon over UTLS region but) but there is a cirrus existence around CPT.

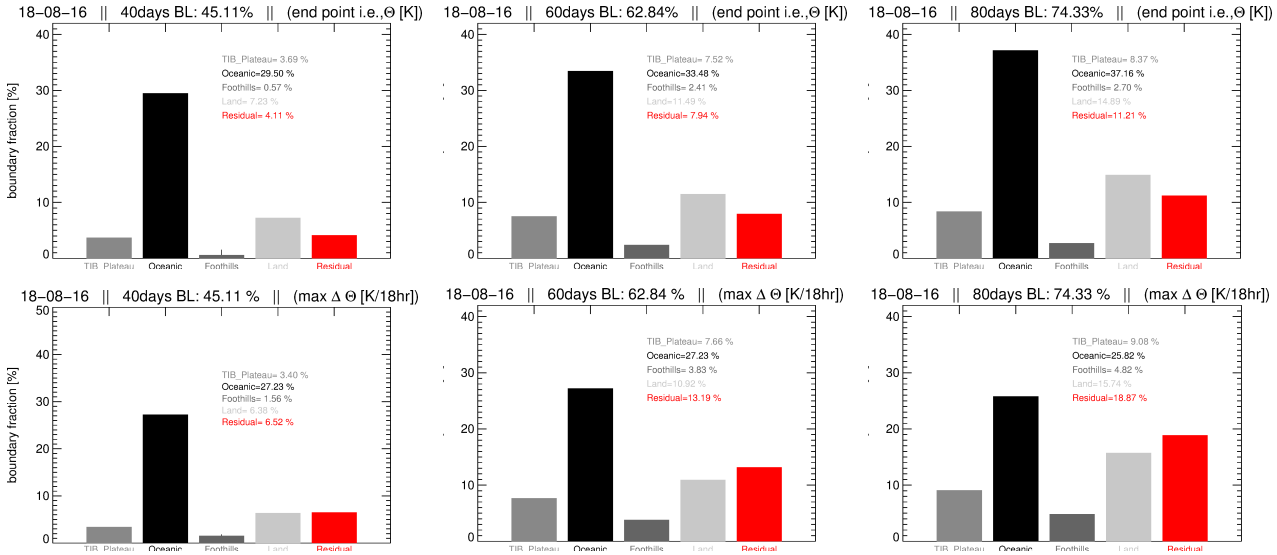

Figure A.31: Fractional outputs from endpoint (top column) and strong updraft (bottom column) criterion followed trajectory sources of a 40, 60 and 80 day backward run of ERA-Interim world of the 18th August 2016, which is considered as weak ATAL with significant spread over the UTLS layer, in addition to that there is a cirrus structure inside of the ATAL.

List of Abbreviations

Asian summer monsoon (ASM)

Asian summer monsoon anticylone (ASMA)

Asian tropopause aerosol layer (ATAL)

Asian tropical transition layer (ATTL)

Back scatter ratio (BSR)

Boundary layer (BL)

Cold point tropopause (CPT)

Chemical legragian model for stratosphere (CLaMS)

Confined lower stratosphere (CLS)

Cryogenic frost-point hygrometer (CFH)

Compact optical backscatter aerosol lidar detector (COBALD)

Central southern Pacific monsoon (CSPM)

Electrical convergence cell (ECC)

East Asian summer monsoon (EASM)

El Niño southern oscillation (ENSO)

Geo potential height (GPH)

Indonesia Australia monsoon (IAM)

Inter tropical convergence zone (ITCZ)

Lapse rate minimum (LRM)

Lapse rate tropopause (LRT)

Lower stratosphere (LS)

Lower troposphere (LT)

North african monsoon (NAfM)

North american summer monsoon or North american monsoon (NAmM)

Optical particle counter (OPC)

probability distribution function (PDF)

printed optical particle spectrometer (POPS)

South american monsoon (SAmM)

South African monsoon (SAfM)

Top of confinement (TOC)

Tropical tropopause transition layer (TTL)

Upper troposphere (UT)

Upper troposphere and lower stratosphere (UTLS)

Western north pacific monsoon (WNPM)

Acknowledgments

First of all, I would like to thank everybody whoever helped me in whatever way possible in order to made me achieve my dreams. It is a great opportunity for me to work in the frame of this project and to do my PhD thesis. It is my privilege to work in such a pleasant environment. My sincere thanks to the research center (Forschungszentrum Jülich GmbH) for such an infrastructure and support.

I am very grateful to my research supervisor PD. Dr. Rolf Müller, Team Leader of Model Theory Group of the Institute of Energy and Climate Research (IEK-7), Forschungszentrum Jülich, Germany for giving me the opportunity to be a part of his research team. His immense knowledge, continuous encouragement and selfless guidance made it possible for me to accomplish this thesis work. His remarks, advice, enthusiasm and suggestions helped me to grow as a researcher.

I would like to thank Dr. Bärbel Vogel, a key member of CLaMS team - Institute of Energy and Climate Research(IEK-7), Forschungszentrum Jülich, Germany, for her supervision during my thesis work. Her experience, guidance, and patience helped me to grow as a researcher. I owe sincere thanks to her for her reviews, valuable comments and treasured guidance.

I would like to thank Prof. Dr. Micheal Volk, Professor at University of Wuppertal, Wuppertal, Germany for his supervision during my thesis work. I owe sincere thanks to him for his reviews, comments and precious guidance.

I would like to thank Prof. Dr. Martin Riese, director of the Institute of Energy and Climate Research (IEK-7), Forschungszentrum Jülich GmbH, Jülich, Germany, and Professor at University of Wuppertal, Wuppertal, Germany for his healthy and encouraging support throughout my thesis work.

My sincere thanks to Dr. Suvarna Fadnavis, IITM, Pune, India, for being my external mentor and also for giving experienced suggestions and conversations regarding my Ph.D. project.

I would like to thank Prof. Dr. Thomas Peter and his group from ETH, Zürich for their valuable collaboration and support during the observational campaigns in Nainital and Dhulikel as part of my Ph.D. program. A big thank you to my friends and fellow researchers, Dr. Simone Brunamonti, Peter Ölsner and Dr. Teresa Jorge for their valuable collaboration throughout my Ph.D. and Asst. Prof. K. Ravi Kumar and Scientist Dr. B. Bupendra Singh and all others for their support in organizing the campaign in Nainital, India.

I reserve special thanks to my fellow office-mates and colleagues Dan Li, Sabine Robrecht and Jonas Sonnabend, who helped me throughout the learning process of my thesis project. Their suggestions

helped me to improve my understanding in the field of data analysis, especially in data processing and programming.

My sincere regards to all my colleagues of IEK-7 for their friendly after lunch and evening coffee breaks gatherings and kickers table sport which was a refreshing atmosphere in my hard times. I am thankful for the IEK-7 student friendly gatherings organized mostly by Isabell, Cornelia and Dina. I always cherish those conversations with Moha, Aurëlion and Lukas. I am thankful to friendly discussions from Luiba, Mengchu, Yun and Xiaolu. A special thanks to Irene for her pleasant friendship. And also to all others who ever I forgot for their presence in my memories from Forschungszentrum Jülich.

I am also very thankful to all colleagues of the IEK-7 theory group. All of you have been patient to answer my curious questions and being helpful when I needed your help.

I am highly grateful for the incessant support from my mother and my younger brother and all family members. They are a constant source of inspiration in all difficult times. Especially, heartiest thanks to all my lovely friends Manohar, Ravi and Ramya. All fellow Ph.D's from IEK-7 institute and also Ph.D's of research center from whom I have learned a lot.

I would like to thank the HITEC graduate school and their staff for the support and encouragement.

Due acknowledgments are to those incredible people, whose names have unintentionally been missed out despite their help with the completion of my thesis.

Bibliography

Ananthakrishnan, R. and Soman, M.: The onset of the southwest monsoon in 1990, Current Science, 61, 447–453, 1991.

Basha, G., Kishore, P., Ratnam, M. V., Ouarda, T. B., Velicogna, I., and Sutterley, T.: Vertical and latitudinal variation of the intertropical convergence zone derived using GPS radio occultation measurements, Remote Sensing of Environment, 163, 262–269, 2015.

Beck, J. W., Zhou, W., Li, C., Wu, Z., White, L., Xian, F., Kong, X., and An, Z.: A 550,000-year record of East Asian monsoon rainfall from 10Be in loess, Science, 360, 877–881, doi:10.1126/science.aam5825, URL https://science.sciencemag.org/content/360/6391/877, 2018.

Becker, G., Grooß, J.-U., McKenna, D. S., and Müller, R.: Stratospheric photolysis frequencies: Impact of an improved numerical solution of the radiative transfer equation, J. Atmos. Chem., 37, 217–229, doi:10.1023/A:1006468926530, 2000.

Bergman, J. W., Jensen, E. J., Pfister, L., and Yang, Q.: Seasonal differences of vertical-transport efficiency in the tropical tropopause layer: On the interplay between tropical deep convection, large-scale vertical ascent, and horizontal circulations, J. Geophys. Res., 117, doi:10.1029/2011JD016992, 2012.

Bergman, J. W., Fierli, F., Jensen, E. J., Honomichl, S., and Pan, L. L.: Boundary layer sources for the Asian anticyclone: Regional contributions to a vertical conduit, J. Geophys. Res., 118, 2560–2575, doi:10.1002/jgrd.50142, 2013.

Bian, J., Pan, L. L., Paulik, L., Vömel, H., and Chen, H.: In situ water vapor and ozone measurements in Lhasa and Kunmin during the Asian summer monsoon, Geophys. Res. Lett., 39, L19808, doi:10.1029/2012GL052996, 2012.

Bian, J., Li, D., Bai, Z., Li, Q., Lyu, D., and Zhou, X.: Transport of Asian surface pollutants to the global stratosphere from the Tibetan Plateau region during the Asian summer monsoon, Natl. Sci. Rev., 7, 516–533, doi:10.1093/nsr/nwaa005, URL https://doi.org/10.1093/nsr/nwaa005, 2020.

Boos, W. R. and Hurley, J. V.: Thermodynamic Bias in the Multimodel Mean Boreal Summer Monsoon, J. Climate, 26, 2279–2287, doi:10.1175/JCLI-D-12-00493.1, URL https://doi.org/10.1175/JCLI-D-12-00493.1, 2013.

Boos, W. R. and Kuang, Z.: Dominant control of the South Asian monsoon by orographic insulation versus plateau heating, Nature, 463, 218–222, doi:10.1038/nature08707, URL https://doi.org/10.1038/nature08707, 2010.

Brabec, M., Wienhold, F. G., Luo, B. P., Vömel, H., Immler, F., Steiner, P., Hausammann, E., Weers, U., and Peter, T.: Particle backscatter and relative humidity measured across cirrus clouds and comparison with microphysical cirrus modelling, Atmos. Chem. Phys., 12, 9135–9148, doi:10.5194/acp-12-9135-2012, URL http://www.atmos-chem-phys.net/12/9135/2012/, 2012.

Brewer, A. W.: Evidence for a world circulation provided by the measurements of helium and water vapour distribution in the stratosphere, Q. J. R. Meteorol. Soc., 75, 351–363, doi:10.1002/qj.49707532603, 1949.

Brunamonti, S.: Balloon-borne measurements of temperature, water vapor, ozone and aerosol backscatter at the southern slopes of the Himalayas, Ph.D. thesis, ETH Zurich, dISS. ETH NO. 25203, 2018.

Brunamonti, S., Jorge, T., Oelsner, P., Hanumanthu, S., Singh, B. B., Kumar, K. R., Sonbawne, S., Meier, S., Singh, D., Wienhold, F. G., Luo, B. P., Boettcher, M., Poltera, Y., Jauhiainen, H., Kayastha, R., Karmacharya, J., Dirksen, R., Naja, M., Rex, M., Fadnavis, S., and Peter, T.: Balloon-borne measurements of temperature, water vapor, ozone and aerosol backscatter on the southern slopes of the Himalayas during StratoClim 2016–2017, Atmos. Chem. Phys., 18, 15 937–15 957, doi:10.5194/acp-18-15937-2018, URL https://www.atmos-chem-phys.net/18/15937/2018/, 2018.

Brunamonti, S., Füzér, L., Jorge, T., Poltera, Y., Oelsner, P., Meier, S., Dirksen, R., Naja, M., Fadnavis, S., Karmacharya, J., Wienhold, F. G., Luo, B. P., Wernli, H., and Peter, T.: Water Vapor in the Asian Summer Monsoon Anticyclone: Comparison of

Balloon-Borne Measurements and ECMWF Data, J. Geophys. Res., 124, 7053–7068, doi:10.1029/2018JD030000, URL https://agupubs.onlinelibrary.wiley.com/doi/abs/10.1029/2018JD030000, 2019.

Bucholtz, A.: Rayleigh-scattering calculations for the terrestrial atmosphere, Appl. Optics, 34, 1995.

Byrne, M. P., Pendergrass, A. G., Rapp, A. D., and Wodzicki, K. R.: Response of the Intertropical Convergence Zone to Climate Change: Location, Width, and Strength, Current Climate Change Reports, doi:10.1007/s40641-018-0110-5, URL https://doi.org/10.1007/s40641-018-0110-5, 2018.

Chowdary, J. S. and Gnanaseelan, C.: Basin-wide warming of the Indian Ocean during El Niño and Indian Ocean dipole years, Int. J. Climatol., 27, 1421–1438, doi:10.1002/joc.1482, URL https://rmets.onlinelibrary.wiley.com/doi/abs/10.1002/joc.1482, 2007.

Chowdary, J. S., Chaudhari, H. S., Gnanaseelan, C., Parekh, A., Suryachandra Rao, A., Sreenivas, P., Pokhrel, S., and Singh, P.: Summer monsoon circulation and precipitation over the tropical Indian Ocean during ENSO in the NCEP climate forecast system, Climate Dynamics, 42, doi:10.1007/s00382-013-1826-5, URL https://doi.org/10.1007/s00382-013-1826-5, 2014.

Chowdary, J. S., Harsha, H. S., Gnanaseelan, C., Srinivas, G., Parekh, A., Pillai, P., and Naidu, C. V.: Indian summer monsoon rainfall variability in response to differences in the decay phase of El Niño, Climate Dynamics, 48, doi:10.1007/s00382-016-3233-1, URL https://doi.org/10.1007/s00382-016-3233-1, 2017.

Cirisan, A., Luo, B. P., Engel, I., Wienhold, F. G., Sprenger, M., Krieger, U. K., Weers, U., Romanens, G., Levrat, G., Jeannet, P., Ruffieux, D., Philipona, R., Calpini, B., Spichtinger, P., and Peter, T.: Balloon-borne match measurements of midlatitude cirrus clouds, Atmos. Chem. Phys., 14, 7341–7365, doi:10.5194/acp-14-7341-2014, URL https://www.atmos-chem-phys.net/14/7341/2014/, 2014.

Cook, E. R., Anchukaitis, K. J., Buckley, B. M., Arrigo, R. D. D., Jacoby, G. C., and Wright, W. E.: Asian monsoon failure and mega drought during the last millennium., Science, 486, 486–490, doi:10.1126/science.1185188, URL https://agupubs.onlinelibrary.wiley.com/doi/abs/10.1029/2018JD029703, 2010.

Dee, D. P., Uppala, S. M., Simmons, A. J., Berrisford, P., Poli, P., Kobayashi, S., Andrae, U., Balmaseda, M. A., Balsamo, G., Bauer, P., Bechtold, P., Beljaars, A. C. M., van de Berg, L., Bidlot, J., Bormann, N., Delsol, C., Dragani, R., Fuentes, M., Geer, A. J., Haimberger, L., Healy, S. B., Hersbach, H., Hólm, E. V., Isaksen, L., Kållberg, P., Köhler, M., Matricardi, M., McNally, A. P., Monge-Sanz, B. M., Morcrette, J.-J., Park, B.-K., Peubey, C., de Rosnay, P., Tavolato, C., Thépaut, J.-N., and Vitart, F.: The ERA-Interim reanalysis: configuration and performance of the data assimilation system, Q. J. R. Meteorol. Soc., 137, 553–597, doi:10.1002/qj.828, 2011.

Deshler, T., Hervig, M. E., Hofmann, D. J., Rosen, J. M., and Liley, J. B.: Thirty years of in situ stratospheric aerosol size distribution measurements from Laramie, Wyoming (41 degrees N), using balloon-borne instruments, J. Geophys. Res., 108, 4167, doi:10.1029/2002JD002514, 2003.

Dirksen, R. J., Sommer, M., Immler, F. J., Hurst, D. F., Kivi, R., and Vömel, H.: Reference quality upper-air measurements: GRUAN data processing for the Vaisala RS92 radiosonde, Atmospheric Measurement Techniques, 7, 4463–4490, doi:10.5194/amt-7-4463-2014, URL https://www.atmos-meas-tech.net/7/4463/2014/, 2014.

Dunkerton, T. J.: Evidence of meridional motion in the summer lower stratosphere adjacent to monsoon regions, J. Geophys. Res., 100, 16,675–16,688, 1995.

Engel, I., Luo, B. P., Khaykin, S. M., Wienhold, F. G., Vömel, H., Kivi, R., Hoyle, C. R., Grooß, J.-U., Pitts, M. C., and Peter, T.: Arctic stratospheric dehydration – Part 2: Microphysical modeling, Atmos. Chem. Phys., 14, 3231–3246, doi:10.5194/acp-14-3231-2014, URL http://www.atmos-chem-phys.net/14/3231/2014/, 2014.

Fadnavis, S., Semeniuk, K., Pozzoli, L., Schultz, M. G., Ghude, S. D., Das, S., and Kakatkar, R.: Transport of aerosols into the UTLS and their impact on the Asian monsoon region as seen in a global model simulation, Atmos. Chem. Phys., 13, 8771–8786, doi:10.5194/acp-13-8771-2013, 2013.

Fadnavis, S., Roy, C., Chattopadhyay, R., Sioris, C. E., Rap, A., Müller, R., Kumar, K. R., and Krishnan, R.: Transport of trace gases via eddy shedding from the Asian summer monsoon anticyclone and associated impacts on ozone heating rates, Atmos. Chem. Phys., 18, 11 493–11 506, doi:10.5194/acp-18-11493-2018, URL https://www.atmos-chem-phys.net/18/11493/2018/, 2018.

Fadnavis, S., Müller, R., Kalita, G., Rowlinson, M., Rap, A., Li, J.-L. F., Gasparini, B., and Laakso, A.: The impact of recent changes in Asian anthropogenic emissions of SO_2 on sulfate loading in the upper troposphere and lower stratosphere and the associated radiative changes, Atmos. Chem. Phys., 19, 9989–10 008, doi:{10.5194/acp-19-9989-2019}, 2019a.

Fadnavis, S., Sabin, T. P., Roy, C., Rowlinson, M., Rap, A., Vernier, J.-P., and Sioris, C. E.: Elevated aerosol layer over South Asia worsens the Indian drought, Sci. Rep., 9, 10268, doi:10.1038/s41598-019-46704-9, 2019b.

Fahey, D. W., Gao, R.-S., Möhler, O., Saathoff, H., Schiller, C., Ebert, V., Krämer, M., Peter, T., Amarouche, N., Avallone, L. M., Bauer, R., Bozóki, Z., Christensen, L. E., Davis, S. M., Durry, G., Dyroff, C., Herman, R. L., Hunsmann, S., Khaykin, S. M., Mackrodt, P., Meyer, J., Smith, J. B., Spelten, N., Troy, R. F., Vömel, H., Wagner, S., and Wienhold, F. G.: The AquaVIT-1 intercomparison of atmospheric water vapor measurement techniques, Atmospheric Measurement Techniques, 7, 3177–3213, doi:10.5194/amt-7-3177-2014, URL https://amt.copernicus.org/articles/7/3177/2014/, 2014.

Fairlie, D., Vernier, J.-P., Natarajan, M., and Bedka, K. M.: Dispersion of the Nabro volcanic plume and its relation to the Asian summer monsoon, Atmos. Chem. Phys., 14, 7045–7057, doi:10.5194/acp-14-7045-2014, 2014.

Fairlie, T. D., Liu, H., Vernier, J.-P., Campuzano-Jost, P., Jimenez, J. L., Jo, D. S., Zhang, B., Natarajan, M., Avery, M. A., and Huey, G.: Estimates of Regional Source Contributions to the Asian Tropopause Aerosol Layer Using a Chemical Transport Model, J. Geophys. Res., 125, e2019JD031 506, doi:10.1029/2019JD031506, URL https://agupubs.onlinelibrary.wiley.com/doi/abs/10.1029/2019JD031506, e2019JD031506 2019JD031506, 2020.

Fu, Q. and Lin, P.: Poleward Shift of Subtropical Jets Inferred from Satellite-Observed Lower-Stratospheric Temperatures, J. Climate, 24, 5597–5603, doi:10.1175/JCLI-D-11-00027.1, URL https://doi.org/10.1175/JCLI-D-11-00027.1, 2011.

Fu, R., Hu, Y., Wright, J. S., Jiang, J. H., Dickinson, R. E., Chen, M., Filipiak, M., Read, W. G., Waters, J. W., and Wu, D. L.: Short circuit of water vapor and polluted air to the global stratosphere by convective transport over Tibetian Plateau, Proc. Nat. Acad. Sci., 103, 5664–5669, 2006.

Fueglistaler, S., Dessler, A. E., Dunkerton, T. J., Folkins, I., Fu, Q., and Mote, P. W.: Tropical tropopause layer, Rev. Geophys., 47, RG1004, doi:10.1029/2008RG000267, 2009.

Gao, R. S., Telg, H., McLaughlin, R. J., Ciciora, S. J., Watts, L. A., Richardson, M. S., Schwarz, J. P., Perring, A. E., Thornberry, T. D., Rollins, A. W., Markovic, M. Z., Bates, T. S., Johnson, J. E., and Fahey, D. W.: A light-weight, high-sensitivity particle spectrometer for PM2.5 aerosol measurements, Aerosol Science and Technology, 50, 88–99, doi:10.1080/02786826.2015.1131809, URL https://doi.org/10.1080/02786826.2015.1131809, 2016.

Garny, H. and Randel, W. J.: Transport pathways from the Asian monsoon anticyclone to the stratosphere, Atmos. Chem. Phys., 16, 2703–2718, doi:10.5194/acp-16-2703-2016, 2016.

Gettelman, A. and de Forster, P. M.: Definition and climatology of the tropical tropopause layer, J. Meteorol. Soc. Jpn., 80, 911–924, 2002.

Gettelman, A., Hoor, P., Pan, L. L., Randel, W. J., Hegglin, M. I., and Birner, T.: The extratropical upper troposphere and lower stratosphere, Rev. Geophys., 49, RG3003, doi:10.1029/2011RG000355, 2011.

Grooß, J.-U. and Müller, R.: Simulation of the record Arctic stratospheric ozone depletion in 2020, J. Geophys. Res. A, 126, e2020JD033 339, doi:https://doi.org/10.1029/2020JD033339, URL https://agupubs.onlinelibrary.wiley.com/doi/abs/10.1029/2020JD033339, e2020JD033339 2020JD033339, 2021.

Grooß, J.-U., Konopka, P., and Müller, R.: Ozone chemistry during the 2002 Antarctic vortex split, J. Atmos. Sci., 62, 860–870, 2005.

Grooß, J.-U., Brautzsch, K., Pommrich, R., Solomon, S., and Müller, R.: Stratospheric ozone chemistry in the Antarctic: What controls the lowest values that can be reached and their recovery?, Atmos. Chem. Phys., 11, 12 217–12 226, 2011.

Grooß, J.-U., Müller, R., Spang, R., Tritscher, I., Wegner, T., Chipperfield, M. P., Feng, W., Kinnison, D. E., and Madronich, S.: On the discrepancy of HCl processing in the core of the wintertime polar vortices, Atmos. Chem. Phys., pp. 8647–8666, doi:10.5194/acp-18-8647-2018, 2018.

Gu, Y., Liao, H., and Bian, J.: Summertime nitrate aerosol in the upper troposphere and lower stratosphere over the Tibetan Plateau and the South Asian summer monsoon region, Atmos. Chem. Phys., 16, 6641–6663, doi:10.5194/acp-16-6641-2016, URL https://www.atmos-chem-phys.net/16/6641/2016/, 2016.

Hall, E. G., Jordan, A. F., Hurst, D. F., Oltmans, S. J., Vömel, H., Kühnreich, B., and Ebert, V.: Advancements, measurement uncertainties, and recent comparisons of the NOAA frost point hygrometer, Atmospheric Measurement Techniques, 9, 4295–4310, doi: 10.5194/amt-9-4295-2016, URL https://www.atmos-meas-tech.net/9/4295/2016/, 2016.

Hanumanthu, S., Vogel, B., Müller, R., Brunamonti, S., Fadnavis, S., Li, D., Ölsner, P., Naja, M., Singh, B. B., Kumar, K. R., Sonbawne, S., Jauhiainen, H., Vömel, H., Luo, B., Jorge, T., Wienhold, F. G., Dirkson, R., and Peter, T.: Strong variability of the Asian Tropopause Aerosol Layer (ATAL) in August 2016 at the Himalayan foothills, Atmos. Chem. Phys., 20, 14 273–14 302, doi:10.5194/acp-20-14273-2020, URL https://acp.copernicus.org/articles/20/14273/2020/, 2020.

Hersbach, H., Bell, B., Berrisford, P., Hirahara, S., Horányi, A., Muñoz Sabater, J., Nicolas, J., Peubey, C., Radu, R., Schepers, D., Simmons, A., Soci, C., Abdalla, S., Abellan, X., Balsamo, G., Bechtold, P., Biavati, G., Bidlot, J., Bonavita, M., De Chiara, G., Dahlgren, P., Dee, D., Diamantakis, M., Dragani, R., Flemming, J., Forbes, R., Fuentes, M., Geer, A., Haimberger, L., Healy, S., Hogan, R. J., Hólm, E., Janisková, M., Keeley, S., Laloyaux, P., Lopez, P., Lupu, C., Radnoti, G., de Rosnay, P., Rozum, I., Vamborg, F., Villaume, S., and Thépaut, J.-N.: The ERA5 global reanalysis, Q. J. R. Meteorol. Soc., 146, 1999–2049, doi:10.1002/qj.3803, URL https://rmets.onlinelibrary.wiley.com/doi/abs/10.1002/qj.3803, 2020.

Hoinka, K. P.: The tropopause: discovery, definition and demarcation, Meteorol. Z., 6, 281–303, 1997.

Homeyer, C. R. and Bowman, K. P.: Rossby Wave Breaking and Transport between the Tropics and Extratropics above the Subtropical Jet, J. Atmos. Sci., 70, 607–626, 2013.

Hong, Y., Liu, G., and Li, J.-L. F.: Assessing the Radiative Effects of Global Ice Clouds Based on CloudSat and CALIPSO Measurements, J. Climate, 29, 7651–7674, doi:10.1175/JCLI-D-15-0799.1, URL https://doi.org/10.1175/JCLI-D-15-0799.1, 2016.

Höpfner, M., Ungermann, J., Borrmann, S., Wagner, R., Spang, R., Riese, M., Stiller, G., Appel, O., Batenburg, A. M., Bucci, S., Cairo, F., Dragoneas, A., Friedl-Vallon, F., Hünig, A., Johansson, S., Krasauskas, L., Legras, B., Leisner, T., Mahnke, C., Möhler, O., Molleker, S., Müller, R., Neubert, T., Orphal, J., Preusse, P., Rex, M., Saathoff, H., Stroh, F., Weigel, R., and Wohltmann, I.: Ammonium nitrate particles formed in upper troposphere from

ground ammonia sources during Asian monsoons, Nature Geoscience, 12, 608–612, doi: {10.1038/s41561-019-0385-8}, 2019.

Hosking, J. S., Russo, M. R., Braesicke, P., and Pyle, J. A.: Tropical convective transport and the Walker circulation, Atmos. Chem. Phys., 12, 9791–9797, doi:10.5194/acp-12-9791-2012, URL https://www.atmos-chem-phys.net/12/9791/2012/, 2012.

Hoskins, B. J. and Ambrizzi, T.: Rossby wave propagation on a realistic longitudinally varying flow, Journal of the atmospheric sciences, 50, 1661–1671, 1993.

Hoskins, B. J. and Rodwell, M. J.: A model of the Asian summer monsoon, I, The global scale, J. Atmos. Sci., 52, 1329–1340, 1995.

Houze Jr., R. A., Wilton, D. C., and Smull, B. F.: Monsoon convection in the Himalayan region as seen by the TRMM Precipitation Radar, Q. J. R. Meteorol. Soc., 133, 1389–1411, doi:10.1002/qj.106, URL https://rmets.onlinelibrary.wiley.com/doi/abs/10.1002/qj.106, 2007.

Huffman, G. J., Bolvin, D. T., Nelkin, E. J., Wolff, D. B., Adler, R. F., Gu, G., Hong, Y., Bowman, K. P., and Stocker, E. F.: The TRMM Multisatellite Precipitation Analysis (TMPA): Quasi-Global, Multiyear, Combined-Sensor Precipitation Estimates at Fine Scales, Journal of Hydrometeorology, 8, 38–55, doi:10.1175/JHM560.1, URL https://doi.org/10.1175/JHM560.1, 2007.

IMD: India Meteorological Department: 2016 Southwest Monsoon End of Season Report, URL https://www.tropmet.res.in/~kolli/MOL/Monsoon/year2016/Monsoon-2016.pdf, 2016.

iMet: InterMet: iMet-1-RS 403 MHz Research Radiosonde, 2006.

Jorge, T., Brunamonti, S., Poltera, Y., Wienhold, F. G., Luo, B. P., Oelsner, P., Hanumanthu, S., Singh, B. B., Meier, S., Dirksen, R., Naja, M., Fadnavis, S., and Peter, T.: Understanding water vapour concentrations measured by cryogenic frost point hygrometers after contamination by mixed-phase clouds, amt, 2021.

Kang, S. M., Shin, Y., and Xie, S.-P.: Extratropical forcing and tropical rainfall distribution: energetics framework and ocean Ekman advection, npj Climate and Atmospheric Science, doi:10.1038/s41612-017-0004-6, URL https://doi.org/10.1038/s41612-017-0004-6, 2018.

Khaykin, S. M., Engel, I., Vömel, H., Formanyuk, I. M., Kivi, R., Korshunov, L. I., Krämer, M., Lykov, A. D., Meier, S., Naebert, T., Pitts, M. C., Santee, M. L., Spelten, N., Wienhold, F. G., Yushkov, V. A., and Peter, T.: Arctic stratospheric dehydration - Part 1: Unprecedented observation of vertical redistribution of water, Atmos. Chem. Phys., 13, 11 503–11 517, doi:10.5194/acp-13-11503-2013, 2013.

Komhyr, W. D.: Electrocemical concentration cells for gas analysis, Ann. Geophys., 25, 203, 1969.

Komhyr, W. D., Barnes, R. A., Brothers, G. B., Lathrop, J. A., and Opperman, D. P.: Electrochemical concentration cell ozonesonde performance evaluation during STOIC 1989, jgr, 100, 9231–9244, doi:10.1029/94JD02175, 1995.

Konopka, P., Günther, G., Müller, R., dos Santos, F. H. S., Schiller, C., Ravegnani, F., Ulanovsky, A., Schlager, H., Volk, C. M., Viciani, S., Pan, L. L., McKenna, D.-S., and Riese, M.: Contribution of mixing to upward transport across the tropical tropopause layer (TTL), Atmos. Chem. Phys., 7, 3285–3308, 2007.

Konopka, P., Grooß, J.-U., Plöger, F., and Müller, R.: Annual cycle of horizontal in-mixing into the lower tropical stratosphere, J. Geophys. Res., 114, D19111, doi:10.1029/2009JD011955, 2009.

Konopka, P., Tao, M., Ploeger, F., Diallo, M., and Riese, M.: Tropospheric mixing and parametrization of unresolved convective updrafts as implemented in the Chemical Lagrangian Model of the Stratosphere (CLaMS v2.0), Geosci. Model Dev., 12, 2441–2462, doi:10.5194/gmd-12-2441-2019, URL https://www.geosci-model-dev.net/12/2441/2019/, 2019.

Krämer, M., Rolf, C., Luebke, A., Afchine, A., Spelten, N., Costa, A., Meyer, J., Zöger, M., Smith, J., Herman, R. L., Buchholz, B., Ebert, V., Baumgardner, D., Borrmann, S., Klingebiel, M., and Avallone, L.: A microphysics guide to cirrus clouds – Part 1: Cirrus types, Atmos. Chem. Phys., 16, 3463–3483, doi:10.5194/acp-16-3463-2016, URL https://www.atmos-chem-phys.net/16/3463/2016/, 2016.

Krishnamurti, T. N. and Bhalme, H. N.: Oscillations of a Monsoon System. Part I. Observational Aspects., J. Atmos. Sci., 33, 1937–1954, doi:10.1175/1520-0469(1976)033<1937:OOAMSP>2.0.CO;2, 1976.

Krishnan, T. P., Sabin, R., Vellore, M., Mujumdar, J., Sanjay, B. N., Goswami, F., Hourdin, J.-L., and Terray., D. P.: Deciphering the desiccation trend of the South Asian monsoon hydro climate in a warming world, Climate Dynamics, 47, 1007–1027, doi: 10.1007/s00382-015-2886-5, URL https://doi.org/10.1007/s00382-015-2886-5, 2016.

Kumar, K. K., Soman, M. K., and Kumar, K. R.: Seasonal forecasting of Indian summer monsoon rainfall: A review, Weather, 50, 449–467, doi:10.1002/j.1477-8696.1995.tb06071.x, URL https://rmets.onlinelibrary.wiley.com/doi/abs/10.1002/j.1477-8696.1995.tb06071.x, 1995.

Kunz, A., Pan, L. L., Konopka, P., Kinnison, D. E., and Tilmes, S.: Chemical and dynamical discontinuity at the extratropical tropopause based on START08 and WACCM analyses, J. Geophys. Res., 116, doi:10.1029/2011JD016686, 2011.

Kunze, M., Braesicke, P., Langematz, U., Stiller, G., Bekki, S., Brühl, C., Chipperfield, M., Dameris, M., Garcia, R., and Giorgetta, M.: Influences of the Indian summer monsoon on water vapor and ozone concentrations in the UTLS as simulated by chemistry-climate models, J. Climate, 23, 3525–3544, 2010.

Lau, W. K. M., Yuan, C., and Li, Z.: Origin, Maintenance and Variability of the Asian Tropopause Aerosol Layer (ATAL): The Roles of Monsoon Dynamics, Sci. Rep., 8, 3960, 2018.

Li, D., Vogel, B., Bian, J., Müller, R., Pan, L. L., Günther, G., Bai, Z., Li, Q., Zhang, J., Fan, Q., and Vömel, H.: Impact of typhoons on the composition of the upper troposphere within the Asian summer monsoon anticyclone: the SWOP campaign in Lhasa 2013, Atmos. Chem. Phys., 17, 4657–4672, 2017.

Li, D., Vogel, B., Müller, R., Bian, J., Günther, G., Li, Q., Zhang, J., Bai, Z., Vömel, H., and Riese, M.: High tropospheric ozone in Lhasa within the Asian summer monsoon anticyclone in 2013: influence of convective transport and stratospheric intrusions, Atmos. Chem. Phys., 18, 17 979–17 994, doi:10.5194/acp-18-17979-2018, URL https://www.atmos-chem-phys.net/18/17979/2018/, 2018.

Li, D., Vogel, B., Müller, R., Bian, J., Günther, G., Ploeger, F., Li, Q., Zhang, J., Bai, Z., Vömel, H., and Riese, M.: Dehydration and low ozone in the tropopause layer over

the Asian monsoon caused by tropical cyclones: Lagrangian transport calculations using ERA-Interim and ERA5 reanalysis data, Atmos. Chem. Phys., 20, 4133–4152, doi:10.5194/acp-20-4133-2020, URL https://www.atmos-chem-phys.net/20/4133/2020/, 2020.

Li, Q., Jiang, J. H., Wu, D. L., Read, W. G., Livesey, N. J., Waters, J. W., Zhang, Y., Wang, B., Filipiak, M. J., Davis, C. P., Turquety, S., Wu, S., Park, R. J., Yantosca, R. M., and Jacob, D. J.: Convective outflow of South Asian pollution: A global CTM simulation compared with EOS MLS observations, Geophys. Res. Lett., 32, L14 826, doi:10.1029/2005GL022762, 2005.

Liu, Y., Wang, Y., Liu, X., Cai, Z., and Chance, K.: Tibetan middle tropospheric ozone minimum in June discovered from GOME observations, Geophys. Res. Lett., 36, L05814, doi:10.1029/2008GL037056, 2009.

Luo, J., Pan, L. L., Honomichl, S. B., Bergman, J. W., Randel, W. J., Francis, G., Clerbaux, C., George, M., Liu, X., and Tian, W.: Space–time variability in UTLS chemical distribution in the Asian summer monsoon viewed by limb and nadir satellite sensors, Atmos. Chem. Phys., 18, 12 511–12 530, doi:10.5194/acp-18-12511-2018, URL https://www.atmos-chem-phys.net/18/12511/2018/, 2018.

Mahowald, N. M., Plumb, R. A., Rasch, P. J., del Corral, J., and Sassi, F.: Stratospheric transport in a three-dimensional isentropic coordinate model, J. Geophys. Res., 107, 4254, doi:10.1029/2001JD001313, 2002.

Martinsson, B. G., Friberg, J., Andersson, S. M., Weigelt, A., Hermann, M., Assmann, D., Voigtländer, J., Brenninkmeijer, C. A. M., van Velthoven, P. J. F., and Zahn, A.: Comparison between CARIBIC Aerosol Samples Analysed by Accelerator-Based Methods and Optical Particle Counter Measurements, Atmos. Meas. Tech., 7, 2581–2596, doi:10.5194/amt-7-2581-2014, URL https://www.atmos-meas-tech.net/7/2581/2014/, 2014.

Mastenbrook, H. J. and Dinger, J. E.: Distribution of water vapor in the stratosphere, J. Geophys. Res., 66, 1437–1444, doi:10.1029/JZ066i005p01437, URL https://agupubs.onlinelibrary.wiley.com/doi/abs/10.1029/JZ066i005p01437, 1961.

Matsuura, T., Yumoto, M., and Iizuka, S.: A mechanism of interdecadal variability of tropical cyclone activity over the western North Pacific, Clim. Dyn., 21, 105–117, doi:10.1007/s00382-003-0327-3, 2003.

McIntyre, M. E. and Palmer, T. N.: The 'surf zone' in the stratosphere, J. Atmos. Terr. Phys., 46, 825–849, 1984.

McKenna, D. S., Grooß, J.-U., Günther, G., Konopka, P., Müller, R., Carver, G., and Sasano, Y.: A new Chemical Lagrangian Model of the Stratosphere (CLaMS): 2. Formulation of chemistry scheme and initialization, J. Geophys. Res., 107, 4256, doi:10.1029/2000JD000113, 2002a.

McKenna, D. S., Konopka, P., Grooß, J.-U., Günther, G., Müller, R., Spang, R., Offermann, D., and Orsolini, Y.: A new Chemical Lagrangian Model of the Stratosphere (CLaMS): 1. Formulation of advection and mixing, J. Geophys. Res., 107, 4309, doi:10.1029/2000JD000114, 2002b.

Miao, Y., Herrmann, M., Wu, F., Yan, X., and Yang, S.: What controlled Mid-Late Miocene long-term aridification in Central Asia? - Global cooling or Tibetan Plateau uplift: A review, Earth-Science Reviews, 112, 155 – 172, doi:https://doi.org/10.1016/j.earscirev.2012.02.003, URL http://www.sciencedirect.com/science/article/pii/S0012825212000141, 2012.

Mishra, V., Tiwari, A. D., Aadhar, S., Shah, R., Xiao, M., Pai, D. S., and Lettenmaier, D.: Drought and Famine in India, 1870-2016, Geophysical Research Letters, 46, 2075–2083, doi:10.1029/2018GL081477, URL https://agupubs.onlinelibrary.wiley.com/doi/abs/10.1029/2018GL081477, 2019.

Müller, R., Grooß, J.-U., Lemmen, C., Heinze, D., Dameris, M., and Bodeker, G.: Simple measures of ozone depletion in the polar stratosphere, Atmos. Chem. Phys., 8, 251–264, 2008.

Müller, S., Hoor, P., Bozem, H., Gute, E., Vogel, B., Zahn, A., Bönisch, H., Keber, T., Krämer, M., Rolf, C., Riese, M., Schlager, H., and Engel, A.: Impact of the Asian monsoon on the extratropical lower stratosphere: trace gas observations during TACTS over Europe 2012, Atmos. Chem. Phys., 16, 10 573–10 589, doi:10.5194/acp-16-10573-2016, 2016.

Murphy, D. M. and Koop, T.: Review of the vapour pressures of ice and supercooled water for atmospheric applications, Q. J. R. Meteorol. Soc., 131, 1539–1565, 2005.

Ninomiya, K. and Shibagaki, Y.: Multi-scale features of the Meiyu-Baiu front and associated precipitation systems, J. Meteorol. Soc. Japan, 85B, 103–122, doi:10.2151/jmsj.85B.103, 2007.

Nützel, M., Dameris, M., and Garny, H.: Movement, drivers and bimodality of the South Asian High, Atmos. Chem. Phys., 16, 14 755–14 774, doi:10.5194/acp-16-14755-2016, URL https://www.atmos-chem-phys.net/16/14755/2016/, 2016.

Pan, L. L., Honomichl, S. B., Kinnison, D. E., Abalos, M., Randel, W. J., Bergman, J. W., and Bian, J.: Transport of chemical tracers from the boundary layer to stratosphere associated with the dynamics of the Asian summer monsoon, J. Geophys. Res., 121, doi:10.1002/2016JD025616, 2016.

Pan, L. L., Honomichl, S. B., Bui, T. V., Thornberry, T., Rollins, A., Hintsa, E., and Jensen, E. J.: Lapse Rate or Cold Point: The Tropical Tropopause Identified by In Situ Trace Gas Measurements, Geophys. Res. Lett., 45, 10 756–10 763, doi:10.1029/2018GL079573, URL https://agupubs.onlinelibrary.wiley.com/doi/abs/10.1029/2018GL079573, 2018.

Park, M., Randel, W. J., Gettleman, A., Massie, S. T., and Jiang, J. H.: Transport above the Asian summer monsoon anticyclone inferred from Aura Microwave Limb Sounder tracers, J. Geophys. Res., 112, D16309, doi:10.1029/2006JD008294, 2007.

Park, M., Randel, W. J., Emmons, L. K., Bernath, P. F., Walker, K. A., and Boone, C. D.: Chemical isolation in the Asian monsoon anticyclone observed in Atmospheric Chemistry Experiment (ACE-FTS) data, Atmos. Chem. Phys., 8, 757–764, 2008.

Park, M., Randel, W. J., Emmons, L. K., and Livesey, N. J.: Transport pathways of carbon monoxide in the Asian summer monsoon diagnosed from Model of Ozone and Related Tracers (MOZART), J. Geophys. Res., 114, D08303, doi:10.1029/2008JD010621, 2009.

Passmore, R.: Famine in India: An historical survey, The Lancet, 258, 303 – 307, doi:https://doi.org/10.1016/S0140-6736(51)93295-3, URL http://www.sciencedirect.com/science/article/pii/S0140673651932953, originally published as Volume 2, Issue 6677, 1951.

Ploeger, F., Konopka, P., Günther, G., Grooß, J.-U., and Müller, R.: Impact of the vertical velocity scheme on modeling transport across the tropical tropopause layer, J. Geophys. Res., 115, D03301, doi:10.1029/2009JD012023, 2010.

Ploeger, F., Konopka, P., Müller, R., Günther, G., Grooß, J.-U., Schiller, C., Ravegnani, F., Ulanovski, A., and Riese, M.: Backtrajectory reconstruction of water vapour and ozone in-situ observations in the TTL, Meteorol. Z., 21, 239–244, 2012.

Ploeger, F., Günther, G., Konopka, P., Fueglistaler, S., Müller, R., Hoppe, C., Kunz, A., Spang, R., Grooß, J.-U., and Riese, M.: Horizontal water vapor transport in the lower stratosphere from subtropics to high latitudes during boreal summer, J. Geophys. Res., 118, 8111–8127, doi:10.1002/jgrd.50636, 2013.

Ploeger, F., Gottschling, C., Grießbach, S., Grooß, J.-U., Günther, G., Konopka, P., Müller, R., Riese, M., Stroh, F., Tao, M., Ungermann, J., Vogel, B., and von Hobe, M.: A potential vorticity-based determination of the transport barrier in the Asian summer monsoon anticyclone, Atmos. Chem. Phys., 15, 13 145–13 159, doi:doi:10.5194/acp-15-13145-2015, 2015.

Ploeger, F., Legras, B., Charlesworth, E., Yan, X., Diallo, M., Konopka, P., Birner, T., Tao, M., Engel, A., and Riese, M.: How robust are stratospheric age of air trends from different reanalyses?, Atmos. Chem. Phys., 19, 6085–6105, doi:doi:10.5194/gmd-12-2441-2019, 2019.

Plumb, R. A.: A "tropical pipe" model of stratospheric transport, J. Geophys. Res., 101, 3957–3972, 1996.

Pommrich, R., Müller, R., Grooß, J.-U., Konopka, P., Ploeger, F., Vogel, B., Tao, M., Hoppe, C. M., Günther, G., Spelten, N., Hoffmann, L., Pumphrey, H.-C., Viciani, S., D'Amato, F., Volk, C. M., Hoor, P., Schlager, H., and Riese, M.: Tropical troposphere to stratosphere transport of carbon monoxide and long-lived trace species in the Chemical Lagrangian Model of the Stratosphere (CLaMS), Geosci. Model Dev., 7, 2895–2916, doi:10.5194/gmd-7-2895-2014, URL http://www.geosci-model-dev.net/7/2895/2014/, 2014.

Poshyvailo, L., Müller, R., Konopka, P., Günther, G., Riese, M., Podglajen, A., and Ploeger, F.: Sensitivities of modelled water vapour in the lower stratosphere: temperature uncertainty, effects of horizontal transport and small-scale mixing, Atmos. Chem. Phys., 18, 8505–8527, doi:10.5194/acp-18-8505-2018, URL https://www.atmos-chem-phys.net/18/8505/2018/, 2018.

Raghavan, K., Jayanarayanan, S., Gnanaseelan, C., Mujumdar, M., Kulkarni, A., and Chakraborty, S., eds.: Assessment of Climate Change over the Indian Region, Springer, doi:10.1007/978-981-15-4327-2, 2020.

Ramanathan, V., Chung, C., Kim, D., Bettge, T., Buja, L., Kiehl, J. T., Washington, W. M., Fu, Q., Sikka, D. R., and Wild, M.: Atmospheric brown clouds: Impacts on South Asian climate and hydrological cycle, Proceedings of the National Academy of Sciences, 102, 5326–5333, doi:10.1073/pnas.0500656102, URL https://www.pnas.org/content/102/15/5326, 2005.

Randel, W. J. and Park, M.: Deep convective influence on the Asian summer monsoon anticyclone and associated tracer variability observed with Atmospheric Infrared Sounder (AIRS), J. Geophys. Res., 111, D12314, doi:10.1029/2005JD006490, 2006.

Randel, W. J., Park, M., Emmons, L., Kinnison, D., Bernath, P., Walker, K. A., Boone, C., and Pumphrey, H.: Asian Monsoon Transport of Pollution to the Stratosphere, Science, 328, 611–613, doi:10.1126/science.1182274, 2010.

Randel, W. J., Zhang, K., and Fu, R.: What controls stratospheric water vapor in the NH summer monsoon regions?, J. Geophys. Res., 120, 7988–8001, doi:doi:10.1002/2015JD023622, 2015.

Rayner, N. A., Parker, D. E., Horton, E. B., Folland, C. K., Alexander, L. V., Rowell, D. P., Kent, E. C., and Kaplan, A.: Global analyses of sea surface temperatures, sea ice, and night marine air temperature since the late nineteenth century, J. Geophys. Res., 108, 4407, doi:10.1029/2002JD002670, 2003.

Ridley, D. A., Solomon, S., Barnes, J. E., Burlakov, V. D., Deshler, T., Dolgii, S. I., Herber, A. B., Nagai, T., Neely III, R. R., Nevzorov, A. V., Ritter, C., Sakai, T., Santer, B. D., Sato, M., Schmidt, A., Uchino, O., and Vernier, J. P.: Total volcanic stratospheric aerosol optical depths and implications for global climate change, Geophys. Res. Lett., 41, 7763–7769, doi:10.1002/2014GL061541, URL https://agupubs.onlinelibrary.wiley.com/doi/abs/10.1002/2014GL061541, 2014.

Rolf, C., Vogel, B., Hoor, P., Afchine, A., Günther, G., Krämer, M., Müller, R., Müller, S., Spelten, N., and Riese, M.: Water vapor increase in the lower stratosphere of the Northern Hemisphere due to the Asian monsoon anticyclone observed during the

TACTS/ESMVal campaigns, Atmospheric Chemistry and Physics, 18, 2973–2983, doi:10.5194/acp-18-2973-2018, URL https://www.atmos-chem-phys.net/18/2973/2018/, 2018.

Rosen, J. M. and Kjome, N. T.: Backscattersonde: a new instrument for atmospheric aerosol research, Appl. Opt., 30, 1552–1561, doi:10.1364/AO.30.001552, URL http://ao.osa.org/abstract.cfm?URI=ao-30-12-1552, 1991.

Rosenlof, K. H. and Reid, G. C.: Trends in the temperature and water vapor content of the tropical lower stratosphere: Sea surface connection, jgr, 113, 2008.

Roy, C., Fadnavis, S., Müller, R., Ayantika, D. C., Ploeger, F., and Rap, A.: Influence of enhanced Asian NO_x emissions on ozone in the upper troposphere and lower stratosphere in chemistry–climate model simulations, Atmos. Chem. Phys., 17, 1297 – 1311, doi:10.5194/acp-17-1297-2017, URL http://juser.fz-juelich.de/record/826977, 2017.

Santee, M. L., Manney, G. L., Livesey, N. J., Schwartz, M. J., Neu, J. L., and Read, W. G.: A comprehensive overview of the climatological composition of the Asian summer monsoon anticyclone based on 10 years of Aura Microwave Limb Sounder measurements, J. Geophys. Res., 122, 5491–5514, doi:10.1002/2016JD026408, URL https://agupubs.onlinelibrary.wiley.com/doi/abs/10.1002/2016JD026408, 2017.

Schiemann, R., Lüthi, D., and Schär, C.: Seasonality and interannual variability of the westerly jet in the Tibetan Plateau region, J. Climate, 22, 2940–2957, 2009.

Schiller, C., Grooß, J.-U., Konopka, P., Plöger, F., Silva dos Santos, F. H., and Spelten, N.: Hydration and dehydration at the tropical tropopause, Atmos. Chem. Phys., 9, 9647–9660, doi:10.5194/acp-9-9647-2009, 2009.

Schwierz, C., Dirren, S., and Davies, H. C.: Forced waves on a zonally aligned jet stream, Journal of the atmospheric sciences, 61, 73–87, 2004.

Simmons, A. J., D., J. P., Bechtold, V. D., Beljaars, A. C. M., Kallberg, P. W., Saarinen, S., Uppala, S. M., Viterbo, P., and Wedi, N.: Comparison of trends and low-frequency variability in CRU, ERA-40, and NCEP/NCAR analyses of surface air temperature, J. Geophys. Res., 109, D24115, 2004.

Singh, B. B., R, K., Choudhury, A. D., Vellore, R. K., Sabin, T. P., Brunamonti, S., Hanumanthu, S., Jorge, T., Ölsner, P., Naja, M., Sonbawne, S., Fadnavis, S., Peter, T., and Srivastava,

M. K.: Linkage of water vapor distribution in the lower stratosphere to organized Asian summer monsoon convection, Climate Dynamics, 2021.

Smit, H. G. J., Straeter, W., Johnson, B. J., Oltmans, S. J., Davies, J., Tarasick, D. W., Hoegger, B., Stubi, R., Schmidlin, F. J., Northam, T., Thompson, A. M., Witte, J. C., Boyd, I., and Posny, F.: Assessment of the performance of ECC-ozonesondes under quasi-flight conditions in the environmental simulation chamber: Insights from the Juelich Ozone Sonde Intercomparison Experiment (JOSIE), J. Geophys. Res., 112, D19306, doi:10.1029/2006jd007308, 2007.

Spang, R., Günther, G., Riese, M., Hoffmann, L., Müller, R., and Griessbach, S.: Satellite observations of cirrus clouds in the Northern Hemisphere lowermost stratosphere, Atmos. Chem. Phys., 15, 927–950, doi:10.5194/acp-15-927-2015, URL http://www.atmos-chem-phys.net/15/927/2015/, 2015.

Spicer, R. A.: Tibet, the Himalaya, Asian monsoons and biodiversity – In what ways are they related?, Plant Diversity, 39, 233 – 244, doi:https://doi.org/10.1016/j.pld.2017.09.001, URL http://www.sciencedirect.com/science/article/pii/S2468265917301142, 2017.

Stroh, F. and Team, T. S. C.: First detailed airborne and balloon measurements of microphysical, dynamical, and chemical processes in the Asian Summer Monsoon Anticyclone: Overview and First Results of the 2016/2017 StratoClim field campaigns, Atmos. Chem. Phys., to be submitted, 2020.

Sutton, R. T., Maclean, H., Swinbank, R., O'Neill, A., and Taylor, F. W.: High-resolution stratospheric tracer fields estimated from satellite observations using Lagrangian trajectory calculations, J. Atmos. Sci., 51, 2995–3005, 1994.

Terao, Y. and Logan, J. A.: Consistency of time series and trends of stratospheric ozone as seen by ozonesonde, SAGE II, HALOE, and SBUV(/2), J. Geophys. Res., 112, doi:10.1029/2006JD007667, 2007.

Thölix, L., Backman, L., Kivi, R., and Karpechko, A. Y.: Variability of water vapour in the Arctic stratosphere, Atmospheric Chemistry and Physics, 16, 4307–4321, doi:10.5194/acp-16-4307-2016, URL https://acp.copernicus.org/articles/16/4307/2016/, 2016.

Thomason, L. W. and Vernier, J.-P.: Improved SAGE II cloud/aerosol categorization and observations of the Asian tropopause aerosol layer: 1989–2005, Atmos. Chem. Phys., 13,

4605–4616, doi:10.5194/acp-13-4605-2013, URL https://www.atmos-chem-phys.net/13/4605/2013/, 2013.

Turner, A. G. and Annamalai, H.: Climate change and the South Asian summer monsoon, Nature Climate Change, 2, 587–595, doi:10.1038/nclimate1495, URL https://doi.org/10.1038/nclimate1495, 2012.

Ueyama, R., Jensen, E. J., and Pfister, L.: Convective Influence on the Humidity and Clouds in the Tropical Tropopause Layer During Boreal Summer, J. Geophys. Res., 123, 7576–7593, doi:10.1029/2018JD028674, URL https://agupubs.onlinelibrary.wiley.com/doi/abs/10.1029/2018JD028674, 2018.

Ungermann, J., Pan, L. L., Kalicinsky, C., Olschewski, F., Knieling, P., Blank, J., Weigel, K., Guggenmoser, T., Stroh, F., Hoffmann, L., and Riese, M.: Filamentary structure in chemical tracer distributions near the subtropical jet following a wave breaking event, Atmos. Chem. Phys., 13, 10 517–10 534, doi:10.5194/acp-13-10517-2013, 2013.

Ungermann, J., Ern, M., Kaufmann, M., Müller, R., Spang, R., Ploeger, F., Vogel, B., and Riese, M.: Observations of PAN and its confinement in the Asian Summer Monsoon Anticyclone in high spatial resolution, Atmos. Chem. Phys., 16, 8389–8403, doi:10.5194/acp-16-8389-2016, 2016.

Vaisala: Vaisala Vaisala DigiCORA Sounding System MW41, 2017.

van Damme, M., Clarisse, L., Whitburn, S., Hadji-Lazaro, J., Hurtmans, D., Clerbaux, C., and Coheur, P.-F.: Industrial and agricultural ammonia point sources exposed, Nature, 564, 99–103, doi:10.1038/s41586-018-0747-1, 2018.

van der A, R. J., Mijling, B., Ding, J., Koukouli, M. E., Liu, F., Li, Q., Mao, H., and Theys, N.: Cleaning up the air: effectiveness of air quality policy for SO_2 and NO_x emissions in China, Atmos. Chem. Phys., 17, 1775–1789, doi:10.5194/acp-17-1775-2017, URL https://www.atmos-chem-phys.net/17/1775/2017/, 2017.

Vellore Ramesh, K., Kaplan Michael, L., Krishnan, R., Lewis John, M., Sabade, S., Deshpande, N., Singh Bhupendra, B., Madhura, R. K., and Rama Rao, M. V. S.: Monsoon-extratropical circulation interactions in Himalayan extreme rainfall, Climate Dynamics, 46, doi:10.1007/s00382-015-2784-x, URL https://doi.org/10.1007/s00382-015-2784-x, 2016.

Vernier, J.-P., Thomason, L. W., and Kar, J.: CALIPSO detection of an Asian tropopause aerosol layer, Geophys. Res. Lett., 38, L07804, doi:10.1029/2010GL046614, 2011.

Vernier, J. P., Fairlie, T. D., Natarajan, M., Wienhold, F. G., Bian, J., Martinsson, B. G., Crumeyrolle, S., Thomason, L. W., and Bedka, K. M.: Increase in upper tropospheric and lower stratospheric aerosol levels and its potential connection with Asian pollution, J. Geophys. Res., 120, 1608–1619, doi:10.1002/2014JD022372, 2015.

Vernier, J.-P., Fairlie, T. D., Deshler, T., Ratnam, M. V., Gadhavi, H., Kumar, B. S., Natarajan, M., Pandit, A. K., Raj, S. T. A., Kumar, A. H., Jayaraman, A., Singh, A. K., Rastogi, N., Sinha, P. R., Kumar, S., Tiwari, S., Wegner, T., Baker, N., Vignelles, D., Stenchikov, G., Shevchenko, I., Smith, J., Bedka, K., Kesarkar, A., Singh, V., Bhate, J., Ravikiran, V., Rao, M. D., Ravindrababu, S., Patel, A., Vernier, H., Wienhold, F. G., Liu, H., Knepp, T. N., Thomason, L., Crawford, J., Ziemba, L., Moore, J., Crumeyrolle, S., Williamson, M., Berthet, G., Jégou, F., and Renard, J.-B.: BATAL: The Balloon Measurement Campaigns of the Asian Tropopause Aerosol Layer, Bull. Am. Meteorol. Soc., 99, 955–973, doi:10.1175/BAMS-D-17-0014.1, 2018.

Vogel, B., Müller, R., Deshler, T., Grooß, J.-U., Karhu, J., McKenna, D. S., Müller, M., Toohey, D., Toon, G. C., and Stroh, F.: Vertical profiles of activated ClO and ozone loss in the Arctic vortex in January and March 2000: In situ observations and model simulations, J. Geophys. Res., 108, 8334, doi:10.1029/2002JD002564, 2003.

Vogel, B., Günther, G., Müller, R., Grooß, J.-U., Hoor, P., Krämer, M., Müller, S., Zahn, A., and Riese, M.: Fast transport from Southeast Asia boundary layer sources to northern Europe: rapid uplift in typhoons and eastward eddy shedding of the Asian monsoon anticyclone, Atmos. Chem. Phys., 14, 12 745–12 762, doi:10.5194/acp-14-12745-2014, URL http://www.atmos-chem-phys.net/14/12745/2014/, 2014.

Vogel, B., Günther, G., Müller, R., Grooß, J.-U., and Riese, M.: Impact of different Asian source regions on the composition of the Asian monsoon anticyclone and of the extratropical lowermost stratosphere, Atmos. Chem. Phys., 15, 13 699–13 716, doi:10.5194/acp-15-13699-2015, URL http://www.atmos-chem-phys.net/15/13699/2015/, 2015.

Vogel, B., Günther, G., Müller, R., Grooß, J.-U., Afchine, A., Bozem, H., Hoor, P., Krämer, M., Müller, S., Riese, M., Rolf, C., Spelten, N., Stiller, G. P., Ungermann, J., and Zahn, A.: Long-range transport pathways of tropospheric source gases originating in Asia into the

northern lower stratosphere during the Asian monsoon season 2012, Atmos. Chem. Phys., 16, 15 301–15 325, doi:10.5194/acp-16-15301-2016, 2016.

Vogel, B., Müller, R., Günther, G., Spang, R., Hanumanthu, S., Li, D., Riese, M., and Stiller, G. P.: Lagrangian simulations of the transport of young air masses to the top of the Asian monsoon anticyclone and into the tropical pipe, Atmos. Chem. Phys., 19, 6007–6034, doi:10.5194/acp-19-6007-2019, URL https://www.atmos-chem-phys.net/19/6007/2019/, 2019.

Volk, C. M., Elkins, J. W., Fahey, D. W., Salawitch, R. J., Dutton, G. S., Gilligan, J. M., Proffitt, M. H., Loewenstein, M., Podolske, J. R., Minschwaner, K., Margitan, J. J., and Chan, K. R.: Quantifying transport between the tropical and mid-latitude lower stratosphere, Science, 272, 1763–1768, 1996.

Vömel, H., Oltmans, S. J., Kley, D., and Crutzen, P. J.: New evidence for stratospheric dehydration mechanism in the equatorial Pacific, Geophys. Res. Lett., 22, 3235 – 3238, 1995.

Vömel, H., Naebert, T., Dirksen, R., and Sommer, M.: An update on the uncertainties of water vapor measurements using cryogenic frost point hygrometers, Atmos. Meas. Tech., 9, 3755–3768, doi:10.5194/amt-9-3755-2016, 2016.

Vömel, H., David, D. E., and Smith, K.: Accuracy of tropospheric and stratospheric water vapor measurements by the cryogenic frost point hygrometer: Instrumental details and observations, J. Geophys. Res., 112, D08305, doi:{10.1029/2006JD007224}, 2007.

Vömel, H., Oltmans, S. J., Johnson, B. J., Hasebe, F., Shiotani, M., Fujiwara, M., Nishi, N., Agama, M., Cornejo, J., Paredes, F., and Enriquez, H.: Balloon-borne observations of water vapor and ozone in the tropical upper troposphere and lower stratosphere, Journal of Geophysical Research: Atmospheres, 107, ACL 8–1–ACL 8–16, doi:10.1029/2001JD000707, URL https://agupubs.onlinelibrary.wiley.com/doi/abs/10.1029/2001JD000707, 2002.

Walker, J. M., Bordoni, S., and Schneider, T.: Interannual variability in the large-scale dynamics of the South Asian summer monsoon, J. Climate, 28, 3731–3750, 2015.

Wang, B. and LinHo: Rainy Season of the Asian-Pacific Summer Monsoon, J. Climate, 15, 386–398, doi:10.1175/1520-0442(2002)015<0386:RSOTAP>2.0.CO;2, URL https://doi.org/10.1175/1520-0442(2002)015<0386:RSOTAP>2.0.CO;2, 2002.

Webster, P. J. and Yang, S.: Monsoon and Enso: Selectively Interactive Systems, Q. J. R. Meteorol. Soc., 118, 877–926, doi:10.1002/qj.49711850705, URL https://rmets.onlinelibrary.wiley.com/doi/abs/10.1002/qj.49711850705, 1992.

Wienhold, F. G.: Compact Backscatter AerosoL Detector (COBALD) Datasheet and Deployment Overview, Tech. rep., Swiss Federal Institute of Technology (ETH), Zürich, Switzerland, URL https://iac.ethz.ch/group/atmospheric-chemistry/research/ballon-soundings.html, last access: 25 April 2020, 2008.

Yan, R.-C., Bian, J.-C., and Fan, Q.-J.: The impact of the South Asia High Bimodality on the chemical composition of the upper troposphere and lower stratosphere, Atmos. Oceanic Sci. Lett., 4, 229–234, 2011.

Yan, X., Konopka, P., Ploeger, F., Podglajen, A., Wright, J. S., Müller, R., and Riese, M.: The efficiency of transport into the stratosphere via the Asian and North American summer monsoon circulations, Atmos. Chem. Phys., 19, 15 629–15 649, doi:10.5194/acp-19-15629-2019, URL https://www.atmos-chem-phys.net/19/15629/2019/, 2019.

Yu, P., Rosenlof, K. H., Liu, S., Telg, H., Thornberry, T. D., Rollins, A. W., Portmann, R. W., Bai, Z., Ray, E. A., Duan, Y., Pan, L. L., Toon, O. B., Bian, J., and Gao, R.-S.: Efficient transport of tropospheric aerosol into the stratosphere via the Asian summer monsoon anticyclone, Proc. Natl. Acad. Sci., 114, 6972–6977, doi:10.1073/pnas.1701170114, URL https://www.pnas.org/content/114/27/6972, 2017.

Yuan, C., Lau, W. K. M., Li, Z., and Cribb, M.: Relationship between Asian monsoon strength and transport of surface aerosols to the Asian Tropopause Aerosol Layer (ATAL): interannual variability and decadal changes, Atmos. Chem. Phys., 19, 1901–1913, doi:10.5194/acp-19-1901-2019, URL https://www.atmos-chem-phys.net/19/1901/2019/, 2019.

Zhang, Q., Wu, G., and Qian, Y.: The Bimodality of the 100 hPa South Asia High and its Relationship to the Climate Anomaly over East Asia in Summer, J. Meteorol. Soc. Jpn., 80, 733–744, 2002.

Zhang, S. and Wang, B.: Global summer monsoon rainy seasons, Int. J. Climatol., 28, 1563–1578, doi:10.1002/joc.1659, URL https://rmets.onlinelibrary.wiley.com/doi/abs/10.1002/joc.1659, 2008.

Zheng, B., Tong, D., Li, M., Liu, F., Hong, C., Geng, G., Li, H., Li, X., Peng, L., Qi, J., Yan, L., Zhang, Y., Zhao, H., Zheng, Y., He, K., and Zhang, Q.: Trends in China's anthropogenic emissions since 2010 as the consequence of clean air actions, Atmos. Chem. Phys., 18, 14 095–14 111, doi:10.5194/acp-18-14095-2018, URL https://www.atmos-chem-phys.net/18/14095/2018/, 2018.

Zhu, Y.: Variations of the summer Somali and Australia cross-equatorial flows and the implications for the Asian summer monsoon, Advances in Atmospheric Sciences, 29, 509–518, 2012.